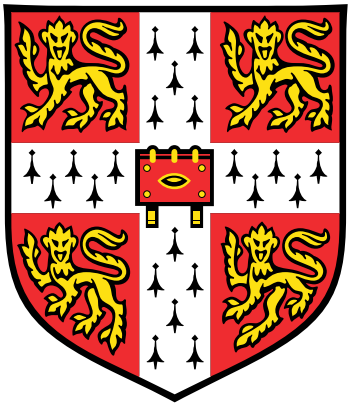
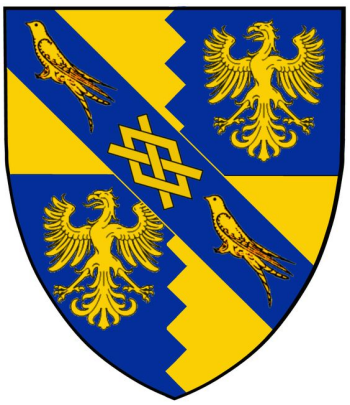


A Theory for Wheezing in Lungs



Alastair Logan Gregory

Department of Engineering

University of Cambridge

This dissertation is submitted for the degree of

Doctor of Philosophy

Magdalene College

October, 2018

Abstract: A Theory for Wheezing in Lungs

Alastair Logan Gregory

A quarter of the world's population experience wheezing. These sounds have been used for diagnosis since the time of the Ebers Papyrus (ca. 1500 BC), but the underlying physical mechanism responsible for the sounds is still poorly understood. The main purpose of this thesis is to change this, developing a theory for the onset of wheezing using both experimental and analytical approaches, with implications for both scientific understanding and clinical diagnosis.

Wheezing is caused by a fluid structure interaction between the airways and the air flowing through them. We have developed the first systematic set of experiments of direct relevance to this physical phenomena. We have also developed new tools in shell theory using geometric algebra to improve our physical understanding of the self-excited oscillations observed when air flows through flexible tubes.

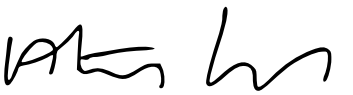
In shell theory, the use of rotors from geometric algebra has enabled us to develop improved physical understanding of how changes of curvature, which are of direct importance to constitutive laws, come about. This has enabled a scaling analysis to be applied to the self-excited oscillations of flexible tubes, showing for the first time that bending energy is dominated by strain energy. We made novel use of multiple camera reconstruction to validate this scaling analysis by directly measuring the bending and strain energies during oscillations. The dominance of strain energy allows a simplification of the governing shell equations.

We have developed the first theory for the onset of self-excited oscillations of flexible tubes based on a flutter instability. This has been validated with our experimental work, and provides a predictive tool that can be used to understand wheezing in the airways of the lung.

Our theory for the onset of wheezing relates the frequency of oscillation to the airway geometry and material properties. This will allow diagnoses based on wheezing sounds to become more specific, which will allow the stethoscope, which has changed little in the last 200 years, to be brought into the 21st century.

Declaration

I declare that except where specific reference is made to the work of others, the contents of this dissertation are original and have not been submitted in whole or in part for consideration for any other degree or qualification in this, or any other university. This dissertation is my own work and contains nothing which is the outcome of work done in collaboration with others, except as specifed in the text and Acknowledgements. This dissertation contains 52 520 (fewer than 65 000) words including appendices, bibliography, footnotes, tables and equations and has 70 (fewer than 150) figures.



Alastair Logan Gregory

October, 2018

Acknowledgements

Firstly to my supervisor Anurag Agarwal, for his patience, advice, and for giving me the oportunity to study something I love. Also to Joan Lasenby, for her advice and help in geometric algebra and computer vision, and for her constant willingness to discuss my work.

To Edwin Chilvers, Sivasothy Pasupathy, John Mclean, and Isla Kuhn for their help with the science and vocabulary of medicine and their advice on clinical practice.

To Will Graham and Stephan Bansmer for reading and advising on articles.

To John Hazelwood, Dave Martin, and Tony Luckett for building my experimental rigs, for their patience, and for helping me to tidy up when the experiments went awry.

To everyone in the Acoustics lab and Fluids group, in particular Ed Kay, Max Nussbaumer, Ben Lyu, and Ross Henrywood, for their dicusssions and tea breaks, it's been great working with you all.

To my parents Caroline and Nigel, and to my sister Ellie, for their unwavering support, and for giving my the chance to spend so much time doing things I enjoy. Also to my friends Michael Sugarman and Wei-Yun Chung for their company, and for regularly putting chocolate in my pigeon hole.

Finally to the Institute of Mechanical Engineers for the Postgraduate Research Scholarship, to the Engineering and Physical Science Reaserch Council for their DTA scholarship, and to Engineering for Clinical Practice for their experimental grant. Without this funding, the work would not have been possible.

Contents

Nomenclature

Acronyms

1 Introduction **1**

1.1 Historical Background . . . 3

1.2 Pros and Cons of Auscultation . . . 5

1.3 Progress in Auscultation . . . 7

2 Literature Review **11**

2.1 Lung Sound Terminology . . . 11

2.2 Clinical Correlations . . . 13

2.3 Anatomy of the Respiratory System . . . 13

2.4 Automated Classification of Lung Sounds . . . 21

2.5 Starling Resistor as a Model for Wheezing . . . 23

2.6 Summary . . . 35

3 Starling Resistor Setup **37**

3.1 Dimensional Analysis . . . 38

3.2 Parameters in Vivo . . . 43

3.3 Previous Experiments . . . 51

3.4 Initial Experiments . . . 54

3.5 Experiment Design Refinement . . . 57

3.6 Experimental Protocol . . . 63

3.7 Summary . . . 66

4 Fundamentals of Elasticity **69**

4.1 Geometric Algebra 69
4.2 Kinematics 71
4.3 Stress 81
4.4 Conservation Laws 86
4.5 Constitutive Laws 88
4.6 Perturbations 89
4.7 Summary 92

5 The Elastic Theory of Shells **93**

5.1 Multivector Frames 93
5.2 Geometry of Curved Surfaces 95
5.3 Kinematics 104
5.4 Stress 119
5.5 Conservation Laws 123
5.6 Constitutive Laws 132
5.7 Perturbations 134
5.8 Summary 138

6 Expt. Repeatability, Defns., Failure of Lin. Theory **141**

6.1 Determining Conditions at Onset 142
6.2 The Effect of Boundary Conditions on Oscillations 144
6.3 Linear Oscillation Modes of Axially Strained Cylinders 148
6.4 Group and Phase Velocity 167
6.5 Summary 169

7 3D Tube Motion: Stereo Reconstr. and Scaling **171**

7.1 Three dimensional Reconstruction 171
7.2 Kinematic Calculations 177
7.3 Scaling Analysis 179
7.4 Summary 184

8 Mechanism for the Onset of Wheezing **187**

8.1 High Speed Video of Onset 188

8.2 Equilibrium of the Tube 189

8.3 Equilibrium of the Fluid 197

8.4 Stability 201

8.5 Applying the Mechanism to the Lung 210

8.6 Summary 214

9 Conclusions **215**

References **217**

Appendix A Work Done by Bivector Torque **233**

Index **235**

Nomenclature

Roman Symbols

a	undeformed inner radius of flexible tube
A_1	cross-sectional area of the rig where p_1 is measured
A_2	cross-sectional area of the rig where p_2 is measured
A_c	cross-sectional area of flexible tube at its narrowest point
$\mathcal{B}$	reference configuration
B	second fundamental form on the reference configuration
b	second fundamental form on the spatial configuration
B	characteristic bivector of the rotor $R = \exp(-B/2)$
b	body force per unit mass
C	Cauchy-Green tensor
c	Cauchy deformation, Piola, or Finger tensor
C	principle curvature of undeformed flexible tube
C_1, C_2	principal curvatures of the reference configuration
c_1, c_2	principal curvatures of the spatial configuration
c_g	group velocity
c	body moment per unit mass (bivector valued)

$\boldsymbol{c}$	body moment per unit mass (vector valued)
c_p	phase velocity
d	undeformed inner diameter of flexible tube
d^n	diameter of airway of order n in Horsfield model
dS	directed boundary element on the reference configuration
ds	directed boundary element on the spatial configuration
dX	directed element of the reference configuration
dx	directed element of the spatial configuration
E	Green-Lagrangian strain tensor
e	spatial, or Eulerian-Almansi, strain tensor
E	Young's modulus
$\{E_A\}$	frame for the tangent space of the reference configuration
$\{e_a\}$	frame for the tangent space of the spatial configuration
$\{E^A\}$	reciprocal frame for the tangent space of the reference configuration
$\{e^a\}$	reciprocal frame for the tangent space of the spatial configuration
$\mathbb{E}^n$	n-dimensional Euclidean space
F	deformation gradient
f	dominant frequency of self-excited oscillations of flexible tube
f_1	function determining the relationship between the pressure drop in the upstream section of the flexible tube rig and the flowrate through it
f_2	function determining the relationship between the pressure drop in the downstream section of the flexible tube rig and the flowrate through it
$\mathbf{F}$	modified deformation gradient

Nomenclature

f_D Darcy friction factor

f_d function determining the relationship between the pressure drop in the downstream sections of the experimental rig and the flowrate through it

f_f fluid law

f_t tube law

f_u function determining the relationship between the pressure drop in the upstream sections of the experimental rig and the flowrate through it

G identity function (metric tensor) on the reference configuration

g identity function (metric tensor) on the spatial configuration

H change of curvature tensor

h shell thickness (undeformed wall thickness of flexible tube)

h^n wall thickness of airway of order n in Horsfield model

I local pseudoscalar on the reference configuration

i local pseudoscalar on the spatial configuration

I_n pseudoscalar of n-dimensional Euclidean space

K_c loss coefficient for contraction

K_d loss coefficient for diffuser

L rate of deformation tensor defined on the reference configuration

l rate of deformation tensor defined on the spatial configuration

l length of flexible tube

l_0 unstrained length of flexible tube

L^- rotation rate tensor defined on the reference configuration

l^- rotation rate tensor defined on the spatial configuration

l^n	length of airway of order n in Horsfield model
L^+	symmetric rate of deformation tensor defined on the reference configuration
l^+	symmetric rate of deformation tensor defined on the spatial configuration
M	first reference couple-stress tensor
m	spatial couple-stress tensor
m	number of camera positions
$\mathbf{M}$	modified first reference couple-stress tensor
$\mathbf{m}$	modified spatial couple-stress tensor
N	second reference couple-stress tensor
N	unit normal vector to surface in the reference configuration
n	§3: airway order in Horsfield model, §§4 and 5: unit normal vector to boundary in the spatial configuration, §8 number of world points
$\mathbf{N}$	modified second reference couple-stress tensor
p	projection operator
p	dimensionless tube length parameter, equal to $l_0/2a$
p_1	pressure just upstream of flexible tube
$\bar{p}_1$	time averaged pressure just upstream of flexible tube
p_2	pressure just downstream of flexible tube
$\bar{p}_2$	time averaged pressure just downstream of flexible tube
p_a	acoustic pressure
p_c	pressure inside flexible tube at its narrowest point
p_e	external or environmental pressure
$\mathsf{p}_\perp$	rejection operator

Nomenclature

p_{tm} transmural pressure

Q time averaged flow rate through flexible tube

$\dot{Q}$ heat addition per unit mass per unit time to a body from external sources, defined on the reference configuration

$\dot{q}$ heat addition per unit mass per unit time to a body from external sources, defined on the spatial configuration

$\mathfrak{Q}$ heat flux per unit area defined on the reference configuration

$\mathfrak{q}$ heat flux per unit area defined on the spatial configuration

R the rotor associated with the rotation function $\mathsf{R}(Y) = RY\tilde{R}$

$\mathsf{RU} = \mathsf{VR}$ polar decomposition of the deformation gradient F

$\mathcal{S}$ spatial configuration

s dimensionless longitudinal coordinate

S second Piola-Kirchhoff stress tensor

t time

t_n surface traction acting on the spatial configuration

T first Piola-Kirchhoff stress tensor

$T_X\mathcal{B}$ tangent space of $\mathcal{B}$ at $X \in \mathcal{B}$

U second order rate of deformation tensor, defined on the reference configuration

u second order rate of deformation tensor, defined on the spatial configuration

$\mathcal{U}$ subregion of the reference configuration $\mathcal{U} \subseteq \mathcal{B}$

U internal energy per unit mass defined over the reference configuration *or* the reference displacement vector

u internal energy per unit mass defined over the spatial configuration *or* the spatial displacement vector

u, v §§7 and 8: pixel coordinates

V local velocity of body defined on the reference configuration

v local velocity of body defined on the spatial configuration

$\mathfrak{V}$ volume form on the reference configuration

$\mathfrak{v}$ volume form on the spatial configuration

W characteristic bivector of the rotation rate tensor L^-, defined on the reference configuration

X material point in the reference configuration

x point in the spatial configuration

$\{X^A\}$ coordinate system over the reference configuration

$\{x^a\}$ coordinate system over the spatial configuration

x, y §8: camera coordinates

Greek Symbols

α dimensionless tube thickness parameter, equal to $h^2/12a^2$

Δ^n recursion index of airway of order n in Horsfield model

ϵ size of perturbation in linear analysis

ε initial axial strain of flexible tube, equal to $(l - l_0)/l_0$ and $\lambda - 1$

Γ^A_{BC} Christoffel coefficients of the frame on the reference configuration

γ^a_{bc} Christoffel coefficients of the frame on the spatial configuration

λ initial axial strain of flexible tube, equal to l/l_0 and $\varepsilon + 1$

λ_a principal strains

μ dynamic viscosity of fluid

ν Poisson's ratio

Nomenclature

Ω §§4 and 5: angular velocity defined on the reference configuration, §6: dimesionless frequency

ω §§4 and 5: characteristic bivector of the rotation rate tensor w, defined on the spatial configuration, equal to the local angular velocity on the spatial configuration, §6: angular frequency

ϕ_t a motion of the spatial configuration $\mathcal{B}$

ρ §3: density of fluid, §§4 and 5: density of elastic material on the spatial configuration

ρ_0 time independent density on the reference configuration, §4: mass per unit volume, §§5 and 6: mass per unit area

ρ_s density of tube material (mass per unit volume)

σ Cauchy stress tensor

τ dimensionless time coordinate

θ dimensionless azimuthal coordinate

Other Symbols

Dc dynamic to collapse pressure ratio

D/Dt material derivative

ΔP_{12} dimensionless pressure drop along flexible tube

$\Delta \bar{P}_{12}$ time averaged dimensionless pressure drop along flexible tube

ΔP_{1e} dimensionless transmural pressure drop at upstream end of flexible tube

$\Delta \bar{P}_{1e}$ time averaged dimensionless transmural pressure drop at upstream end of flexible tube

ΔP_{2e} dimensionless transmural pressure drop at downstream end of flexible tube

$\Delta \bar{P}_{2e}$ time averaged dimensionless transmural pressure drop at downstream end of flexible tube

∇	vector derivative
∂	vector derivative intrinsic to a manifold
$(\cdot)'$	prime indicates a quantity associated with a small perturbation to a body
Re	Reynolds number
St	Strouhal number
$(\cdot)_0$	subscript 0 indicates a quantity associated with an in general large deformation that satisfies the static equations of equilibrium
Wo	Womersley number

Acronyms

CFI clean flow inlet. 59, 60

CFT clean flow tube. 60

COPD Chronic Obstructive Pulmonary Disease. 15, 16

CT Computed Tomography. 5

DCFT downstream clean flow tube. 59, 60, 64, 65, 67, 144, 146, 147

DSC downstream settling chamber. 62, 64, 66

FT flexible tube. 57, 59–62, 64–66

GP General Practitioner. 6, 8

ID inner diameter. 37, 59, 61

PEFR peak expiratory flow rate. 49

RH relative humidity. 43–45

SC settling chamber. 57, 59

UCFT upstream clean flow tube. 59, 60, 64, 65, 67, 144, 146, 147

USC upstream settling chamber. 59, 62, 64, 66

VCD Vocal Chord Dysfunction. 7

Chapter 1

Introduction

Lung sounds offer a cheap, non-invasive, non-radioactive source of information on pathology in the upper chest [Weitz and Mangione, 2008], but diagnoses based on these sounds lack specificity [Bohadana et al., 2014] and repeatability [Francis et al., 2013; Williams et al., 2009]. We can improve specificity by understanding the mechanisms producing lung sounds. Wheezing is one of the most common lung sounds, present in around one quarter of the population [Bohadana et al., 2014; Forgacs, 1978a], but we still do not understand the mechanism behind its onset.

The frequencies of wheezing sounds are largely independent of the density of the fluid flowing in the airways [Forgacs, 1978a; Shabtai-Musih et al., 1992]. This rules out mechanisms based on the resonance of the air cavity [Forgacs, 1978a]. In addition, in an excised dog trachea it was found that when air was sucked through it, under certain conditions, the trachea itself began to oscillate, creating wheezing sounds [Gavriely et al., 1989]. These observations provide strong evidence that wheezing is heard when the flexible tubes that make up the airways of the lung oscillate as air flows through them, as was first suggested by Grotberg and Davis [Grotberg and Davis, 1980]. The work of [Gavriely et al., 1989] has inspired us to develop a quantitatively accurate model for the onset of wheezing as a step towards improving specificity of diagnosis. To do this we need to extend the experimental results of [Gavriely et al., 1989], specifically sweeping over the variety of geometric parameters that define the flexible tubes that make up the airways of the lung. We must consider a wider variety of tube lengths, diameters and wall thicknesses, and most significantly, must consider the effect of axial pre-tension, which is present in the airways [Hoppin et al., 1977].

Understanding self excited oscillations as fluid flows through flexible tubes has been the subject of many studies, both experimental and theoretical. The experimental setup of a flexible tube clamped at both ends with a fluid flowing through it is referred to as a Starling resistor. [Kamm and Pedley, 1989] provides a review of work prior to 1989, and gives the following useful conclusion,

> "One of the main lessons to be learned is that it is vital for experimentalists to describe, quantitatively, all aspects of their experiment, because no one yet knows that any of them are unimportant, especially during oscillations, and for theoreticians to recognize that just because they have a model that produces something qualitatively similar to what is observed (e.g. an oscillation) it does not mean that have given a mechanical explanation for any particular observation."

Our first aim is to achieve the requirement for experimentalists with our present work. The theoreticians being referred to by [Kamm and Pedley, 1989] produce various low order lumped parameter models of flow through flexible tubes (for example [Bertram and Pedley, 1982; Cancelli and Pedley, 1985]). As [Kamm and Pedley, 1989] says, these models produce interesting phenomenology, but are not quantitatively accurate, which we require here. Our second aim is to produce a quantitative model based on our experimental work that can be applied directly to the lung.

More recent work in the field is reviewed by [Bertram, 2003; Grotberg and Jensen, 2004; Heil and Hazel, 2011; Heil and Jensen, 2003; Jensen, 2013; Kizilova et al., 2012]. With the exception of [Gavriely et al., 1989], the experimental work has used water as the working fluid. These experiments have produced an extensive catalogue of behaviour, but the use of water means that the ratio of the density of the fluid to the tube wall is wrong for the lung by a factor of around 10^3. Theoretical work has gradually increased the complexity of the models under consideration, starting with a two dimensional analogue of the Starling resistor. Both linear stability [Burke et al., 2014; Davies and Carpenter, 1997; Huang, 1998, 2001; Liu et al., 2009a, 2011, 2009b; Luo et al., 2008, 2007; Stewart et al., 2010] and direct numerical simulation [Cai and Luo, 2002; Luo and Pedley, 1996, 1998; Xu et al., 2013, 2014; Zhang et al., 2005] have been considered. In a similar way to the lumped parameter models, the two dimensional models produce interesting phenomenology, but cannot be used quantitatively. Theoretical work on the three dimensional system has progressed a lot since

the 1990s. Linear stability analysis has been completed by [Hamadiche and Gad-el Hak, 2002; Kumaran, 1995a,b, 1998], and more recently [Whittaker et al., 2010b]. While [Whittaker et al., 2010b] had some success predicting the frequency of self excited oscillations, it assumed that the inertia of the tube wall could be ignored, and this reduces its relevance to the lung, since the density of the tube wall is so much greater than the fluid. Wall inertia has been included in a linear stability by [Walters et al., 2017], however, this work assumes that the instability has a long wavelength. In the lung the tubes generally have lengths less than four times their diameters, which reduces the applicability of this work.

Huge strides have been made in developing our theoretical understanding of Starling resistors, producing plenty of candidate mechanisms, but as yet they do not allow quantitative predictions to be made for the frequencies and flowrates at onset in the specific context of the lung. One approach might be to attempt to extend the linear stability analysis of [Walters et al., 2017], but we have instead chosen to combine a new approach using the shell theory of large deformations with a return to simpler lumped parameter modelling, in particular taking inspiration from [Cancelli and Pedley, 1985]. Our reason for this is that we have observed in our experiments that oscillations are seen to start when the flexible tube is already strongly collapsed, when the Reynolds number (based on the undeformed tube diameter) is around 10^3, hence the state about which we would need to linearise in order for a linear stability analysis to be useful is currently too complex to be practical, and should be regarded as a possible avenue for further study. Rather, we intend to look for a basic physical mechanism supported by evidence that allows the development of a quantitatively useful but simple model.

The remainder of this introduction will be spent providing the clinical background to the problem we are interested in solving. The next chapter will then be used to give a much more detailed review of previous research.

1.1 Historical Background

There are records of techniques for medical diagnosis from various historical sources. Examples include the Edwin Smith Papyrus (ca. 2600 BC), the Ebers Papyrus (ca. 1500 BC), the Hindu Vedas (ca. 1400 BC), a diagnostic handbook written by Esagil-kin-apli (ca. 1000 BC), the Yellow Emperor's Inner Canon (ca. 100 BC), and writings of Hippocrates (ca. 400

BC). The Ebers Papyrus, the Hindu Vedas and Hippocrates all mention listening, usually at the chest, as a method of investigating a patients health, known as **auscultation**. However it was not until 1816 that the use of a **stethoscope** was suggested by René Laënnec (1781–1826), who published his seminal work on the subject in 1819 [Laënnec, 1819b], which was later translated into English [Laënnec, 1819a] with the help of John Forbes (1787–1861)*.

The 19th century saw an explosion in the development of medical devices and the discovery of new physical signs useful to diagnosis. For example, the stethoscope, thermometer, sphygmomanometer and spirometer brought the observation of chest sounds, body temperature, blood pressure and lung capacity into standard medical practice during this period. At the same time specimen analysis in the lab was becoming increasingly sophisticated, and the development of X-rays marked the birth of increasingly complex imaging methods [Röntgen, 1896]. These trends continued into the 20th century, with the result that the field of diagnosis started to split into different areas, with larger and larger portions of textbooks taken up by the complicated laboratory methods and imaging techniques that required less interaction with the patient [Verghese et al., 2010]. There have also been an increasing number of bedside devices developed that a doctor may use with the patient, but that provide an objective image or numerical output. Examples of this include ultrasound [Sarvazyan et al., 2013], printable transistors for protein biomarker detection [Medina-Sánchez et al., 2014], and glucose monitoring devices [Malhotra and Chaubey, 2003], with the last of these demonstrating a further progression from the bedside to self diagnosis. The devices used in these techniques represent a midway point between the laboratory and the more old fashioned physical exam. They allow quick and cheap evaluation of a patient, but with an objective output. They do not replace the lab, but rather make it more cost effective, helping to ensure that complex tests are not undergone needlessly. A thorough review of all of the diagnostic techniques currently in use is beyond the scope of this thesis, and arguably beyond the scope of any textbook published today. Instead the focus here is on a single technique, auscultation. We make the argument that this particular technique offers a good opportunity for development using expertise in vibrations, acoustics, and fluid mechanics, and could be developed into a good example of a bedside diagnostic technique.

*Entertainingly, it has been suggested that the main reason that Laënnec invented the stethoscope was that he was too embarrassed to put his ear to the chests of his female patients, and the improvement in the quality of the sounds heard was a happy accident.

1.2 Pros and Cons of Auscultation

A commonly used stethoscope is the Littmann Cardiology III [Finkelstein, 2008]. This is on the market for approximately £150, while an electronic version of the stethoscope costs around £300 (Littmann 3200). This compares with a cost of around $8000 for a bedside ultrasound unit and $100 000 for a Computed Tomography (CT) scanner. The simplicity of the technology results in a relatively low cost, and lends itself to the small bedside device market. Auscultation also shares the advantages of being non-invasive and non-radioactive with ultrasound. The risks of radiation are well documented [Cousins and Sharp, 2004; Jung et al., 2013; Pantos et al., 2009; Picano and Vano, 2011], indeed, a recent National Council on Radiation Protection and Measurements report put the contribution of CT and nuclear imaging to the total radiation exposure of Americans at 36 % [National Council on Radiation Protection and Measurements, 1987]. Auscultation provides an ideal bedside test used to reduce the need to put patients through the risks of more sophisticated imaging.

Given the shared advantages of auscultation and ultrasound it is natural to ask what advantage auscultation has over ultrasound. Ultrasound waves have a frequency of at least 10 kHz, and more usually over 1 MHz. The propagation speed of these waves through tissue is at least $1000\,\mathrm{m\,s^{-1}}$ [Rueter et al., 2010]. By contrast, the sounds used in auscultation have a frequency of less than 2 kHz, and a propagation speed closer to $30\,\mathrm{m\,s^{-1}}$ [Kraman, 1983]. Between 2 kHz and 10 kHz waves do not appear to propagate through the chest [Rueter et al., 2010], meaning that if we desire to probe the state of the inner chest we are restricted to ultrasound and auscultation. This empirical dependence of propagation speed on frequency is shown in Figure 1.1. The high frequency, and corresponding small wavelength, of ultrasound waves allows high resolution images to be produced of the chest. However, due to the high impedance mismatch between air and tissue, ultrasound waves are almost completely reflected at boundaries between the two. This means that in the lung, ultrasound waves can propagate at most a few centimetres into the chest, making imaging of the inner lung impossible. Therefore, the low frequency sounds of auscultation provide a good opportunity to investigate the internal structure of the upper chest not offered by ultrasound.

Given the advantages of auscultation outlined above, the obvious question is, why is its use at the bedside regarded by some as defunct? Two main criticisms have been levelled.

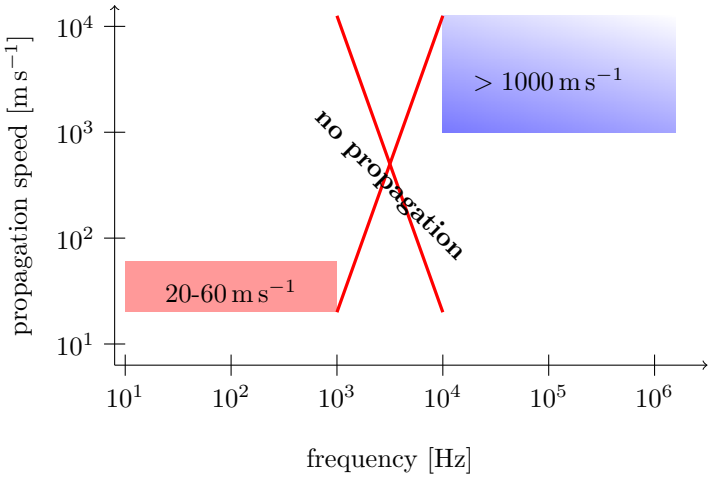


Figure 1.1: The empirical dependence of wave propagation speed through the human chest on frequency, adapted from [Rueter et al., 2010].

[Leuppi et al., 2005] reviewed the use of auscultation in an emergency room setting with mixed results regarding its effectiveness as a predictor of outcome. [Markel, 2006, p.552] assures the reader that,

> "the stethoscope has not yet achieved quaintness, like the medieval physician's urine flask, but it is safe to assume that it, too, will someday be relegated to a museum shelf."

Markel's argument is one of obsolescence. The stethoscope is too subjective as a diagnostic tool, relying heavily on training. [Williams et al., 2009] has indicated that the teaching of lung sounds is possibly flawed, and [Francis et al., 2013] has shown possible deficiencies in their use by General Practitioners (GPs). Good use of a stethoscope relies on training and experience, and it is possible that less time is being spent on this due to the need to train new practitioners in the use of more sophisticated diagnostic methods. Whatever the reason, it would appear that the subjective nature of the use of lung sounds in diagnosis is limiting their utility, though it should be noted that teaching of the method has by no means been abandoned completely [Ferns and West, 2008]. As will be seen in §2.4, there has been a considerable effort to reduce the subjectivity of lung sound analysis, however, this is not the only problem with auscultation. As well as identifying particular lung sounds, these sounds must be linked with a particular pathology. These links are often referred to as **clinical correlations**. The second problem with auscultation is that the clinical correlations associated with a particular identified sound are not very specific. Hearing a

wheeze can indicate any of the conditions listed in table 2.2. This creates a difficulty in producing an accurate diagnosis, which has been noted in particular in asthma. [Dodge and Burrows, 1980] gives the percentage of the population suffering from asthma as 7 %, while around 25 % present wheezing, so it is perhaps not surprising that misdiagnosis of conditions such as Vocal Chord Dysfunction (VCD) as asthma have been reported [Traister et al., 2014]. Hence the two problems that must be dealt with if auscultation is to be a useful diagnostic tool are the subjectivity, and lack of specificity of the technique.

1.3 Progress in Auscultation

Now the questions become, what are the reasons for the problems with auscultation, and how can they best be fixed? We have already outlined the significant advantages of using lung sounds, which should motivate a desire to try to improve the technique so that these advantages may be exploited.

First we consider the reason for the lack of specificity of the diagnosis using auscultation. This is fundamentally linked to the lung sound classification system in current use, since it is these classifications that are linked to particular pathologies. In fact, there is still some controversy over how lung sounds should be classified. The sounds heard at the chest through a stethoscope during normal breathing are called **vesicular sounds**, while sounds that are associated with pathology are termed **adventitious**. A sub-classification of adventitious sounds was made by [Robertson and Coope, 1957] and supported by [Forgacs, 1967], who said that sounds with identifiable tone(s) should be referred to as **wheezes**, and sounds without identifiable tone(s) should be referred to as **crackles**. This definition has survived to today, as can be seen from reviews of lung sounds made since 1957 [Bohadana et al., 2014; Forgacs, 1978b; Pasterkamp et al., 1997; Reichert et al., 2008], however, more specific sub-classification is still contentious. The most recent review attempted a more sophisticated classification, for example using the word **rhonchus** to refer to a low pitched tonal sound heard on inspiration or expiration, but this was not well received by all, with some preferring the original definitions of Robertson and Coope, [Coleman et al., 2014]. A review of terminology used in Brazil between 1980 and 2003 shows similar confusion [Staszko et al., 2006]. A relatively complete dictionary of terms used was compiled as part of the Computerised Respiratory Sound Analysis (CORSA) project [Sovijarvi et al., 2000], but the point is

that not all of these terms are universally understood or have universally agreed definitions. The fact remains therefore that lung sound classifications have barely changed in the last 50 years, and this puts a fundamental limit on the sophistication of the clinical correlations that can be discovered. A possible reason for the lack of a more sophisticated classification lies in current clinical understanding of how the sounds are produced and propagate. This will be discussed in much more detail in §2, and is ultimately the main subject of this project, but for now it is noted that much of current understanding, at least within a clinical setting, of the mechanisms behind the sounds heard through the chest originates in a short book on the subject [Forgacs, 1978a]. While this book is in itself excellent, this clearly illustrates the need to bring understanding up to date, and in doing so aim to introduce a rational classification for use in diagnosis.

Second we consider the subjectivity of lung sound classification. This has already been discussed at some length above, the problem being that good use of auscultation relies on training that is hard to guarantee. On top of this can be added confusion over terminology, as discussed in the previous paragraph, which can make communication of subtle differences difficult. A clear solution to these problems is an automated system of classification (i.e. computerised), which provides an easily interpreted numerical or visual output. Conversations between this author and GPs have indicated that at the bedside the immediacy of a numerical output could be preferable, but it is really too early for this argument. Computerised lung sound analysis is reviewed in more detail in §2.4, but it is noted here that such automation must make use of the classifications already discussed, and hence would benefit from a better fundamental understanding of the sounds, which would allow more specific classification. It is also worth noting that automated classification typically relies upon extracting significant metrics from the recordings, which are then used in k-nearest neighbour or artificial neural network algorithms [Reichert et al., 2008], and the rational definition of metrics can benefit from fundamental understanding of propagation and production mechanisms.

To conclude the introduction, hopefully the reader will have been persuaded that auscultation provides many advantages as a diagnostic tool, in particular in a bedside setting, which are currently not being exploited, and that development of the technique requires better understanding of the fundamental mechanisms of sound production and propagation. This argument is further developed in the literature review which follows, and it is the pri-

mary aim of this project to work towards a better fundamental understanding of lung sounds, with the ultimate aim of bringing the stethoscope into the 21st century.

Chapter 2

Literature Review

We begin with a detailed review of terminology (§2.1) and clinical correlations (§2.2), building on §1.3, and provide an overview of the relevant anatomy in §2.3, since this will inform later sections. Automated classification methods are reviewed in §2.4, revealing a mature field, but one which is still hampered by a lack of physical understanding of lung sounds. In §2.5 we review work relevant to understanding the mechanism behind the onset of wheezing. The introductory literature for this is reviewed in §2.5.1, revealing a promising proposed mechanism based on an experimental rig referred to as a Starling resistor. A citation analysis is used in §2.5.2 to show that while there is a considerable literature investigating this experiment, there has been little work connecting this to wheezing, and this is where our work will focus. The Starling resistor literature is reviewed in §2.5.3 and §2.5.4, revealing a need both for new experiments that have direct relevance to wheezing, and modelling to understand these new experiments. In §2.5.5 we review shell theory, since this is necessary for the modelling of the starling resistor. Since much of our focus is on physical understanding of the mechanism, this reveals a need for the development of our own shell theory.

2.1 Lung Sound Terminology

The terminology presented by several recent reviews is summarised in table 2.1. We have chosen recent reviews since terminology has changed significantly since the invention of the stethoscope [Weitz and Mangione, 2008]. [Sovijarvi et al., 2000] provides a large dictionary of terms, including several used for particular types of lung sound. [Staszko et al., 2006] tabulates different terms along with frequency of use in their sample of publications. Staszko

et al. also split their terms into "continuous" and "intermittent" sounds. Earlier it was suggested that sounds should be split into tonal and non-tonal sounds (wheezes and crackles), and while the pairs "continuous" and "tonal", and "intermittent" and "non-tonal" are not technically synonymous, looking at the terms used under each of the two categories in [Staszko et al., 2006], it is clear that these two broad classification systems are in fact equivalent. A list of sounds with definitions is provided by [Reichert et al., 2008], and tables with both definitions and clinical correlations for each sound are provided by [Andrès et al., 2012] and [Bohadana et al., 2014]. The controversy of Bohadana et al.'s use of more sophisticated terms than wheeze and crackle has already been noted, and [Andrès et al., 2012, p.6] makes the comment,

> "only a small number of sounds are currently well identified in clinical practice, including wheezing and crackles".

The basic definition of the terms wheeze and crackle are agreed upon by all of the above authors, however, it should now be clear that a general consensus over sound classifications more complex than the simple wheeze and crackle is lacking. [Staszko et al., 2006] provides further evidence for this, pointing out that correct use of the terminology associated with lung sounds, as defined by these authors, is present in only 1/3 of the papers they review. Therefore, in this thesis only the terms **wheeze** and **crackle** will be used as already defined. As already noted the term **vesicular sound** will refer to healthy sounds, and **adventitious** to sounds associated with pathology.

The term **pleural rub** refers to the rubbing sound of the lung against the chest wall heard in conditions such as pleural inflammation or pleural tumours. We suspect that this sound is produced by a stick slip interaction between the pleura and chest wall, however, we will not be focussing on this since the sound is very rare, and consequently understanding the sound will have a limited impact. **Rhonchus** is simply snoring, and is beyond the scope of this project, though it has been investigated with some success already [Ellis et al., 1992; Huang and Ffowcs Williams, 1999; Huang et al., 1995]. Coughing is similarly outside the scope of this project, which is limited to sounds generated within the lung.

It should be noted that while a general consensus over terminology does not appear to have been reached, this does not mean that a more sophisticated classification is not used by some individual doctors. However, the lack of consensus means that such practitioners

will not be able to reliably communicate the subtle variations in sound that they observe, severely limiting the utility of lung sounds.

2.2 Clinical Correlations

The **clinical correlations** of lung sounds were discussed in §1.2, highlighting the lack of specificity. Tables 2.2 and 2.3 summarise a more detailed review of correlations of wheezing and crackling (crackling is included for completeness, though it will not influence this work). This should highlight more clearly the large number of conditions associated with the sounds, and also indicates that a general consensus is yet to be reached. Easily the most cited correlation is that between wheezing and asthma, however, the validity of asthma as a single clinical condition has recently come into question itself. An editorial in the Lancet [Lancet, 2006] argues that asthma should not be regarded as a single disease. This further demonstrates the possible confusion surrounding diagnosis using lung sounds as they are currently classified. Better classifications are needed, and for this a better understanding of how sounds are produced is required.

2.3 Anatomy of the Respiratory System

There are a very large number of sources for the anatomy of the respiratory system. We have found that the software package "Complete Anatomy" [Complete Anatomy, 2017] provides a good introduction, together with discussions with medical practitioners. The classic text on the subject is Gray's Anatomy [Standring, 2015].

2.3.1 Gross Anatomy

The primary purpose of the respiratory system is gas exchange, i.e. to extract carbon dioxide from the circulatory system, and replenish oxygen. It consists of a network of airways starting at the mouth and nose, and terminating with alveoli. At the alveoli gasses are exchanged with capillaries of the pulmonary circulatory system.

The **upper respiratory tract** joins the nose and mouth to the top of the **trachea**. It consists of both the **oral** and **nasal cavities**, which are joined at the back of the throat by the **pharynx**. The pharynx travels down to the top of the oesophagus and **larynx**. The

	Sovijarvi et al. [2000]	Staszko et al. [2006]*	Reichert et al. [2008]	Andrès et al. [2012]	Bohadana et al. [2014]
Healthy sounds, or sounds defined by microphone position.	vesicular sound bronchial sound tracheal sound	– – –	– – –	vesicular murmur bronchial breathing –	– bronchial breathing tracheal sound
Non-tonal sounds.	crackle fine crackle course crackle	crackle/rale fine crackle/rale course rale	crackle – –	– fine crackle/rale coarse crackle/rale	– fine crackle coarse crackle
Tonal sounds.	wheeze – – squawk stridor	wheeze sibilance deep wheeze – –	wheeze – – squawk stridor	wheeze whistle amphoric breathing – –	wheeze – – squawk stridor
Other sounds.	pleural friction sound rhonchus –	– rhonchi –	– rhonchus cough	pleural rub rhonchi/snoring –	pleural friction rub rhonchus –

Table 2.1: Lung sound terminology used by various authors. The terms defined by several reviews are listed. These are put into 4 general groups, and repetition, near repetition, or equivalence of terms is indicated by rows in the table.

*This review also provides a large number of terms for non-tonal sounds which are not provided by the other sources; these are wet rale, rhonchial rale, crackling rale, subcrackling rale, bullae, small-bulla rale, medium-bulla rale, large-bulla rale, small-bulla subcrackling rale, medium-bulla subcrackling rale, and large-bulla subcrackling rale.

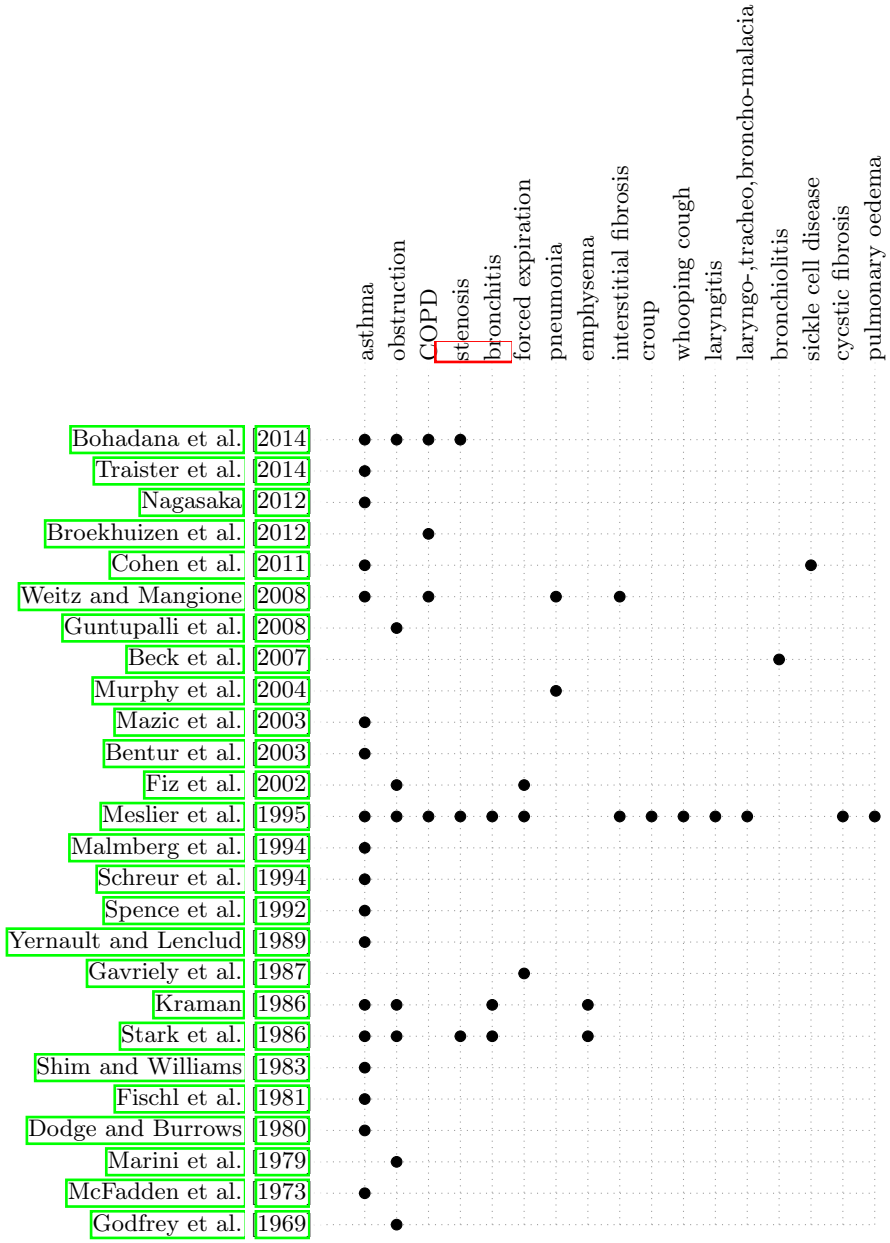


Table 2.2: Clinical correlations of wheezing according to the literature.

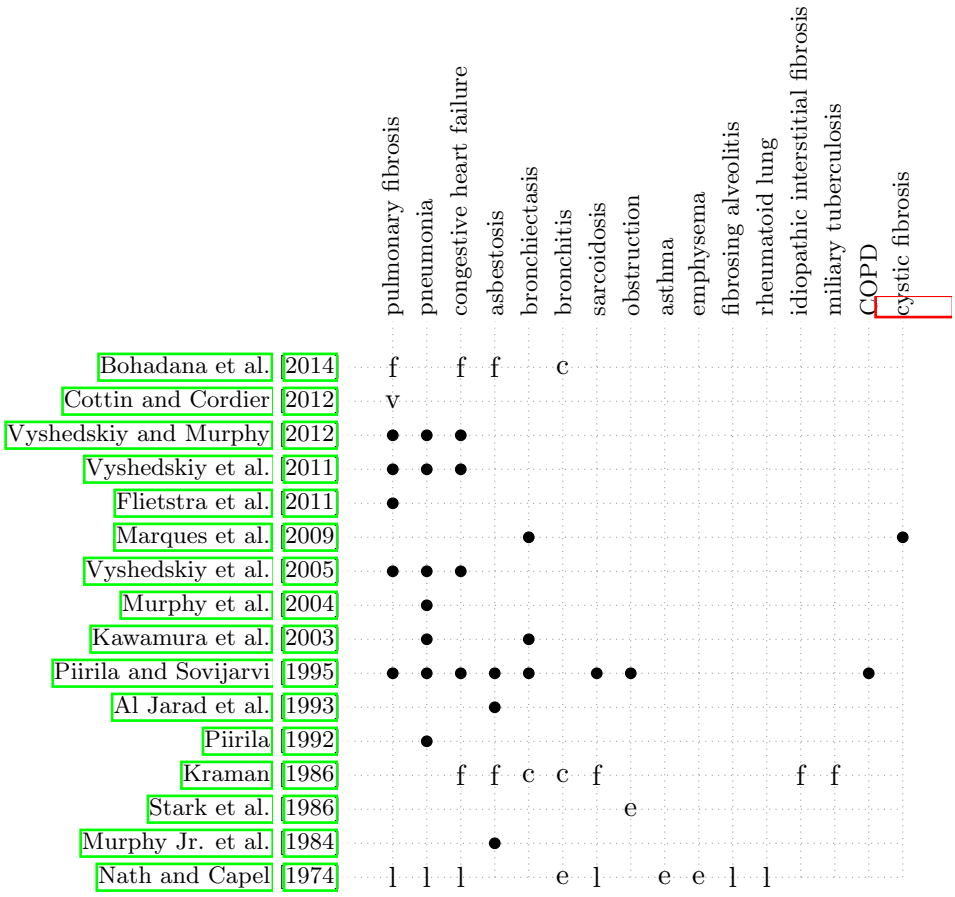


Table 2.3: Clinical correlations of crackling according to the literature (letters indicate the following adjectives for the crackle; e="early", l="late", f="fine",c="course", v="velcro").

larynx is a complex structure, containing the vocal chords, that is attached to the top of the trachea, marking the top of the lower respiratory tract.

The trachea travels downwards until it branches into the primary (or main) **bronchi**. These in turn branch into the secondary (or lobar) bronchi, followed by the tertiary (or segmental) bronchi. After this the branches of the airways are called **bronchioles** (technically, the difference between bronchi and bronchioles is that the former have cartilage in the walls, which the latter lack), which keep on dividing, and eventually terminate in clusters of **alveoli**. This branching network of tubes is called the respiratory tree, and consists on average of around 23 generations and 150 million alveoli (in humans).

There is a second branching network in the lungs made up of the pulmonary circulatory system. This differs from the respiratory tree in that the blood vessels do not terminate. Rather there are effectively two circulatory trees, one of arteries and the other of veins, that are connected together by capillaries that surround the alveoli. The tree of arteries tends to follow the respiratory tree towards the alveoli, meaning that bronchioles are frequently accompanied by an artery. By contrast the tree of veins is largely independent of the respiratory tree.

The respiratory and circulatory trees meet at the alveoli. Alveoli are generally clustered together around the final parts of the respiratory tree, usually called the **alveolar ducts**. The alveoli cluster together so tightly that the alveolar ducts do no usually have any well defined wall, rather there is a complex network of walls that break up the space within the lungs into small volumes. These walls contain the capillaries, as well as various tissues (the histology is discussed further in §2.3.2). This complex network of walls containing capillaries and elastic tissue is called the **parenchyma**, or simply **lung tissue**. From the perspective of someone holding an excised lung, this feels like a delicate spongy and elastic material, which is interspersed with larger airway tubes.

The term “tree” is often used to describe the branching network of airways in the lung, however this misleading in some respects. Topologically the two are similar in that they both involve the gradual subdivision of branches. However, the purpose for a botanical tree is to create a reasonably uniform covering in which all leaves get enough sunlight to photosynthesise. This is not the case in the lung. Gas exchange can happen at any point throughout the lung as long as there are alveoli connected to capillaries present. The respiratory tree doubles back on itself, and the smallest airways are distributed throughout the lung, as is illustrated

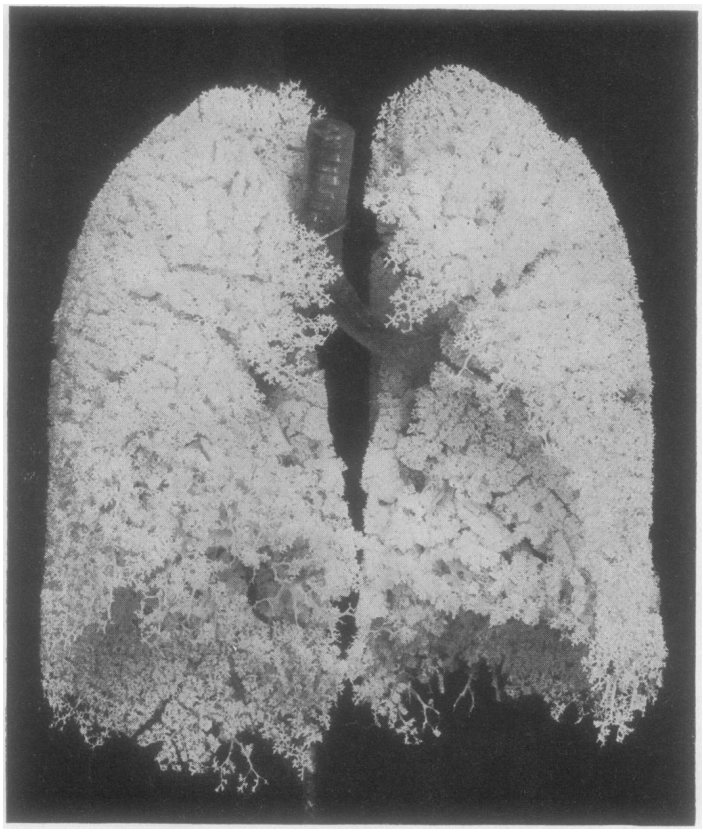


Figure 2.1: Cast of adult human bronchial tree, before pruning (reproduced from [Tompsett, 1952] with permission).

by the lung cast in fig. 2.1, with the larger bronchi and bronchioles passing through the parenchyma as they divide, as can be seen in fig. 2.2, where the smaller airways have been pruned away. In fig. 2.3, casts of the artery and vein trees have been included alongside the airways. Further informative images of this are provided by [de Jong et al., 2006; Gutiérrez and Leon, 2000].

2.3.2 Histology

The airways are divided into two categories in terms of their main function. These are the conducting airways and the respiratory airways. The conducting airways consist of the trachea, bronchi, and bronchioles. The respiratory airways consist of the respiratory bronchioles, alveolar ducts, and alveoli. We will work our way down these airways and discuss their microscopic structure (histology). The main takeaway from this section will be some material properties, which will be important in §3.2.1.

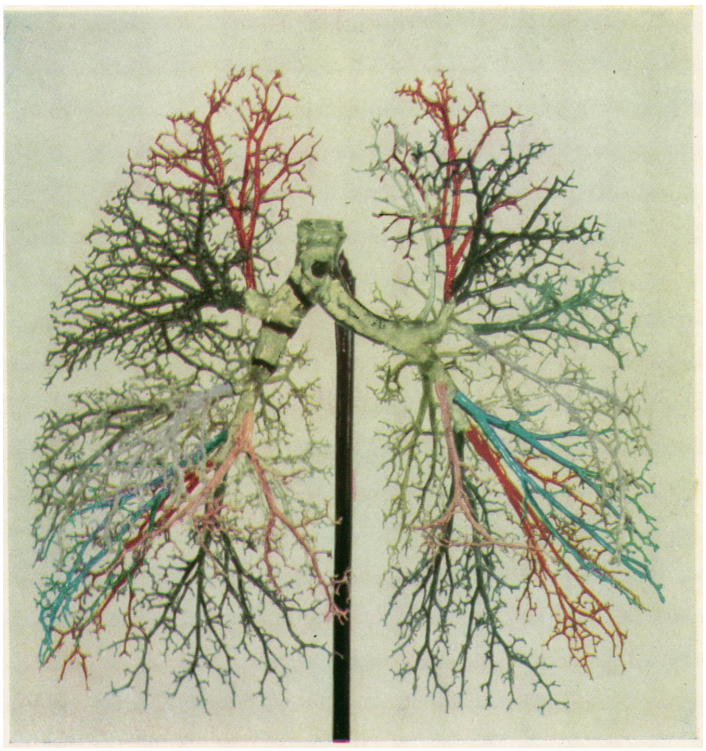


Figure 2.2: Cast of adult human bronchial tree, after pruning (reproduced from [Tompsett, 1952] with permission).

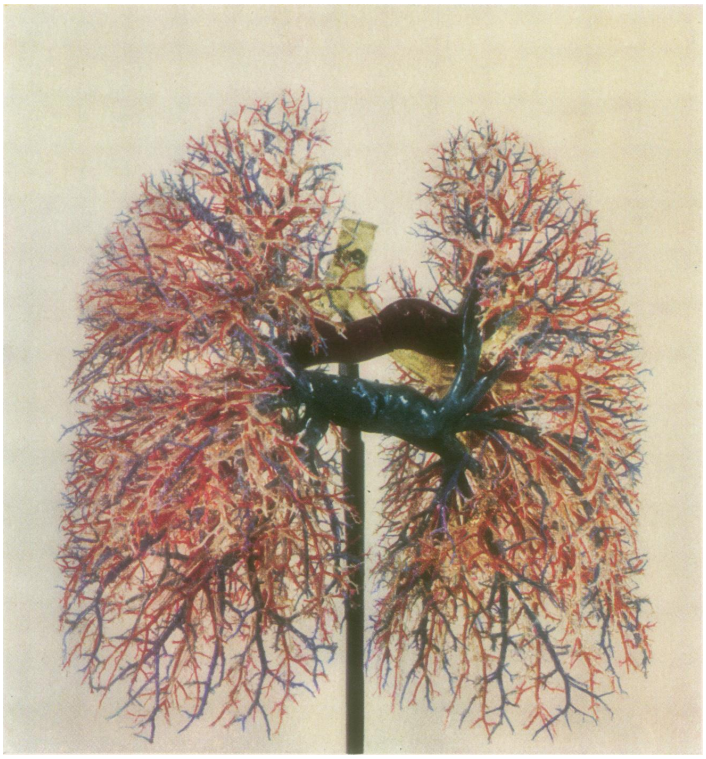


Figure 2.3: Cast of adult human bronchial tree, after pruning, with arteries and veins (reproduced from [Tompsett, 1952] with permission).

The trachea wall consists of 4 layers. Moving from the inside to the outside we have a **mucosa**, **submucosa**, **fibrocartilage layer**, and an **adventitia**. The mucosa consists of an **epithelium** and **lamina propria**. The epithelium consists primarily of **ciliated columnar cells**, on top of which **cilia** beat to propel mucus up towards the throat. Underneath these the laminar propria consists of elastic fibres. The submucosa consists of loose connective tissue within which are various (serous and mucous) glands, which secrete the mucous lining the inside of the trachea, which traps particulates to be transported back to the throat. The fibrocartilage layer consists of 16–20 c-shaped cartilage rings, each surrounded by a dense band of connective tissue called the **perichondrium**. The perichondrium merges with both the submucosa and the adventitia. The open ends of the cartilage are joined by a band of smooth muscle. The region between the rings is occupied by fibroelastic connective tissue. The adventita is a layer of connective tissue that binds the trachea to other structures in the neck.

The histology of the bronchi is very similar to the trachea, but changes gradually as we progress into the lung. The c-shaped cartilage rings are gradually replaced with cartilage plates. These plates become more sparse and eventually disappear, at which point the airway is classified as a bronchiole. The lamina propria of the mucosa gradually becomes surrounded by a layer of **smooth muscle**, which becomes more conspicuous as cartilage diminishes. The lamina propria is also diminished. The **serous** and **mucous glands** reduce in number, and the thickness of the epithelium reduces.

As we proceed through the bronchioles the epithelium continues to become thinner. By this stage the smooth muscle is very close to the epithelium. The lamina propria becomes a thin band with many elastic fibres. The smooth muscle in these airways effectively controls the resistance to air flow in the lungs.

The conducting part of the airways is ended with the **terminal bronchioles**. At this stage in the lung the ciliated columnar structure of the epithelium abruptly changes to a **simple cuboidal epithelium** made up from **Clara cells**, which secrete a **lipoprotein** that prevents the bronchiole walls from sticking together during expiration. Through the transition to respiratory bronchioles the smooth muscle is also gradually reduced.

In respiratory bronchioles Clara cells lie almost directly over the smooth muscle. It is at this point that alveoli start to appear off the sides of the respiratory bronchioles. The alveoli gradually become more frequent as the respiratory bronchioles continue to branch.

Eventually the alveoli become so frequent that they are separated only by their own walls. At this point the alveolar ducts are said to have started. To begin with the alveoli walls (**septal walls**) that face onto the ducts are terminated with smooth muscle, but this gradually becomes less prominent and disappears. Eventually all paths though the lung are terminated by alveoli. The septal walls contain the capillary network necessary for gas exchange, **collagen** and **elastin** fibres, **fibroblasts** and **macrophages**.

The elastin content of the lung in humans is approximately 28 % [Starcher, 1986]. The stretch and recoil of the lung is usually attributed to this material, whose fibres can be stretched to around 40 % strain before breaking, and exhibit approximately linear behaviour [Fung and Cowin, 1993]. Both elastin and collagen fibres from the alveoli, bronchi, and pleura have connections with fibres of the pulmonary arteries, meaning that the lung is held together with an effective continuum of fibres. In larger airways and pulmonary arteries elastin fibres are present as both longitudinal and circumferential bundles, generally in the submucosal layer of the airways. Elastin becomes more distinct in the respiratory airways, appearing either as circumferential or helical bundles in the respiratory bronchioles. [Fung and Cowin, 1993] quotes the typical Young's modulus of elastin as 0.6 MPa.

2.4 Automated Classification of Lung Sounds

Methods for the analysis of lung sounds, beyond simply listening, started with examination of the wave-form in the time domain [Murphy et al., 1977]. Crackle wave-forms are abrupt and quickly damped, while wheeze wave-forms have a sinusoidal appearance. This method of looking at the wave-form has remained to the present day. [Bohadana et al., 2014] provides example wave-forms of the different lung sounds. Such wave-forms are referred to as phonopneumograms when the sound signal is plotted simultaneously against a trace of the breathing cycle. However, this cannot be regarded as an automated process since pattern recognition is still left to the clinician.

A similar argument can be made for the next main step in the analysis of lung sounds: the inspection of the frequency spectrum of the sound signal. [Charbonneau et al., 1983; Gavriely et al., 1984] provide early examples of this, however, researchers started to move towards automated analysis with the proposal of metrics based upon the frequency spectrum. [Fenton et al., 1985] suggests the frequency at peak power, and [Malmberg et al., 1994] adds

root mean square amplitude and the median frequency. Such metrics can be used to define thresholds to automate detection of particular sounds, in particular wheezes. This use of metrics can be thought of as a precursor to the use of k-nearest neighbour algorithms, and this is also done by [Cohen and Landsberg, 1984] who uses the ratio of the peak amplitude to the root mean square amplitude, along with linear prediction coefficients as metrics. [Kahya and Yilmaz, 2000] uses Prony modelling coefficients[*] as metrics for crackles in a similar way, while [Alsmadi and Kahya, 2008] attempts to use an autoregressive model to find the best metrics for use in a k-nearest neighbour algorithm.

Fourier analysis was developed further through the use of the **spectrogram**. Though they do not give it this name, [Baughman and Loudon, 1984, 1985] use this technique, and introduce the metric Wh%, the percentage of the breathing cycle in which wheezing is present. [Fenton et al., 1985; Lenclud et al., 1996] also use this metric. [Fiz et al., 2002] explicitly combines the metric with a k-nearest neighbour algorithm. [Pasterkamp et al., 1989] introduces the contour plot spectrogram explicitly, giving it the name "digital respirosonography", though for Pasterkamp et al., inspection was still by the clinician. Automated analysis of the spectrogram is presented by several authors, [Homs-Corbera et al., 2004; Lin et al., 2006; Mazic et al., 2003; Qiu et al., 2005], with the last of these using a 2-dimensional bilateral filter to extract the features of wheezes.

So far metrics have been based on spectral analysis, with automated classification usually performed by a k-nearest neighbour algorithm, but other forms of filter should be noted. [Taplidou et al., 2004] first suggested the use of the **wavelet transform** in place of the Fourier transform for this application[†]. [Bahoura, 2006] uses thresholds in the transform to distinguish crackles, and more advanced metrics have been extracted [Yeginer and Kahya, 2009], such as fractal dimension [Hadjileontiadis, 2005a,b]. The Hilbert-Huang spectrum has also been considered [Reyes et al., 2008]. Alternatives to k-nearest neighbour have also been considered. [Kandaswamy et al., 2004] combines a wavelet transform with an artificial neural network, while [Güler et al., 2005] combines an artificial neural network with a genetic algorithm, which is used to search for effective metrics based on the spectrogram. [Riella et al., 2009] similarly uses the spectrogram and a 2-dimensional convolution filter with a half threshold as inputs to an artificial neural network.

[*] Prony's method is similar to Fourier analysis, but includes damping parameters as well as frequency parameters.

[†] For an introduction to the wavelet transformation see [Addison, 2002].

Further alternative analysis methods have included time-variant autoregressive models [Dorantes-Méndez et al., 2008a,b], state space analysis [Gnitecki et al., 2008], in which time delay and Lyapunov exponents are suggested as useful metrics, Gaussian mixed models [Mayorga et al., 2012, 2010], adaptive Kalman filters [Kaya and Elhilali, 2013], empirical mode decomposition [Charleston-Villalobos et al., 2006], modulation filtering [Falk and Chan, 2008], singular spectrum analysis [Ghaderi et al., 2011], fuzzy logic [Shamsi and Ozbek, 2012] and cyclostationarity [Li et al., 2013].

A considerable effort has gone into automating classification, with a wide variety of signal processing methods being considered. We must ask how successful these methods are. [Gurung et al., 2011] provides a meta-analysis and review of the techniques, and shows that methods for detecting wheezes and crackles have a sensitivity and specificity of 80 % and 85 % respectively. The standard against which success is measured here is still a human assessment of the sound. These accuracy levels already exceed those seen in some educational studies [Allingame et al., 1995; Williams et al., 2009], and is approaching the best scores achieved by various clinicians in [Wilkins and Dexter, 1990]. This suggests that the factor preventing further development of automated systems is the sound classification system itself, which as was shown in §2.1 is far from settled. It was noted in the introduction that an improved classification system is necessary to overcome the fundamental problem of low specificity in diagnosis, and it should now also be seen that it is required in order that the analysis methods already described can be effectively made use of. A consistent, rational classification system requires an understanding of how the sounds are produced. Research into this fundamental area, focussing on wheezing, will now be reviewed.

2.5 Starling Resistor as a Model for Wheezing

2.5.1 Preliminary Studies into Wheezing

Forgacs [Forgacs, 1967, 1978a,b] considers three possible mechanisms for wheezing based upon wind instruments. The first is represented by a flute, and involves the excitation by turbulent airflow of a resonant mode of the air contained within a rigid tube. The second is represented by the reed of a clarinet or oboe, in which the oscillation of the reed excites a resonant mode of the air within the tube. The third is represented by the toy trumpet. Sound here is generated by a reed, but the note produced is dependent only on the mechanical

properties of the reed. Forgacs makes several arguments against the first two mechanisms. The first is that in order for a rigid tube to produce tones corresponding to the frequencies observed in wheezes, the tube would need to be several feet long, longer than any of the branches of the airways. The second is that the length of the tube containing the stenosis has no observable correlation with the frequency of the tone produced by the wheeze. Thirdly, Forgacs claims that the pitch of wheezes originating at a single location often has a different pitch on inspiration and expiration. Finally, Forgacs observes that if a Helium-Air mixture is breathed by a wheezing person, the pitch is not significantly affected, a claim that has been supported more recently by [Shabtai-Musih et al., 1992]. The resonant modes of air in a rigid tube *are* affected if the air density is changed, so this mechanism, sometimes called the organ pipe mechanism, seems to have been conclusively ruled out. For Forgacs this left the toy trumpet. He claims that the walls of the tube play the role of the reed, however, this rather vague description of the wheezing mechanism has been improved upon.

[Grotberg and Davis, 1980] proposes that flutter that occurs when a fluid flows through a flexible channel is responsible for wheezing sounds. This article and two others [Grotberg and Reiss, 1982, 1984] look at the stability of flow through a 2-dimensional channel. The 2-dimensional model is further investigated in [Grotberg and Gavriely, 1989]. An experimental approach is taken by [Gavriely et al., 1989] using a **Starling resistor** model. This consists of a flexible tube held between two rigid tubes (see fig. 2.4), along with some way of regulating the pressure of the fluid in the tube up- and downstream of the flexible section, and the external pressure. Gavriely et al. investigates the relationships between the flow rate, up- and downstream pressures, and the occurrence of self-excited oscillations. A relationship between flow limitation and the self-excited oscillations is observed, which is to to some extent in agreement with previous observations [Gavriely et al., 1987]. A circuit analogy model of the wheeze source is presented by [Lu et al., 2011].

While these studies provide good evidence that wheezing is caused by the self-excited oscillation of the airways as air flows through them, they do not allow a thorough and quantitative understanding of the mechanism, importantly not including the effects of axial pre-tension, which is present in the lung [Hoppin et al., 1977]. We require a quantitative model to improve diagnosis. Therefore, we need to look more thoroughly at the broader literature that attempts to explain self-excited oscillations in flexible tubes.

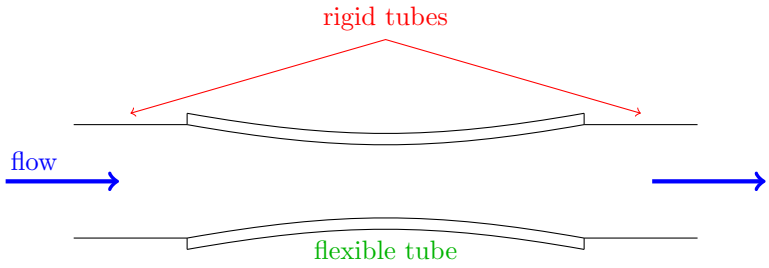


Figure 2.4: The Starling resistor.

or		**or**		**or**
lung bronchi bronchioles airways flexible tube collapsible tube starling resistor	**and**	wheeze squawk stridor oscillation oscillate onset self excited collapse	**and**	production produce mechanism model generate generation

language limited to English

included subject areas

respiratory system, general internal medicine, engineering, research experimental medicine, science technology other topics, biophysics, computer science, mathematical computational biology, mechanics, life science biomedicine other topics, physics, mathematics, materials science, medical informatics, emergency medicine, acoustics, medical laboratory technology, instruments instrumentation, nursing

Table 2.4: Searching the literature for production mechanisms for wheezing using Web of Science.

2.5.2 An Overview of Wheezing Mechanism Research

The articles in the previous section make an explicit link between oscillations in a flexible channel and wheezing. However, the fluid mechanics associated with the Starling resistor have been studied in their own right for a considerable period. [Heil and Jensen, 2003] gives a review of the theoretical work done in this area, and [Bertram, 2003] gives a review of the experimental work. [Grotberg and Jensen, 2004; Heil and Hazel, 2011; Jensen, 2013; Kizilova et al., 2012] provide more recent reviews focussed on biologically related fluid structure interaction problems. In the following sections we will review work on Starling resistors that has relevance to our application, but first we will consider a citation analysis based on the Web of Science database, since it illuminates some of the wider issues in the field of biomedical engineering.

Throughout this project we have used Web of Science (webofknowledge.com), Scopus (scopus.com), and PubMed (ncbi.nlm.nih.gov/pubmed) to search the literature. We can perform a citation analysis on information from these databases, which means that we draw a graph in which nodes represent documents, and are connected by and edge if one cites the other [Eck and Waltman, 2014]. We use the search detailed in table 2.4 with the Web of Science database for information on wheezing mechanisms[‡]. The citation graph based on the data from this search is shown in fig. 2.5. This figure indicates two main areas of research, one associated with the clinical implications of wheezing, and the other attempting to understand Starling resistors, as well as a significant number of documents unrelated by citation. The fact that in fig. 2.5 the two networks are unconnected tells us that our aim to use results from Starling resistors to better understand wheezing and its clinical implications is a relatively novel one, and is also an example of the more general need to try to link basic research in the physical sciences to applications in medicine, which is one of the aims of this thesis. It is worth noting that Starling resistors have been linked more explicitly to voice production [Kucinschi et al., 2006; Titze et al., 1995] and obstructive sleep apnea [Schwartz and Smith, 2013; Wellman et al., 2014], but this remains untrue for the lower airways. The following sections will review work on the Starling resistor, specifically investigating the possible relevance of this work to wheezing.

2.5.3 Experimental Studies into Starling Resistors

Early studies [Brower and Noordergraaf, 1973; Conrad, 1969] map out the relationship between the time averaged up- and downstream pressures ($\bar{p}_1$ and $\bar{p}_2$), the external pressure p_e, and the flow rate Q. We will repeat our quote from [Kamm and Pedley, 1989], since their

[‡]Obtained on Friday 24th March, 2017 using the search TS=(lung OR bronchi OR bronchioles OR airways OR (flexible AND tube) OR (starling AND resistor) OR (collapsible AND tube)) AND TS=(wheeze OR squawk OR stridor OR oscillation OR oscillate OR onset OR (self AND excited) OR collapse) AND TS=(production OR mechanism OR model OR generate OR generation) AND SU=(respiratory system OR general internal medicine OR engineering OR research experimental medicine OR science technology other topics OR biophysics OR computer science OR mathematical computational biology OR mechanics OR life science biomedicine other topics OR physics OR mathematics OR materials science OR medical informatics OR emergency medicine OR acoustics OR medical laboratory technology OR instruments instrumentation OR nursing) NOT TS=((positive AND end AND expiratory AND pressure) OR (end AND expiratory AND pressure) OR (respiratory AND impedance) OR (airway AND impedance) OR (impulse AND oscillometry) OR (impulse AND oscillation) OR (recruitment AND manoeuvres) OR recruitment OR (transpulmonary AND driving AND pressure) OR (secondary AND flow AND augmentation) OR (pressure AND support AND ventilation) OR (mechanical AND ventilation) OR (mechanically AND ventilated) OR (high AND frequency AND ventilation) OR (airway AND opening) OR (airway AND reopening) OR (sleep AND apnea) OR (pharyngeal AND collapsibility) OR (pharyngeal AND collapse) OR (upper AND airway AND hypotonia) OR surfactant) producing 2279 results.

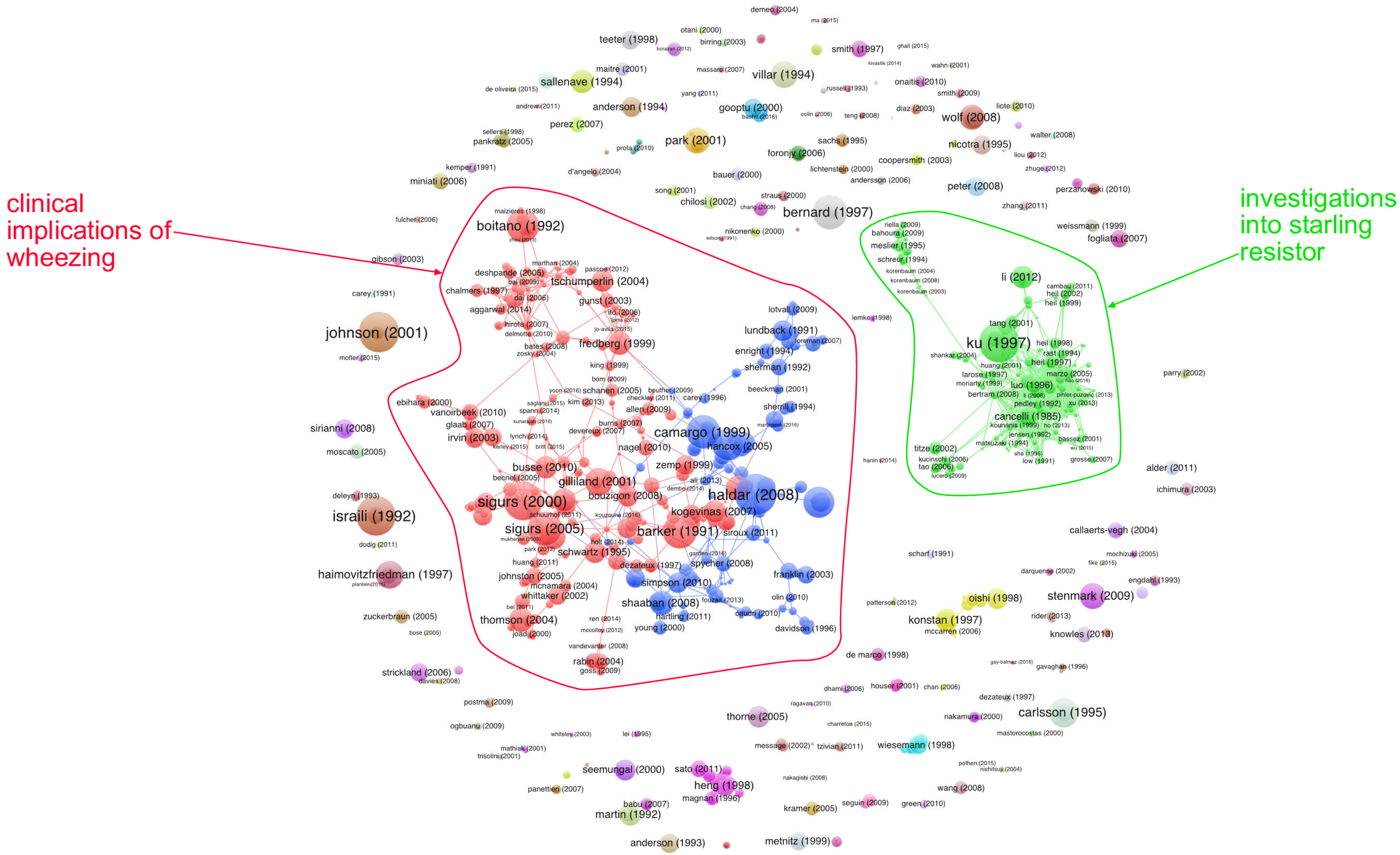


Figure 2.5: Citation analysis from Web of Science. Nodes, representing papers, are larger if they are more cited. An edge between nodes indicates that one of the documents cites the other. Not all nodes are labelled in order to prevent overlap. Nodes are grouped according to a clustering algorithm which is used to define the colour.

comment is particularly significant,

> "One of the main lessons to be learned is that it is vital for experimentalists to describe, quantitatively, all aspects of their experiment, because no one yet knows that any of them are unimportant, especially during oscillations, and for theoreticians to recognize that just because they have a model that produces something qualitatively similar to what is observed (e.g. an oscillation) it does not mean that have given a mechanical explanation for any particular observation."

[Gavriely et al., 1989] obtains similar flow-pressure relationships, but uses air as the working fluid. This and a later study [Oruç et al., 2011] remain the only ones of direct relevance to wheezing, but as already noted, lack the detail necessary for any quantitative model to be developed.

Systematic mapping of instabilities has only been completed using water as the working fluid [Bertram, 1986; Bertram and Butcher, 1992; Bertram and Castles, 1999; Bertram et al., 1990, 1991; Bertram and Sheppeard, 2000]. As well as providing detailed maps of oscillations, the importance of up- and downstream boundary conditions is again noted, which was investigated in more detail by [Wang et al., 2009]. In these studies the downstream conditions are characterised in terms of an inertiance and resistance of the rigid downstream tube. The fact that these studies use water limits application to the lung, since the ratio of tube wall density to fluid density is wrong by three orders of magnitude. In addition, it is well known that the airways are held in axial tension [Hoppin et al., 1977] within the lung. The studies listed here do not look at the effects of axial tension on the observed oscillations, which further limits their utility in understanding wheezing.

The applicability of experiments using tubes of constant wall thickness has been questioned, however, no qualitatively new behaviours are observed when tapered wall tubes are used by [Bertram and Elliott, 2003], who claims that the Starling resistor is, therefore, applicable to the lung.

More recently work has concentrated on flow visualisation in a particular class of oscillations denoted LU oscillations [Bertram and Nugent, 2005; Bertram et al., 2008; Bertram and Tscherry, 2006; Truong and Bertram, 2009], however these are of limited use to us as LU oscillations are of a low frequency not consistent with wheezing and have only been observed with water as the working fluid.

While a reasonable number of experimental studies have been completed, the precise set-ups vary quite significantly, so comparison is difficult. This is exacerbated by the lack of a rational set of dimensionless parameters with which to compare different sets of results. This will be the subject of §3.1, which will then allow a rational comparison of different experimental studies in §3.3. This will show a need for a new set of experiments, largely because most of the previous experiments use water as the working fluid, which means that the ratio between the density of the fluid and the tube wall does not match that seen in the lung. The need for further experiments is detailed in §3.1, and these experiments form a fundamental part of this thesis.

2.5.4 Theoretical Studies into Starling Resistors

Theoretical models have gradually increased in complexity, starting with cross-sectionally averaged 1-dimensional models, and moving up to simulations of the Navier-Stokes equations coupled to an elastic tube model. A recent review of modelling of the Starling resistor is presented by [Jensen, 2013], while [Pedley and Luo, 1998] provides a review of earlier work on 2-dimensional models.

Much early work looks at 1-dimensional models that reproduce some of the phenomena of Starling resistors. Many authors consider a cross-sectionally averaged form of the Navier-Stokes equations and a tube law [Dawson and Elliott, 1977; Morgan and Ferrante, 1955; Morgan and Kiely, 1954; Shapiro, 1977]. This was largely applied to blood flow, though some consider the lung [Elliott and Dawson, 1977]. There were some suggestions that self-excited oscillations are related to choking, however, the reality of the situation seems to be more complex [Bertram and Raymond, 1991; Gavriely et al., 1989]. 1-dimensional lumped parameter models are also presented by [Armitstead et al., 1996; She and Bertram, 1996]. These show some qualitative agreement, and provide some evidence of limit cycles, and perhaps bifurcations to chaos, but have not been able to give quantitative predictions.

A considerable body of work looks at an analogous 2-dimensional model of the Starling resistor. This has included linear stability analyses [Burke et al., 2014; Davies and Carpenter, 1997; Huang, 1998, 2001; Liu et al., 2009a, 2011, 2009b; Luo et al., 2008, 2007; Stewart et al., 2010] and numerical simulations of the system as a whole [Cai and Luo, 2002; Luo and Pedley, 1996, 1998; Xu et al., 2013, 2014; Zhang et al., 2005]. Several instabilities have been identified: travelling wave flutter, Tollmien Schlichting waves, and static divergence.

These are yet to be fully verified in a 3-dimensional system. More interestingly, the nature of the instabilities seen, and the critical values of flow rate or wall properties at which they are observed, are seen to be highly dependent on the boundary conditions imposed up- and downstream. "Slamming" and "sloshing" mechanisms are also suggested beyond linear analysis, the latter of which has attracted some attention from 3-dimensional studies. These qualitative conclusions are interesting to our work, however, the 2-dimensional analogous model is too different to the lung for quantitative predictions.

Computational complexity has meant that 3-dimensional models have been slower in arriving. Some studies have prescribed wall motions and looked at the resulting flows, [Heil and Waters, 2006, 2008; Whittaker et al., 2010c]. An interesting conclusion of this work is that oscillation must be about a non-axisymmetric mean configuration in order for self-excited oscillation to occur. These studies also show some evidence of the sloshing mechanism. Linear stability analyses have been completed [Hamadiche and Gad-el Hak, 2002; Kumaran, 1995a,b, 1998], considering a flexible tube of infinite length. Dimensionless parameters have been identified by these authors (though these have not then been used by experimental researchers), including the Reynolds number, the ratio of the fluid and solid viscosity, the ratio of the outer to inner radius of the tube, and a variable defined by $\Sigma = \rho G R^2/\mu^2$ [§]. We consider dimensional analysis in §3.1. More complete numerical simulations have also been attempted [Whittaker et al., 2010b], and have had some success producing examples of high frequency oscillations.

Theoretical studies have had reasonable success in predicting the qualitative behaviour of starling resistors, but the sophistication of the system has resisted accurate quantitative predictions. Some mechanisms have been suggested, though experimental validation of these is still lacking. Our interest is in quantitative relationships between the geometry and material properties of the tube, and the conditions for the onset of oscillations, so the impact of the work reviewed above is limited. One area strangely little explored is a dimensional analysis of the problem. This could be particularly productive for our purposes since it allows the study of the full 3-dimensional problem, while looking for simple scaling relationships that would be of significant clinical value.

Much of the theoretical work's value is also limited because it neglects wall inertia. It

[§] ρ is the fluid density, G is the shear modulus of the tube wall, R is the tube radius, and μ is the fluid's dynamic viscosity.

has been made clear by the early experimental work [Forgacs, 1978a; Shabtai-Musih et al., 1992] that wall inertia is important in wheezing, and this is reflected in the large value of the tube wall density when compared to the fluid density in the lung ($\sim 1000\,\mathrm{kg\,m^{-3}}$ vs $\sim 1\,\mathrm{kg\,m^{-3}}$). It has been included by [Luo and Pedley, 1998], but only as part of a two-dimensional model problem. Very recently, it has also been included in a linear stability analysis for the first time by [Walters et al., 2017], but here oscillations are assumed to have a very long wavelength, which is not applicable to the relatively short tubes of the airways (see §3.2.2). We require wall inertia in a model that includes large deformations in three dimensions to produce practically useful predictions, and this is lacking in the literature at this time.

Our model must include the tube and the fluid. The largest Mach number of the flows under consideration is around 0.1 [Nunn and Gregg, 1989], so the fluid can be modelled as incompressible, and air is Newtonian to a good approximation. The tube is more complex, but will require some form of shell theory. For this reason, we will briefly outline this field and its relevance to our modelling.

2.5.5 Shell Theory

The shell theory that we use to gain understanding of the mechanism behind wheezing must satisfy two, often opposing, requirements; it must be simple enough to enable physical interpretation, and it must be able to model the important aspects of the deformation. The need for both of these has ultimately driven us to derive a shell theory of our own, and in the process develop some new ways of understanding curvature and its changes using geometric algebra. It is odd in some ways that this has been necessary given the maturity of shell theory as a field, and in this section we will give some justification for this, which will be fleshed out more as the experimental results and mathematical analysis are completed throughout this thesis.

The earliest truly general approach to shell theory was arguably provided by [Naghdi, 1972], and this forms the basis for more modern works such as [Antman, 2005; Ciarlet, 2005], though the theory of [Koiter, 1966] has also been popular with many authors. In this the shell is modelled as a Cosserat surface [Altenbach et al., 2010; Cosserat and Cosserat, 1909], by which the shell, which is a continuum that occupies a three-dimensional region of three-dimensional space that is thinner in one direction (i.e. the thickness) than in all others,

can be modelled mathematically by considering equations over a surface lying within the continuum. Two approaches are used. Firstly, equations of motion are derived directly on the two-dimensional surface, and secondly, the three-dimensional continuum is considered, and its thickness is then taken to be small. One important result of Naghdi is the equivalence of these approaches. The important part of the Cosserat approach is the use of director fields. More specifically, a point in the three dimensional continuum $\boldsymbol{p}$ is written as,

$$\boldsymbol{p} = \boldsymbol{r} + \sum_{i=1}^{\infty} \xi^i \boldsymbol{d}_i, \tag{2.1}$$

where $\boldsymbol{r}$ is a point on the two-dimensional surface and ξ is a thickness coordinate. The equations of motion for the shell are then written in terms of $\boldsymbol{r}$ and its derivatives, and $\boldsymbol{d}_i$ and their derivatives, using the language of differential geometry. Shell equations are obtained by truncating the series of director fields. In the simplest case only one director field is used. A further simplification is obtained by restricting $\boldsymbol{d} = \boldsymbol{d}_1$ to always be a unit vector normal to the surface, in what Naghdi calls the restricted theory. It is this restricted theory that has applied to almost all work since, and is what lies behind the shell theory of [Koiter, 1966]. More recently mathematical work has focussed on justifying the kinematic assumptions of Naghdi and others using asymptotic methods. This work is well summarised by [Ciarlet, 2000], and thus far has been able to derive equations that are equivalent to assuming that $\boldsymbol{d}$ is always a unit vector normal to the plane.

Shell theories have been used to investigate buckling [Edlund, 2007; Gavrilenko and Croll, 2004; Riks and Rankin, 1997; Shamass et al., 2015; Simitses, 1996; von Mises, 1914, 1931, 1933], ribbed shells [Du et al., 2015; Zarutskii, 2001], laminated shells [Alijani and Amabili, 2014; Lomboy et al., 2009; Piskunov and Rasskazov, 2002; Reddy and Arciniega, 2004; Tahani et al., 2016], composite shells [Simitses, 1996], and vibrations [Alijani and Amabili, 2014; Altay and Dokmeci, 2001; Arnold and Warburton, 1949; Avramov and Mikhlin, 2013; Farshidianfar and Oliazadeh, 2012; Leissa, 1973; Soedel, 1981; Weingarten, 1964; Zhu et al., 2017], using various solution methods [Agalovyan, 2002; Du et al., 2015; Gavrilenko and Croll, 2004; Grigorenko and Gulyaev, 1991; Guz et al., 1979; Li et al., 2014; Shevchenko, 2007], and producing various developments in finite elements [Carrera, 2002; Cen and Shang, 2015; Grigorenko and Gulyaev, 1991; Lomboy et al., 2009; Mackerle, 2000; Mukhopadhyay et al., 2017; Riks and Rankin, 1997; Tornabene et al., 2015; Yang et al., 2000], among other

areas. We have attempted here to cite work that is more review-like where possible. Having described the basis for much of the existing work, we are now in a position to describe our problems with it.

The tool of choice to describe shell theories has been differential geometry, with [Ciarlet, 2005] providing the most recent treatise along these lines, probably influenced by the use of differential geometry in three-dimensional elasticity by [Marsden et al., 1994]. This is undoubtedly a rigorous way of describing the theories, however, we feel that this mathematical tool introduces large barriers to physical interpretation of the equations. Redundancy in differential geometry due to the way in which it is developed has been discussed by [Hestenes and Sobczyk, 1984] (for a standard text on differential geometry, see for example [Nakahara, 2003]), and this is particularly true in a field where the manifold under consideration is two-dimensional and embedded in a flat three-dimensional space. Understanding curvature via the Riemann curvature tensor in this situation is highly redundant. Differential geometry distinguishes vectors and covectors, linking them on Riemannian manifolds with a metric, but in our application there will never be a time when there is no metric, meaning we are better off starting with a single vector space, endowed with an inner product, meaning that the metric is simply the identity function. Differential geometry makes use of at least three different derivatives (exterior derivative, covariant derivative, lie derivative), but all of these can be simply expressed in terms of the vector derivative in geometric algebra. Differential geometry almost always needs to express its equations of motion in terms of complex index expressions, which hide much of the physical meaning behind them, and physical understanding is one of our primary aims. We do not wish the reader to misunderstand us. Differential geometry is a powerful, and sometimes sublime and beautiful, field, but we feel that its practical utility in this context is severely limited. For more discussion of the relationship between differential geometry and geometric algebra we recommend [Hestenes, 2011]. We will elaborate on the advantages of geometric algebra shortly, but first we will outline some other limitations the current theory of shells has.

We have already alluded to the difficulty gaining physical understanding of current shell theories. One aspect of [Naghdi, 1972] that underlines this is the use of angular velocity. Naghdi finds it necessary to use a definition of angular velocity rotated by 90° from the usual one, with no apparent justification, and this has not been addressed elsewhere to our knowledge. One of our aims is to clarify the roles of angular velocity and moments in shell

theory.

One outcome of the work on shell theories has been a very wide variety of slightly different theories. This is particularly visible with linearised shell theories, of which there are at least 10 [Leissa, 1973]. This is equally well reflected in the very wide variety of finite elements that have been proposed. This wide variety of theories lacks a rational way to compare them, which is confused by an equally wide variety of notations and coordinate systems. In addition, the linearised shell theories almost all lack a way of including prior-strain of the shell, which as we will see, is a necessary component of our own analysis.

We are in need of a shell theory that enables lucid physical interpretation of the phenomena we are investigating, while still maintaining the ability to model the important aspects of the deformations. We propose to use geometric algebra to do this. This mathematical framework has already been established as an alternative to differential geometry [Doran and Lasenby, 2003; Hestenes and Sobczyk, 1984]. It allows coordinate free representations of the governing equations, removes the redundancies of differential geometry, and is particularly adept at dealing with rotations. Geometric algebra has already been used to great effect in the fields of elastic rods [McRobie and Lasenby, 1999], static elastic geometry [McRobie, 2017], aeroacoustics [Gregory et al., 2015, 2014], electromagnetism [Arthur, 2011; Chappell et al., 2010; Doran and Lasenby, 2003], information engineering, and computer vision [Dorst et al., 2002; Dorst and Lasenby, 2011]. One of the most powerful aspects of geometric algebra lies in the use of rotors to represent rotations. In [McRobie and Lasenby, 1999] these have been used to simplify Simo and Vu Quoc's numerical algorithm [Simo and Vu-Quoc, 1988] for modelling the nonlinear behaviour of rods. In projective and conformal geometry [Doran and Lasenby, 2003, §10] rotors have allowed geometric primitives to be represented in a more simple and lucid manner, and in relativity [Lasenby et al., 1998] and relativistic analogies [Gregory et al., 2014] rotors can simplify transformation between frames of reference. We make use of rotors to better understand the change of curvature of a shell, which is of prime importance to the constitutive law, but whose representation has long caused controversy. We will focus on the theory that assumes a single director field that remains a unit vector perpendicular to the surface, since this is the simplest theory capable of dealing with large deformations.

2.6 Summary

There is a clear need for a new set of experiments to systematically investigate self-excited oscillations of flexible tubes with air flowing through them in order to develop a theory for wheezing. This must include a new dimensional analysis of the problem, both to provide physical understanding, and to ensure the relevance of the experiments to wheezing sounds. The dimensional analysis and experimental setup are described in §3, and results from these experiments form the fundamental basis for the conclusions of §§6 to 8.

There is also a need for theoretical models capable of quantitative predictions. These models need to be based on physical understanding of the mechanism, and not just replicate of its qualitative behaviour. As part of this we will need to extend understanding in shell theory, and this is the focus of §§4 and 5. §§6 to 8 then combine this theoretical understanding with experimental results to gain an understanding of self-excited oscillations, and develop predictive tools that can be applied in a clinical context.

Chapter 3

Starling Resistor Setup

It has long been known that under certain specific conditions, self-excited oscillations are seen when a fluid flows through a tube with flexible walls. Here we intend to investigate these oscillations in the context of the lung. We use an experimental set up that has been in use for some time [Brower and Noordergraaf, 1973; Conrad, 1969] called a **Starling resistor**. This consists of a flexible tube held between two rigid tubes, as shown in fig. 3.1. The external pressure p_e, upstream pressure p_1, downstream pressure p_2, and time average flow rate Q are all measured and/or controlled. Experiments involving starling resistors generally try to map out the different types of behaviour observed as a function of the time averaged values of these parameters. We denote the length of the flexible tube l, its undeformed inner radius a, and its undeformed thickness h. We also define the inner diameter (ID) $d = 2a$ for convenience.

To begin our examination of this experimental setup we will perform a dimensional analysis of the problem. However, before we can do this, we must state the modelling

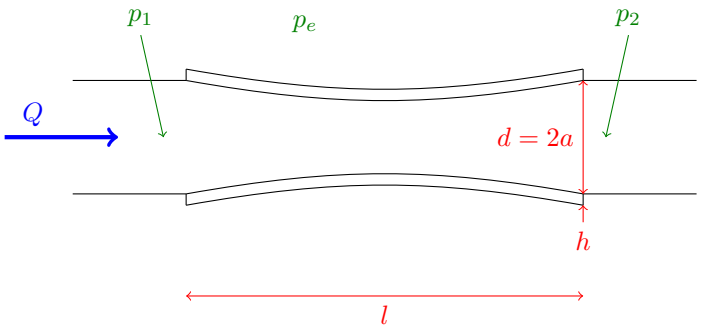


Figure 3.1: The Starling resistor.

assumptions that we will make regarding the fluid in the tube, the tube itself, and the environment surrounding the tube.

The Fluid Within the Tube We take the fluid within the tube to be Newtonian, with uniform and isotropic properties. We also assume that the fluid can be described as incompressible. Therefore the only relevant material properties are the dynamic viscosity μ and density ρ.

The Tube Wall We take the wall of the tube to be isotropic and homogeneous. We model the tube material to be linearly elastic, so its material properties can be defined by any pair of elastic moduli, for example the Young's Modulus E and Poisson's Ratio ν. Rubber is used for the flexible tube, and in this case the solid is very nearly incompressible. In this instance we may take $\nu = 0.5$. In addition we must define the tube material density ρ_s.

The deformations of the tube are in general large, so it may be questioned whether a linear elastic material law is acceptable. [Wang et al., 2009] considered this, and found that for the latex tubes used, the Young's modulus of the tube was constant up to 10 % strain, compared to a maximum strain when the tubed collapsed of 5 % validating the use of a linear material law.

The Tube Surroundings A given airway will be surrounded by the parenchyma. The pressure in this material will be what sets p_e in fig. 3.1. It is useful to note that the pressure in the parenchyma is also what sets the pressure far upstream of the flexible tube under consideration. Hence we will consider a model in which the far upstream pressure is equal to the pressure external to the flexible tube. During a given oscillation, we will take this pressure to be constant.

The unsteady behaviour of the tube surroundings, and its effect on the oscillations, is somewhat more subtle, so we delay discussion of this to §3.2.4.

3.1 Dimensional Analysis

In order to ensure that our experiment is relevant to a study of the lung we first develop a simple dimensional analysis and identify the relevant dimensionless parameters that we must match.

Let us say that we are interested in the observed dominant frequency of self-excited oscillations, f. This will depend on the geometry of the problem (a, l, h), and the material properties of the tube wall and fluid $(\rho, \mu, \rho_s, E, \nu)$. In addition we have the pressures p_1, p_2, p_e, and the flow rate Q. It was mentioned in §2.5.3 that in the lung the airways are held in axial tension [Hoppin et al., 1977], so we must add a fourth geometric parameter, l_0, the unstrained length of the tube.

It has been observed that for a particular geometry and set of material properties, the time averaged flow rate Q can be regarded as a function of the time averaged pressures $\bar{p}_1, \bar{p}_2$ and p_e. Moreover, it has been observed that by prescribing any two out of the three pressure *differences*, $\bar{p}_1 - \bar{p}_2$, $\bar{p}_1 - p_e$, and $\bar{p}_2 - p_e$, the flow rate Q and the remaining pressure difference are fixed. A schematic plot of Q vs $\bar{p}_1 - p_e$ and $\bar{p}_2 - p_e$ is shown in fig. 3.2, which is adapted from [Conrad, 1969]. There is no flow along the line corresponding to $\bar{p}_1 = \bar{p}_2$, and there are 3 main regions to the graph, corresponding to an open tube, collapsed tube, and a transition region between the two. The tube tends to be open when both $\bar{p}_1$ and $\bar{p}_2$ are larger than p_e. In this region the flow rate is a function only of $\bar{p}_1 - \bar{p}_2$. If we imagine raising p_e eventually the tube will start to collapse, generally once p_e is above the downstream pressure $\bar{p}_2$. Increasing p_e further eventually causes the tube to collapse completely. In this region flow is once again only dependent on $\bar{p}_1 - \bar{p}_2$.

Various self-excited oscillations have been observed, in particular throughout the transition region of fig. 3.2. Initially we assume that the type of unsteady behaviour observed depends only on the geometry (a, l, l_0, h), material properties $(\rho, \mu, \rho_s, E, \nu)$, and any 2 out of the following 4 variables,

$$\bar{p}_1 - \bar{p}_2, \quad \bar{p}_1 - p_e, \quad \bar{p}_2 - p_e, \quad Q. \tag{3.1}$$

Hence we can write the frequency f as,

$$f = \Pi(a, l, l_0, h, \rho, \mu, \rho_s, E, \nu, a_1, a_2), \tag{3.2}$$

where a_1 and a_2 are any 2 of the 4 variables listed in eq. (3.1). Here we have 12 variables in terms of 3 dimensions, so we should be able to find a dimensionless relationship in terms of 9 dimensionless variables [Barenblatt, 2003].

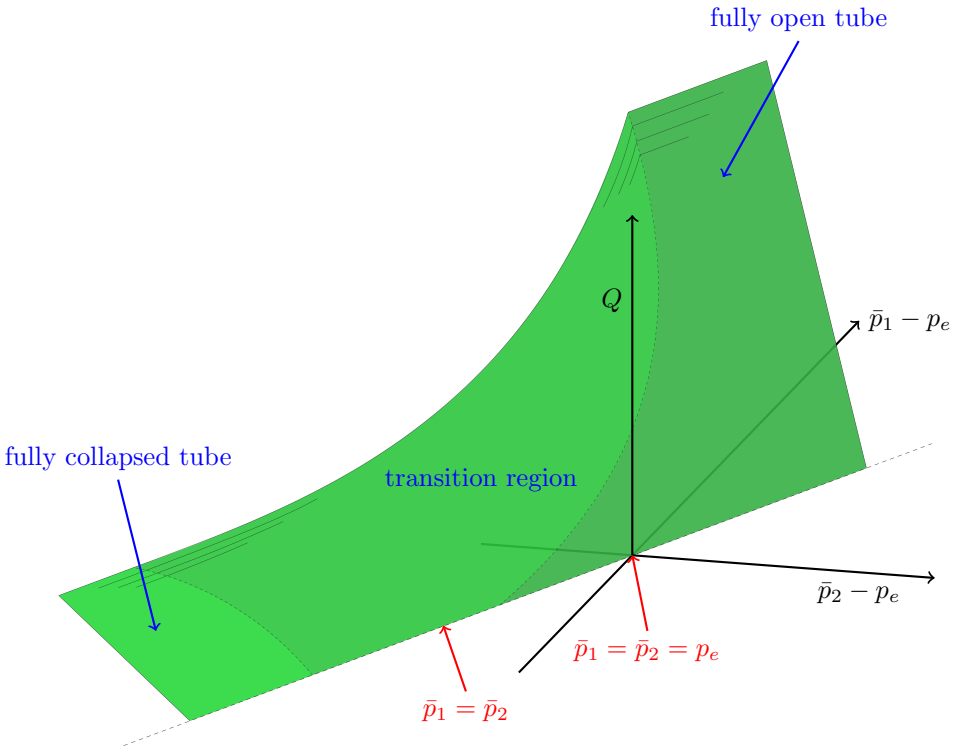


Figure 3.2: The dependence of flow rate on pressure differences for a starling resistor, adapted from [Conrad, 1969].

To define the necessary dimensionless variables we need a relevant pressure scale. Self-excited oscillations are observed to occur in a flow regime between total collapse and an open tube. When there is no flow through the tube collapse is controlled by the **transmural pressure** $p_2 - p_e$ (when there is no flow the pressures are steady and $p_1 = p_2$). If the $h/a \ll 1$, $l/a \gg 1$, and $l/l_0 = 1$ there is an analytical value for the transmural pressure at which this collapse first occurs [Bertram, 1987] which is,

$$p_2 - p_e = -3P_k, \text{ where } P_k = \frac{h^3}{a^3}\frac{E}{12(1-\nu^2)}. \tag{3.3}$$

It was also observed by [Bertram, 1987] that the critical collapse pressure was close to $-3P_k$ even when the wall thickness was 30 % of the radius, which exceeds the maximum usually seen in the lung. However, $l/a \gg 1$ and $l/l_0 = 1$ do not apply in the lung (see §3.2.2). We will not be able to use P_k to predict the collapse of the flexible tubes in our experiments, however, it is still useful as a pressure scale in this preliminary dimensional analysis. Using P_k we can define the following dimensionless pressure differences,

$$\Delta P_{12} = \frac{p_1 - p_2}{P_k}, \quad \Delta P_{1e} = \frac{p_1 - p_e}{P_k}, \quad \Delta P_{2e} = \frac{p_2 - p_e}{P_k}. \tag{3.4}$$

P_k is not time dependent, so it makes sense for us to also write,

$$\Delta \bar{P}_{12} = \frac{\bar{p}_1 - \bar{p}_2}{P_k}, \quad \Delta \bar{P}_{1e} = \frac{\bar{p}_1 - p_e}{P_k}, \quad \Delta \bar{P}_{2e} = \frac{\bar{p}_2 - p_e}{P_k}. \tag{3.5}$$

We need a dimensionless number that compares the fluid and structure. To obtain this we compare the dynamic pressure of the fluid (which scales with $\rho Q^2/a^4$) to the collapse pressure of the tube (which scales with P_k),

$$Dc = \frac{\rho Q^2/a^4}{P_k}, \tag{3.6}$$

where Dc is short for dynamic to collapse pressure ratio. If we imagine a completely closed tube, just held shut by external pressure, we might expect Dc to be of order 1 when the incoming flow is able to start to open the tube again.

Instead of dynamic pressure we could have used a shear stress to compare to P_k. Rather

than do this we will use the Reynolds number separately,

$$Re = \frac{\rho Q}{\mu a} \tag{3.7}$$

which represents the ratio of inertial (fluid) forces to viscous (fluid) forces.

In addition to these we have the density and geometric ratios,

$$\frac{\rho_s}{\rho}, \quad \frac{l}{l_0}, \quad \frac{l}{a}, \quad \frac{h}{a}. \tag{3.8}$$

Finally we need a dimensionless number containing the frequency observed. Two options for this are the Strouhal number and the Womersley number. The Strouhal number can be though of as the ratio of the radius a to the wavelength of a wave with frequency f that is convected with the flow,

$$St = \frac{fa^3}{Q}. \tag{3.9}$$

The Womersley number is the ratio of the transient inertial fluid force to the viscous fluid force, which can be written as,

$$Wo = \frac{\rho f a^2}{\mu}. \tag{3.10}$$

The dimensionless numbers Dc, Re, and St all contain the flow rate Q. Therefore we only need a single pressure difference, and so only one of $\Delta\bar{P}_{12}$, $\Delta\bar{P}_{1e}$, and $\Delta\bar{P}_{2e}$, is needed. Our dimensionless relationship in terms of 8 variables may therefore be written as either,

$$St = \Pi(\Delta\bar{P}, Dc, Re, \rho_s/\rho, \nu, l/l_0, l/a, h/a) \tag{3.11}$$

or,

$$Wo = \Pi(\Delta\bar{P}, Dc, Re, \rho_s/\rho, \nu, l/l_0, l/a, h/a) \tag{3.12}$$

where $\Delta\bar{P}$ is one of $\Delta\bar{P}_{12}$, $\Delta\bar{P}_{1e}$, or $\Delta\bar{P}_{2e}$. It is possible to include 2 pressure difference variables, but then Dc must be regarded as a dependent rather than independent variable.

Some of the scales used in this dimensional analysis will be called into question later, in particular the use of P_k, and the relevance of Dc. However, the work here is sufficient for us to compare the relevance of previously completed experiments to wheezing. The dimensional analysis is refined in §8.4.3.

3.2 Parameters in Vivo

In order to ensure that our experiments are of relevance to wheezing in the human lung, we will look at the ranges of the dimensionless parameters, identified in the previous section, in the airways of the human lung. To be of relevance our experiments must encompass these ranges.

3.2.1 Material Properties

The body is held at a relatively constant temperature of 37 °C [Negus, 1952]. We take atmospheric pressure to be 101 325 Pa. Pressure changes in the lung are rarely more than 50 cmH_2O = 4903 Pa [West, 2016], so the absolute pressure rarely changes by more than 5 %, and more commonly by no more than 2 %. We will assume that material properties of the fluid and tube do not change over the course of an oscillation.

Air in the lungs must be kept moist. This makes respiratory exchange in the alveoli and ciliary action possible, among other things. The air we breath in has a varying temperature and humidity, however, it is believed that by the time the air enters the bronchi, it has usually been brought to body temperature (37 °C) and a relative humidity (RH) of 95 % [Negus, 1952].

[Tsilingiris, 2008] provides a method to calculate the density and viscosity of moist air as a function of RH, temperature, and pressure. We expect temperature to be in the range 35 °C to 39 °C, while pressure should be in the range 101.325 kPa ± 5 kPa. The RH is harder to predict. Air commonly has an RH around 0.45, and this must rise to around 0.95 in the lower airways. It is believed that the RH is in the range 0.85 to 0.95 by the time it reaches the trachea, with most of the humidification happening in the nose [Negus, 1952], but we will consider a larger variation to be on the safe side.

For the ranges of pressure, temperature and RH dealt with here, density is maximised when pressure is maximised and temperature is minimised, while viscosity is maximised when temperature and pressure are maximised. This is illustrated in fig. 3.3, where density and viscosity are shown as functions of pressure and temperature at an RH of 0.95. We can use this to estimate the overall variation in density and viscosity in our application. We plot density as a function of RH in fig. 3.4a, at the largest pressure and smallest temperature we expect to see, and vice versa. Similarly, we plot viscosity as a function of RH in fig. 3.4b, at

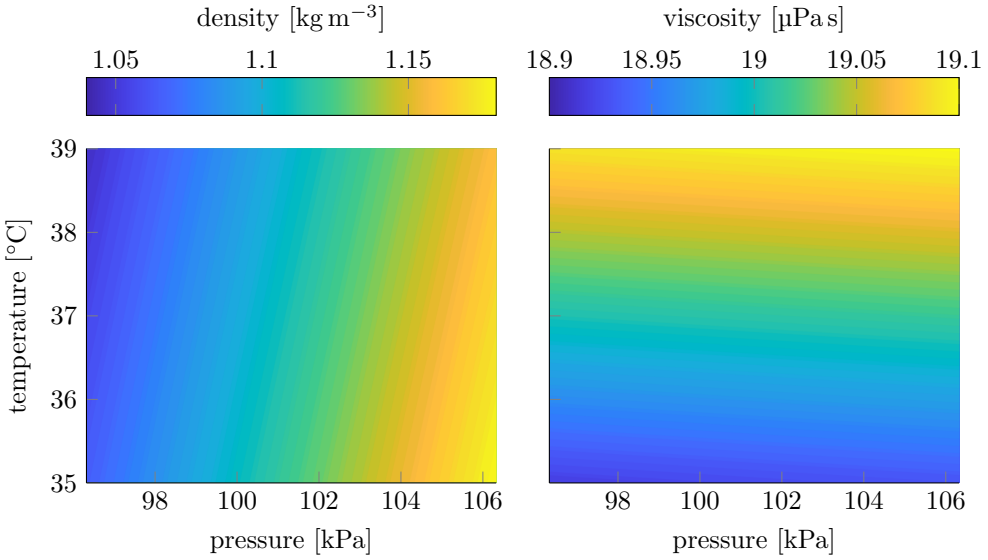


Figure 3.3: Transport properties of air at a relative humidity of 0.95.

the largest pressure and largest temperature we expect to see, and vice versa. This shows that, given our uncertainty over pressure, temperature and relative humidity, we expect the viscosity to lie in the range 18.9 µPa s to 19.2 µPa s, and the density to lie in the range 1.04 kg m^{-3} to 1.20 kg m^{-3}. This is a variation of 1.6 % and 15 % respectively.

We now consider the material properties of the tube wall. Soft tissues in the body are generally considered to be incompressible, with Poisson's ratio in the range 0.45 to 0.49 [Chen et al., 1996; Fung and Cowin, 1993; Wang et al., 2011b]. The Young's modulus is harder to accurately quantify. As is discussed in §2.3.2, the elastic behaviour of the lung is thought to be due, at least in part, to the presence of elastin. [Fung and Cowin, 1993] quotes the Young's modulus of elastin to be 0.6 MPa. [Wang et al., 2011a] provides estimates of the Young's modulus of the trachea and first 3 bronchi in a pig, whose respiratory systems are similar to those of humans in terms of histology and anatomy, and these are shown in fig. 3.5. [Wang et al., 2011b] provides measurements of Young's modulus for human bronchi, and these are generally in the range 0.1 MPa to 1 MPa. Taking this information into account, as a first estimate we will take the Young's modulus to lie in the range 0.1 MPa to 2 MPa, but we must acknowledge that this is a very large degree of uncertainty. If we consider a single airway (trachea, first bronchi, etc.) we could use the ranges indicated in fig. 3.5 to reduce this uncertainty.

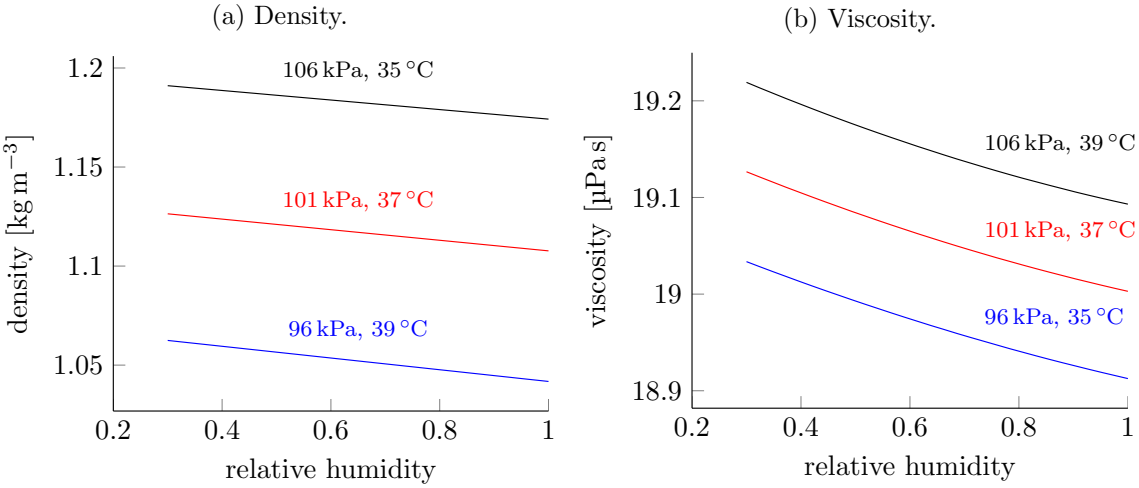


Figure 3.4: Transport properties of air as a function of relative humidity.

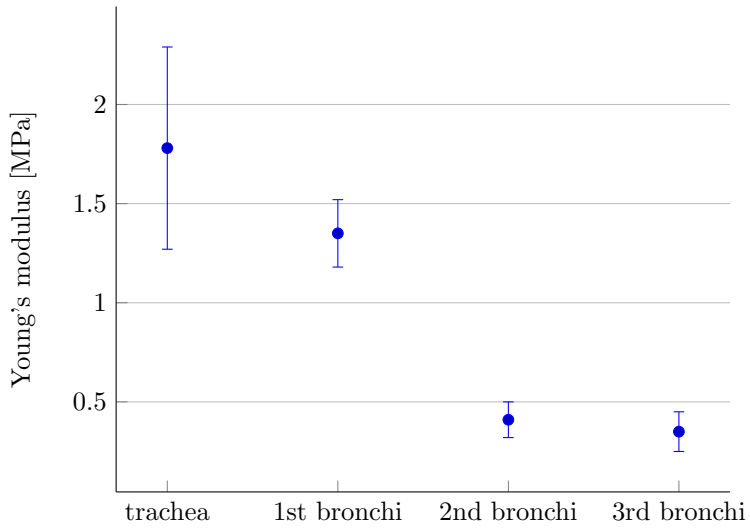


Figure 3.5: Young's modulus of pig airways, reproduced from [Wang et al., 2011a].

3.2.2 Geometry

We must have an idea of the geometry of the tubes that make up the airways of the lung. For this we make use of the Horsfield lung model for humans [Horsfield and Cumming, 1968; Horsfield et al., 1982]. This model categorises the human lung network into 35 different segment sizes, starting with the trachea ($n = 35$) and ending with a final airway ($n = 1$), which is assumed to then terminate in two alveoli. Each segment size has an associated length l^n, diameter d^n, wall thickness h^n, and area fraction of cartilage c^n (which we do not use). The model specifies the level of asymmetry at each bifurcation through a recursion index Δ^n. An airway of order n bifurcates into two airways of order $n-1$ and $n-1-\Delta^n$. The specific data for the human lung is given in fig. 3.6. From the Horsfield model we can calculate the ratios l/d and h/d for each of the 35 different segment sizes. These are shown in fig. 3.7. We also know from [Hoppin et al., 1977] that l/l_0 is between 1.1 and 1.8 in the lung.

3.2.3 Flow

We can use the Horsfield lung model to estimate the flow conditions within the lung. It is possible to follow a particular path into the lung, starting at the trachea and deciding which way to go at each bifurcation. Along this path cross-sectional area can be regarded as a function of distance into the lung, which in the Horsfield model will be a piecewise constant function, with discontinuities corresponding to bifurcations. Given a particular distance into the lung (x), we can find every distinct path into the lung of that length. The tubes at the end of these paths will have a cross-sectional area, and we can sum all of these areas to obtain a cumulative cross-sectional area as a function of distance into the lung, which we denote $A(x)$. We denote the velocity at the top of the trachea V_i, and the area at the top of the trachea A_i. A very crude model for the velocity of the fluid at a distance x into the lung is then,

$$V(x) = \frac{A_i}{A(x)} V_i. \tag{3.13}$$

From this we can obtain a very crude estimate of Reynolds number as a function of distance into the lung,

$$Re(x) = \frac{\rho V(x) d(x)}{\mu}, \tag{3.14}$$

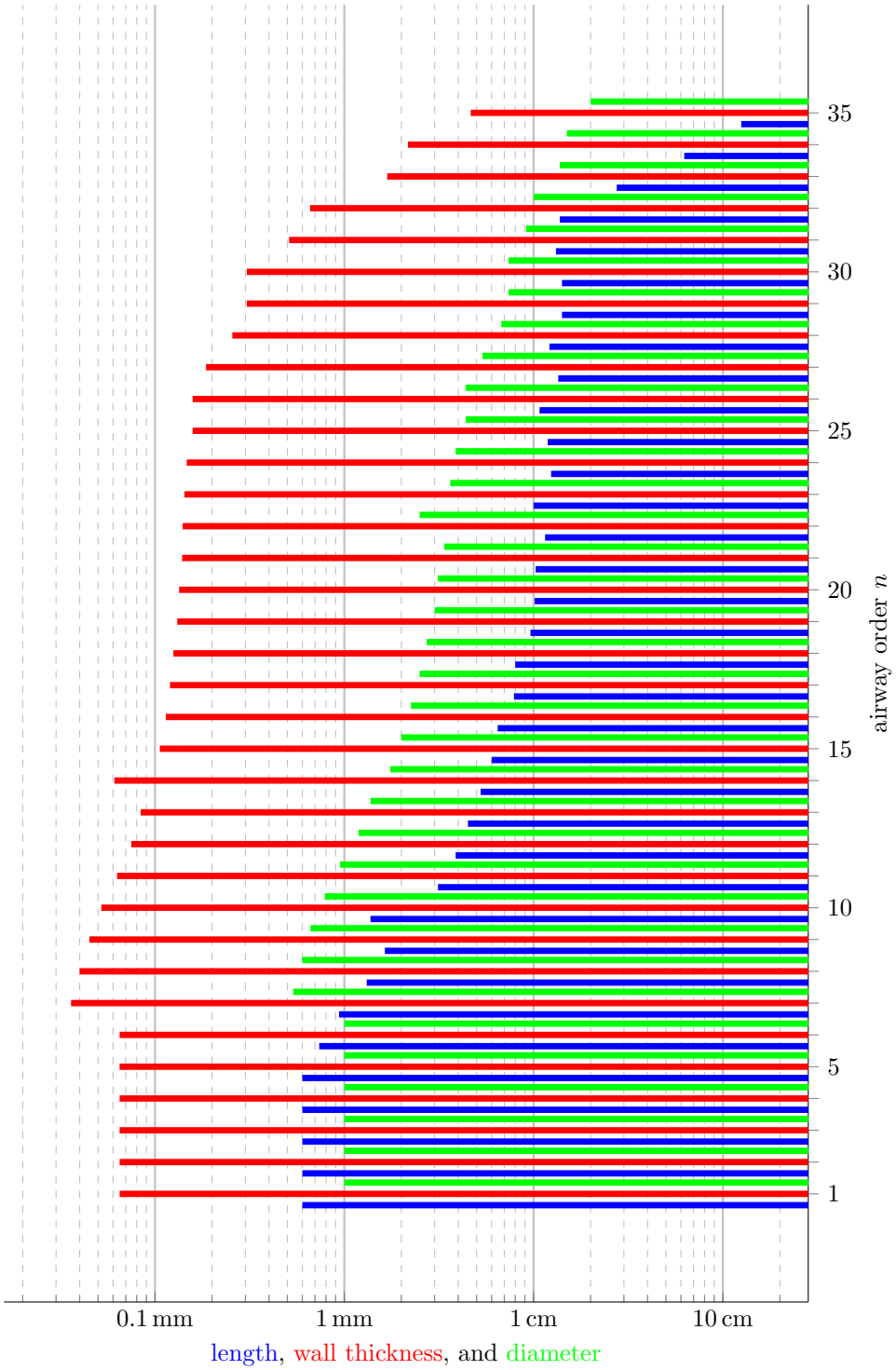
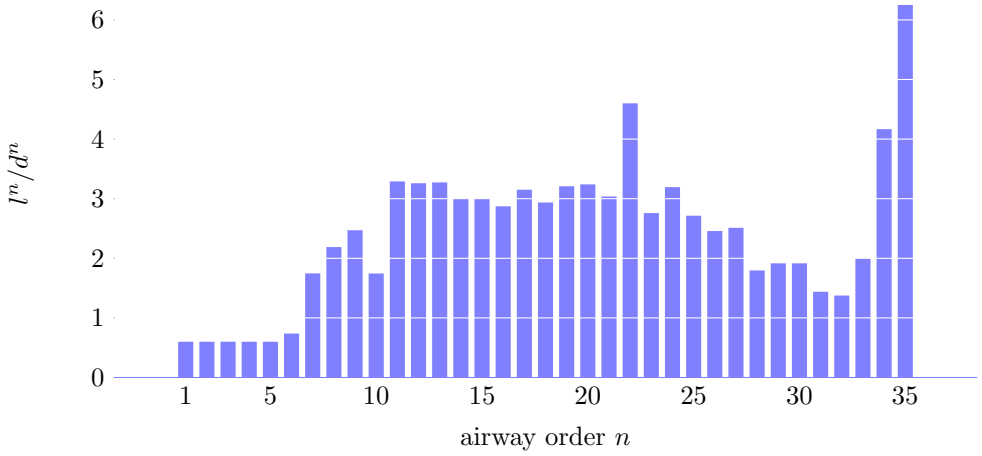


Figure 3.6: Horsfield lung dimensions.

(a) Airway length divided by diameter.



(b) Airway wall thickness divided by diameter.

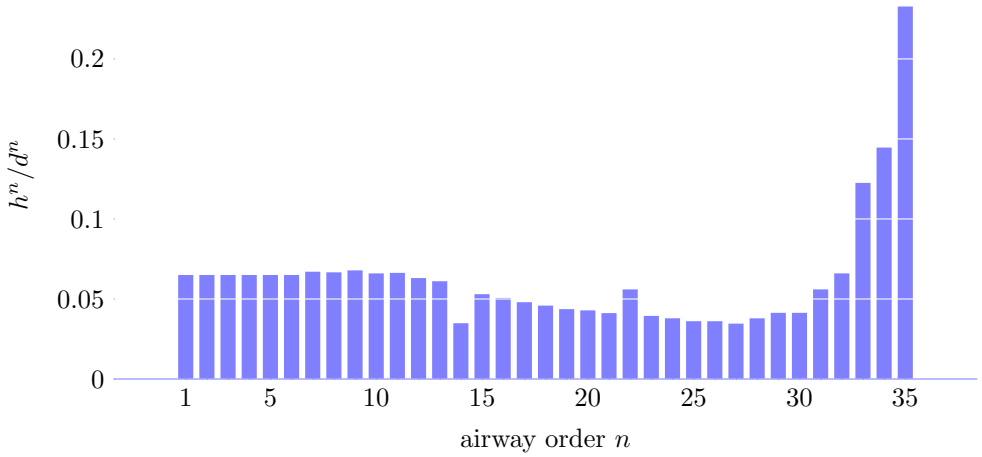


Figure 3.7: Geometry ratios in the airways of the human lung according to the Horsefield model.

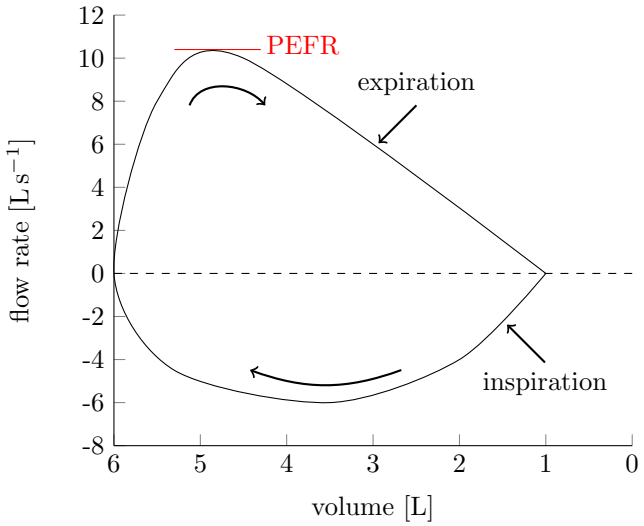


Figure 3.8: A typical flow volume loop for an adult human.

where $d(x)$ is the average tube diameter at a distance x into the lung. If the number of distinct paths at distance x into the lung is $N(x)$, then $d(x)$ is given by $d(x) = \sqrt{4(A(x)/N(x))/\pi}$. To complete this model we must supply the inlet condition. We can do this from estimates of the flow rate into the lung.

A typical flow volume curve is shown in fig. 3.8, which indicates a peak expiratory flow rate (PEFR) of around $10\,\mathrm{L\,s^{-1}}$. [Nunn and Gregg, 1989] provide an investigation into how the PEFR varies in adults. Their results indicate that men typically have a PEFR between $9\,\mathrm{L\,s^{-1}}$ and $11.5\,\mathrm{L\,s^{-1}}$, while women are typically between $6.5\,\mathrm{L\,s^{-1}}$ and $10\,\mathrm{L\,s^{-1}}$. For adults generally we see that the largest flow rate during normal breathing is generally between $6.5\,\mathrm{L\,s^{-1}}$ and $11.5\,\mathrm{L\,s^{-1}}$. We can use these to estimate the largest Reynolds number seen during the breathing cycle at various distances into the lung. Proceeding from the discussion in §3.2.1, we take $\mu = 19\,\mu\mathrm{Pa\,s}$ and $\rho = 1.12\,\mathrm{kg\,m^{-3}}$. This is plotted in fig. 3.9.

In a similar manner we can estimate an average flow rate in the individual tubes as a function of distance into the lung. We can calculate the average velocity and tube diameter at a given distance into the lung as before, and from this we can find an average flow rate $Q(x) = \pi d(x)^2 V(x)/4$. From this we obtain the plot shown in fig. 3.9.

3.2.4 The Parenchyma

The material surrounding the oscillating tubes in the lung is assumed to be homogeneous, following the approach of [Rice, 1983]. We must account for any variations in pressure present

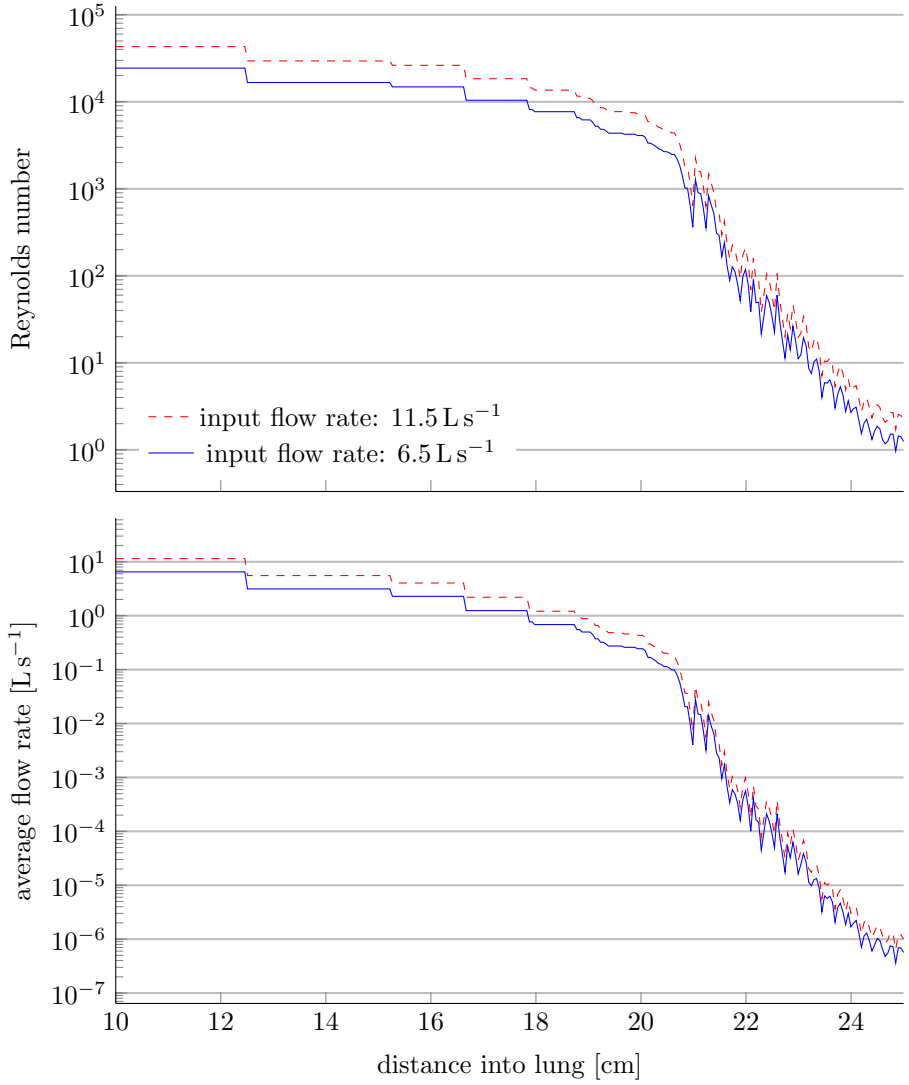


Figure 3.9: Reynolds number and flow rate as a function of distance into the lung.

in the parenchyma caused by the oscillations of the airways.

Close to the tube we can treat the response of the surrounding medium as incompressible. In this region the local velocity u of the medium will be equal to that of the tube wall, and the local pressure variation will be of the order $0.5\rho_p u^2$, where ρ_p is the density of the parenchyma. We can estimate u using the radius of the tube a and the frequency of oscillation f, $u \approx af$. Hence variations in pressure close to the tube will be approximately $0.5\rho_p(af)^2$. Taking typical values of $\rho_p = 100\,\mathrm{kg\,m^{-3}}$, $a = 3\,\mathrm{mm}$, and $f = 100\,\mathrm{Hz}$, we obtain a pressure variation estimate of 5 Pa. This is small compared to the transmural pressure drop, which is typically 1000 Pa, so we will ignore the effect of these pressure variations. Note that in our experiments, where the surrounding material is air, the pressure variations will be even smaller ($\sim 0.05\,\mathrm{Pa}$) since the density of air is around $1.2\,\mathrm{kg\,m^{-3}}$.

3.3 Previous Experiments

Firstly we consider the geometry of the tubes under consideration. From the Horsfield lung model, in the region of the lung where we believe wheezing to originate, l/d is in the range 1.3–4, and h/d in the range 0.03–0.2. From [Hoppin et al., 1977] we know that l/l_0 is in the range 1.1–1.8. In the literature l/d spans the range 4–92. [Gavriely et al., 1989], who uses air as the working fluid, is the author that uses the highest l/d, well outside that needed to get relevant information on wheezing, and [Oruç et al., 2011] uses an l/d between 5 and 10. h/d is in the range 0.07–0.3 in the literature, which much more closely matches what is expected in the lung. l/l_0 is only ever 1 in the literature.

The pressure drops considered by different authors are summarised in fig. 3.10. In all cases $p_e - p_2$ covers a range that includes $3P_k$, which reflects the fact that oscillations are always observed when the tube is collapsed or partially collapsed. Several authors only provided enough information for either $(p_1 - p_2)/P_k$ or $(p_e - p_2)/P_k$ to be calculated [Brower and Noordergraaf, 1973; Conrad, 1969; Gavriely et al., 1989; Wang et al., 2009], and the only author who does not include $3P_k$ in their range is Wang et al., whose range of $(p_1 - p_2)/P_k$ is 7–34. The relevance of P_k to self-excited oscillations depends on P_k being a good measure of the pressure at which the tube collapses. In our work, the fact that the tube is held in axial strain means that P_k, as defined in eq. (3.3), is less relevant, but we will find that the collapse pressure of the tube will be important. This will be considered in more detail in §8.

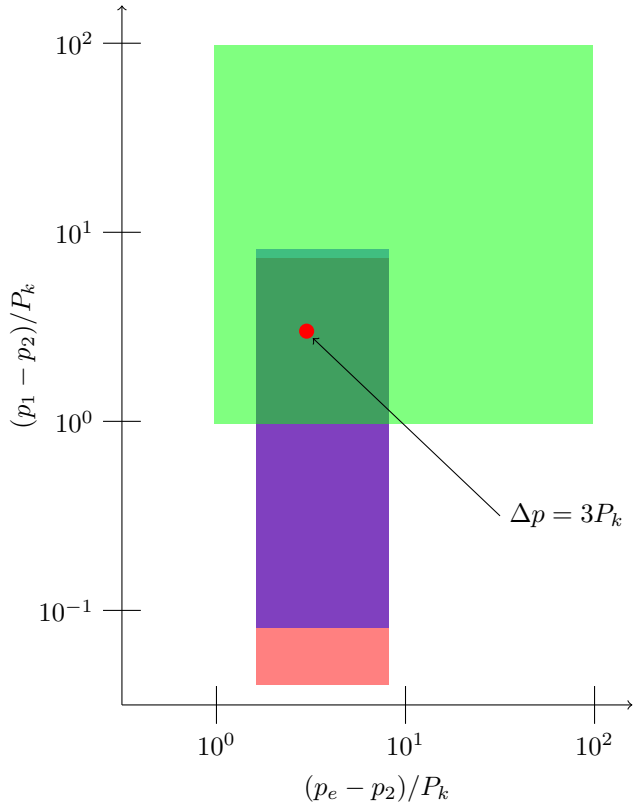


Figure 3.10: Pressure differences spanned by the literature. Red: [Bertram, 1986], blue: [Bertram et al., 1990], green: [Bertram and Elliott, 2003].

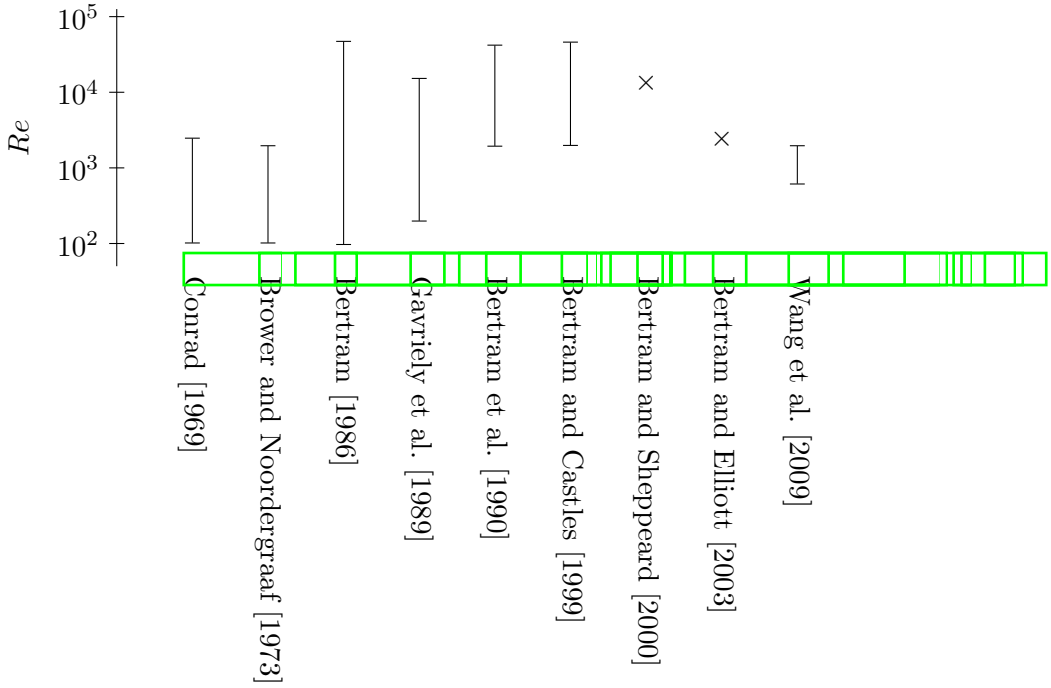


Figure 3.11: Reynolds numbers considered by the literature.

The Reynolds number at which various authors perform their experiments are shown in fig. 3.11. This indicates that, as already mentioned, self-excited oscillations are not generally seen below $Re = 200$. The range of Reynolds numbers investigated here matches the estimated range of Reynolds numbers seen in the upper portions of the lung quite well (see fig. 3.9).

All experimental work assumes that the tube wall is not viscoelastic. Lung tissue is phenomenologically observed to be viscoelastic, but accurate values of its viscosity are difficult to measure. At this stage only computational studies give any idea of the effect of viscosity [Hamadiche and Gad-el Hak, 2002]. We will not consider viscoelastic effects in our experiments.

The density ratio is easy to calculate. This is close to 1 for most authors, with the exception of [Grotberg and Gavriely, 1989; Oruç et al., 2011], who use air, and for whom $\rho/\rho_s = 1.3 \times 10^{-3}$. This is a significant difference between the majority of the experimental work and the lung, in which ρ/ρ_s is of the order 10^{-3}. Further evidence for this lies in the fact that the fluid density has little effect on the observed frequency of wheezing, indicating that it is the inertia of the wall and not the fluid that is significant. It could be that this means that the effects of up- and downstream inertiance observed by [Wang et al., 2009] could be less important in our application, and this is investigated in §6.2.

Figure 3.12 shows the range over which the variable $(\rho Q^2/a^4)/P_k$ is investigated by various authors. It is important to note that this takes a very small value in all of the studies, indicating that pressure changes due to the inertia of the fluid are much smaller than the pressure changes down the tube or across the tube wall. Interestingly, this is the equally true when the fluid is water or air. It is possible to estimate $(\rho Q^2/a^4)/P_k$ in the Horsfield model, which gives values of the order 10^{-3}. It is interesting to note that in none of the experimental work does $(\rho Q^2/a^4)/P_k$ approach 1, indicating that our initial arguments regarding the importance of the dynamic pressure in reopening the tube are incomplete. We will clarify this in some detail once we have obtained experimental results of our own in §8.4.3.

The dimensionless numbers that have not been matched to the approximate values in the lung by previous experiments are ρ/ρ_s, l/d, and l/l_0. Our own experiments must address this.

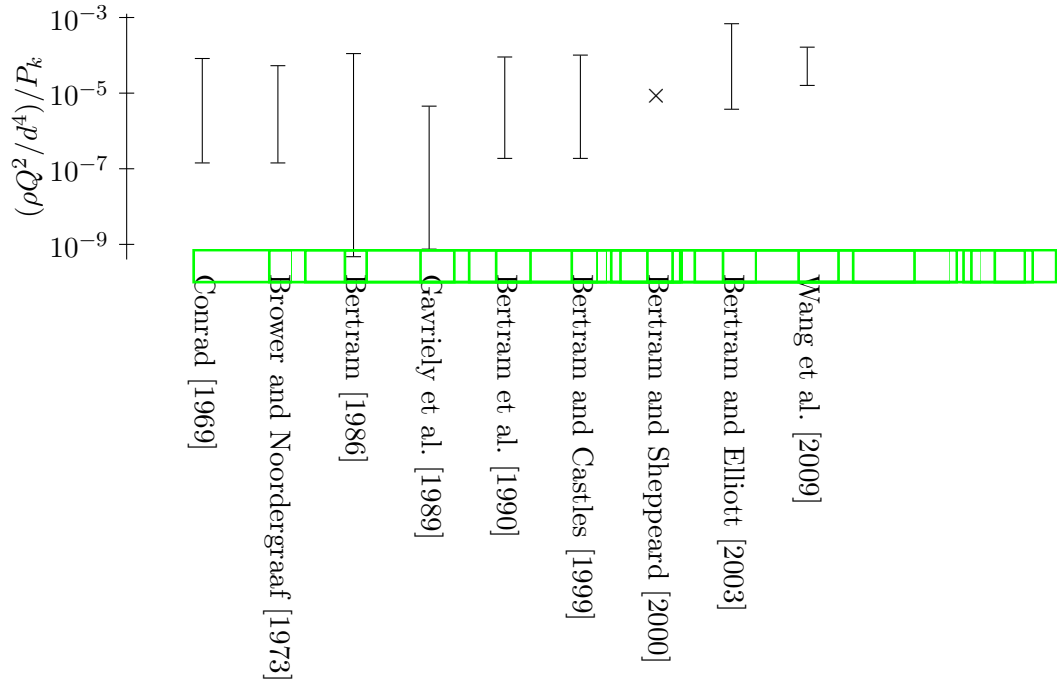


Figure 3.12: Ratio of dynamic pressure to characteristic collapse pressure considered by the literature

3.4 Initial Experiments

The purpose of the experiment is to investigate the dependence of self-excited oscillations of a flexible tube on the flow though the tube, the tube geometry and its material properties. We wish to find out whether it is possible to deduce information about the geometry or material properties based on the oscillations observed.

Initial experiments were performed investigating the oscillating modes of rocket balloon exit tubes. In a rocket balloon, sound is produced as air is forced through the exit tube and sets up a self-excited oscillation in a way that we believe is similar to that of wheezing. A high speed video was taken of the rocket balloon exit tube, from which frames are shown in fig. 3.13. The time interval between frames is 0.24 ms, and the frequency of the oscillations observed is approximately 350 Hz. This shows a large deformation of the tube wall as the oscillation progresses, and it would seem likely that the oscillations are accompanied by significant variations in mass flux. Both the tube wall movement and the unsteady mass flux could behave as sources of sound, with the former being rather like a quadrupole, due to the type of wall motion observed, and the latter being like a monopole.

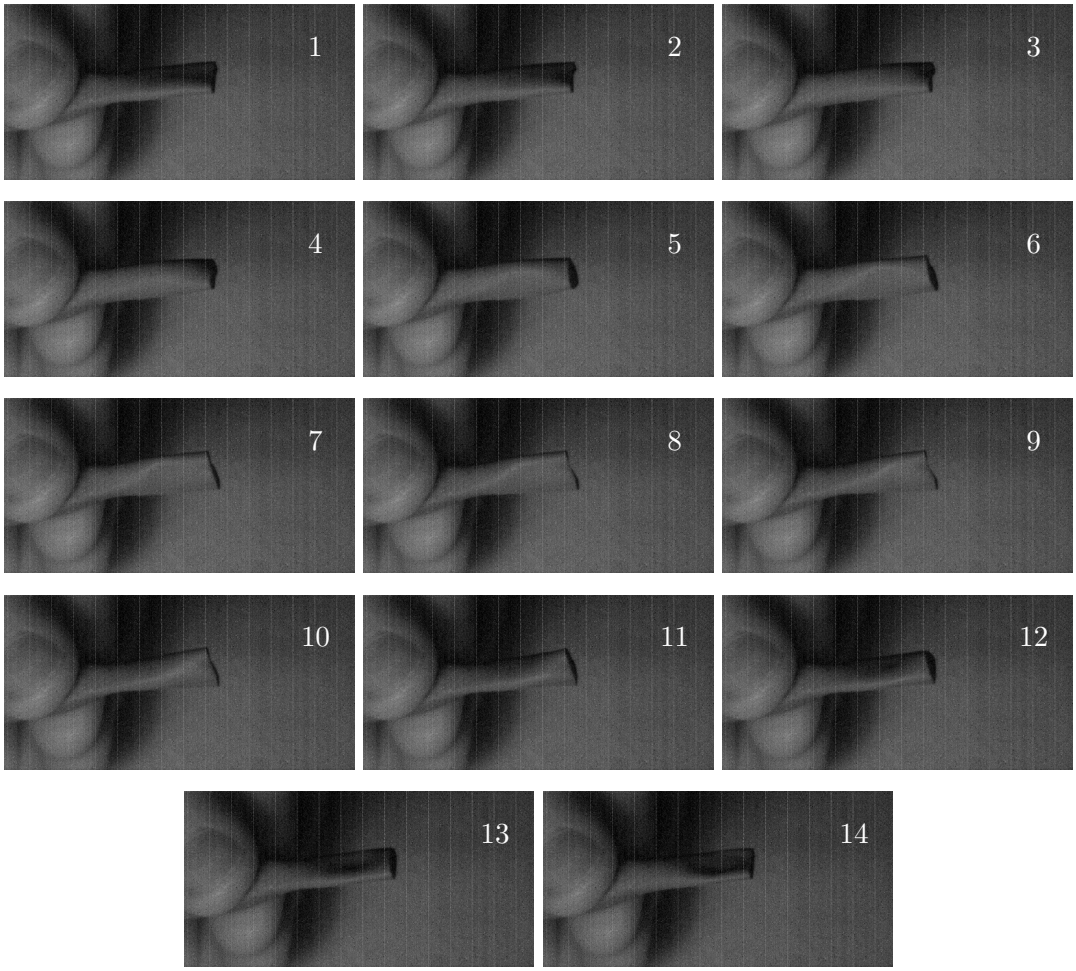


Figure 3.13: Stills from high speed video of rocket balloon ($\Delta t = 0.24\,\text{ms}$).

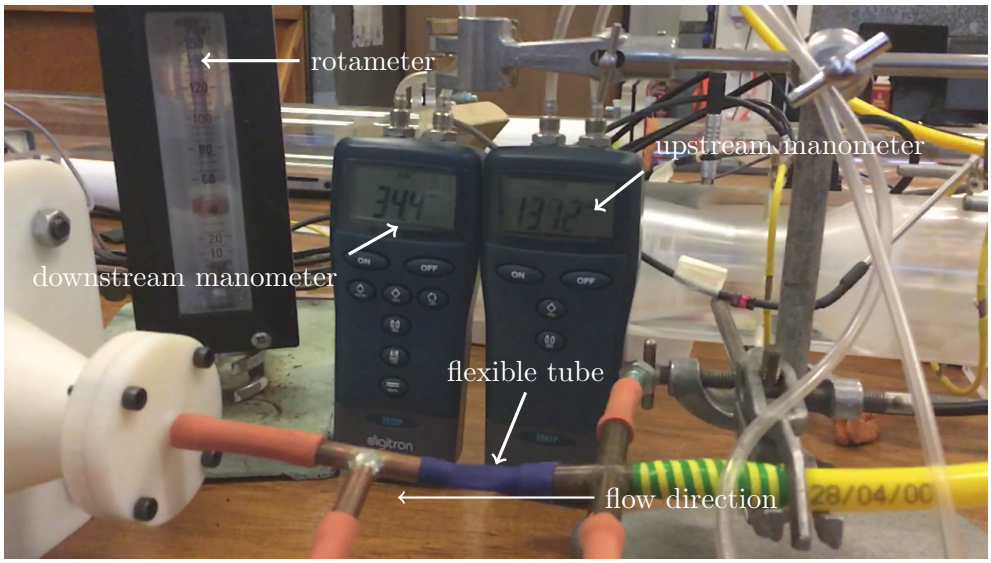


Figure 3.14: Set-up for preliminary Starling resistor experiment.

The biggest disadvantage of using a rocket balloon is that the downstream boundary condition does not match that seen in the lung, which more closely resembles a Starling resistor in which both the up and downstream parts of the tube are held open. Therefore we set up a preliminary experiment, shown in fig. 3.14, in which the exit tube of a rocket balloon was held between two rigid tubes. The rocket balloon exit tube had a length of approximately 20 mm, a diameter of approximately 6 mm, and wall thickness of 0.39 mm. The tube was made of natural rubber latex, for which the material properties are $\nu = 0.5$ and $E = 1\,\mathrm{MPa}$. These geometric and material parameters match those in the lung well.

Air was drawn through the flexible tube using a suction pump at the downstream end. The upstream end of the flexible tube was attached to a rigid plastic tube, which led to the downstream end of a Platon rotameter, which was used to monitor flow rate. Pressure was measured just up- and downstream of the flexible tube using Digitron manometers.

A single experimental run involved starting with no flow in the system, then gradually increasing the speed of the suction fan up to a maximum, before gradually bringing the flow back down to zero. This was done slowly enough for a quasi-steady state solution to be set up at any particular moment in the experimental run. Pressure and flow rate readings were all locally time averaged values, due to the response times of the instruments used. Pressure readings were taken in mbar and were accurate to within $\pm 0.3\,\mathrm{mbar}$. Flow rate was measured in $\mathrm{L/\,min}$ and was accurate to within $\pm 5\,\mathrm{L/\,min}$. A video was taken of the experiment. This

video included an audio recording with a sampling frequency of 44.1 kHz. Using the video, pressure and flow rate readings were recorded every 5 s throughout the run. $\bar{p}_1 - p_e$, $\bar{p}_2 - p_e$ and Q are shown over the course of the experiment in fig. 3.15 along with a spectrogram of the audio file. At the start of the experiment the flexible tube was open, and while this remained the case, decreasing the downstream pressure gave rise to a quickly increasing flow rate. As suction was further increased, the pressure inside the tube got lower relative to the environment, due to the presence of the rotameter upstream. Eventually, the pressure within the tube got low enough for it to collapse. The start of collapse corresponds in fig. 3.15 to the levelling of of the flow rate Q ($t \approx 50$ s), quickly followed by the start of oscillations ($t \approx 60$ s), which are visible in the spectrogram. As the suction is further increased, the tube goes through 3 modes of oscillation before eventually collapsing completely ($t \approx 150$ s). The tube is held collapsed for a short period, before the suction is gradually decreased to nothing. As the suction is reduced, the 3 oscillations modes are seen again in reverse before the tube opens fully at $t \approx 250$ s.

This preliminary experiment confirms the existence of self-excited oscillations in tubes with air flowing through them, with geometry comparable to that seen in the lung. It is very clear from the literature that the exact flow conditions can have a significant impact on oscillations, so we will now detail a much more refined experimental setup, based on the preliminary one, which we use to investigate these oscillations in more detail.

3.5 Experiment Design Refinement

A large issue with previous Starling resistor experiments has been repeatability. To avoid this problem we need to carefully control the airflow through the flexible tube (FT), and the surrounding environment of the FT. An experimental set-up is shown schematically in fig. 3.16, and we will now discuss various aspects of this rig.

3.5.1 Controlling the Flow

Flow is driven by suction at the downstream end ((8) in fig. 3.16). The suction fan and the rotameter (2) introduce significant noise into the flow, which could interfere with the oscillations of the FT (7). Therefore, the FT is separated from these sources of noise at the up and downstream ends by settling chambers (SCs) (3/3′), whose volumes are at least

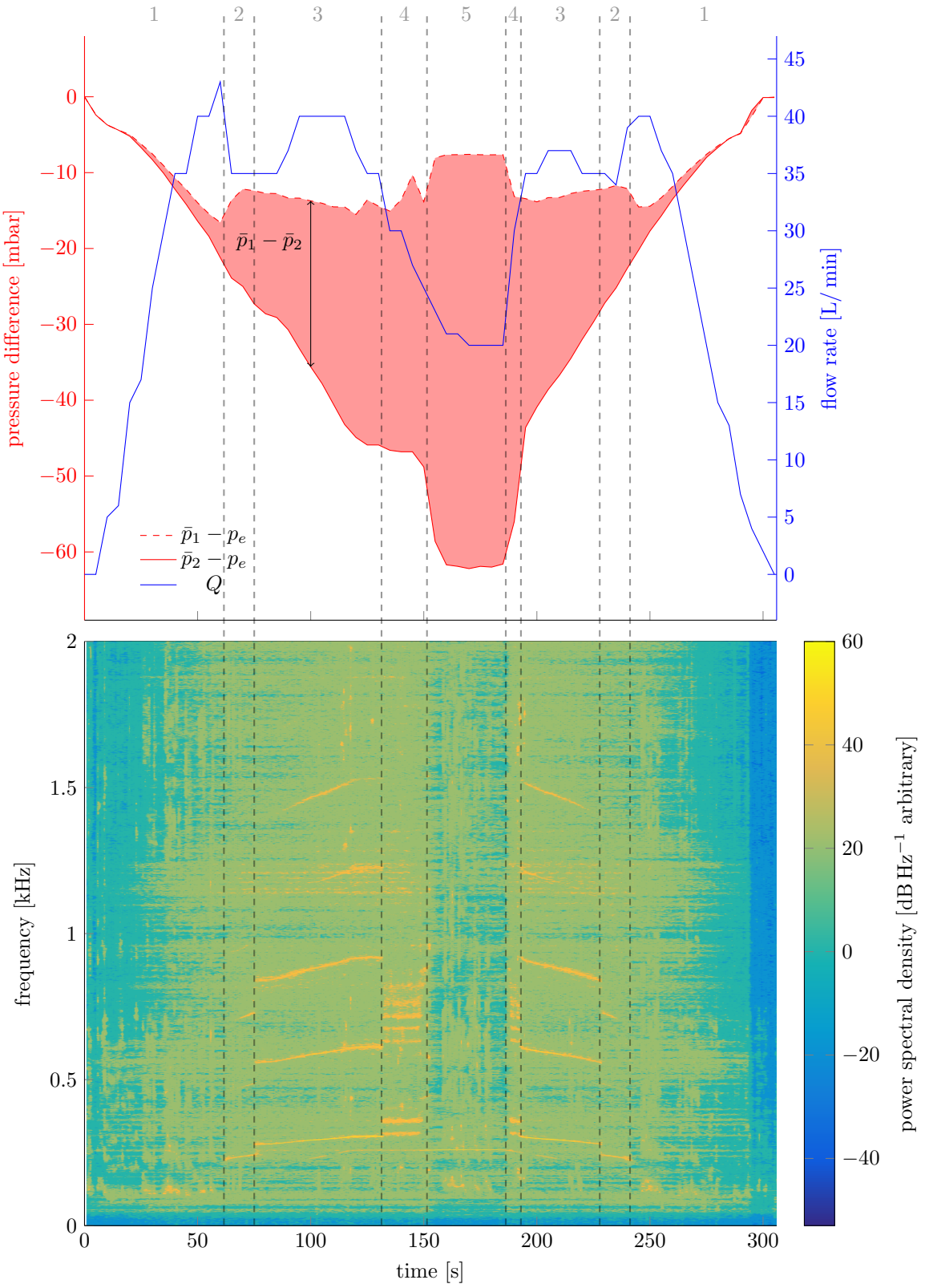


Figure 3.15: Preliminary experimental run using the thick walled rocket balloon exit tube. 1: fully open tube (no oscillation), 2: first oscillatory mode, 3: second oscillatory mode, 4: tube almost fully collapsed with some oscillation, 5: fully collapsed tube (no oscillation).

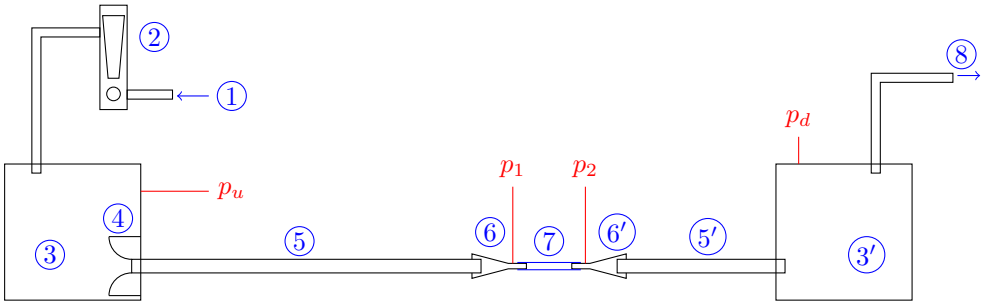


Figure 3.16: Schematic of Starling resistor experiment. (1): Flow inlet, (2): rotameter, (3/3′): settling chambers, (4): clean flow inlet, (5/5′): clean flow tubes, (6/6′): contraction and expansion, (7): flexible tube, (8): tube to suction fan. The downstream settling chamber is approximately $4\,\mathrm{m}^3$ while the upstream settling chamber is $0.03\,\mathrm{m}^3$. Pressure is monitored at the four locations indicated, p_u, p_1, p_2, and p_d.

$0.03\,\mathrm{m}^3$. The inlets and exits of the SCs must be aligned so that the jet from the entry does not impinge on the exit, otherwise noise will not be removed effectively.

The condition of the flow as it enters the FT is controlled by the clean flow inlet (CFI) (4), the upstream clean flow tube (UCFT) (5), and the contraction (6). These are discussed in turn.

The entry from the upstream settling chamber (USC) to the UCFT (via the CFI) must be designed to minimise separation, as this gives the best chance of clean and controlled flow into the FT. For this reason we use a rounded inlet of the form shown in fig. 3.17.

The UCFT (5) is chosen to have a length at least 30 times its diameter, and in this way we can be sure that by the time flow reaches the contraction it is fully developed. If we decide that a more plug-like flow is desired at the FT inlet, we can make the UCFT very short. We also ensure that the UCFT is straight to be sure that no secondary flows are introduced.

We design the contraction (6) so that inner wall radius, and its first and second derivatives, are a continuous function of distance down the tube. We also choose the contraction length so that the contraction angle is less than 10° (see fig. 3.18). The ID at the exit of the contraction is set by the ID of the particular FT in use. This illustrated in the detailed design shown in fig. 3.18.

For simplicity of manufacture the expansion (6′) is the same as the contraction. The fact that we make the contraction so that the contraction angle is less than 10° minimises separation in the expansion. From the expansion flow travels into the downstream clean flow

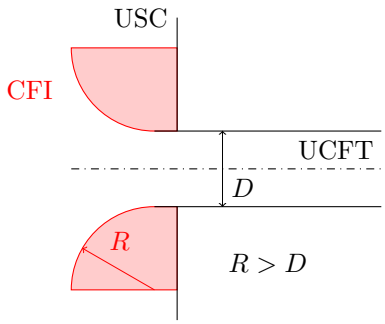


Figure 3.17: Detailed design of the clean flow inlet.

tube (DCFT) (5′). The length of this tube is not critical, but it must be straight so that reflections back into the FT are minimised. Together we refer to the UCFT and DCFT as the clean flow tubes (CFTs).

In order to investigate the effect of the CFTs on the oscillations we use several different lengths. In most experiments we use a UCFT length of 948 mm and a DCFT length of 440 mm, but in a set of experiments where the FT is not changed we use three different UCFT lengths (988 mm, 440 mm, 152 mm) and three different DCFT lengths (989 mm, 440 mm, 152 mm), in a total of nine different setups (see §6.2).

We need to control the suction (8) in a repeatable way. If the suction power is increased (or decreased) too quickly, then we will not be able to regard the tube behaviour as quasi-steady. To ensure that the behaviour of the tube is independent of the rate at which the suction is ramped up, we perform initial experiments at various ramping rates, and choose a ramping rate at which we see no change in tube behaviour if the ramping rate is increased of decreased. The suction fan is controlled by an external voltage, which in turn in produced by a signal generator, which allows the ramping rate to always be the same.

The experimental rig is set up so that the external pressure p_e is also the pressure far upstream of the flexible tube. This is done to mimic exhalation in the lung. Exhalation is when wheezing is most common [Forgacs, 1978a], so it is logical for us to design our rig in this way. In the lung p_e is the pressure in the parenchyma, but this is also the pressure far upstream of the airway under consideration, and during exhalation, the pressure in the parenchyma is raised by contraction of the chest. Hence by lowering the pressure far downstream in our rig, while holding p_e and the far upstream pressure constant, we are mimicking the far upstream pressure and p_e being raised together in the lung while the far downstream pressure (the pressure at the mouth) is held constant.

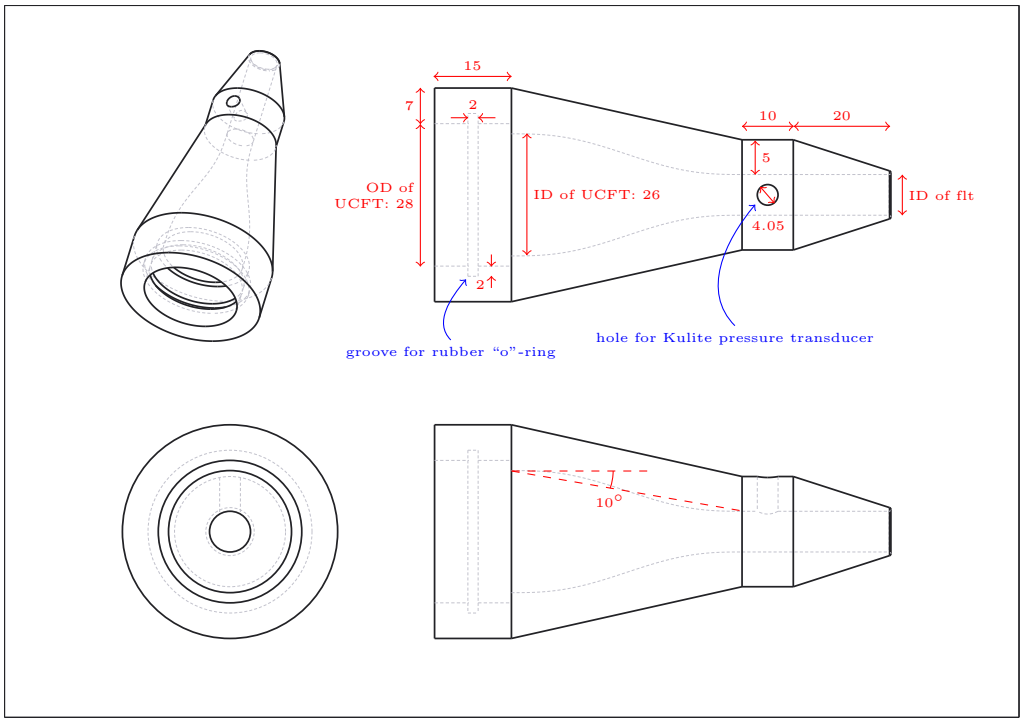


Figure 3.18: Detailed design of the contraction and expansion, all dimensions in mm.

3.5.2 Controlling the Flexible Tube

In order for flow into the FT to be controlled we design the contraction such that the ID at the exit of the contraction matches that of the FT. It has been observed several times by previous studies that the way the FT is attached can affect the oscillations observed. To make our attachment method as repeatable as possible we make the attachment point conical, as shown in fig. 3.18, allowing us to pull the flexible tube a given distance onto the contraction.

3.5.3 Controlling the Surrounding Environment

Experiments are performed in the acoustics laboratory of Cambridge University Engineering Department. A uniform ambient pressure and temperature is maintained in this environment.

3.5.4 Measurements

Measurements are taken of various quantities using the following methods:

Pressure Measured using Kulite pressure transducers (model number XCS-093-5PSID or

XCQ-093-0.35BARD). We denote pressure measured in the USC p_u, the downstream settling chamber (DSC) p_d, just upstream of the FT p_1, and just downstream of the FT p_2, as shown in fig. 3.16.

Flow Rate Time averaged flow rate is obtained using a rotameter placed upstream of the USC ((2) in fig. 3.16). Key instruments MR3000 series rotameters were used. Video of the rotameter was taken at 30 fps using an iPhone 6s.

Acoustic Pressure Measured using GRAS 1/8 in prepolarised pressure microphones (part number 40DD), along with a GRAS 1/4 in preamplifier (part number 26CB). To use this as a free field microphone it is oriented at 90° to the expected direction of sound propagation. We denote this acoustic pressure p_a.

High Speed Video Two FASTCAM-ultima APX high speed cameras (produced by Photron) are used, recording at 12 500 fps with a resolution of 512×256 pixels (greyscale). These have an adaptor that allows any Nikon lens to be attached. Our experiments require us to focus on a small FT at reasonably close range, so 50 mm lens's are used combined with a 7 mm extension tube. An aperture of $f/2.8$ is used.

Data is logged using a National Instruments CompactDAQ chassis (NI cDAQ-9178) with 4 NI 9234 analogue input modules, giving 16 data channels in total. In addition, an NI 9263 analogue output module is used to provide repeatable control of the suction fan downstream of the DSC. The NI 9234 analogue input modules can provide the 3 mA power supply to the prepolarised microphone, however, the Kulite pressure transducers require an intermediate amplifier to provide 10 V excitation. This amplifier is produced in house.

The NI cDAQ-9178 can run up to 7 data channels simultaneously, which are used for the pressure and acoustic measurements. This captures data at a sampling frequency of 51.2 kHz, and automatically filters the signals to avoid aliasing.

The time averaged flow rate data from the rotameter is collected in the form of a video. The rotameter ball is found in the frame using the MATLAB® function `imfindcircles`; the rotameter and camera are surrounded by a translucent covering to ensure that lighting conditions remain constant throughout the experimental run. The rotameter markings are found in the image using the MATLAB® function `findpeaks`, and this allows the ball position to be converted into a flow rate value for each frame. This is synchronised with measurements

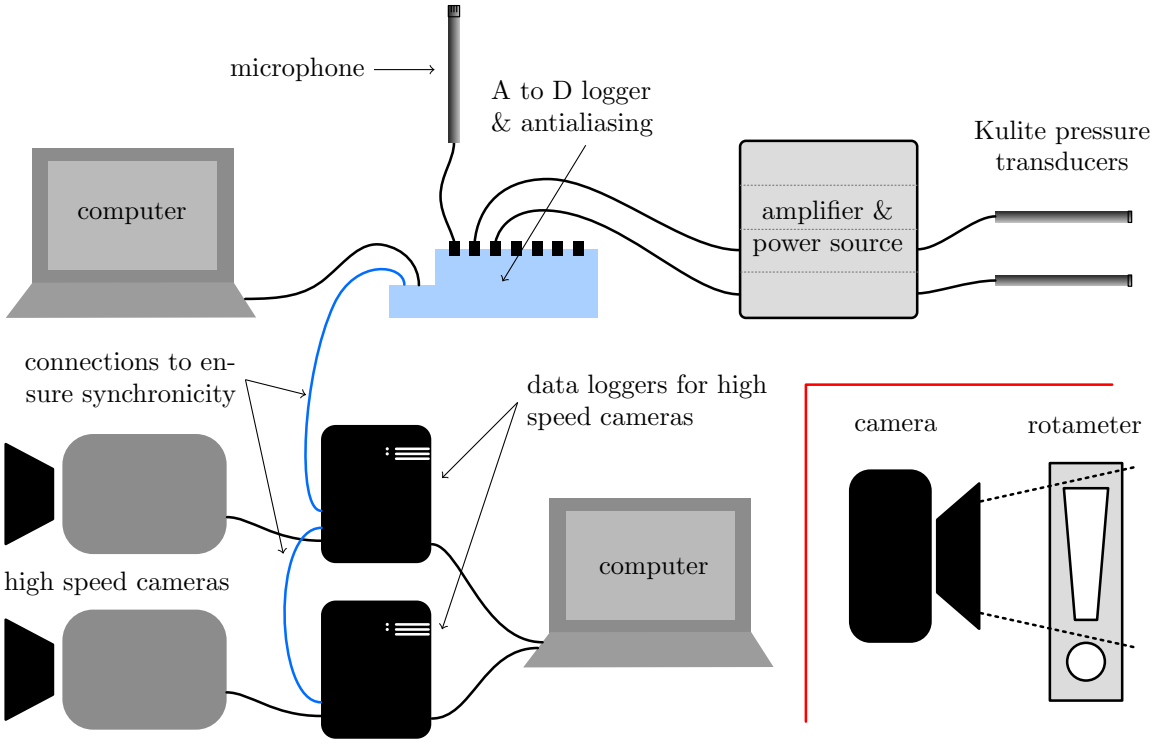


Figure 3.19: Data logging equipment.

taken using the NI cDAQ-9178 by finding the cross correlation of the sound signal recorded from the GRAS microphone and the video sound signal.

To achieve simultaneous recordings from two high speed cameras and the NI cDAQ-9178, the timing signal and a triggering signal, which marks the start of the recording period, are taken from the output of one of the cameras, and used to drive the second camera. The triggering signal is also used to trigger the start of recording on the NI cDAQ-9178. The time averaged flow rate from the rotameter takes only one value throughout the short period over which video is recorded, which is read off and recorded manually.

The data logging equipment used is illustrated in fig. 3.19. The suction fan can be controlled automatically by a voltage output from the NI 9263 analogue output module, or manually.

3.6 Experimental Protocol

The experimental rig described in the previous section will allow us to investigate self-excited oscillations in flexible tubes, and control the effects of up- and downstream conditions in a

predictable way.

It was made clear in the preliminary experiments that flexible tubes exhibit a very wide variety of behaviours, showing multiple modes of oscillation as flow conditions are changed. Our aim is to be able to make predictions regarding wheezing, so we will concentrate on the *onset* of oscillations. By understanding onset, we hope to be able to understand what it is that makes wheezing happen in the lung, which is the overall aim of this project.

Given this aim, we conduct two types of experiment. For a given flexible tube we will use one experiment to get detailed data on what *leads* to the onset of oscillation, and the other experiment to get data on the oscillations observed once self-excited oscillations have started. These two experiment types are detailed in the protocols below.

3.6.1 Investigating the Cause of Onset

To investigate the cause of the onset of self-excited oscillations we use an experimental protocol based on that used in the initial experiments (see fig. 3.15). For a flexible tube of a given geometry, the following protocol is followed,

Protocol 1.

1. (a) Align rig so that flow though the UCFT, FT, and DCFT is straight.
   (b) Move upstream section of rig so that the contraction is in contact with the expansion. Zero the length measurement so that the length of the tube under observation can be read off.
2. (a) Attach the FT to the expansion by pulling the rubber over the conical shape and then taping over the top with electrical tape to prevent the FT from pulling off.
   (b) Attach the FT to the contraction in the same way, ensuring no twist in the FT.
   (c) Mark the FT at the points where it is attached to the contraction and expansion to allow the unstrained tube length l_0 to be measured later.
   (d) $\star$ Move the upstream section of the rig so that the tube is held at the desired length l, which can be read off.
3. (a) Ensure that the rotameter is held vertically, and place video camera so that it can read the rotameter, and is covered to keep lighting conditions constant.
   (b) Ensure that Kulite transducers are reading pressure in the USC (p_u), DSC (p_d), and directly up- and downstream of the FT (p_1 and p_2). Ensure that microphone

is in place to record free-field acoustic pressure approximately 25 cm away from the FT (p_a).

(c) Take a 10 s recording to ensure that all transducers are functioning correctly.

4. (a) ⋆ Perform automated experimental run, remembering to take video recording of the rotameter, 2–6 times, in which the downstream suction fan is slowly run up to its maximum power, and then slowly run back down again (controlled by a voltage produced by a signal generator), while p_u, p_d, p_1, p_2, and p_a are simultaneously recorded.

(b) Create plots of from the runs to ensure results are as expected.

5. ⋆ Remove FT from rig and measure its unstrained length l_0, wall thickness h, and diameter d. Store the FT.

Performing more repetitions in step 3 allows a better understanding of repeatability, but also wears out the tubes more quickly, so we perform 6 repetitions with a few tubes, but with most only perform 2 or 3. Items that have been marked with a ⋆ in the above protocol are ones where data must be recorded. For every experimental run in the above protocol, it is possible to produce a plot similar to fig. 3.15, but the fidelity of the flow rate and pressure readings is much higher (see fig. 6.2).

3.6.2 Investigating Oscillations After Onset

To investigate the oscillations just after onset in more detail, we use a setup with two high speed cameras to allow multiple camera reconstruction of the surface of the flexible tube as it oscillates. We simultaneously record the pressures p_u, p_1, p_2, and p_d as well. For a flexible tube of a given geometry, the following protocol is followed,

Protocol 2. 1. (a) Align rig so that flow though the UCFT, FT, and DCFT is straight.

(b) Move upstream section of rig so that the contraction is in contact with the expansion. Zero the length measurement so that the length of the tube under observation can be read off.

2. (a) Arrange the two high speed cameras to have a good view of the FT, in focus with good lighting. Ensure that the black background for recording is in place.

(b) ⋆ Take a set of at least 12 calibration photos with the high speed cameras. Perform the calibration to ensure that the set up will allow 3-dimensional reconstruction.

3. (a) Mark the surface of the FT with dots.

   (b) Attach the FT to the expansion by pulling the rubber over the conical shape and then taping over the top with electrical tape to prevent the FT from pulling off.

   (c) Attach the FT to the contraction in the same way.

   (d) Mark the FT at the points where it is attached to the contraction and expansion to allow the unstrained tube length l_0 to be measured off later.

   (e) ⋆ Move the upstream section of the rig so that the FT is held just taut. Take a set of stereo images so that the unstressed state of the tube is known.

   (f) ⋆ Move the upstream section of the rig so that the tube is held at the desired length l, which can be read off.

4. (a) Ensure that the rotameter is held vertically.

   (b) Ensure that Kulite transducers are reading pressure in the USC (p_u), DSC (p_d), and directly up- and downstream of the FT (p_1 and p_2).

   (c) Take a 10 s recording to ensure that all transducers are functioning correctly.

5. (a) ⋆ Take a 10 s simultaneous recording of p_u, p_d, p_1, p_2, and the high speed cameras with no flow through the system.

   (b) ⋆ Manually run the suction fan so that the FT just starts to oscillate, then take a 10 s simultaneous recording of p_u, p_d, p_1, p_2, and the high speed cameras. Run the fan back down again.

6. ⋆ Remove FT from rig and measure its unstrained length l_0, wall thickness h, and diameter d. Store the FT.

Once again, items marked with a ⋆ show where data will be recorded.

3.7 Summary

Using the first comprehensive dimensional analysis of self-excited oscillations of flexible tubes, we have shown that, if our aim is to understand oscillations of direct relevance to wheezing,

we need to conduct new experiments. Specifically, we need to match ρ/ρ_s, l/d, and l/l_0 to those values in the lung. In addition, the experimental rig has been set up so that the external pressure p_e is also the pressure far upstream of the flexible tube. This has been done to mimic exhalation in the lung. The exact ranges of the relevant dimensionless variables that we span in our experiments are given in fig. 6.1.

It is also clear from previous work that it is necessary to consider in detail *all* aspects of the rig, up and downstream of the flexible tube, since this can have a significant effect on the oscillations observed. Hence, the rig shown in fig. 3.16 is carefully designed to allow repeatability, and also enables us to investigate the effect of changing the upstream and downstream conditions by changing the lengths of the UCFT and DCFT. This is addressed specifically in §6.2.

The detailed experimental protocols in §3.6 will allow us to investigate conditions in the flexible tube in the lead up to onset, and to get a detailed picture of the oscillations themselves. For the first protocol (§3.6.1), we have not yet detailed how we will extract information specific to the onset of oscillations. This is done in §6.1. For the second protocol (§3.6.2), we have not yet detailed how the use of high speed cameras will allow us to reconstruct the three dimensional motion of the shell. This is done in §7.1.

Before proceeding to investigate the experimental results, we will develop the mathematical theory of shells that will be used to understand the results.

Chapter 4

Fundamentals of Elasticity

We are interested in developing the elastic theory of shells, however, we will start by reviewing three dimensional elasticity since many of the concepts will carry over when considering elasticity on a curved two-dimensional surface. This chapter will enable us to introduce some of the methods of geometric algebra in a familiar context. Readers already familiar with elasticity may wish to only read the section on geometric algebra, and go straight to the chapter on elasticity in shells (§5). A good text on elasticity is [Marsden et al., 1994], and [Doran and Lasenby, 2003; Hestenes and Sobczyk, 1984] provide a good introduction to geometric algebra.

4.1 Geometric Algebra

We wish to use geometric algebra in place of differential geometry in order to give a more lucid description of the theory of shells, with a particular interest in using rotors to represent rotations. In this section and chapter however, we will focus on the more fundamental tools, and introduce more sophisticated topics in §5.

Geometric algebra begins with vectors, and the geometric product. Let us imagine that we have three vectors, a, b and c, in a flat vector space. The geometric product satisfies three axioms,

1. The geometric product is associative, $a(bc) = (ab)c = abc$.
2. The geometric product is distributive, $a(b + c) = ab + ac$.
3. The square of any vector is a real scalar, $a^2 \in \mathbb{R}$.

It is the third axiom that distinguishes geometric algebra from general associative algebras. For general multivectors the geometric product satisfies just the first two axioms. It is significant that under these axioms we can always find a vector's *inverse* $a^{-1} = a/a^2$ such that $aa^{-1} = 1$.

If we square $(a + b)$ we obtain,

$$(a+b)^2 = a^2 + ab + ba + b^2 \quad \Rightarrow \quad ab + ba = (a+b)^2 - a^2 - b^2 \in \mathbb{R}, \tag{4.1}$$

by the third axiom. We therefore *define* the (symmetric) **inner product** as,

$$a \cdot b = \frac{1}{2}(ab + ba). \tag{4.2}$$

The remaining, antisymmetric part of the geometric product defines the **exterior**, or **outer product**,

$$a \wedge b = \frac{1}{2}(ab - ba). \tag{4.3}$$

This leads to the decomposition of the geometric product of two vectors,

$$ab = a \cdot b + a \wedge b. \tag{4.4}$$

$a \cdot b$ is scalar, but $a \wedge b$ is a **bivector**, or a grade 2 vector. Using the outer product, we can construct vectors of any grade up to the dimension of the vector space. By adding together vectors of various grades we obtain **multivectors**.

If a and b are orthogonal then $a \cdot b = 0$, and so $a \wedge b = ab$. It is always possible to express a grade r vector A as the geometric product of a set of r orthogonal vectors $A = a_1 a_2 \cdots a_r$ [Doran and Lasenby, 2003, §4.1.1]. The **reverse** of A is then given by $\tilde{A} = a_r \cdots a_2 a_1$.

In Euclidean spaces, if A is a vector of any grade then $A\tilde{A}$ is always a scalar greater than or equal to zero, with $A\tilde{A} = 0$ implying that $A = 0$. We define the **magnitude** of A as $|A| = \sqrt{A\tilde{A}}$.

If n is the dimension of the space, then the maximum number of grade r vectors that we can construct that are not linearly dependent is $\binom{n}{r} = n!/(r!(n-r)!)$. Hence there is a single linearly independent grade n vector, and we define the grade n vector that satisfies $I^2 = \pm 1$ (in Euclidean spaces $I^2 = -1$) to be the **pseudoscalar** of the vector space. If

$\{e_i\}, i = 1, \ldots, n$ form a **frame** of the vector space then,

$$I = \frac{e_1 \wedge e_2 \wedge \cdots \wedge e_n}{|e_1 \wedge e_2 \wedge \cdots \wedge e_n|}. \tag{4.5}$$

In three dimensional Euclidean space ($\mathbb{E}^3$), the outer product between two vectors $a \wedge b$ is related to the **cross product** $a \times b$ by,

$$a \times b = -Ia \wedge b, \tag{4.6}$$

where I, in this equation, is the pseudoscalar of $\mathbb{E}^3$. Another common product in geometric algebra, which is not confined to objects in $\mathbb{E}^3$, is the **commutator product**, defined by,

$$A \times B = \frac{1}{2}(AB - BA), \tag{4.7}$$

where A and B are general multivectors. Note the difference between our symbols for the cross ($\times$) and commutator ($\times$) products. Both of these products will be used during the development of shell theory.

This introduces the geometric product, multivectors, and the pseudoscalar, which are all fundamental to geometric algebra. We will now consider the theory of elasticity in earnest, with these basic tools in mind. Bivectors in particular will become very important when we consider angular momentum and rotations in shell theory. For a more complete introduction to this subject, see [Doran and Lasenby, 2003, §§2,4].

4.2 Kinematics

We consider a body as consisting of a set of material points in three-dimensional Euclidean space $\mathbb{E}^3$. A **material point** is defined by its location in a **reference configuration**. The reference configuration is denoted $\mathcal{B} \subset \mathbb{E}^3$, and a material point is denoted $X \in \mathcal{B}$. As time progresses the body moves through $\mathbb{E}^3$. The portion of space the body occupies at time t is called the **spatial configuration** and is denoted $\mathcal{S} \subset \mathbb{E}^3$. At time t, the material point defined by $X \in \mathcal{B}$ lies at the point $\phi_t(X) \in \mathcal{S}$. $\phi_t(X)$ is a **motion** of the material point X, and we can generalise this concept to the whole body so that $\phi_t(\mathcal{B})$ is a motion of the body $\mathcal{B}$. We denote a general point in the spatial configuration $x \in \mathcal{S}$.

We introduce two coordinate systems, one on $\mathcal{B}$, and one on $\mathcal{S}$. On $\mathcal{B}$ we use the three functions $\{X^A(X)\}, A = 1, 2, 3$, which are sufficiently well behaved to allow us to write $X = X(X^1, X^2, X^3)$. On $\mathcal{S}$ we use the three functions $\{x^a\}, a = 1, 2, 3$ which can be inverted to obtain $x = x(x^1, x^2, x^3)$.

The tangent space of $\mathcal{B}$ at X, denoted $T_X\mathcal{B}$, is spanned by the **frame** $\{E_A\}$, defined by,

$$E_A = \frac{\partial X}{\partial X^A}. \tag{4.8}$$

The reciprocal frame, denoted $\{E^A\}$ also spans $T_X\mathcal{B}$, and is defined to satisfy $E^A \cdot E_B = \delta^A_B$. We can define this frame using the **vector derivative** ∇,

$$E^A = \nabla X^A. \tag{4.9}$$

The tangent space of $\mathcal{S}$ at x, denoted $T_x\mathcal{S}$, is similarly spanned by a frame and reciprocal frame defined by,

$$e_a = \frac{\partial x}{\partial x^a}, \quad e^a = \nabla x^a. \tag{4.10}$$

Given the general multivector valued functions $F(X)$ and $f(x)$, the vector derivative is defined by one of the properties,

$$\begin{aligned} Y \cdot \nabla F(X) &= \lim_{\epsilon \to 0} \frac{F(X + \epsilon Y) - F(X)}{\epsilon} \quad \forall Y \in T_X\mathcal{B}, \\ y \cdot \nabla f(x) &= \lim_{\epsilon \to 0} \frac{f(x + \epsilon y) - f(x)}{\epsilon} \quad \forall y \in T_x\mathcal{S}, \end{aligned} \tag{4.11}$$

depending on whether it is acting on the reference or spatial configurations. In these circumstances the vector derivative can be written as $\nabla = E^A \partial / \partial X^A = E^A \partial_A$ and $\nabla = e^a \partial / \partial x^a = e^a \partial_a$ respectively, where we have also defined ∂_A and ∂_a.

On the reference and spatial configurations we define the **metrics** G and g, which are really just the identity functions,

$$\mathsf{G}(Y) = Y, \quad \mathsf{g}(y) = y. \tag{4.12}$$

These satisfy the following coordinate expressions,

$$\begin{gathered}\mathsf{G}_{AB} = E_A \cdot E_B, \quad \mathsf{G}^{AB} = E^A \cdot E^B, \quad \mathsf{G}^A{}_B = \mathsf{G}_B{}^A = \delta^A_B, \\ \mathsf{g}_{ab} = e_a \cdot e_b, \quad \mathsf{g}^{ab} = e^a \cdot e^b, \quad \mathsf{g}^a{}_b = \mathsf{g}_b{}^a = \delta^a_b.\end{gathered} \tag{4.13}$$

We will make little use of these functions in three-dimensional elasticity, but the role of the metric in shell theory is something we wish to clarify. We will occasionally use the **Christoffel coefficients**, which are defined by,

$$\Gamma^A_{BC} = E^A \cdot \frac{\partial E_C}{\partial X^B} = -E_C \cdot \frac{\partial E^A}{\partial X^B}, \quad \gamma^a_{bc} = e^a \cdot \frac{\partial e_c}{\partial x^b} = -e_c \cdot \frac{\partial e^a}{\partial x^b}. \tag{4.14}$$

Again, these play a bigger role in shell theory, where their relationship to the curvature tensor is something we wish to clarify.

Given the frames $\{E_A\}$ and $\{e_a\}$, we can define the **pseudoscalar** on the reference and spatial configurations as,

$$I = \frac{E_1 \wedge E_2 \wedge E_3}{|E_1 \wedge E_2 \wedge E_3|}, \quad i = \frac{e_1 \wedge e_2 \wedge e_3}{|e_1 \wedge e_2 \wedge e_3|}. \tag{4.15}$$

Because we are considering three dimensional bodies embedded in $\mathbb{E}^3$, I and i are the same so long as the orientation of the two frames is the same, but this will no longer be the case when we consider thin shells.

4.2.1 The Deformation Gradient

$\phi_t(X)$ is a function of position in $\mathcal{B}$, but gives a position in $\mathcal{S}$. We can take the vector derivative of $\phi_t(X)$, $Y \cdot \partial\phi_t(X)$, for any $Y \in T_X\mathcal{B}$. This will produce a vector in the tangent space $T_{\phi_t(X)}\mathcal{S}$, which can be decomposed in terms of the basis $\{e_a\}$, i.e. if $w = Y \cdot \nabla\phi_t(X)$, then w may be written $w = w^a e_a$. We define $\phi^a_t(X) = x^a(\phi_t(X))$ to be the components of the point $\phi_t(X) \in \mathcal{S}$. The component w^a is then given by,

$$w^a = (Y \cdot \nabla\phi_t(X))^a = Y \cdot \nabla\phi^a_t(X). \tag{4.16}$$

We now consider how the vector between two nearby points, X and $X + \epsilon Y$ ($Y \in T_X\mathcal{B}$),

is mapped by the motion ϕ_t,

$$(X + \epsilon Y) - X \mapsto \phi_t(X + \epsilon Y) - \phi_t(X) = \epsilon \mathsf{F}(Y) + \mathcal{O}(\epsilon^2), \tag{4.17}$$

where F is the **deformation gradient**, and is given by,

$$\mathsf{F}(Y) = Y \cdot \nabla \phi_t(X). \tag{4.18}$$

Given the tangent vectors $Y \in T_X\mathcal{B}$ and $y \in T_{\phi_t(X)}\mathcal{S}$, the adjoint function $\bar{\mathsf{F}}$ is defined to satisfy,

$$\mathsf{F}(Y) \cdot y = Y \cdot \bar{\mathsf{F}}(y). \tag{4.19}$$

A coordinate free definition of $\bar{\mathsf{F}}$ that satisfies this is,

$$\bar{\mathsf{F}}(y) = \dot{\nabla}(y \cdot \dot{\phi}_t(X)) = E^A(y \cdot (E_A \cdot \nabla \phi_t(X))). \tag{4.20}$$

The coordinate systems $\{X^A\}$ and $\{x^a\}$ are independent. However, it is useful to define another coordinate system on the spatial configuration, which we call the **convected coordinate system** $\{x^A\}$, to satisfy,

$$x^A(x) = X^A\left(\phi_t^{-1}(x)\right). \tag{4.21}$$

The frame and reciprocal frame associated with this coordinate system satisfy,

$$e_A = \mathsf{F}(E_A), \quad \bar{\mathsf{F}}(e^A) = E^A. \tag{4.22}$$

In this chapter, the use of upper case indices on objects in the spatial configuration implies the use of the convected coordinate system.

4.2.2 Strain Tensors

The deformation gradient F describes how the material is locally stretched and rotated by the motion ϕ_t. The stresses within the material are expected to be a function of F, however, there are certain kinds of deformation that will not result in any internal stress. F will be the identity function if the body undergoes a pure translation, but will not if the body undergoes

a pure rigid body rotation, in which case we expect there to be no resultant internal stress. In order to develop a constitutive law we must extract a description of the stretching undergone by a material element. We can use the **polar decomposition** theorem to write F as,

$$\mathsf{F} = \mathsf{RU} = \mathsf{VR}, \tag{4.23}$$

where R is proper orthogonal ($\bar{\mathsf{R}} = \mathsf{R}^{-1}$, $\det \mathsf{R} = 1$), and U and V are symmetric and positive definite ($\mathsf{U} = \bar{\mathsf{U}}$, $\mathsf{V} = \bar{\mathsf{V}}$). R is a pure rotation, and the stretch is encoded in either U or V, and hence the internal stresses in the material will depend either on U or V. It is possible to write $\mathsf{U}^2 = \bar{\mathsf{F}}\mathsf{F}$, and this is referred to as the **Cauchy-Green tensor**, defined by,

$$\mathsf{C}(Y) = \bar{\mathsf{F}}\mathsf{F}(Y). \tag{4.24}$$

C is conventionally used instead of U or V. If an element of the material undergoes only rotation, then we expect no internal forces to result. In this case C (and U and V) will be the identity function. In order to obtain a function that is only *non-zero* when a material element is stretched, we must subtract the identity function from C. Conventionally the **Green-Lagrangian strain tensor** is defined as,

$$\mathsf{E}(Y) = \tfrac{1}{2}\left(\mathsf{C}(Y) - Y\right). \tag{4.25}$$

The factor of $1/2$ is convenient for linearisation. E is symmetric ($\bar{\mathsf{E}} = \mathsf{E}$), and will only be non-zero if a material element undergoes stretching. Hence we expect the internal stresses in the material to be a function only of E. Two alternative strain tensors are listed here for completeness,

$$\begin{array}{ll} \textbf{Biot strain tensor} & \mathsf{C}^{1/2}(Y) - Y, \\ \textbf{Logarithmic strain tensor} & \tfrac{1}{2}\ln(\mathsf{C}(Y)). \end{array} \tag{4.26}$$

The eigenvectors of U are the directions in which simple stretching of the material occurs, and the eigenvalues are the **principal strains**, which we denote $\lambda_a, a = 1, 2, 3$. The eigenvectors of C are the same as those of U, and the eigenvalues are λ_a^2. It follows that the eigenvectors of E are also the same as those of U, and the eigenvalues are $\frac{1}{2}(\lambda_a^2 - 1)$.

Both C and E are functions on the reference configuration $\mathcal{B}$. Alternatively we can

construct elasticity tensors on the spatial configuration. To do this we use V instead of U. We define c, referred to as the **Cauchy deformation tensor**, the **Piola tensor** or the **Finger tensor**, as,

$$\mathsf{c}(y) = \bar{\mathsf{F}}^{-1}\mathsf{F}^{-1}(y) = (\mathsf{V}^{-1})^2(y). \tag{4.27}$$

Using this we can define the **spatial (or Eulerian-Almansi) strain tensor** as,

$$\mathsf{e}(y) = \tfrac{1}{2}\left(y - \mathsf{c}(y)\right). \tag{4.28}$$

c is a symmetric function defined on the spatial configuration with eigenvalues $1/\lambda_a^2$. The symmetry of C implies that its eigenvectors will be orthogonal. It also implies that these eigenvectors will *remain* orthogonal under the transformation F. The orthogonal basis obtained by transforming the eigenvectors of C with F are in fact the eigenvectors of c. The eigenvectors of c are also the same as the eigenvectors of V, whose eigenvalues are λ_a. The eigenvectors of e will be the same as those of c, and its eigenvalues will be $\frac{1}{2}(1 - 1/\lambda_a^2)$.

E and e are related to each other by,

$$\mathsf{e}(y) = \bar{\mathsf{F}}^{-1}\mathsf{E}\mathsf{F}^{-1}(y), \quad \mathsf{E}(Y) = \bar{\mathsf{F}}\mathsf{e}\mathsf{F}(Y). \tag{4.29}$$

This implies that when using convected coordinates we can write,

$$\mathsf{E}_{AB} = \mathsf{e}_{AB}. \tag{4.30}$$

4.2.3 Displacements

Both $\mathcal{B}$ and $\mathcal{S}$ are embedded in Euclidean space, so it makes sense to define a **reference displacement vector** U as,

$$U(X) = \phi_t(X) - X. \tag{4.31}$$

This is a vector field on the reference configuration. We may express the deformation gradient in terms of this vector field as,

$$\mathsf{F}(Y) = Y + Y \cdot \nabla U. \tag{4.32}$$

$U(X)$ is a vector field on $\mathcal{B}$, but we can equally well regard it as a vector field on $\mathcal{S}$. To

distinguish this we use upper case to denote the **spatial displacement vector**,

$$u(x) = x - \phi_t^{-1}(x) = U(\phi_t^{-1}(x)). \tag{4.33}$$

Using this we may express F^{-1} as,

$$\mathsf{F}^{-1}(y) = y - y \cdot \nabla u. \tag{4.34}$$

We can also express the adjoint functions $\bar{\mathsf{F}}$ and $\bar{\mathsf{F}}^{-1}$ as,

$$\begin{aligned} \bar{\mathsf{F}}(y) &= y + \dot{\nabla}(y \cdot \dot{U}), \\ \bar{\mathsf{F}}^{-1}(Y) &= Y - \dot{\nabla}(Y \cdot \dot{u}). \end{aligned} \tag{4.35}$$

Using these definitions we can express the strain tensors E and e as,

$$2\mathsf{E}(Y) = Y \cdot \nabla U + \dot{\nabla}(Y \cdot \dot{U}) + \dot{\nabla}((Y \cdot \nabla U) \cdot \dot{U}), \tag{4.36}$$

$$2\mathsf{e}(y) = y \cdot \nabla u + \dot{\nabla}(y \cdot \dot{u}) - \dot{\nabla}((y \cdot \nabla u) \cdot \dot{u}). \tag{4.37}$$

Note that these two definitions involve quantities only on the reference and spatial configurations respectively, but in order to make any sense, both $\mathcal{B}$ and $\mathcal{S}$ must be embedded in the same, flat, background space.

We will make use of displacements when we consider perturbations to the elasticity equations.

4.2.4 Strain Rate and Spin

We now focus on how the *rate* of strain varies given a particular motion ϕ_t. We consider a vector that is convected with the material. The evolution over time of $Y \in T_X\mathcal{B}$ will be described by $\mathsf{F}(Y)$. The tangent vector Y can be expressed as $Y = \partial X/\partial\eta$ for some scalar parameter η defined on the reference configuration $\mathcal{B}$. $\mathsf{F}(Y)$ can then be expressed as $\mathsf{F}(Y) = \partial\phi_t(X)/\partial\eta$. We wish to know what the rate of change of $\mathsf{F}(Y)$ is with time, i.e.

$$\frac{\partial \mathsf{F}(Y)}{\partial t} = \frac{\partial^2 \phi_t(X)}{\partial t \partial \eta} = \frac{\partial}{\partial \eta}\frac{\partial \phi_t(X)}{\partial t} = \mathsf{F}(Y) \cdot \nabla v = Y \cdot \nabla V, \tag{4.38}$$

where v and V are the velocity fields defined on the spatial and reference configurations respectively, called the **spatial velocity** and **reference velocity**, which satisfy $V(X) = v(\phi_t(X))$. Hence we see that the rate of change of a tangent vector with time is equal to the gradient of the velocity field in the direction specified by that tangent vector. We can use this to define the **rate of deformation tensor** I as,

$$\mathsf{I}(y) = y \cdot \nabla v. \tag{4.39}$$

This takes a vector y, and returns the rate of change with time of that vector, assuming that the vector is convected with the material. The components of I are given by,

$$\mathsf{I}_{ab} = v_{a|b} = \frac{\partial v_a}{\partial x^b} - v_c \gamma^c_{ba}. \tag{4.40}$$

The adjoint function $\bar{\mathsf{I}}$ and its components are given by,

$$\bar{\mathsf{I}}(y) = \dot{\nabla}(y \cdot \dot{v}), \quad \bar{\mathsf{I}}_{ab} = v_{b|a}. \tag{4.41}$$

It is convenient to additively decompose I into its symmetric and skew-symmetric parts,

$$\mathsf{I}(y) = \tfrac{1}{2}\left(\mathsf{I}(y) + \bar{\mathsf{I}}(y)\right) + \tfrac{1}{2}\left(\mathsf{I}(y) - \bar{\mathsf{I}}(y)\right) = \mathsf{I}^+(y) + \mathsf{I}^-(y), \tag{4.42}$$

where the final equality defines the **symmetric rate of deformation tensor** I^+ and the **rotation rate tensor** I^-. The components of I^+ and I^- are given by,

$$\mathsf{I}^+_{ab} = \tfrac{1}{2}\left(v_{a|b} + v_{b|a}\right), \quad \mathsf{I}^-_{ab} = \tfrac{1}{2}\left(v_{a|b} - v_{b|a}\right). \tag{4.43}$$

The symmetry of I^+ means that its eigenvalues are real, and its eigenvectors are orthogonal. The eigenvalues are the local rates of strain in the directions defined by the eigenvectors.

I^- is skew-symmetric, and defined in 3-dimensional Euclidean space. This means that it has one zero eigenvalue with an associated eigenvector, and one eigenbivector (with an associated eigenvalue). It is useful to define the bivector ω, which characterises the skew-

symmetric function I^-, by,

$$\begin{aligned}\omega &= \tfrac{1}{2}e^a \wedge \mathsf{I}^-(e_a) = \tfrac{1}{2}\mathsf{I}^-_{ab}e^b \wedge e^a \\ &= \mathsf{I}^-_{12}e^2 \wedge e^1 + \mathsf{I}^-_{13}e^3 \wedge e^1 + \mathsf{I}^-_{23}e^3 \wedge e^2.\end{aligned} \tag{4.44}$$

This definition of ω is frame independent (see [Doran and Lasenby, 2003, §4.4.7] and [Hestenes and Sobczyk, 1984, §3.4] for more details). Given this definition we can write,

$$\mathsf{I}^-(y) = y \cdot \omega. \tag{4.45}$$

Therefore, the eigenvector corresponding to the zero eigenvalue must satisfy $y \cdot \omega = 0$. Hence this eigenvector is given by (any scalar multiple of),

$$\mathsf{I}^-_{23}e_1 - \mathsf{I}^-_{13}e_2 + \mathsf{I}^-_{12}e_3. \tag{4.46}$$

The action of I^- on a bivector B may be written as $l^-(B) = -(B \cdot \omega)\omega$ [Hestenes and Sobczyk, 1984, §3.4]. Hence we see that ω is the eigenbivector of I^- with the eigenvalue $-\omega \cdot \omega$. ω is the plane of rotation, while the eigenvector is perpendicular to this plane. The eigenvalue corresponding to ω is the square of the angular velocity in the plane of rotation. Moreover, ω itself represents the average angular velocity of a material element. The outer derivative of the velocity v is given by,

$$\begin{aligned}\nabla \wedge v &= e^a \wedge \partial_a(v_b e^b) = v_{b|a}e^a \wedge e^b \\ &= \left(v_{1|2} - v_{2|1}\right)e^2 \wedge e^1 + \left(v_{1|3} - v_{3|1}\right)e^3 \wedge e^1 + \left(v_{2|3} - v_{3|2}\right)e^3 \wedge e^2 \\ &= 2\omega.\end{aligned} \tag{4.47}$$

Hence we see that the outer derivative of velocity gives twice the average angular velocity of a material element.

I is a function on the spatial configuration. We can construct a rate of deformation tensor on the reference configuration by writing,

$$\mathsf{L}(Y) = \bar{\mathsf{F}}\mathsf{I}\mathsf{F}(Y). \tag{4.48}$$

If we use convected coordinates then we can write,

$$\mathsf{L}_{AB} = \mathsf{l}_{AB}. \tag{4.49}$$

$\mathsf{L}(Y)$ returns the rate of change with time of the vector Y as it is convected with the material, and then brings this back to the tangent space $T_X\mathcal{B}$ using $\bar{\mathsf{F}}$, i.e.

$$\mathsf{L}(Y) = \bar{\mathsf{F}}\left(\frac{\partial \mathsf{F}(Y)}{\partial t}\right) = \bar{\mathsf{F}}\left(\mathsf{F}(Y)\cdot\nabla v\right) = \bar{\mathsf{F}}\left(Y\cdot\nabla V\right). \tag{4.50}$$

We can split L into symmetric and antisymmetric parts to obtain,

$$\mathsf{L}(Y) = \tfrac{1}{2}\left(\mathsf{L}(Y) + \bar{\mathsf{L}}(Y)\right) + \tfrac{1}{2}\left(\mathsf{L}(Y) - \bar{\mathsf{L}}(Y)\right) = \mathsf{L}^{+}(Y) + \mathsf{L}^{-}(Y). \tag{4.51}$$

The antisymmetric function L^{-} can be written in terms of its characteristic bivector,

$$\mathsf{L}^{-}(Y) = Y\cdot W \text{ where } W = \tfrac{1}{2}E^A \wedge \mathsf{L}^{-}(E_A). \tag{4.52}$$

W is related to ω by $W = \bar{\mathsf{F}}(\omega)$.

The strain tensor $\mathsf{E}(Y)$ is implicitly a function of time. Hence it is meaningful to define $\dot{\mathsf{E}}(Y) = \partial\mathsf{E}(Y)/\partial t$, where Y is held constant. We can write the components $\dot{\mathsf{E}}_{AB}$ as,

$$\begin{aligned}
\dot{\mathsf{E}}_{AB} = \frac{\partial \mathsf{E}_{AB}}{\partial t} &= \frac{\partial}{\partial t}\left(\tfrac{1}{2}\left(E_A\cdot\bar{\mathsf{F}}\mathsf{F}(E_B) - E_A\cdot E_B\right)\right) \\
&= \frac{1}{2}\frac{\partial}{\partial t}\left(\mathsf{F}(E_A)\cdot\mathsf{F}(E_B)\right) \\
&= \frac{1}{2}\left(\mathsf{F}(E_A)\cdot\frac{\partial\mathsf{F}(E_B)}{\partial t} + \mathsf{F}(E_B)\cdot\frac{\partial\mathsf{F}(E_A)}{\partial t}\right) \\
&= \frac{1}{2}\left(E_A\cdot\mathsf{L}(E_B) + E_B\cdot\mathsf{L}(E_A)\right) = \mathsf{L}^{+}_{AB}.
\end{aligned} \tag{4.53}$$

Hence we have,

$$\dot{\mathsf{E}}(Y) = \mathsf{L}^{+}(Y). \tag{4.54}$$

The spatial strain tensor $\mathsf{e}(y)$ is also an implicit function of time, but it is more useful to take the **material derivative** on the spatial configuration. Hence we define, $\dot{\mathsf{e}}(y) = D\mathsf{e}(y)/Dt$

where y is convected with the motion. This allows us to write,

$$\begin{aligned}\dot{\mathsf{e}}_{ab} = \frac{D\mathsf{e}_{ab}}{Dt} &= \frac{D}{Dt}\left(\tfrac{1}{2}\left(e_a \cdot e_b - e_a \cdot \bar{\mathsf{F}}^{-1}\mathsf{F}^{-1}(e_b)\right)\right) \\ &= \frac{1}{2}\frac{D}{Dt}\left(e_a \cdot e_b\right) \\ &= \mathsf{I}^{+}_{ab},\end{aligned} \tag{4.55}$$

and so we can write,

$$\dot{\mathsf{e}}(y) = \mathsf{I}^{+}(y). \tag{4.56}$$

Note that using convected coordinates we have,

$$\dot{\mathsf{e}}_{AB} = \dot{\mathsf{E}}_{AB}. \tag{4.57}$$

4.3 Stress

In classical mechanics, there are two ways in which particles can exert forces on each other, by colliding, and by action at a distance. If we were to consider all the particles making up a body we would need to consider the way in which one particle is influenced by every other particle. In a continuum we must consider the effect of one part of the body on every other part, but in describing this it is impractical to consider all the particles that make up the body. Hence, in a continuum we use the concept of **stress**.

We consider a sub-region of the body, which occupies $\mathcal{U} \subseteq \mathcal{B}$ in the reference configuration and $\phi_t(\mathcal{U}) \subseteq \mathcal{S}$ in the spatial configuration. The boundary to this region is a closed surface $\partial\phi_t(\mathcal{U})$. We wish to express the interaction between the material outside $\partial\phi_t(\mathcal{U})$ with the material inside it. We consider two kinds of interaction. Action at a distance interactions are described by **body forces**, and local interactions are described by **surface forces**.

Body forces are expressed as a force per unit mass $b(x,t)$, and to obtain the total force on the region $\phi_t(\mathcal{U})$ due to body forces, we must perform the integration,

$$\int_{\phi_t(\mathcal{U})} \rho b \left|dx\right|, \tag{4.58}$$

where $\rho(x,t)$ is the **density**, and dx is a **directed volume element** of the spatial configuration. The scalar volume element $|dx|$ can be expressed using the pseudoscalar on the

spatial configuration, denoted i, as $|dx| = dxi^{-1}$ (see [Doran and Lasenby, 2003, §6.4] for an introduction to integration using geometric algebra). The total force on the region $\phi_t(\mathcal{U})$ due to body forces can also be expressed as an integral over $\mathcal{U}$,

$$\int_{\mathcal{U}} \rho b \det \mathsf{F} \, |dX| \tag{4.59}$$

Here ρ and b are taken to be functions of position on the reference configuration such that $\rho(X,t) = \rho(\phi_t(X),t)$ and $b(X,t) = b(\phi_t(X),t)$. $\det \mathsf{F}$ is the determinant of the deformation gradient, and dX is a directed volume element of the reference configuration. The scalar volume element $|dX|$ can be expressed using the pseudoscalar on the spatial configuration, denoted I, as $|dX| = dXI^{-1}$.

To express the surface force we consider a small portion of the boundary $\partial\phi_t(\mathcal{U})$, which we denote Δs. We define the unit normal n to this so that it points *out* of the volume contained by $\partial\phi_t(\mathcal{U})$. The material on the outside of Δs exerts a force Δf on the material on the inside. Δf depends on the size of the area Δs, the location of the area (x), the orientation of the normal n, and time. Note that Δf depends on the position x, and not on the state of the rest of the body in its entirety. This is because surface forces are defined to be local effects. The **stress principle of Euler and Cauchy** states that at a particular time,

> as the area Δs tends to zero, the ratio $\Delta f/\Delta s$ tends to a definite limit, and the moment of the force acting on the surface Δs about any point with the area vanishes in the limit. Moreover, if two surfaces passing through a point x have the same normal n, then $\Delta f/\Delta s$ tends to the same value for both of these surfaces [Fung, 1969].

This is a basic assumption that seems to meet the needs of most conventional continuum mechanics problems, and it allows us to define the **surface traction** t_n as,

$$t_n(x,t) = \lim_{\Delta s \to 0} \frac{\Delta f}{\Delta s}. \tag{4.60}$$

The assumption that the moment of the force acting on Δs is zero in the limit has been generalised by some to say that,

> across any infinitesimal surface element in a material the action of the exterior

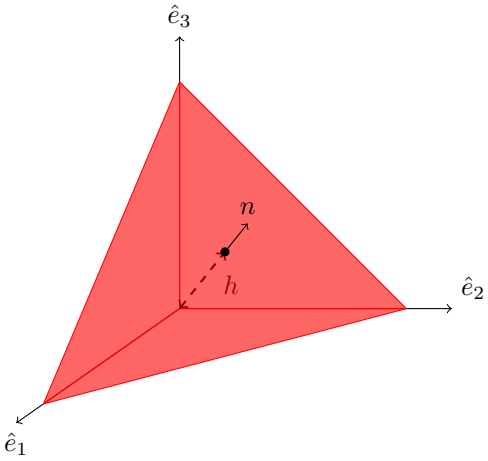


Figure 4.1: Tetrahedral control volume used to show the linearity of t_n in n.

material on the interior is equipollent* to a force and a couple (per unit area).

This requires the concept of a **couple-stress**, and increases the complexity of the theory considerably. In 3-dimensional solid mechanics this is often not necessary, and we will not include it here, however, when we consider thin shells we will need to return to this concept.

Thus far the surface traction t_n has had to be considered an arbitrary function of its arguments x, t, n, however, t_n is in fact a linear function of its argument n. This can be shown by first realising that Newton's 3rd law implies that the stress vectors acting on opposite sides of the same surface are equal in magnitude and opposite in direction, i.e. $t_{-n} = -t_n$. Next, a small tetrahedral control volume, illustrated in fig. 4.1, is considered. Conservation of linear momentum gives us,

$$t_n dA + t_{-\hat{e}_1} dA_1 + t_{-\hat{e}_2} dA_2 + t_{-\hat{e}_3} dA_3 = \rho \left(\frac{h}{3} dA \right) a - \rho \left(\frac{h}{3} dA \right) b, \tag{4.61}$$

where dA_a are the areas of the faces normal to $\hat{e}_a$ (which are orthonormal), dA is the area of the face normal to n, h is the height of the tetrahedron, and a is the acceleration. Using the results $t_{-n} = -t_n$ and $dA_a = (n \cdot \hat{e}_a) dA$, we obtain,

$$t_n - t_{\hat{e}_a} n_a = \rho \frac{h}{3} (a - b). \tag{4.62}$$

* "Equal in power, effectiveness, or validity", Oxford English dictionary.

If we allow $h \to 0$, then we obtain the expression,

$$t_n - t_{\hat{e}_a} n_a = 0 \quad \Rightarrow \quad t_{n_a \hat{e}_a} = n_a t_{\hat{e}_a}, \tag{4.63}$$

which implies that t_n is linear in n (see also [Fung, 1969, §3.4]). Hence we can express this function as a tensor, which we denote σ, that satisfies,

$$\sigma(n) = \sigma(n; x, t) = t_n(x, t). \tag{4.64}$$

σ is the **Cauchy stress tensor**, and it encodes all of the internal stresses at a particular point in the body at a particular time. Using σ we can express the total force on $\phi_t(\mathcal{U})$ due to surface forces as,

$$\int_{\partial\phi_t(\mathcal{U})} \sigma(n) \, |ds| = \int_{\phi_t(\mathcal{U})} \dot{\sigma}(\dot{\nabla}) \, |dx| \,. \tag{4.65}$$

where ds is a **directed boundary element** of the spatial configuration. The scalar surface element $|ds|$ can be expressed in terms of the pseudoscalar on the spatial configuration and the unit normal vector n, that is normal to the surface and points *out* of the body, as $n|ds| = ds i^{-1}$.

We have expressed the body force in terms of integrals over both the spatial and reference configurations. We would like to do the same for the surface force. To achieve this we will define a tensor that takes the normal to a surface element in the reference configuration and returns the force acting on the corresponding surface element in the spatial configuration, per unit area of the surface in the reference configuration. This can then be integrated over a surface in the reference configuration to obtain the surface force acting on the spatial configuration.

First we let A and B be two vectors in the tangent space $T_X\mathcal{B}$. These define a surface element $A \wedge B$, and the normal to this surface element is given by $N = (A \wedge B)I^{-1}$. Under the motion ϕ_t these vectors will transform to $\mathsf{F}(A)$ and $\mathsf{F}(B)$, hence N will transform to $n = (\mathsf{f}(a) \wedge \mathsf{f}(b))i^{-1}$. We can express this in a more useful form by making use of the two identities,

$$\begin{aligned} A_r \cdot \bar{\mathsf{F}}(B_s) &= \bar{\mathsf{F}}(\mathsf{F}(A_r) \cdot B_s), \quad r \leqslant s, \\ A_r \cdot (B_s \cdot C_t) &= (A_r \wedge B_s) \cdot C_t, \quad r + s \leqslant t \text{ and } r, s \geqslant 0, \end{aligned} \tag{4.66}$$

which are derived in [Doran and Lasenby, 2003, §4.4.3] and [Hestenes and Sobczyk, 1984, p.7]

respectively, and apply when A_r, B_s, and C_t are multivectors of grade r, s, and t respectively, and F is an arbitrary linear function. Using these we can express the normal vector n as,

$$\begin{aligned} n &= I^2\ \mathsf{F}(A)\cdot(\mathsf{F}(B)\cdot i) \\ &= I^2\ \mathsf{F}(A)\cdot\bar{\mathsf{F}}^{-1}\bar{\mathsf{F}}(\mathsf{F}(B)\cdot i) \\ &= I^2\ \mathsf{F}(A)\cdot\bar{\mathsf{F}}^{-1}(B\cdot\bar{\mathsf{F}}(i)) \\ &= I^2\ \det\mathsf{F}\ \mathsf{F}(A)\cdot\bar{\mathsf{F}}^{-1}(B\cdot I) \\ &= I^2\ \det\mathsf{F}\ \bar{\mathsf{F}}^{-1}\bar{\mathsf{F}}\left(\mathsf{F}(A)\cdot\bar{\mathsf{F}}^{-1}(B\cdot I)\right) \\ &= I^2\ \det\mathsf{F}\ \bar{\mathsf{F}}^{-1}\left(A\cdot\bar{\mathsf{F}}\bar{\mathsf{F}}^{-1}(B\cdot I)\right) \\ &= I^2\ \det\mathsf{F}\ \bar{\mathsf{F}}^{-1}\left(A\cdot(B\cdot I)\right) \\ &= \det\mathsf{F}\ \bar{\mathsf{F}}^{-1}\left((A\wedge B)\cdot I^{-1}\right). \end{aligned} \tag{4.67}$$

$(A\wedge B)\cdot I^{-1}$ is the normal vector in the reference configuration. Therefore, given σ, we can construct T, which takes the normal vector to a surface element in the *reference* configuration and returns the force acting on the surface after it has been transformed by ϕ_t,

$$\mathsf{T}(N) = \det\mathsf{F}\ \sigma\bar{\mathsf{F}}^{-1}(N) \tag{4.68}$$

This is often referred to as the **first Piola-Kirchhoff stress tensor**. Hence the total force acting on the surface of the region $\mathcal{U}$ after it has been transformed by ϕ_t is,

$$\int_{\partial\mathcal{U}}\mathsf{T}(N)\,|dS| = \int_{\mathcal{U}}\dot{\mathsf{T}}(\dot{\nabla})\,|dX|\,. \tag{4.69}$$

The first Piola-Kirchhoff stress tensor is useful in writing conservation laws, however, we will also find it useful to define a second stress tensor, the **second Piola-Kirchhoff stress tensor**, denoted S, by,

$$\mathsf{S}(N) = \mathsf{F}^{-1}\mathsf{T}(N) = \det\mathsf{F}\ \mathsf{F}^{-1}\sigma\bar{\mathsf{F}}^{-1}(N). \tag{4.70}$$

Note that both the range and domain of this tensor are T_XB, which will be useful when considering conservation of energy.

4.4 Conservation Laws

We express each of the conservation laws in integral form on the spatial and reference configurations, and then in local form on the spatial and reference configurations. Where necessary we also introduce new definitions.

Each of the integral forms is defined over an arbitrary subregion $\mathcal{U}$ (or $\phi_t(\mathcal{U})$. To get from the integral to local configurations this arbitrariness is used along with an assumption of the appropriate smoothness of the functions involved. For each of the subsequent conservation laws it is necessary to use the previous conservation laws to simplify the local expressions. The fundamental theorem of geometric calculus, which relates boundary integrals to volume integrals using the vector derivative [Doran and Lasenby, 2003, §6.4.4], is also frequently used.

4.4.1 Mass

$$\frac{d}{dt}\int_{\phi_t(\mathcal{U})} \rho \, |dx| = 0, \tag{4.71}$$

$$\frac{d}{dt}\int_{\mathcal{U}} \rho \det \mathsf{F} \, |dX| = 0, \tag{4.72}$$

$$\frac{\partial \rho}{\partial t} + \nabla \cdot (\rho v) = 0, \tag{4.73}$$

$$\frac{\partial}{\partial t}(\rho \det \mathsf{F}) = 0. \tag{4.74}$$

We define the time invariant density ρ_0 as,

$$\rho_0 = \rho \det \mathsf{F}. \tag{4.75}$$

4.4.2 Momentum

$$\frac{d}{dt}\int_{\phi_t(\mathcal{U})} \rho v \, |dx| = \int_{\partial\phi_t(\mathcal{U})} \sigma(n) \, |ds| + \int_{\phi_t(\mathcal{U})} \rho b \, |dx| \,, \tag{4.76}$$

$$\frac{d}{dt}\int_{\mathcal{U}} \rho_0 V \, |dX| = \int_{\partial\mathcal{U}} \mathsf{T}(N) \, |dS| + \int_{\mathcal{U}} \rho_0 b \, |dX| \,, \tag{4.77}$$

$$\rho \frac{Dv}{Dt} = \dot{\sigma}(\dot{\nabla}) + \rho b, \tag{4.78}$$

$$\rho_0 \frac{\partial V}{\partial t} = \dot{\mathsf{T}}(\dot{\nabla}) + \rho_0 b. \tag{4.79}$$

4.4.3 Angular Momentum

$$\frac{d}{dt}\int_{\phi_t(\mathcal{U})} \rho\, x \wedge v\, |dx| = \int_{\partial\phi_t(\mathcal{U})} x \wedge \sigma(n)\, |ds| + \int_{\phi_t(\mathcal{U})} \rho\, x \wedge b\, |dx|\,, \tag{4.80}$$

$$\frac{d}{dt}\int_{\mathcal{U}} \rho_0\, \phi_t(X) \wedge V\, |dX| = \int_{\partial\mathcal{U}} \phi_t(X) \wedge \mathsf{T}(N)\, |dS| + \int_{\mathcal{U}} \rho_0\, \phi_t(X) \wedge b\, |dX|\,, \tag{4.81}$$

$$\bar{\sigma} = \sigma, \tag{4.82}$$

$$\bar{\mathsf{S}} = \mathsf{S}. \tag{4.83}$$

4.4.4 Energy

- u: internal energy per unit mass defined over the spatial configuration
- U: internal energy per unit mass defined over the reference configuration
- $\dot{q}$: heat addition per unit mass per unit time from external sources, defined on the spatial configuration
- $\mathfrak{q}$: heat flux per unit area defined on the spatial configuration
- $\dot{Q}$: heat addition per unit mass per unit time from external sources, defined on the reference configuration
- $\mathfrak{Q}$: heat flux per unit area defined on the spatial configuration

These defined quantities are related by,

$$U(X,t) = u(\phi_t(X),t), \quad \dot{Q}(X,t) = \dot{q}(\phi_t(X),t), \quad \mathfrak{Q} = \det \mathsf{F}\mathsf{F}^{-1}(\mathfrak{q}). \tag{4.84}$$

Using these definitions we can write conservation of energy as,

$$\frac{d}{dt}\int_{\phi_t(\mathcal{U})} \rho\left(u + \frac{v^2}{2}\right)|dx| = \int_{\partial\phi_t(\mathcal{U})} v\cdot\sigma(n) - \mathfrak{q}\cdot n\, |ds| + \int_{\phi_t(\mathcal{U})} \rho v\cdot b + \rho\dot{q}\, |dx|\,, \tag{4.85}$$

$$\frac{d}{dt}\int_{\mathcal{U}} \rho_0\left(U + \frac{V^2}{2}\right)|dX| = \int_{\partial\mathcal{U}} V\cdot\mathsf{T}(N) - \mathfrak{Q}\cdot N\, |ds| + \int_{\mathcal{U}} \rho_0 V\cdot b + \rho_0\dot{Q}\, |dX|\,, \tag{4.86}$$

$$\rho\frac{Du}{Dt} = \rho\dot{q} - \nabla\cdot\mathfrak{q} + \mathrm{tr}(\sigma\mathsf{l}^+), \tag{4.87}$$

$$\rho_0\frac{\partial U}{\partial t} = \rho_0\dot{Q} - \nabla\cdot\mathfrak{Q} + \mathrm{tr}(\mathsf{S}\mathsf{L}^+). \tag{4.88}$$

The terms $\int_{\partial\phi_t(\mathcal{U})} v\cdot\sigma(n)|ds|$ and $\int_{\partial\mathcal{U}} V\cdot\mathsf{T}(N)|dS|$ require a some manipulation to arrive at the local forms of the equations. First the fundamental theorem of geometric calculus is

used to obtain,

$$\int_{\phi_t(\mathcal{U})} \dot{v} \cdot \sigma(\dot{\nabla}) + v \cdot \dot{\sigma}(\dot{\nabla}) |dx| \text{ and } \int_{\mathcal{U}} \dot{V} \cdot \mathsf{T}(\dot{\nabla}) + V \cdot \dot{\mathsf{T}}(\dot{\nabla}) |dX| \,. \tag{4.89}$$

The second term in each of these integrands is removed using conservation of momentum, so we will concentrate on the first terms. Conservation of angular momentum implies the symmetry of σ and S. Using this, on the spatial configuration we obtain,

$$\begin{aligned} \dot{v} \cdot \sigma(\dot{\nabla}) &= (e_a \cdot \nabla v) \cdot \sigma(e^a) \\ &= \mathsf{l}(e_a) \cdot \sigma(e^a) \\ &= \mathsf{l}_{ab} \sigma^{ab} \\ &= \sigma^{ab} \mathsf{l}^+_{ab} = \operatorname{tr}(\sigma \mathsf{l}^+), \end{aligned} \tag{4.90}$$

and on the reference configuration we obtain,

$$\begin{aligned} \dot{V} \cdot \mathsf{T}(\dot{\nabla}) = \dot{V} \cdot \mathsf{FS}(\dot{\nabla}) &= (E_A \cdot \nabla V) \cdot \mathsf{FS}(E^A) \\ &= \bar{\mathsf{F}}(E_A \cdot \nabla V) \cdot \mathsf{S}(E^A) \\ &= \mathsf{L}(E_A) \cdot \mathsf{S}(E^A) \\ &= \mathsf{L}_{AB} \mathsf{S}^{AB} \\ &= \mathsf{S}^{AB} \mathsf{L}^+_{AB} = \operatorname{tr}(\mathsf{S}\mathsf{L}^+). \end{aligned} \tag{4.91}$$

This is why these terms appear in the local conservation of energy equations.

4.5 Constitutive Laws

We consider the **isothermal** case, which means that we take $\dot{q} = \dot{Q} = 0$ and $\nabla \cdot \mathfrak{q} = \nabla \cdot \mathfrak{Q} = 0$. We also assume that the constitutive relationships are **local** (see [Marsden et al., 1994, §3.2] for more discussion of this). In these circumstances conservation of energy simplifies to,

$$\rho \frac{Du}{Dt} = \operatorname{tr}(\sigma \mathsf{l}^+), \tag{4.92}$$

$$\rho_0 \frac{\partial U}{\partial t} = \operatorname{tr}(\mathsf{S}\mathsf{l}^+). \tag{4.93}$$

We make the **constitutive assumption** that u is a function of e_{ab}, or equivalently, U is a function of E_{AB}. Using the chain rule of differentiation we obtain,

$$\frac{Du}{Dt} = \frac{\partial u}{\partial \mathsf{e}_{ab}} \frac{D\mathsf{e}_{ab}}{Dt} = \frac{\partial u}{\partial \mathsf{e}_{ab}} \mathsf{l}^{+}_{ab}, \tag{4.94}$$

$$\frac{\partial U}{\partial t} = \frac{\partial U}{\partial \mathsf{E}_{AB}} \frac{\partial \mathsf{E}_{AB}}{\partial t} = \frac{\partial U}{\partial \mathsf{E}_{AB}} \mathsf{L}^{+}_{AB}. \tag{4.95}$$

Substituting these results into conservation of energy we obtain,

$$\sigma(y) = \rho \frac{\partial u}{\partial \mathsf{e}(y)}, \quad \mathsf{S}(Y) = \rho_0 \frac{\partial U}{\partial \mathsf{E}(Y)}. \tag{4.96}$$

For more details on how to differentiate with respect to tensors see [Doran and Lasenby, 2003, §11.1.2].

4.5.1 The Energy of Deformation

For a **Saint Venant-Kirchhoff elastic material**, the internal strain energy of deformation per unit volume of the reference configuration is given by,

$$\rho_0 U = \frac{E\nu}{2(1+\nu)(1-2\nu)} \operatorname{tr}(\mathsf{E})^2 + \frac{E}{2(1+\nu)} \operatorname{tr}(\mathsf{E}^2), \tag{4.97}$$

where E is Young's modulus and ν is Poisson's ratio. Given the constitutive relation already derived, this allows us to write,

$$\mathsf{S}(Y) = \frac{E\nu}{(1+\nu)(1-2\nu)} \operatorname{tr}(\mathsf{E}) Y + \frac{E}{1+\nu} \mathsf{E}(Y). \tag{4.98}$$

4.6 Perturbations

In order to generate general linearised equations for three-dimensional elasticity, we assume that initially the body $\mathcal{B}$ is deformed according to the displacement U_0, and that this satisfies the steady governing equations. We then imagine that we perturb this state so that the displacement is given by $U_0 + \epsilon U'$, where ϵ is a small enough parameter that we can neglect all terms in the governing equations preceded by ϵ^2 or a greater power. This gives rise to the following approximations,

Deformation gradient

$$\mathsf{F}(Y) = Y + Y \cdot \nabla U_0 + \epsilon Y \cdot \nabla U' = \mathsf{F}_0(Y) + \epsilon \mathsf{F}'(Y). \tag{4.99}$$

Strain tensor

$$\begin{aligned} 2\mathsf{E}(Y) &= \bar{\mathsf{F}}\mathsf{F}(Y) - Y \\ &\approx \bar{\mathsf{F}}_0\mathsf{F}_0(Y) - Y + \epsilon\left(\bar{\mathsf{F}}_0\mathsf{F}'(Y) + \bar{\mathsf{F}}'\mathsf{F}_0(Y)\right) \\ &= 2\mathsf{E}_0(Y) + 2\epsilon\mathsf{E}'(Y). \end{aligned} \tag{4.100}$$

Determinant of F

$$\begin{aligned} \det\mathsf{F} = \det(\mathsf{F}_0 + \epsilon\mathsf{F}') = \det\left(\mathsf{F}_0(\mathsf{G} + \epsilon\mathsf{F}_0^{-1}\mathsf{F}')\right) &= \det\mathsf{F}_0 \det(\mathsf{G} + \epsilon\mathsf{F}_0^{-1}\mathsf{F}') \\ &\approx \det\mathsf{F}_0\left(1 + \epsilon\,\mathrm{tr}(\mathsf{F}_0^{-1}\mathsf{F}')\right) \\ &= \det\mathsf{F}_0 + \epsilon\det\mathsf{F}_0\,\mathrm{tr}(\mathsf{F}_0^{-1}\mathsf{F}'). \end{aligned} \tag{4.101}$$

Second Piola-Kirchhoff stress tensor Assuming a Saint Venant-Kirchhoff material,

$$\begin{aligned} \mathsf{S}(Y) &= \frac{E\nu}{(1+\nu)(1-2\nu)}\left(\mathrm{tr}(\mathsf{E}_0) + \epsilon\,\mathrm{tr}(\mathsf{E}')\right)Y + \frac{E}{1+\nu}\left(\mathsf{E}_0(Y) + \epsilon\mathsf{E}'(Y)\right) \\ &= \frac{E\nu}{(1+\nu)(1-2\nu)}\,\mathrm{tr}(\mathsf{E}_0)Y + \frac{E}{1+\nu}\mathsf{E}_0(Y) \\ &\quad + \epsilon\left(\frac{E\nu}{(1+\nu)(1-2\nu)}\,\mathrm{tr}(\mathsf{E}')Y + \frac{E}{1+\nu}\mathsf{E}'(Y)\right) \\ &= \mathsf{S}_0(Y) + \epsilon\mathsf{S}'(Y). \end{aligned} \tag{4.102}$$

First Piola-Kirchhoff stress tensor

$$\mathsf{T}(Y) = \mathsf{F}\mathsf{S}(Y) \approx \mathsf{F}_0\mathsf{S}_0(Y) + \epsilon\left(\mathsf{F}_0\mathsf{S}'(Y) + \mathsf{F}'\mathsf{S}_0(Y)\right) = \mathsf{T}_0(Y) + \epsilon\mathsf{T}'(Y). \tag{4.103}$$

Conservation of mass

$$\frac{\partial}{\partial t}\left(\rho\left(\det\mathsf{F}_0 + \epsilon\det\mathsf{F}_0\,\mathrm{tr}(\mathsf{F}_0^{-1}\mathsf{F}')\right)\right) = 0. \tag{4.104}$$

We define $\rho_0 = \rho\det\mathsf{F}_0$ and $\rho' = \det\mathsf{F}_0\,\mathrm{tr}(\mathsf{F}_0^{-1}\mathsf{F}')$, and conservation of mass implies that both of these do not vary with time.

Conservation of momentum

$$\rho_0 \frac{\partial^2 U'}{\partial t^2} = \dot{\mathsf{T}}'(\dot{\nabla}) + \rho' b_0 + \rho_0 b'. \tag{4.105}$$

Note that we have decomposed b into $b = b_0 + \epsilon b'$.

4.6.1 Small Deformations

A further simplification is to assume that $U_0 = 0$. In this case we obtain the following,

Deformation gradient

$$\mathsf{F}_0(Y) = Y, \quad \mathsf{F}'(Y) = Y \cdot \nabla U'. \tag{4.106}$$

Strain tensor

$$\mathsf{E}_0(Y) = 0, \quad 2\mathsf{E}'(Y) = \mathsf{F}'(Y) + \bar{\mathsf{F}}'(Y), \quad \operatorname{tr}(\mathsf{E}') = \nabla \cdot U'. \tag{4.107}$$

Determinant of F

$$\det \mathsf{F} \approx 1 + \epsilon \operatorname{tr}(\mathsf{F}') = 1 + \epsilon \nabla \cdot U'. \tag{4.108}$$

Second Piola-Kirchhoff stress tensor

$$\mathsf{S}_0(Y) = 0, \quad \mathsf{S}'(Y) = \frac{E\nu}{(1+\nu)(1-2\nu)} \operatorname{tr}(\mathsf{E}')Y + \frac{E}{1+\nu}\mathsf{E}'(Y). \tag{4.109}$$

First Piola-Kirchhoff stress tensor

$$\mathsf{T}_0(Y) = 0, \quad \mathsf{T}'(Y) = \mathsf{S}'(Y). \tag{4.110}$$

Conservation of mass

$$\frac{\partial}{\partial t}(\nabla \cdot U') = 0. \tag{4.111}$$

Conservation of momentum Assuming a homogeneous material, i.e. E and ν are independent of position, then we can write,

$$\begin{aligned} \rho_0 \frac{\partial^2 U'}{\partial t^2} &= \frac{E}{2(1+\nu)} \left(\nabla^2 U' + \nabla(\nabla \cdot U') \right) + \frac{E\nu}{(1+\nu)(1-2\nu)} \nabla(\nabla \cdot U') \\ &= \frac{E}{2(1+\nu)} \nabla^2 U' + \frac{E}{2(1+\nu)(1-2\nu)} \nabla(\nabla \cdot U'). \end{aligned} \tag{4.112}$$

4.7 Summary

The results of this chapter are not new, but three dimensional elasticity has provided a familiar setting in which to introduce the fundamentals of geometric algebra. The logical sequence of this chapter also provides the blueprint for work on shell theory. The final section on linearisation will also be used in later sections to validate our theory of shells.

Chapter 5

The Elastic Theory of Shells

We now consider the case where the **reference configuration** $\mathcal{B} \subset \mathbb{E}^3$ and **spatial configuration** $\mathcal{S} \subset \mathbb{E}^3$ are 2-dimensional surfaces embedded in $\mathbb{E}^3$. The work here forms the basis for our article [Gregory et al., 2017d]. The coordinate systems we introduce are altered. Over $\mathcal{B}$ we let there be the coordinates $\{X^i\}, i = 1, 2$, and over $\mathcal{S}$ we have $\{x^i\}, i = 1, 2$. We will follow the convention that indices $i, j, k, \ldots$ run over $1, 2$ and indices $a, b, c, \ldots$ run over $1, 2, 3$. As before, X indicates a position in $\mathcal{B}$, and x a position in $\mathcal{S}$. When considering shells, we will always assume that $\{x^i\}$ are **convected coordinates**, i.e. $x^i(x) = X^i(\phi_t^{-1}(x))$. This means that capitalised indices will not be used as they were when considering three-dimensional elasticity. Instead, when we consider shell theory, capitalised indices will be used to indicate **bivector indices**. To explain this, we will digress and consider multivector frames for general n-dimensional vector spaces.

5.1 Multivector Frames

Given a vector a in a vector space with a frame $\{e_i\}$ and reciprocal frame $\{e^i\}$, a can be written as,

$$a = a_i e^i = a^i e_i, \quad a_i = a \cdot e_i, \quad a^i = a \cdot e^i. \tag{5.1}$$

The frames for the vector space can be used to create bases for all the multivector spaces. A frame for all bivectors can be formed by $\{e_i \wedge e_j | i < j\}$, a frame for all trivectors can be formed by $\{e_i \wedge e_j \wedge e_k | i < j < k\}$, and so on up to the dimension of the vector space. For a three-dimensional space we have the following frames,

scalars	vectors	bivectors	trivectors
1	$\{e_1, e_2, e_3\}$	$\{e_1 \wedge e_2, e_1 \wedge e_3, e_2 \wedge e_3\}$	$\{e_1 \wedge e_2 \wedge e_3\}$

We can also form a reciprocal frame for all bivectors by $\{e^j \wedge e^i | i < j\}$, a reciprocal frame for all trivectors by $\{e^k \wedge e^j \wedge e^i | i < j < k\}$, and so on up to the dimension of the vector space. For a three-dimensional space we have the following reciprocal frames,

scalars	vectors	bivectors	trivectors
1	$\{e^1, e^2, e^3\}$	$\{e^2 \wedge e^1, e^3 \wedge e^1, e^3 \wedge e^2\}$	$\{e^3 \wedge e^2 \wedge e^1\}$

We use capital indices to denote sequences of integers in which the integers always increase, and there is no repetition. We use a subscript to indicate the number of integers in the list. For example, in a three-dimensional space, I_2 can take any of the values $(1,2)$, $(1,3)$, or $(2,3)$, and I_3 can take the value $(1,2,3)$, with the same possibilities for J_k, K_k, etc. We can use this to denote the multivector bases. If the index I_m represents the list of m entries $(i, j, \ldots, k)$, then we write,

$$e_{I_m} = \overbrace{e_i \wedge e_j \wedge \cdots \wedge e_k}^{m \text{ vectors}}, \quad e^{I_m} = \underbrace{e^k \wedge \cdots \wedge e^j \wedge e^i}_{m \text{ vectors}}. \tag{5.2}$$

Defined in this way, these multivectors satisfy,

$$e^{I_m} \cdot e_{J_m} = \delta^{I_m}_{J_m}, \tag{5.3}$$

where $\delta^{I_m}_{J_m}$ is the extension of the Kronecker delta to lists of indices, and returns 1 only when the lists are identical. This allows us to write the frames and reciprocal frames of an n-dimensional space as,

	scalars	vectors	bivectors	$\ldots$	n-vectors
frames	1	$\{e_i\}$	$\{e_{I_2}\}$	$\cdots$	$\{e_{I_n}\}$
reciprocal frames	1	$\{e^i\}$	$\{e^{I_2}\}$	$\cdots$	$\{e^{I_n}\}$

Note that I_n, where n is the dimension of the space, will always consist of a single ascending list of integers from 1 to n, and hence,

$$\{e_{I_n}\} = \{e_1 \wedge e_2 \wedge \cdots \wedge e_n\}, \quad \{e^{I_n}\} = \{e^n \wedge \cdots \wedge e^2 \wedge e^1\}. \tag{5.4}$$

More generally, the number of different k-vectors in the frame or reciprocal frame of the space of k-vectors, or alternatively, the number of values that I_k can take, is $\binom{n}{k} = \frac{n!}{k!(n-k)!}$. Also note that a general m-vector Ω can be written as,

$$\Omega = \Omega_{I_m} e^{I_m} = \Omega^{I_m} e_{I_m}, \quad \Omega_{I_m} = \Omega \cdot e_{I_m}, \quad \Omega^{I_m} = \Omega \cdot e^{I_m}. \tag{5.5}$$

In a three-dimensional space, the space of vectors is spanned by $\{e_a\}$, and trivectors will always be a multiple of $e_1 \wedge e_2 \wedge e_3$. Hence, the only non-trivial frame left to deal with is the space of bivectors. We use the capital index notation already outlined, but because we will only need to deal with bivectors when using capital indices, we will drop the use of the subscript, hence the frames for three-dimensional space are,

	scalars	vectors	bivectors	trivectors
frames	1	$\{e_a\}$	$\{e_A\}$	$\{e_1 \wedge e_2 \wedge e_3\}$
reciprocal frames	1	$\{e^a\}$	$\{e^A\}$	$\{e^3 \wedge e^2 \wedge e^1\}$

The indices $a, b, c, \ldots$ run over $1, 2, 3$, and the capital indices $A, B, C, \ldots$ run over $(1, 2)$, $(1, 3), (2, 3)$. We have already noted the convention that the indices $i, j, k, \ldots$ only run over $1, 2$ when we are considering shell theory, and it is useful to also use the convention that the capital indices $I, J, K, \ldots$ only run over $(1, 3), (2, 3)$.

5.2 Geometry of Curved Surfaces

We consider the surface $\mathcal{S}$. The geometric results we obtain can be analogously applied to $\mathcal{B}$. Using the coordinate system $\{x^i\}$ we can define a **frame** $\{e_i\}$ of the tangent space $T_x\mathcal{S}$,

$$e_i = \frac{\partial x}{\partial x^i}. \tag{5.6}$$

The **local pseudoscalar** of the surface $\mathcal{S}$ is denoted i, and is defined by,

$$i = \frac{e_1 \wedge e_2}{|e_1 \wedge e_2|}. \tag{5.7}$$

This is a unit plane element (bivector) that defines the local tangent space of the surface, along with an orientation, and satisfies $i^2 = -1$.

Using the two basis vectors we can define a third **normal basis vector** e_3 so that we

have a frame for the local tangent space of $\mathbb{E}^3$, and not just $\mathcal{S}$. e_3 is chosen to be of unit length, perpendicular to e_1 and e_2, and in the direction such that e_1, e_2, e_3 form a right handed set. If I_3 is the pseudoscalar of $\mathbb{E}^3$, then we can can write e_3 as,

$$e_3 = -I_3 \frac{e_1 \wedge e_2}{|e_1 \wedge e_2|} = -I_3 i. \tag{5.8}$$

e_3 is a unit vector perpendicular to e_1 and e_2, so it is clear that $e^3 = e_3$. The frame $\{e_a\}, a = 1, 2, 3$ provides a basis of the tangent space of $\mathbb{E}^3$, but only on the surface $\mathcal{S} \subset \mathbb{E}^3$.

5.2.1 Intrinsic Vector Derivative

A multivector A in $\mathbb{E}^3$ can be projected onto $T_x\mathcal{S}$ by the **projection operator** p,

$$\mathsf{p}(A) = A \cdot i \; i^{-1}. \tag{5.9}$$

We can extract the perpendicular part of A using the **rejection operator** $\mathsf{p}_\perp$,

$$\mathsf{p}_\perp(A) = A - \mathsf{p}(A) = A \wedge i \; i^{-1}. \tag{5.10}$$

The **intrinsic vector derivative** of the surface can be defined as the projection of ∇ (the vector derivative of $\mathbb{E}^3$) onto the surface. This is denoted by $\partial = \mathsf{p}(\nabla)$. Using this the reciprocal frame $\{e^i\}$ can be defined by,

$$e^i = \partial x^i. \tag{5.11}$$

Using the coordinate system $\{x^i\}$, ∂ can be expanded as,

$$\partial = e^i \frac{\partial}{\partial x^i} = e^i \partial_i, \tag{5.12}$$

where the final equality defines ∂_i.

5.2.2 First Fundamental Form

$\mathfrak{g}$ is the identity function on the surface $\mathcal{S}$. Given a vector y which lies on the surface $\mathcal{S}$, but is not restricted to the tangent space of the surface, $\mathfrak{g}$ is defined by,

$$\mathfrak{g}(y) = y. \tag{5.13}$$

$\mathfrak{g}$ is more commonly called the **metric** or the **first fundamental form** of the surface, which is usually defined using indicial notation as $\mathfrak{g}_{ij} = e_i \cdot e_j$. We can see that our definition is equivalent by restricting the argument of $\mathfrak{g}$ to vectors in the tangent space of $\mathcal{S}$, and writing $\mathfrak{g}_{ij} = e_i \cdot \mathfrak{g}(e_j) = e_i \cdot e_j$. It is possible to extend $\mathfrak{g}$ to 3 dimensions using e_3, in which case we have $\mathfrak{g}_{ab} = e_a \cdot e_b$. From the definition of e_3, we can see that $\mathfrak{g}_{33} = 1$ and $\mathfrak{g}_{i3} = \mathfrak{g}_{3i} = 0$. Using the reciprocal frame we have $\mathfrak{g}^{ab} = e^a \cdot e^b$, and it is also clear that $\mathfrak{g}^a{}_b = \mathfrak{g}_b{}^a = \delta^a_b$.

The **volume form** $\mathfrak{v}$ is a scalar function over the surface $\mathcal{S}$ that is defined to satisfy,

$$e_1 \wedge e_2 = \mathfrak{v}\, i. \tag{5.14}$$

The volume form is closely related to the determinant $\det(\mathfrak{g}_{ij})$. The determinant of the tensor $\mathfrak{g}$ is defined independently of coordinates by the equation $\mathfrak{g}(i) = \det(\mathfrak{g})i$, from which it is clear that $\det \mathfrak{g} = 1$. By contrast, $\det(\mathfrak{g}_{ij})$ is defined in terms of components as $\det(\mathfrak{g}_{ij}) = \mathfrak{g}_{11}\mathfrak{g}_{22} - \mathfrak{g}_{21}\mathfrak{g}_{12}$. To relate these two definitions we can expand $\mathfrak{g}(y)$ (assuming the argument lies in the tangent space of $\mathcal{S}$) as,

$$\mathfrak{g}(y) = (y \cdot e_1)e^1 + (y \cdot e_2)e^2. \tag{5.15}$$

Applying this expansion of $\mathfrak{g}$ to $\mathfrak{g}(i) = \mathfrak{g}(e_1 \wedge e_2 / \mathfrak{v})$ we obtain,

$$\begin{aligned} \mathfrak{g}(i) &= \frac{1}{\mathfrak{v}} \left[(e_1 \cdot e_1)e^1 + (e_2 \cdot e_1)e^2\right] \wedge \left[(e_1 \cdot e_2)e^1 + (e_2 \cdot e_2)e^2\right] \\ &= \frac{1}{\mathfrak{v}} \left(\mathfrak{g}_{11}\mathfrak{g}_{22} - \mathfrak{g}_{21}\mathfrak{g}_{12}\right) e^1 \wedge e^2. \end{aligned} \tag{5.16}$$

Since the reciprocal frame $\{e^i\}$ spans the same space as $\{e_i\}$, $e^1 \wedge e^2$ will be a multiple of i.

In fact, we can show that $e^1 \wedge e^2 = i/\mathfrak{v}$*. Using this result we obtain,

$$\mathsf{g}(i) = \frac{1}{\mathfrak{v}^2}\left(\mathsf{g}_{11}\mathsf{g}_{22} - \mathsf{g}_{21}\mathsf{g}_{12}\right) i. \tag{5.17}$$

We know that $\det \mathsf{g} = 1$, and so we obtain the result,

$$\mathsf{g}_{11}\mathsf{g}_{22} - \mathsf{g}_{21}\mathsf{g}_{12} = \det(\mathsf{g}_{ij}) = \mathfrak{v}^2, \tag{5.18}$$

or, taking the square root, $\mathfrak{v} = \sqrt{\det(\mathsf{g}_{ij})}$. This useful result shows in a more geometric sense what $\sqrt{\det(\mathsf{g}_{ij})}$ represents, clarifies the difference between $\det \mathsf{g}$ and $\det(\mathsf{g}_{ij})$, and gives an early example of how the notation of geometric algebra can provide a more lucid representation.

5.2.3 Second Fundamental Form

By asking how tangent vectors to the surface $\mathcal{B}$ change under the motion ϕ_t we can obtain information about how the material is locally stretched. When considering the elasticity of shells however, we also need to know how the local **curvature** of the shell changes under ϕ_t. To do this we must first understand how to describe the curvature of a surface.

It is clear that unless the surface is curved, the normal vector e_3 will be the same at every point on the surface (which is equivalent to i being the same at every point on the surface). If y is any tangent vector to $\mathcal{S}$, then we can define the vector valued function $\bar{\mathsf{b}}(y)$ to be,

$$\bar{\mathsf{b}}(y) = -y \cdot \partial e_3. \tag{5.19}$$

The over-bar and minus sign are so that our definition agrees with convention. This function tells us how e_3 changes in the direction specified by y, and is clearly a linear function of its argument. By construction, e_3 always has unit length, and consequently, any change in e_3 will be tangential to the surface. Hence, both the range and domain of $\bar{\mathsf{b}}$ are the tangent

*Let $e_1 \wedge e_2 = \mathfrak{v}\, i$ and $e^1 \wedge e^2 = \mathfrak{q} i$. Using the identity $(a \wedge b) \cdot (c \wedge d) = c \cdot ba \cdot d - c \cdot ab \cdot d$ [Doran and Lasenby, 2003] we obtain,

$$(e_1 \wedge e_2) \cdot (e^1 \wedge e^2) = e^1 \cdot e_2 e_1 \cdot e^2 - e^1 \cdot e_1 e_2 \cdot e^2 = -1.$$

Substituting the definitions given we obtain $\mathfrak{v}\,\mathfrak{q} i^2 = -1$, and since $i^2 = -1$, we obtain $\mathfrak{q} = 1/\mathfrak{v}$.

space of $\mathcal{S}$. The adjoint function b is defined by,

$$\mathsf{b}(y) = -\dot{\partial}(y \cdot \dot{e}_3). \tag{5.20}$$

This is the **second fundamental form** of the surface. It encodes information about curvature, and takes and returns a vector in the tangent space of $\mathcal{S}$. In component form we have,

$$\mathsf{b}_{ij} = e_i \cdot \mathsf{b}(e_j) = -e_j \cdot \frac{\partial e_3}{\partial x^i}. \tag{5.21}$$

By construction we have $e_j \cdot e_3 = 0$ and $\partial e_j / \partial x^i = \partial e_i / \partial x^j$, and so we can write b_{ij} as,

$$\mathsf{b}_{ij} = e_3 \cdot \frac{\partial e_j}{\partial x^i} = e_3 \cdot \frac{\partial e_i}{\partial x^j} = \mathsf{b}_{ji}. \tag{5.22}$$

b_{ij} may be expressed as $e_i \cdot \mathsf{b}(e_j)$, but we have just shown that $\mathsf{b}_{ij} = \mathsf{b}_{ji}$, and so we may write $e_i \cdot \mathsf{b}(e_j) = \mathsf{b}(e_i) \cdot e_j$. By definition the adjoint operator must satisfy $e_i \cdot \mathsf{b}(e_j) = \bar{\mathsf{b}}(e_i) \cdot e_j$. Combining these two results we can see that b is symmetric, i.e. $\bar{\mathsf{b}} = \mathsf{b}$.

The eigenvalues of b are the principal curvatures of $\mathcal{S}$, which we denote c_1 and c_2, and they satisfy the following component expressions,

$$\begin{aligned} c_1 + c_2 &= \mathsf{b}_1{}^1 + \mathsf{b}_2{}^2 = \operatorname{tr} \mathsf{b}, \\ c_1 c_2 &= \mathsf{b}_1{}^1 \mathsf{b}_2{}^2 - \mathsf{b}_1{}^2 \mathsf{b}_2{}^1 = \det \mathsf{b}. \end{aligned} \tag{5.23}$$

$c_1 + c_2$ is twice the **mean curvature**, and $c_1 c_2$ is the **Gaussian curvature**. b has already been shown to be symmetric, so we know that the eigenvectors of b will be perpendicular.

5.2.4 Christoffel Coefficients

It makes sense for us to define the following **Christoffel coefficients**,

$$\gamma^b_{ia} = e^b \cdot (e_i \cdot \partial e_a) = e^b \cdot \frac{\partial e_a}{\partial x^i}. \tag{5.24}$$

Note that since $e_a \cdot e^b = \delta^b_a$ these also satisfy,

$$e_a \cdot \frac{\partial e^b}{\partial x^i} = -\gamma^b_{ia}. \tag{5.25}$$

Care must be taken with the indices here. It makes sense for use to ask how any three of the basis vectors change as we move over the surface, hence why the a index goes over $1, 2, 3$, but only in directions tangential to the surface, since the frame is not defined away from the surface. Hence the i index only goes over $1, 2$. There is no restriction on how the basis vectors changes as we move over the surface, so the b index must go over $1, 2, 3$. Note that we have extended the usual definition of Christoffel coefficients, by including components outside the tangent space of the manifold.

In 3-dimensional elasticity, the body is a portion of $\mathbb{E}^3$, so the Christoffel coefficients are purely dependent on how we choose our coordinate system, and we can always choose this coordinate system to be Cartesian, meaning all of the coefficients are zero, but this is not the case when the body is a two dimensional surface. We do have some choice over the coordinate system. The coefficients γ^i_{jk} tell us how the tangent vectors change in the direction tangential to the surface, but we can control this by our choice of the coordinate system, so there is not any fundamental information about the curvature of the surface contained within these coefficients. This leaves the components γ^3_{ia} and γ^a_{i3}. The first of these describe how the basis vectors change in the direction normal to the surface. In the case of e_1 and e_2, this will only be non-zero when the surface is curved. e_3 is constructed to always have unit length, so changes in e_3 as it moves over the surface will always be tangential to the surface, meaning that $\gamma^3_{i3} = 0$, leaving only γ^3_{ij} non-zero. γ^a_{i3} describe how e_3 changes over the surface, and as already discussed this change will always be tangential to the surface, meaning that only γ^i_{j3} are non-zero. We can also note that these are only non-zero when the surface is curved.

We have identified γ^3_{ij} and γ^i_{j3} as of interest in describing the curvature of the surface. By construction $e_3 \cdot e_i = 0$, so we may write,

$$\begin{aligned} 0 = \frac{\partial}{\partial x^i}(e_3 \cdot e_j) &= e_3 \cdot \frac{\partial e_j}{\partial x^i} + e_j \cdot \frac{\partial e_3}{\partial x^i} \\ &= e^3 \cdot \frac{\partial e_j}{\partial x^i} + \mathtt{g}_{jk} e^k \cdot \frac{\partial e_3}{\partial x^i} \\ &= \gamma^3_{ij} + \mathtt{g}_{jk}\gamma^k_{i3}. \end{aligned} \tag{5.26}$$

We can rearrange this to obtain,

$$\gamma^3_{ij} = -\mathtt{g}_{jk}\gamma^k_{i3}. \tag{5.27}$$

Hence we see that only a single 2-dimensional matrix of components is required to describe

the curvature of the surface. The Christoffel coefficients identified are directly related to the second fundamental form by,

$$\begin{aligned} \mathsf{b}_{ij} = e_3 \cdot \frac{\partial e_j}{\partial x^i} = -e_j \cdot \frac{\partial e_3}{\partial x^i} = \gamma^3_{ij}, \\ \mathsf{b}_i{}^j = \mathsf{b}^j{}_i = -\gamma^j_{i3}. \end{aligned} \tag{5.28}$$

We can extend the idea of Christoffel coefficients to the frame of bivectors $\{e_A\}$, and define,

$$\gamma^B_{iA} = e^B \cdot \frac{\partial e_A}{\partial x^i} = -e_A * \frac{\partial e^B}{\partial x^i}. \tag{5.29}$$

By application of the chain rule we can relate the bivector Christoffel coefficients to the vector ones. For an arbitrary frame in $\mathbb{E}^3$ we have,

$$\begin{aligned} \gamma^{(1,2)}_{i(1,2)} = \gamma^1_{i1} + \gamma^2_{i2}, \quad \gamma^{(1,3)}_{i(1,2)} = \gamma^3_{i2}, \quad \gamma^{(2,3)}_{i(1,2)} = -\gamma^3_{i1}, \\ \gamma^{(1,2)}_{i(1,3)} = \gamma^2_{i3}, \quad \gamma^{(1,3)}_{i(1,3)} = \gamma^1_{i1} + \gamma^3_{i3}, \quad \gamma^{(2,3)}_{i(1,3)} = \gamma^2_{i1}, \\ \gamma^{(1,2)}_{i(2,3)} = -\gamma^1_{i3}, \quad \gamma^{(1,3)}_{i(2,3)} = \gamma^1_{i2}, \quad \gamma^{(2,3)}_{i(2,3)} = \gamma^2_{i2} + \gamma^3_{i3}. \end{aligned} \tag{5.30}$$

For the specific frame used on a shell, in which e_3 is a unit vector and perpendicular to e_1 and e_2, this simplifies to,

$$\begin{aligned} \gamma^{(1,2)}_{i(1,2)} = \gamma^1_{i1} + \gamma^2_{i2}, \quad \gamma^{(1,3)}_{i(1,2)} = \mathsf{b}_{i2}, \quad \gamma^{(2,3)}_{i(1,2)} = -\mathsf{b}_{i1}, \\ \gamma^{(1,2)}_{i(1,3)} = -\mathsf{b}^2{}_i, \quad \gamma^{(1,3)}_{i(1,3)} = \gamma^1_{i1}, \quad \gamma^{(2,3)}_{i(1,3)} = \gamma^2_{i1}, \\ \gamma^{(1,2)}_{i(2,3)} = \mathsf{b}^1{}_i, \quad \gamma^{(1,3)}_{i(2,3)} = \gamma^1_{i2}, \quad \gamma^{(2,3)}_{i(2,3)} = \gamma^2_{i2}. \end{aligned} \tag{5.31}$$

The Christoffel coefficients are used to express derivatives when using coordinates. We will generally try to avoid this and keep out expressions component free, but it is useful to note the following results. First, let v be an arbitrary vector field defined over $\mathcal{S}$. For any tangent vector field y we then have,

$$\begin{aligned} y \cdot \partial v &= y^i \left(\frac{\partial v_a}{\partial x^i} - v_b \gamma^b_{ia} \right) e^a = y^i v_{a|i} e^a \\ &= y^i \left(\frac{\partial v^a}{\partial x^i} + v^b \gamma^a_{ib} \right) e_a = y^i v^a{}_{|i} e_a, \end{aligned} \tag{5.32}$$

which defines $v_{a|i}$ and $v^a{}_{|i}$. Using the results presented above we can write these as,

$$\begin{aligned} v^i{}_{|j} &= \frac{\partial v^i}{\partial x^j} + v^k \gamma^i_{jk} - v^3 \mathsf{b}^i{}_j, \quad v^3{}_{|i} = \frac{\partial v^3}{\partial x^i} + v^j \mathsf{b}_{ij}, \\ v_{i|j} &= \frac{\partial v_i}{\partial x^j} - v_k \gamma^k_{ji} - v_3 \mathsf{b}_{ji}, \quad v_{3|i} = \frac{\partial v_3}{\partial x^i} + v_j \mathsf{b}^j{}_i. \end{aligned} \tag{5.33}$$

Let y and z be arbitrary tangent vector fields defined over $\mathcal{S}$, and let $\mathsf{f}(y)$ be an arbitrary, vector valued, linear function defined over $\mathcal{S}$. The derivative of the function f over $\mathcal{S}$ is given by,

$$\begin{aligned} y \cdot \dot{\partial}\dot{\mathsf{f}}(z) &= y \cdot \partial\left(\mathsf{f}(z)\right) - \mathsf{f}\left(y \cdot \partial z\right) \\ &= y^i \partial_i(\mathsf{f}_{aj} z^j e^a) - \mathsf{f}\left(y^i \partial_i (z^j e_j)\right) \\ &= y^i \left(\partial_i(\mathsf{f}_{aj}) z^j e^a + \mathsf{f}_{aj} \partial_i(z^j) e^a + \mathsf{f}_{aj} z^j \partial_i(e^a) - \partial_i(z^j) \mathsf{f}(e_j) - z^j \mathsf{f}\left(\partial_i(e_j)\right)\right) \\ &= y^i z^j \left(\partial_i(\mathsf{f}_{aj}) e^a - \mathsf{f}_{aj} \gamma^a_{ib} e^b - \gamma^a_{ij} \mathsf{f}_{ba} e^b\right) \\ &= y^i z^j \left(\partial_i \mathsf{f}_{aj} - \gamma^k_{ij} \mathsf{f}_{ak} - \gamma^b_{ia} \mathsf{f}_{bj}\right) e^a = y^i z^j e^a \mathsf{f}_{aj|i}, \end{aligned} \tag{5.34}$$

which defines $\mathsf{f}_{aj|i}$. Alternatively we can write this as,

$$\begin{aligned} y \cdot \dot{\partial}\dot{\mathsf{f}}(z) &= y \cdot \partial\left(\mathsf{f}(z)\right) - \mathsf{f}\left(y \cdot \partial z\right) \\ &= y^i \partial_i(\mathsf{f}^{aj} z_j e_a) - \mathsf{f}\left(y^i \partial_i (z_j e^j)\right) \\ &= y^i \left(\partial_i(\mathsf{f}^{aj}) z_j e_a + \mathsf{f}^{aj} \partial_i(z_j) e_a + \mathsf{f}^{aj} z_j \partial_i(e_a) - \partial_i(z_j) \mathsf{f}(e^j) - z_j \mathsf{f}\left(\partial_i(e^j)\right)\right) \\ &= y^i z_j \left(\partial_i(\mathsf{f}^{aj}) e_a + \mathsf{f}^{aj} \gamma^b_{ia} e_b + \gamma^j_{ia} \mathsf{f}^{ba} e_b\right) \\ &= y^i z_j \left(\partial_i(\mathsf{f}^{aj}) + \gamma^a_{ib} \mathsf{f}^{bj} + \gamma^j_{ik} \mathsf{f}^{ak}\right) e_a = y^i z_j e_a \mathsf{f}^{aj}{}_{|i}. \end{aligned} \tag{5.35}$$

The divergence of a tensor is given by,

$$\begin{aligned} \dot{\mathsf{f}}(\dot{\partial}) = e_l \cdot \dot{\partial}\dot{\mathsf{f}}(e^l) &= \delta^i_l \delta^l_j \left(\partial_i(\mathsf{f}^{aj}) + \gamma^a_{ib} \mathsf{f}^{bj} + \gamma^j_{ik} \mathsf{f}^{ak}\right) e_a \\ &= \left(\partial_i(\mathsf{f}^{ai}) + \gamma^a_{ib} \mathsf{b}^{bi} + \gamma^i_{ik} \mathsf{f}^{ak}\right) e_a = \mathsf{f}^{ai}{}_{|i} e_a. \end{aligned} \tag{5.36}$$

Now let $\mathsf{f}(y)$ be a bivector valued linear function on $\mathcal{S}$, whose domain is $T_x\mathcal{S}$. The

derivative of f is now given by,

$$\begin{aligned} y \cdot \dot{\partial}\dot{\mathsf{f}}(z) &= y \cdot \partial\left(\mathsf{f}(z)\right) - \mathsf{f}\left(y \cdot \partial z\right) \\ &= y^i \partial_i(\mathsf{f}^{Aj} z_j e_A) - \mathsf{f}\left(y^i \partial_i(z_j e^j)\right) \\ &= y^i \left(\partial_i(\mathsf{f}^{Aj}) z_j e_A + \mathsf{f}^{Aj} \partial_i(z_j) e_A + \mathsf{f}^{Aj} z_j \partial_i(e_A) - \partial_i(z_j)\mathsf{f}(e^j) - z_j \mathsf{f}\left(\partial_i(e^j)\right)\right) \\ &= y^i z_j \left(\partial_i(\mathsf{f}^{Aj}) e_A + \mathsf{f}^{Aj} \gamma^B_{iA} e_B + \gamma^j_{ia} \mathsf{f}^{Aa} e_A\right) \\ &= y^i z_j \left(\partial_i(\mathsf{f}^{Aj}) + \gamma^A_{iB} \mathsf{f}^{Bj} + \gamma^j_{ik} \mathsf{f}^{Ak}\right) e_A = y^i z_j \mathsf{f}^{Aj}{}_{|i} e_A. \end{aligned} \tag{5.37}$$

The divergence of this bivector valued function is given by,

$$\begin{aligned} \dot{\mathsf{f}}(\dot{\partial}) = e_l \cdot \dot{\partial}\dot{\mathsf{f}}(e^l) &= \delta^i_l \delta^l_j \left(\partial_i(\mathsf{f}^{Aj}) + \gamma^A_{iB} \mathsf{f}^{Bj} + \gamma^j_{ik} \mathsf{f}^{Ak}\right) e_A \\ &= \left(\partial_i(\mathsf{f}^{Ai}) + \gamma^A_{iB} \mathsf{f}^{Bi} + \gamma^i_{ik} \mathsf{f}^{Ak}\right) e_A = \mathsf{f}^{Ai}{}_{|i} e_A. \end{aligned} \tag{5.38}$$

5.2.5 Summary

For convenience, we show a summary of the geometric entities defined over the surface $\mathcal{S}$, and list the equivalent entities on the reference configuration $\mathcal{B}$,

	$\mathcal{B}$	$\mathcal{S}$
coordinates	$\{X^i\}$	$\{x^i\}$
vector frame	$\{E_i\}$	$\{e_i\}$
reciprocal vector frame	$\{E^i\}$	$\{e^i\}$
local pseudoscalar	I	i
volume form	$\mathfrak{V}$	$\mathfrak{v}$
normal vector	E_3	e_3
bivector frame	$\{E_A\}$	$\{e_A\}$
reciprocal bivector frame	$\{E^A\}$	$\{e^A\}$
intrinsic vector derivative	∂	∂
metric	G	g
second fundamental form	B	b
Christoffel coefficients	$\Gamma^a_{ib}, \Gamma^A_{iB}$	$\gamma^a_{ib}, \gamma^A_{iB}$

Note that the intrinsic vector derivative uses the same symbol on both the reference and spatial configurations, and which manifold is being differentiated over must be inferred from

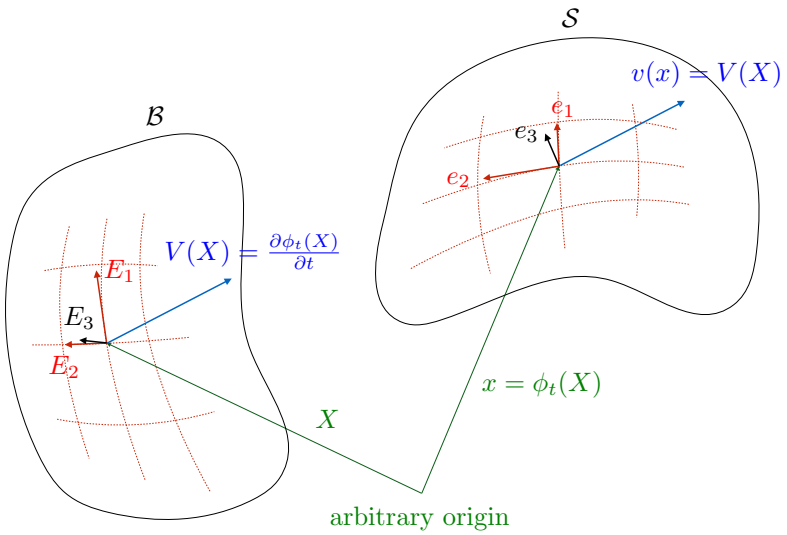


Figure 5.1: Shell geometry and deformation.

context.

5.3 Kinematics

The basic geometry of the reference and spatial configurations are illustrated in fig. 5.1.

5.3.1 Stretching

In three-dimensional elasticity information on stretching is extracted from the **deformation gradient**. Defining the deformation gradient for the motion of a surface requires some care. Let $X(\eta)$ be a path over the surface $\mathcal{B}$ parametrised by the scalar variable η. A tangent vector to the surface can be defined by,

$$\lim_{\epsilon \to 0} \frac{X(\eta + \epsilon) - X(\eta)}{\epsilon} = \frac{dX(\eta)}{d\eta}. \tag{5.39}$$

This tangent vector will be transformed by the motion ϕ_t to a tangent vector to $\mathcal{S}$,

$$\lim_{\epsilon \to 0} \frac{\phi_t\left(X(\eta + \epsilon)\right) - \phi_t\left(X(\eta)\right)}{\epsilon} = \frac{d\phi_t(X(\eta))}{d\eta}. \tag{5.40}$$

Note that we have had to define this using a path rather than explicitly using the tangent vector in the argument of ϕ_t. This is because if the surface is curved $X + \epsilon Y,\ X \in \mathcal{B}, Y \in T_X\mathcal{B}$ will not necessarily be a point on the surface. The **deformation gradient** is the

transformation of any tangent vector Y on $\mathcal{B}$ to its corresponding tangent vector on $\mathcal{S}$. We may write this as,

$$\mathsf{F}(Y) = Y \cdot \partial\phi_t(X), \tag{5.41}$$

The adjoint function $\bar{\mathsf{F}}$ of any tangent vector $y \in T_x\mathcal{S}$ is given by,

$$\bar{\mathsf{F}}(y) = \dot{\partial}(y \cdot \dot{\phi}_t(X)) = E^i(y \cdot (E_i \cdot \partial\phi_t(X)). \tag{5.42}$$

To extract stretching information from the deformation gradient we construct the **Cauchy-Green tensor**,

$$\mathsf{C}(Y) = \bar{\mathsf{F}}\mathsf{F}(Y). \tag{5.43}$$

It is clear that this tensor is symmetric, i.e. $\bar{\mathsf{C}} = \mathsf{C}$. From this it follows that the eigenvectors will be orthogonal, and the eigenvalues will be real. Furthermore, we restrict ourselves to deformations that leave the orientation of $\mathcal{B}$ unchanged, which means that the eigenvalues of C will be real and *positive*. It is therefore meaningful to define λ_i as the *square roots* of the eigenvalues of C. λ_i then represent the **principal strains** of a small element of the surface in the directions specified by the eigenvectors. Using the Cauchy-Green tensor we can construct a strain tensor that will only be non-zero when the material is locally stretched,

$$\mathsf{E}(Y) = \tfrac{1}{2}\left(\mathsf{C}(Y) - Y\right). \tag{5.44}$$

This is the **Green-Lagrangian strain tensor**, and it inherits the symmetric property from C, so we may write $\bar{\mathsf{E}} = \mathsf{E}$. The eigenvectors of E are the same as those of c, and the eigenvalues are $\frac{1}{2}(\lambda_i^2 - 1)$.

An alternative route is taken by [Ciarlet, 2005] to obtain a tensor describing local stretching of the material, making use of the convected coordinates. The components g_{ij} are given by,

$$\mathsf{g}_{ij} = e_i \cdot e_j = \mathsf{F}(E_i) \cdot \mathsf{F}(E_j). \tag{5.45}$$

Using the definition of the adjoint function $\bar{\mathsf{F}}$ we obtain,

$$\mathsf{g}_{ij} = E_i \cdot \bar{\mathsf{F}}\mathsf{F}(E_j) = E_i \cdot \mathsf{C}(E_j) = \mathsf{C}_{ij}, \tag{5.46}$$

and so we see that using the metric and convected coordinates we can obtain the Cauchy-Green tensor. We can also obtain the elasticity tensor using g,

$$\mathsf{g}_{ij} - \mathsf{G}_{ij} = E_i \cdot \mathsf{C}(E_j) - E_i \cdot E_j = 2E_i \cdot \mathsf{E}(E_j) = 2\mathsf{E}_{ij}. \tag{5.47}$$

Our definition, however, does not rely on the use of any particular coordinate system, and helps to keep clear that G and g are simply identity functions, while C and E encode important information about local stretching of the shell.

The polar decomposition of F used in three-dimensional elasticity can still be used in the two-dimensional case. This decomposition can still be written as,

$$\mathsf{F}(Y) = \mathsf{RU}(Y) = \mathsf{VR}(Y), \tag{5.48}$$

where $\bar{\mathsf{R}} = \mathsf{R}^{-1}$, $\det \mathsf{R} = 1$, $\bar{\mathsf{U}} = \mathsf{U}$, and $\bar{\mathsf{V}} = \mathsf{V}$. As before, we can write U as $\mathsf{U} = \mathsf{C}^{1/2}$, so its eigenvalues are λ_i. Note though that now, extra care must be taken considering the range and domain of these function, which we summarise here for convenience,

	domain	$\mapsto$	range
F:	$T_X\mathcal{B}$	$\mapsto$	$T_{\phi_t(X)}\mathcal{S}$
$\bar{\mathsf{F}}$:	$T_{\phi_t(X)}\mathcal{S}$	$\mapsto$	$T_X\mathcal{B}$
C:	$T_X\mathcal{B}$	$\mapsto$	$T_X\mathcal{B}$
E:	$T_X\mathcal{B}$	$\mapsto$	$T_X\mathcal{B}$
R:	$T_X\mathcal{B}$	$\mapsto$	$T_{\phi_t(X)}\mathcal{S}$
U:	$T_X\mathcal{B}$	$\mapsto$	$T_X\mathcal{B}$
V:	$T_{\phi_t(X)}\mathcal{S}$	$\mapsto$	$T_{\phi_t(X)}\mathcal{S}$

These are valid for all $X \in \mathcal{B}$. For a shell, all of the tangent spaces are two-dimensional, but $T_X\mathcal{B}$ and $T_{\phi_t(X)}\mathcal{S}$ can occupy different planes within $\mathbb{E}^3$.

We have defined a strain tensor on the reference configuration, but as with three-dimensional elasticity, it is also possible to define a strain tensor on the spatial configuration. The definition of c, referred to as the **Cauchy deformation tensor**, the **Piola tensor** or the **Finger tensor**, is the same as in three-dimensional elasticity,

$$\mathsf{c}(y) = \bar{\mathsf{F}}^{-1}\mathsf{F}^{-1}(y) = (\mathsf{V}^{-1})^2(y), \tag{5.49}$$

as is the definition of the **spatial (or Eulerian-Almansi) strain tensor** as,

$$\mathsf{e}(y) = \tfrac{1}{2}\left(y - \mathsf{c}(y)\right). \tag{5.50}$$

As before, E and e are related by,

$$\mathsf{e}(y) = \bar{\mathsf{F}}^{-1}\mathsf{E}\mathsf{F}^{-1}(y), \quad \mathsf{E}(Y) = \bar{\mathsf{F}}\mathsf{e}\mathsf{F}(Y), \quad \mathsf{E}_{ij} = \mathsf{e}_{ij}. \tag{5.51}$$

If the deformation gradient F is given an argument normal to $\mathcal{B}$ (e.g. E_3), it returns zero, since its basic definition involves taking the inner product with ∂. Similarly, F^{-1} returns zero if it is given an argument normal to $\mathcal{S}$. It is convenient to define a **modified deformation gradient** by choosing $\mathbf{F}(E_3) = e_3$. In full, we can write,

$$\mathbf{F}(Y) = Y \cdot \partial\phi_t(X) + (Y \cdot E_3)e_3 = \mathsf{F}(Y) + (Y \cdot E_3)e_3. \tag{5.52}$$

The inverse $\mathbf{F}^{-1}$ is then given by,

$$\mathbf{F}^{-1}(y) = y \cdot \phi_t^{-1}(x) + (y \cdot e_3)E_3 = \mathsf{F}^{-1}(y) + (y \cdot e_3)E_3. \tag{5.53}$$

For completeness we also give the adjoint $\bar{\mathbf{F}}$ and its inverse $\bar{\mathbf{F}}^{-1}$,

$$\begin{aligned} \bar{\mathbf{F}}(y) &= \dot{\partial}(y \cdot \dot{\phi}_t(X)) + (y \cdot e_3)E_3 = \bar{\mathsf{F}}(y) + (y \cdot e_3)E_3, \\ \bar{\mathbf{F}}^{-1}(Y) &= \dot{\partial}(Y \cdot \dot{\phi}_t^{-1}(x)) + (Y \cdot E_3)e_3 = \bar{\mathsf{F}}^{-1}(Y) + (Y \cdot E_3)e_3. \end{aligned} \tag{5.54}$$

5.3.2 Mapping Derivatives

The deformation gradient can be used to map derivatives between the two manifolds. Let $A = A(x)\ \forall x \in \mathcal{S}$ be a general multivector valued field defined on $\mathcal{S}$. The derivative of A in the direction defined by y, a tangential vector field on $\mathcal{S}$, is given by $y \cdot \partial A$.

We can map $A = A(x)\ \forall x \in \mathcal{S}$ onto $\mathcal{B}$ using the motion ϕ_t,

$$A(X) = A(\phi_t(X)) \quad \forall X \in \mathcal{B}. \tag{5.55}$$

If Y is a tangential vector field on $\mathcal{B}$ that satisfies,

$$\mathsf{F}(Y) = y, \tag{5.56}$$

then we can write,

$$Y \cdot \partial A(X) = y \cdot \partial A(x). \tag{5.57}$$

The derivative on the left is taken over $\mathcal{B}$, while the derivative on the right is taken over $\mathcal{S}$. Proof of this result is given by [Hestenes and Sobczyk, 1984].

It will later be necessary to take the derivative of functions that take vectors from $T_X\mathcal{B}$, but return vectors or bivectors on $\mathcal{S}$. Therefore, here we present some basic results for functions of this type. First, let Y and Z be tangential vector fields on $\mathcal{B}$, and let f be a vector valued function that whose domain in $T_X\mathcal{B}$, but whose range is $\mathbb{E}^3$, located at $\phi_t(X)$. The components of f are given by $\mathsf{f}^{ai} = e^a \cdot \mathsf{f}(E^i)$. This allows us to write,

$$\begin{aligned} Y \cdot \dot{\partial}\dot{\mathsf{f}}(Z) &= Y \cdot \partial\left(\mathsf{f}(Z)\right) - \mathsf{f}(Y \cdot \partial Z) \\ &= Y^i \partial_i(\mathsf{f}^{aj} Z_j e_a) - \mathsf{f}\left(Y^i \partial_i(Z_j E^j)\right) \\ &= Y^i \left(\partial_i(\mathsf{f}^{aj}) Z_j e_a + \mathsf{f}^{aj} \partial_i(Z_j) e_a + \mathsf{f}^{aj} Z_j \partial_i(e_a) - \partial_i(Z_j)\mathsf{f}(E^j) - Z_j \mathsf{f}\left(\partial_i(E^j)\right)\right) \\ &= Y^i Z_j \left(\partial_i(\mathsf{f}^{aj}) e_a + \mathsf{f}^{aj} \gamma^b_{ia} e_b + \Gamma^j_{ia} \mathsf{f}^{ba} e_b\right) \\ &= Y^i Z_j \left(\partial_i(\mathsf{f}^{aj}) + \gamma^a_{ib} \mathsf{f}^{bj} + \Gamma^j_{ik} \mathsf{f}^{ak}\right) e_a = Y^i Z_j \mathsf{f}^{aj}{}_{|i} e_a. \end{aligned} \tag{5.58}$$

This allows us to define the divergence of f as,

$$\begin{aligned} \dot{\mathsf{f}}(\dot{\partial}) = E_l \cdot \dot{\partial}\dot{\mathsf{f}}(E^l) &= \delta^i_l \delta^l_j \left(\partial_i(\mathsf{f}^{aj}) + \gamma^a_{ib} \mathsf{f}^{bj} + \Gamma^j_{ik} \mathsf{f}^{ak}\right) e_a \\ &= \left(\partial_i(\mathsf{f}^{ai}) + \gamma^a_{ib} \mathsf{f}^{bi} + \Gamma^i_{ik} \mathsf{f}^{ak}\right) e_a = \mathsf{f}^{ai}{}_{|i} e_a. \end{aligned} \tag{5.59}$$

If f is instead bivector valued on $\mathcal{S}$, then the components of f are given by $\mathsf{f}^{Ai} = e^A \cdot \mathsf{f}(E^i)$.

In this case the derivative of f is given by,

$$\begin{aligned} Y \cdot \dot{\partial}\dot{\mathsf{f}}(Z) &= Y \cdot \partial\left(\mathsf{f}(Z)\right) - \mathsf{f}(Y \cdot \partial Z) \\ &= Y^i \partial_i(\mathsf{f}^{Aj} Z_j e_A) - \mathsf{f}\left(Y^i \partial_i(Z_j E^j)\right) \\ &= Y^i \left(\partial_i(\mathsf{f}^{Aj}) Z_j e_A + \mathsf{f}^{Aj} \partial_i(Z_j) e_A + \mathsf{f}^{Aj} Z_j \partial_i(e_A) - \partial_i(Z_j)\mathsf{f}(E^j) - Z_j \mathsf{f}\left(\partial_i(E^j)\right)\right) \\ &= Y^i Z_j \left(\partial_i(\mathsf{f}^{Aj}) e_A + \mathsf{f}^{Aj} \gamma^B_{iA} e_A + \Gamma^j_{ia} \mathsf{f}^{Aa} e_A\right) \\ &= Y^i Z_j \left(\partial_i(\mathsf{f}^{Aj}) + \gamma^A_{iB} \mathsf{f}^{Bj} + \Gamma^j_{ik} \mathsf{f}^{Ak}\right) e_A = Y^i Z_j \mathsf{f}^{Aj}{}_{|i} e_A. \end{aligned} \tag{5.60}$$

In this case the divergence of f is given by,

$$\begin{aligned} \dot{\mathsf{f}}(\dot{\partial}) = E_l \cdot \dot{\partial}\dot{\mathsf{f}}(E^l) &= \delta^i_l \delta^l_j \left(\partial_i(\mathsf{f}^{Aj}) + \gamma^A_{iB} \mathsf{f}^{Bj} + \Gamma^j_{ik} \mathsf{f}^{Ak}\right) e_A \\ &= \left(\partial_i(\mathsf{f}^{Ai}) + \gamma^A_{iB} \mathsf{f}^{Bi} + \Gamma^i_{ik} \mathsf{f}^{Ak}\right) e_A = \mathsf{f}^{Ai}{}_{|i} e_A. \end{aligned} \tag{5.61}$$

5.3.3 Displacements

The definition of the **displacement vector** $U(X) = \phi_t(X) - X$ still holds when $\mathcal{B}$ and $\mathcal{S}$ are surfaces, and we can still use this definition to express F and E as,

$$\begin{aligned} \mathsf{F}(Y) &= Y + Y \cdot \partial U, \\ 2\mathsf{E}(Y) &= Y \cdot \partial U + \dot{\partial}(Y \cdot \dot{U}) + \dot{\partial}(Y \cdot \partial U) \cdot \dot{U}). \end{aligned} \tag{5.62}$$

5.3.4 Changes of Curvature

In asking whether curvature has changed we need a way of comparing the eigenvectors and eigenvalues of b and B. This is complicated by the fact that the eigenvectors occupy different vector spaces, $T_X B$ and $T_{\phi_t(X)} S$. These tangent spaces are related to each other by the deformation gradient F. To compare b and B we construct a new tensor, which we call the **convected second fundamental form**, that uses b but whose range and domain are $T_X B$. We define the convected second fundamental form as,

$$\bar{\mathsf{F}}\mathsf{b}\mathsf{F}(Y). \tag{5.63}$$

Using this the **change of curvature tensor** is defined by,

$$\mathsf{H}(Y) = \bar{\mathsf{F}}\mathsf{b}\mathsf{F}(Y) - \mathsf{B}(Y). \tag{5.64}$$

B and b are symmetric, from which it follows that H is also symmetric.

H is defined on the reference configuration. We can define its analogy on the spatial configuration, h, as,

$$\mathsf{h}(y) = \mathsf{b}(y) - \bar{\mathsf{F}}^{-1}\mathsf{B}\mathsf{F}^{-1}(y) = \bar{\mathsf{F}}^{-1}\mathsf{H}\mathsf{F}^{-1}(y). \tag{5.65}$$

This satisfies,

$$\mathsf{h}_{ij} = \mathsf{H}_{ij}. \tag{5.66}$$

5.3.5 Using Rotors to Represent Changes of Curvature

Understanding changes of curvature lies at the heart of many problems in shell theory. Our expression for the change of curvature tensor $\mathsf{H}(Y) = \bar{\mathsf{F}}\mathsf{b}\mathsf{F}(Y) - \mathsf{B}(Y)$ already differs from most others (for example [Ciarlet, 2005]) because is is coordinate free. The change of curvature tensor is more usually defined by the coordinate expression,

$$\mathsf{H}_{ij} = \mathsf{b}_{ij} - \mathsf{B}_{ij}, \tag{5.67}$$

which relies on the use of convected coordinates. This hides the presence of the deformation gradient F. By including this in a coordinate free definition, it is much more obvious that stretching can have an influence on change of curvature under some circumstances. This is something that we will now clarify further by representing the change of curvature tensor using **rotors**.

In geometric algebra the rotation of an arbitrary multivector A can be expressed as [Doran and Lasenby, 2003, §4.2],

$$A \mapsto RA\tilde{R}. \tag{5.68}$$

R is called a **rotor**, and it can be any even multivector that satisfies $R\tilde{R} = \tilde{R}R = 1$. $\tilde{R}$ is the **reverse** of R. If we wish to rotate a multivector in a Euclidean space in a plane defined by the bivector B, where the orientation of B defines the direction of the rotation and its magnitude defines the angle of rotation (in radians), then the corresponding rotor R is given

by,

$$R = \exp(-B/2). \tag{5.69}$$

This is essentially an extension of the complex number notation for rotations $e^{\imath\theta}$ to spaces of arbitrary dimension. A useful result, which follows from the property $R\tilde{R} = 1$, is that the derivative of $\tilde{R}$ can be written in terms of the derivative of R,

$$Y \cdot \partial\tilde{R} = -\tilde{R}(Y \cdot \partial R)\tilde{R}. \tag{5.70}$$

We can represent the rotation portion of F by $\mathsf{R}(Y) = RY\tilde{R}$. The first thing that we can do with this is extend the range and domain of R into $\mathbb{E}^3$. We take $\{\hat{E}_i\}$ to be an orthonormal frame of $T_X\mathcal{B}$. Given this, E_3 is given by $E_3 = -I_3(\hat{E}_1 \wedge \hat{E}_2) = -I_3(\hat{E}_1\hat{E}_2)$. To obtain e_3 we need two unit vectors in the tangent space of the spatial configuration that are oriented in the same way as the pair $\mathsf{F}(E_1)$, $\mathsf{F}(E_2)$, and are orthonormal. This pair of unit vectors is given by $\mathsf{R}(\hat{E}_1)$, $\mathsf{R}(\hat{E}_2)$, and so e_3 is given by,

$$\begin{aligned} e_3 = -I_3(\mathsf{R}(\hat{E}_1) \wedge \mathsf{R}(\hat{E}_2)) &= -I_3(\mathsf{R}(\hat{E}_1)\mathsf{R}(\hat{E}_2)) \\ &= -I_3(R\hat{E}_1\tilde{R}R\hat{E}_2\tilde{R}) \\ &= -I_3(R\hat{E}_1\hat{E}_2\tilde{R}) \\ &= R(-I_3(\hat{E}_1\hat{E}_2))\tilde{R} \\ &= RE_3\tilde{R}, \end{aligned} \tag{5.71}$$

where we have used the fact that any rotor will commute with I_3. Thus we have shown that the rotation associated with the deformation is also the rotation between the normal vectors E_3 and e_3, which makes intuitive sense. We have extended the range and domain of R to $\mathbb{E}^3$, while the range and domain of U is still constrained to the tangent space of the reference configuration, and the range and domain of F are constrained to the tangent spaces of the spatial and reference configuration respectively.

Next we consider the convected second fundamental form. Using the definition of b we can write this as,

$$\bar{\mathsf{F}}\mathsf{b}\mathsf{F}(Y) = -\bar{\mathsf{F}}\left(\mathsf{F}(Y) \cdot \partial e_3\right). \tag{5.72}$$

$e_3(x)$ is defined over $\mathcal{S}$, but if we define $e_3(X) = e_3(\phi_t(X))$ then we can write the convected

second fundamental form as,

$$\bar{\mathsf{F}}\mathsf{b}\mathsf{F}(Y) = -\bar{\mathsf{F}}\left(Y \cdot \partial e_3\right). \tag{5.73}$$

where the derivative is now being taken over $\mathcal{B}$. If we now use $e_3 = RE_3\tilde{R}$, and apply the chain rule, then we obtain,

$$\begin{aligned} Y \cdot \partial e_3 = Y \cdot \partial(RE_3\tilde{R}) &= (Y \cdot \partial R)E_3\tilde{R} + R(Y \cdot \partial E_3)\tilde{R} + RE_3(-\tilde{R}(Y \cdot \partial R)\tilde{R}) \\ &= R(Y \cdot \partial E_3)\tilde{R} + [(Y \cdot \partial R)\tilde{R}]RE_3\tilde{R} - RE_3\tilde{R}[(Y \cdot \partial R)\tilde{R}] \\ &= R(Y \cdot \partial E_3)\tilde{R} + [(Y \cdot \partial R)\tilde{R}]e_3 - e_3[(Y \cdot \partial R)\tilde{R}] \\ &= R(Y \cdot \partial E_3)\tilde{R} + [2(Y \cdot \partial R)\tilde{R}] \times e_3 \\ &= \mathsf{R}(Y \cdot \partial E_3) + [2(Y \cdot \partial R)\tilde{R}] \times e_3, \end{aligned} \tag{5.74}$$

where $\times$ is the commutator product [Doran and Lasenby, 2003, §4.1.3]. Hence we can express $\bar{\mathsf{F}}\mathsf{b}\mathsf{F}$ as,

$$\begin{aligned} \bar{\mathsf{F}}\mathsf{b}\mathsf{F}(Y) &= -\bar{\mathsf{F}}\mathsf{R}(Y \cdot \partial E_3) - \bar{\mathsf{F}}\left([2(Y \cdot \partial R)\tilde{R}] \times e_3\right) \\ &= -\mathsf{U}(Y \cdot \partial E_3) - \bar{\mathsf{F}}\left([2(Y \cdot \partial R)\tilde{R}] \times e_3\right) \\ &= \mathsf{U}\mathsf{B}(Y) + \bar{\mathsf{F}}\left(e_3 \times [2(Y \cdot \partial R)\tilde{R}]\right), \end{aligned} \tag{5.75}$$

and finally we obtain an expression for H,

$$\begin{aligned} \mathsf{H}(Y) &= (\mathsf{U} - \mathsf{G})\mathsf{B}(Y) + \bar{\mathsf{F}}\left(e_3 \times [2(Y \cdot \partial R)\tilde{R}]\right) \\ &= (\mathsf{U} - \mathsf{G})\mathsf{B}(Y) + \bar{\mathsf{F}}\left([RE_3\tilde{R}] \times [2(Y \cdot \partial R)\tilde{R}]\right). \end{aligned} \tag{5.76}$$

This shows that there are two contributions to H. Firstly, if the reference configuration is at all curved (i.e. $\mathsf{B}(Y)$ is non-zero), then straining of the shell, encoded in $\mathsf{U} - \mathsf{G}$, will result in a change of curvature. The second contribution is due to variation of the rotor R over the shell. These two kinds of change of curvature are illustrated well by an inflating sphere and deformation of a flat plate. As a sphere is inflated to become a larger sphere, the normal vector is unchanged, i.e. $e_3 = E_3$, hence $R = 1$ everywhere. This means that the second term in our expression for H will be zero. However, the surface of the sphere will stretch, meaning that $\mathsf{U} - \mathsf{G}$ will be non-zero. In addition, B will be non-zero for a sphere, which tells us that the first term in our expression for H will be non-zero. By contrast, for a flat plate $\mathsf{B}(Y)$ will be zero, meaning that R must vary over the plate in order for there to be

any change of curvature.

A variant on this expression for H can be obtained if we express the rotor R as $R = \exp(-B/2)$. We can express $Y \cdot \partial R$ as,

$$Y \cdot \partial R = -\frac{Y \cdot \partial B}{2} \exp(-B/2) = -\frac{Y \cdot \partial B}{2} R. \tag{5.77}$$

Using this we can express H as,

$$\mathsf{H}(Y) = (\mathsf{U} - \mathsf{G})\mathsf{B}(Y) - \bar{\mathsf{F}}\left((RE_3\tilde{R}) \times (Y \cdot \partial B)\right). \tag{5.78}$$

The term that $\bar{\mathsf{F}}$ operates on is the commutator product of a vector and bivector, so we can replace the commutator product with a dot product,

$$\mathsf{H}(Y) = (\mathsf{U} - \mathsf{G})\mathsf{B}(Y) - \bar{\mathsf{F}}\left((RE_3\tilde{R}) \cdot (Y \cdot \partial B)\right). \tag{5.79}$$

Taking the inner product of a bivector with $RE_3\tilde{R} = e_3$ means that only vectors tangential to the spatial configuration are retained, which then means that $\bar{\mathsf{F}}$ can operate and return vectors tangential to the reference configuration. Hence our description confirms that the range and domain of H are both the tangent space of the reference configuration.

This representation of H clarifies the different possible contributions to changes of curvature, and shows under what circumstances stretching can result in a change of curvature as well. This is a significant improvement over the coordinate definition provided by [Ciarlet, 2005].

5.3.6 Strain Rate and Spin

Let y be a vector defined on $\mathcal{S}$. We can consider what happens as y is convected with the surface by the motion. If y is tangential to $\mathcal{S}$, then we can write it as $y = \mathsf{F}(Y)$, and the convection of of y is obtained by considering $\mathsf{F}(Y)$ over time, while keeping Y constant. In three-dimensional elasticity this is all that is necessary, but for shells, the situation is complicated if y has a component normal to the shell. We have already shown that e_3 is convected with the surface by rotating it according to $\mathsf{R}(Y) = RY\tilde{R}$, so it is logical to say that to convect a vector y with the surface, when $y \cdot e_3 \neq 0$, the part tangential to the surface is convected as already described, and the part normal to the surface is convected such that

$y \cdot e_3$ remains constant. This corresponds to following $\mathsf{F}(Y)$ over time, while keeping Y constant.

We are interested in the rate of change of y as it is convected. If y is tangential to $\mathcal{S}$, then we can follow the same approach as for three-dimensional elasticity. We take $y = \mathsf{F}(Y)$, and $Y = \partial X/\partial\eta$, for some scalar parameter η. Then we can write,

$$\frac{Dy}{Dt} = \frac{\partial \mathsf{F}(Y)}{\partial t} = \frac{\partial^2 \phi_t(X)}{\partial t \partial \eta} = \frac{\partial}{\partial \eta}\frac{\partial \phi_t(X)}{\partial t} = \mathsf{F}(Y) \cdot \partial v = Y \cdot \partial V. \tag{5.80}$$

where v and V are the **spatial** and **reference velocities** respectively ($V(X) = v(\phi_t(X)) = \partial\phi_t(X)/\partial t$), and D/Dt is the **material derivative**. We can find the rate of change of e_3 with time as it is convected with the surface using $e_3 \cdot e_i = 0$ and the fact that e_3 is of unit length,

$$\frac{De_3}{Dt} = -(e_3 \cdot (e_i \cdot \partial v))e^i = -v_{3|i}e^i. \tag{5.81}$$

This allows us to express the rate of change of a vector y as it is convected with the surface, including the case where y has a component normal to the surface,

$$\frac{Dy}{Dt} = \mathsf{I}(y) = y \cdot \partial v - y^3(e_3 \cdot (e_i \cdot \partial v))e^i = y^i v_{a|i}e^a - y^3 v_{3|i}e^i, \tag{5.82}$$

which defines I, the **rate of deformation tensor**. The adjoint $\bar{\mathsf{I}}$ is given by,

$$\bar{\mathsf{I}}(y) = \dot{\partial}(y \cdot \dot{v}) - y^j(e_3 \cdot (e_j \cdot \partial v))e^3 = y^a v_{a|i}e^i - y^j v_{3|j}e^3. \tag{5.83}$$

The components of I are given by,

$$\mathsf{I}_{ij} = v_{i|j}, \quad \mathsf{I}_{3i} = v_{3|i}, \quad \mathsf{I}_{i3} = -v_{3|i}, \quad \mathsf{I}_{33} = 0. \tag{5.84}$$

It is useful to additively decompose I into symmetric and antisymmetric parts,

$$\mathsf{I}(y) = \tfrac{1}{2}\left(\mathsf{I}(y) + \bar{\mathsf{I}}(y)\right) + \tfrac{1}{2}\left(\mathsf{I}(y) - \bar{\mathsf{I}}(y)\right) = \mathsf{I}^+(y) + \mathsf{I}^-(y), \tag{5.85}$$

where the final equality defines the **symmetric rate of deformation tensor** I^+ ($\bar{\mathsf{I}}^+ = \mathsf{I}^+$) and the **rotation rate tensor** I^- ($\bar{\mathsf{I}}^- = -\mathsf{I}^-$). The components of I^+ and I^- in terms of the

convected frame are,

$$\begin{aligned} 2\mathsf{I}^+_{ij} = 2\mathsf{I}^+_{ji} = v_{i|j} + v_{j|i}, \quad \mathsf{I}^+_{3i} = \mathsf{I}^+_{i3} = \mathsf{I}^+_{33} = 0, \\ 2\mathsf{I}^-_{ij} = -2\mathsf{I}^-_{ji} = v_{i|j} - v_{j|i}, \quad \mathsf{I}^-_{3i} = -\mathsf{I}^-_{i3} = v_{3|i}, \quad \mathsf{I}^-_{33} = 0. \end{aligned} \tag{5.86}$$

As in the three-dimensional case we can express I^- in terms of its characteristic bivector ω,

$$\mathsf{I}^-(y) = y \cdot \omega, \quad \omega = \tfrac{1}{2} e^a \wedge \mathsf{I}^-(e_a). \tag{5.87}$$

The **angular velocity** is a bivector defined such that if y is a vector being convected with the surface, then the rate of change of y, ignoring stretching, is given by $y \cdot$ (bivector), from which it is obvious that ω is the angular velocity. We can relate ω to the rotor R which characterises R. First let $y = \mathsf{R}(Y)$. The rate of change of a vector being convected with the surface, ignoring stretching, is given by $\partial(\mathsf{R}(Y))/\partial t$, with Y held constant. Using the expressions $\mathsf{R}(Y) = RY\tilde{R}$ and $\dot{\tilde{R}} = -\tilde{R}\dot{R}\tilde{R}$, we can write,

$$\begin{aligned} \frac{\partial \mathsf{R}(Y)}{\partial t} &= \dot{R}Y\tilde{R} + RY\dot{\tilde{R}} \\ &= \dot{R}Y\tilde{R} - RY\tilde{R}\dot{R}\tilde{R} \\ &= \dot{R}\tilde{R}RY\tilde{R} - RY\tilde{R}\dot{R}\tilde{R} \\ &= 2(\dot{R}\tilde{R}) \times (RY\tilde{R}) \end{aligned} \tag{5.88}$$

where an overdot is used as shorthand for differentiation with respect to time, and $\times$ is the commutator product. Using $R = \exp(-B/2)$, which implies that $\dot{R} = -(\dot{B}/2)R$, we can write this as,

$$\frac{\partial \mathsf{R}(Y)}{\partial t} = (RY\tilde{R}) \times \dot{B} = (RY\tilde{R}) \cdot \dot{B} = y \cdot \dot{B}. \tag{5.89}$$

From this it is clear that $\omega = \dot{B}$.

The analogies of I, I^+, and I^-, defined on the reference configuration, are given by,

$$\mathsf{L}(Y) = \bar{\mathsf{F}}\mathsf{I}\mathsf{F}(Y), \quad \mathsf{L}^+(Y) = \bar{\mathsf{F}}\mathsf{I}^+\mathsf{F}(Y), \quad \mathsf{L}^-(Y) = \bar{\mathsf{F}}\mathsf{I}^-\mathsf{F}(Y). \tag{5.90}$$

Note the use of the modified deformation gradient, as I and L can take and return arguments normal to the shell. The following component expressions, which rely on the use of convected

coordinates, hold as well,

$$\mathsf{L}_{ab} = \mathsf{I}_{ab}, \quad \mathsf{L}^{+}_{ab} = \mathsf{I}^{+}_{ab}, \quad \mathsf{L}^{-}_{ab} = \mathsf{I}^{-}_{ab}. \tag{5.91}$$

The strain tensor $\mathsf{E}(Y)$ is implicitly a function of time. Hence it is meaningful to define $\dot{\mathsf{E}}(Y) = \partial \mathsf{E}(Y)/\partial t$ where Y is held constant. Equivalently, it also makes sense to define $\dot{\mathsf{e}}(y) = D\mathsf{e}(y)/Dt$, using the material derivative. We can write the components of $\dot{\mathsf{E}}_{ij}$ and $\dot{\mathsf{e}}_{ij}$ as,

$$\begin{aligned} \dot{\mathsf{E}}_{ij} = \dot{\mathsf{e}}_{ij} = \frac{\partial \mathsf{E}_{ij}}{\partial t} = \frac{D\mathsf{e}_{ij}}{Dt} &= \frac{\partial}{\partial t}\left(\tfrac{1}{2}\left(E_i \cdot \bar{\mathsf{F}}\mathsf{F}(E_j) - E_i \cdot E_j\right)\right) \\ &= \frac{1}{2}\frac{\partial}{\partial t}\left(\mathsf{F}(E_i) \cdot \mathsf{F}(E_j)\right) \\ &= \frac{1}{2}\frac{\partial}{\partial t}\left(e_i \cdot e_j\right) \\ &= \mathsf{I}^{+}_{ij} = \mathsf{L}^{+}_{ij}. \end{aligned} \tag{5.92}$$

Hence we can see that,

$$\dot{\mathsf{E}}(Y) = \mathsf{L}^{+}(Y), \quad \dot{\mathsf{e}}(y) = \mathsf{I}^{+}(y). \tag{5.93}$$

The change of curvature tensor H is also an implicit function of time, so we can define $\dot{\mathsf{H}}(Y) = \partial \mathsf{H}(Y)/\partial t$ with Y held constant, and $\dot{\mathsf{h}}(y) = D\mathsf{h}(y)/Dt$. The components $\dot{\mathsf{H}}_{ij}$ and $\dot{\mathsf{h}}_{ij}$ can then be written as,

$$\begin{aligned} \dot{\mathsf{H}}_{ij} = \dot{\mathsf{h}}_{ij} = \frac{\partial \mathsf{H}_{ij}}{\partial t} = \frac{D\mathsf{h}_{ij}}{Dt} = \frac{\partial}{\partial t}(\mathsf{b}_{ij} - \mathsf{B}_{ij}) = \frac{\partial \mathsf{b}_{ij}}{\partial t} &= \frac{\partial}{\partial t}\left(e_3 \cdot \frac{\partial e_j}{\partial x^i}\right) \\ &= \frac{\partial e_3}{\partial t} \cdot \frac{\partial e_j}{\partial x^i} + e_3 \cdot \frac{\partial}{\partial x^i}\frac{\partial e_j}{\partial t} \\ &= \mathsf{I}_{a3}\gamma^a_{ij} + e_3 \cdot \partial_i(\mathsf{I}_{aj}e^a) \\ &= -\mathsf{I}_{3a}\gamma^a_{ij} + \partial_i \mathsf{I}_{3j} - \mathsf{I}_{aj}\gamma^a_{i3} \\ &= \partial_i \mathsf{I}_{3j} - \gamma^k_{ij}\mathsf{I}_{3k} - \gamma^a_{i3}\mathsf{I}_{aj}. \end{aligned} \tag{5.94}$$

Note that we have used the fact that $\mathsf{I}_{3i} = -\mathsf{I}_{i3}$ and $\mathsf{I}_{33} = 0$. This expression is equal to $\mathsf{I}_{3j|i}$, hence we can write,

$$\dot{\mathsf{H}}_{ij} = \dot{\mathsf{h}}_{ij} = \partial_i \mathsf{I}_{3j} - \gamma^k_{ij}\mathsf{I}_{3k} - \gamma^a_{i3}\mathsf{I}_{aj} = \mathsf{I}_{3j|i} = e_3 \cdot (e_i \cdot \dot{\partial}\dot{\mathsf{I}}(e_j)). \tag{5.95}$$

We define the **second order rate of deformation tensor**, on the spatial configuration as

$\mathsf{u}(y)$, and on the reference configuration as $\mathsf{U}(Y)$,

$$\mathsf{u}(y) = e_3 \cdot (e_i \cdot \dot{\partial}\dot{\mathsf{l}}(y))e^i, \quad \mathsf{U}(Y) = \bar{\mathsf{F}}\mathsf{u}\mathsf{F}(Y). \tag{5.96}$$

Using this we can write $\dot{\mathsf{H}}(Y)$ and $\dot{\mathsf{h}}(y)$ as,

$$\dot{\mathsf{H}}(Y) = \mathsf{U}(Y), \quad \dot{\mathsf{h}}(y) = \mathsf{u}(y). \tag{5.97}$$

Note that both U and u are symmetric.

5.3.7 The Rate of Change of the Determinant

Let $f(x)$ be an arbitrary multivector valued function on the spatial configuration $\mathcal{S}$, and let this function be mapped to the reference configuration by $f(X) = f(\phi_t(X))$. Conservation laws generally take the form,

$$\frac{d}{dt}\int_{\phi_t(\mathcal{U})} f \, |dx| = \text{RHS}, \tag{5.98}$$

where the right hand side is prescribed by the conservation law. The aim with expressions like this is to move the time differential inside the integral. In three-dimensional elasticity there are two approaches to this. The integral can be referred back to the reference configuration, in which case the domain of the integral does not change over time, and hence the time derivative can be moved inside the integral as a partial derivative. The other option is to make use of Reynolds' Transport Theorem [Kundu et al., 2012, §3.6], which requires that the time derivative be converted into a material derivative when it is moved inside the integral on the spatial configuration. Unfortunately, Reynolds' Transport Theorem is not valid for two-dimensional shells, so we must take an alternative approach if we wish to obtain conservation laws expressed on the spatial configuration. Our method is refer the integral back to the reference configuration, move the time derivative inside the integral, then refer it back to the spatial configuration. To begin we write,

$$\frac{d}{dt}\int_{\phi_t(\mathcal{U})} f \, |dx| = \int_{\mathcal{U}} \frac{\partial}{\partial t}\left(f \det \mathsf{F}\right)|dX| = \int_{\mathcal{U}} \left(\frac{\partial f}{\partial t} + \frac{f}{\det \mathsf{F}}\frac{\partial \det \mathsf{F}}{\partial t}\right) \det \mathsf{F} \, |dX| \,. \tag{5.99}$$

To refer this back to the spatial configuration we need an expression for $\dot{\det}\,\mathsf{F}/\det \mathsf{F}$.

Firstly we obtain an alternative expression for $\det \mathsf{F}$. To do this we take f to be scalar

valued, but otherwise arbitrary, and start with the well known relation,

$$\int_{\phi_t(\mathcal{U})} f \, |dx| = \int_{\mathcal{U}} f \det \mathsf{F} \, |dX| \, . \tag{5.100}$$

Using the volume forms $\mathfrak{V}$ and $\mathfrak{v}$ we can express the scalar elements $|dX|$ and $|dx|$ as,

$$|dX| = \mathfrak{V} \; dX^1 dX^2, \quad |dx| = \mathfrak{v} \; dx^1 dx^2. \tag{5.101}$$

$\{x^i\}$ are convected coordinates, so the boundaries of integration expressed in terms of the coordinates $\{x^i\}$ and $\{X^i\}$ are identical. Using the fact that $\mathcal{U}$ and f are both arbitrary, we then obtain $\det \mathsf{F} \, \mathfrak{V} = \mathfrak{v}$, which allows us to write $\det \mathsf{F}$ as,

$$\det \mathsf{F} = \frac{\mathfrak{v}}{\mathfrak{V}} = \sqrt{\frac{\det(\mathsf{g}_{ij})}{\det(\mathsf{G}_{ij})}}. \tag{5.102}$$

$\det(\mathsf{G}_{ij})$ is independent of time, so to find the rate of change of $\det \mathsf{F}$ we must find the rate of change of $\det(\mathsf{g}_{ij})$. Using Jacobi's formula for the rate of change of a determinant we obtain,

$$\frac{\partial}{\partial t} \left(\det(\mathsf{g}_{kl}) \right) = \det(\mathsf{g}_{kl}) \mathsf{g}^{ij} \frac{\partial \mathsf{g}_{ji}}{\partial t}. \tag{5.103}$$

We are using convected coordinates so we can write the range of change of the components g_{ij} as,

$$\frac{\partial \mathsf{g}_{ij}}{\partial t} = 2 \mathsf{l}^+_{ij}. \tag{5.104}$$

Using this our expression for the rate of change of $\det(\mathsf{g}_{ij})$ becomes,

$$\frac{\partial}{\partial t} \left(\det(\mathsf{g}_{kl}) \right) = 2 \det(\mathsf{g}_{kl}) (\mathsf{l}^+)^i{}_i = 2 \det(\mathsf{g}_{kl}) \left(v^i{}_{|i} - v_3 \mathsf{b}^i{}_i \right). \tag{5.105}$$

This allows us to write $\dot{\det} \mathsf{F} / \det \mathsf{F}$ as,

$$\begin{aligned} \frac{\dot{\det} \mathsf{F}}{\det \mathsf{F}} &= \frac{1}{2} \frac{1}{\det(\mathsf{g}_{ij})} \frac{\partial}{\partial t} \det(\mathsf{g}_{ij}) \\ &= v^i{}_{|i} - v_3 \mathsf{b}^i{}_i \\ &= \partial \cdot v_{\parallel} - v_3 \operatorname{tr}(\mathsf{b}), \end{aligned} \tag{5.106}$$

where $v_{\parallel}$ is the part of the velocity that lies in the tangent space $T_x \mathcal{S}$. Using this expression

we can refer the result in eq. (5.99) back to the spatial configuration and obtain,

$$\frac{d}{dt}\int_{\phi_t(\mathcal{U})} f\,|dx| = \int_{\phi_t(\mathcal{U})} \frac{Df}{Dt} + f\left(\partial\cdot v_{\|} - v_3\,\mathrm{tr}(\mathsf{b})\right)|dx| \tag{5.107}$$

Note that [Marsden et al., 1994, §1.5] define the second fundamental form with the opposite sign to us, so their result appears slightly different to this, but in fact agrees.

5.4 Stress

In three-dimensional elasticity we considered **body forces** and **surface forces**, however, in shell theory, surface forces must be replaced with **boundary forces**, as they are forces acting around the edge of a region of the shell, and do not act over the surface of the shell. Forces acting over the surface of the shell are described by body forces.

$b(x,t)$ is still the force per unit mass acting acting at a point $x\in\mathcal{S}$, so the total body force acting on the region $\phi_t(\mathcal{U})$ is given by,

$$\int_{\phi_t(\mathcal{U})} \rho b\,|dx|\,, \tag{5.108}$$

where $\rho(x,t)$ is the **density**, though for shells ρ is mass per unit *area*. We can refer this integral back to the reference configuration,

$$\int_{\phi_t(\mathcal{U})} \rho b\,|dx| = \int_{\mathcal{U}} \rho b \det\mathsf{F}\,|dX|\,. \tag{5.109}$$

In shell theory we must also consider **body moments** and **boundary moments**. The second of these will be dealt with when we consider stress. Body moments are represented via $c(x,t)$, the moment per unit mass acting at a point $x\in\mathcal{S}$. The total body moment acting on a region $\phi_t(\mathcal{U})$ is given by,

$$\int_{\phi_t(\mathcal{U})} \rho c\,|dx| = \int_{\mathcal{U}} \rho c \det\mathsf{F}\,|dX|\,. \tag{5.110}$$

c is **bivector** valued. The space of bivectors at $x\in\mathcal{S}$ is spanned by $\{e_A\} = \{e_1\wedge e_2, e_1\wedge e_3, e_2\wedge e_3\}$. We only consider body moments that are due to opposing shear forces acting on the upper and lower surfaces of the real shell, separated by the shell thickness. In this case, the $e_1\wedge e_2$ component of c will be zero, so c may be written $c = c^I e_I$. For convenience

we also define the vector $\boldsymbol{c} = c \cdot e_3$, whose components satisfy $\boldsymbol{c}^1 = c^{(1,3)}$ and $\boldsymbol{c}^2 = c^{(2,3)}$.

To express the boundary force and moment we consider a small portion of the boundary $\partial\phi_t(\mathcal{U})$, which we denote Δs. We define the unit normal n to this so that it points out of the area contained within $\partial\phi_t(\mathcal{U})$, and also lies in the tangent space of the surface $\mathcal{S}$. As with the three-dimensional case the material on the outside of Δs exerts a force Δf on the material on the inside. Δf depends on the size of the boundary element Δs, the location of the boundary element (x), the orientation of the normal n, and time. Note that Δf depends on the position x, and not on the state of the rest of the body in its entirety. This is because boundary forces are defined to be local effects. We cannot use the stress principle of Euler and Cauchy as it appears in three-dimensional elasticity. For shells, it is possible for the material outside of boundary to exert a moment on the material inside. We denote this moment Δm. The stress principal now reads,

> as the length Δs tends to zero, the ratios $\Delta f/\Delta s$ and $\Delta m/\Delta s$ tend to definite limits. Moreover, if two paths passing through a point x have the same normal n, then $\Delta f/\Delta s$ and $\Delta m/\Delta s$ tend to the same value for both of these paths.

The definition of the boundary traction,

$$t_n(x,t) = \lim_{\Delta s \to 0} \frac{\Delta f}{\Delta s}, \tag{5.111}$$

is still valid. t_n is also still linear in n, allowing us to define the **Cauchy stress tensor** for a shell, $\sigma(n) = \sigma(n; x, t) = t_n(x, t)$. Note that while the domain of $\sigma(n)$ is $T_x\mathcal{S}$, the range is the local tangent space of $\mathbb{E}^3$ (which is just $\mathbb{E}^3$), i.e. the normal vector n must lie in the tangent space $T_x\mathcal{S}$, but the force on the shell does not have any such restriction. We can write the force on a portion of the shell due to boundary forces as,

$$\int_{\partial\phi_t(\mathcal{U})} \sigma(n)\, |ds| = \int_{\phi_t(\mathcal{U})} \dot{\sigma}(\dot{\partial})\, |dx|\,. \tag{5.112}$$

We must also take into account the limit of $\Delta m/\Delta s$, the moment per unit length. By considering conservation of angular momentum for small control volumes in a similar way to what is done for t_n, we can show that the moment per unit length is also a linear function

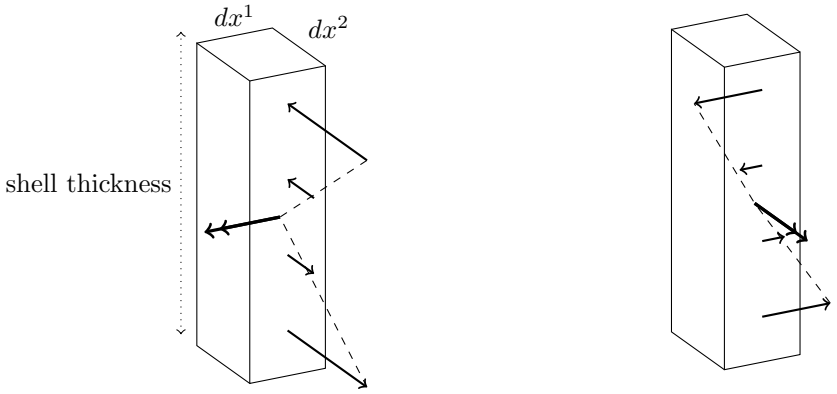


Figure 5.2: The two possible moments due to stresses within the shell acting on a small shell element.

of n. We can therefore define the **spatial couple-stress tensor** to satisfy,

$$\mathsf{m}(n) = \mathsf{m}(n; x, t) = \lim_{\Delta s \to 0} \frac{\Delta m}{\Delta s}. \tag{5.113}$$

The total moment acting on a portion of the body $\phi_t(\mathcal{U})$ due to boundary moments can now be expressed as,

$$\int_{\partial\phi_t(\mathcal{U})} \mathsf{m}(n)\ |ds| = \int_{\phi_t(\mathcal{U})} \dot{\mathsf{m}}(\dot{\partial})\ |dx|\,. \tag{5.114}$$

The domain of m is $T_x\mathcal{S}$, but it is bivector valued, with its range spanned by the bivector frame $\{e_A\}$. However, we can restrict the range by considering the origin of the moments represented by m. In three dimensional elasticity, there is no couple stress tensor because as an element of the material is allowed to become infinitesimal, moments acting on the element due to the stresses tend to zero due to the surfaces of the element becoming infinitely small. In shell theory, this is no longer the case. An element of the shell is a surface element, meaning that as we allow the element to become infinitesimal, the thickness of the physical shell being represented remains finite. Consequently the stresses within the shell can exert a moment on the material element even when the element is small. Stress distributions that give rise to no resultant force but non-zero moment are illustrated in fig. 5.2. We can see that while the moment need not be zero, it is restricted. Specifically, the $e_1 \wedge e_2$ component ($\mathsf{m}^{(1,2)i}$) will be zero, so the range of m is actually spanned by $\{e_I\}$, rather than $\{e_A\}$.

To obtain stresses and couple-stresses on the reference configuration we follow the same approach as in three-dimensional elasticity. First let Y be a line element on the reference

configuration. The normal to this line element is given by $N = YI^{-1}$, and Y will be transformed to $\mathsf{F}(Y)$ under the motion ϕ_t. Therefore N will be transformed to $n = \mathsf{F}(Y)i^{-1}$. We can express this using the identity,

$$A_r \cdot \bar{\mathsf{F}}(B_s) = \bar{\mathsf{F}}(\mathsf{F}(A_r) \cdot B_s), \quad r \leqslant s, \tag{5.115}$$

in order to write n as,

$$\begin{aligned} n &= \mathsf{F}(Y) \cdot i^{-1} \\ &= \bar{\mathsf{F}}^{-1}\bar{\mathsf{F}}(\mathsf{F}(Y) \cdot i^{-1}) \\ &= \bar{\mathsf{F}}^{-1}(Y \cdot \bar{\mathsf{F}}(i^{-1})) \\ &= \det \mathsf{F}\bar{\mathsf{F}}^{-1}(Y \cdot I^{-1}) = \det \mathsf{F}\bar{\mathsf{F}}^{-1}(N). \end{aligned} \tag{5.116}$$

Therefore, given σ, we can construct the **first Piola-Kirchhoff stress tensor** T for a shell,

$$\mathsf{T}(N) = \det \mathsf{F}\sigma\bar{\mathsf{F}}^{-1}(N), \tag{5.117}$$

and given m, we can construct the **first reference couple-stress tensor** M,

$$\mathsf{M}(N) = \det \mathsf{F}\ \mathsf{m}\bar{\mathsf{F}}^{-1}(N). \tag{5.118}$$

Using these we can write the force due to boundary forces and moment due to boundary moments acting on a portion of the shell $\mathcal{U}$ as,

$$\int_{\partial\mathcal{U}} \mathsf{T}(N)\ |dS| = \int_{\mathcal{U}} \dot{\mathsf{T}}(\dot{\partial})\ |dX|\,, \quad \int_{\partial\mathcal{U}} \mathsf{M}(N)\ |dS| = \int_{\mathcal{U}} \dot{\mathsf{M}}(\dot{\partial})\ |dX|\,. \tag{5.119}$$

The **second Piola-Kirchhoff stress tensor** , and its analogous couple stress tensor, the **second reference couple-stress tensor** , are more difficult to define in shell theory. In three-dimensional elasticity F^{-1} is used to bring the stresses, which lie in $T_x\mathcal{S}$, back into $T_X\mathcal{B}$, but in shell theory, the stress and couple-stress do not necessarily lie completely within $T_x\mathcal{S}$. Therefore, F^{-1} will remove the part of the stress normal to the shell. To avoid this we use a **modified deformation gradient** ,

$$\mathsf{S}(Y) = \mathbf{F}^{-1}\mathsf{T}(Y), \quad \mathsf{N}(Y) = \mathbf{F}^{-1}\mathsf{M}(Y). \tag{5.120}$$

The fact that the range of M is spanned by $\{e_I\}$ means that the range of N is spanned by $\{E_I\}$.

m, M, and N are all bivector valued functions. It is convenient to also construct related vector valued functions, which we call the **modified spatial couple-stress tensor** ($\mathbf{m}$), and the **modified first and second reference couple-stress tensors** ($\mathbf{M}$ and $\mathbf{N}$). These are given by,

$$\mathbf{m}(y) = \mathsf{m}(y) \cdot e_3, \quad \mathbf{M}(Y) = \mathsf{M}(Y) \cdot e_3, \quad \mathbf{N}(Y) = \mathsf{N}(Y) \cdot E_3. \tag{5.121}$$

The ranges and domains of the functions defined in this section are shown below in terms of the frames that span them. The component versions of these functions are also defined,

	domain	$\mapsto$	range	components
σ:	$\{e_i\}$	$\mapsto$	$\{e_a\}$	$\sigma^{ai} = e^a \cdot \sigma(e^i)$
T:	$\{E_i\}$	$\mapsto$	$\{e_a\}$	$\mathsf{T}^{ai} = e^a \cdot \mathsf{T}(E^i)$
S:	$\{E_i\}$	$\mapsto$	$\{E_a\}$	$\mathsf{S}^{ai} = E^a \cdot \mathsf{S}(E^i)$
m:	$\{e_i\}$	$\mapsto$	$\{e_I\}$	$\mathsf{m}^{Ii} = e^I \cdot \mathsf{m}(e^i)$
M:	$\{E_i\}$	$\mapsto$	$\{e_I\}$	$\mathsf{M}^{Ii} = e^I \cdot \mathsf{M}(E^i)$
N:	$\{E_i\}$	$\mapsto$	$\{E_I\}$	$\mathsf{N}^{Ii} = E^I \cdot \mathsf{N}(E^i)$
$\mathbf{m}$:	$\{e_i\}$	$\mapsto$	$\{e_i\}$	$\mathbf{m}^{ij} = e^i \cdot \mathbf{m}(e^j)$
$\mathbf{M}$:	$\{E_i\}$	$\mapsto$	$\{e_i\}$	$\mathbf{M}^{ij} = e^i \cdot \mathbf{M}(E^j)$
$\mathbf{N}$:	$\{E_i\}$	$\mapsto$	$\{E_i\}$	$\mathbf{N}^{ij} = E^i \cdot \mathbf{N}(E^j)$

Recalling that we are using convected coordinates, the following component relationships hold,

$$\begin{aligned} \mathsf{T}^{ai} &= \mathsf{S}^{ai}, \\ \mathsf{M}^{(1,3)i} &= \mathsf{N}^{(1,3)i} = \mathbf{M}^{1i} = \mathbf{N}^{1i}, \\ \mathsf{M}^{(2,3)i} &= \mathsf{N}^{(2,3)i} = \mathbf{M}^{2i} = \mathbf{N}^{2i}. \end{aligned} \tag{5.122}$$

5.5 Conservation Laws

We present each of the conservation laws in integral and local forms on both the spatial and reference configurations. Where necessary we include additional definitions, and for conservation of angular momentum and energy, we provide further explanation of the laws

and their consequences.

5.5.1 Mass

$$\frac{d}{dt}\int_{\phi_t(\mathcal{U})} \rho \, |dx| = 0, \tag{5.123}$$

$$\frac{d}{dt}\int_{\mathcal{U}} \rho \det \mathsf{F} \, |dX| = 0, \tag{5.124}$$

$$\frac{D\rho}{Dt} + \rho\left(\partial \cdot v_{\|} - v_3 \operatorname{tr}(\mathsf{b})\right) = 0, \tag{5.125}$$

$$\frac{\partial}{\partial t}\left(\rho \det \mathsf{F}\right) = 0. \tag{5.126}$$

We define the time invariant density ρ_0 as,

$$\rho_0 = \rho \det \mathsf{F}. \tag{5.127}$$

5.5.2 Momentum

$$\frac{d}{dt}\int_{\phi_t(\mathcal{U})} \rho v \, |dx| = \int_{\partial\phi_t(\mathcal{U})} \sigma(n) \, |ds| + \int_{\phi_t(\mathcal{U})} \rho b \, |dx| \,, \tag{5.128}$$

$$\frac{d}{dt}\int_{\mathcal{U}} \rho_0 V \, |dX| = \int_{\partial\mathcal{U}} \mathsf{T}(N) \, |dS| + \int_{\mathcal{U}} \rho_0 b \, |dX| \,, \tag{5.129}$$

$$\rho\frac{Dv}{Dt} = \dot{\sigma}(\dot{\partial}) + \rho b, \tag{5.130}$$

$$\rho_0\frac{\partial V}{\partial t} = \dot{\mathsf{T}}(\dot{\partial}) + \rho_0 b. \tag{5.131}$$

5.5.3 Angular Momentum

$$\frac{d}{dt}\int_{\phi_t(\mathcal{U})} \rho x \wedge v \, |dx| = \int_{\partial\phi_t(\mathcal{U})} x \wedge \sigma(n) + \mathsf{m}(n) \, |ds| + \int_{\phi_t(\mathcal{U})} \rho x \wedge b + \rho c \, |dx| \,, \tag{5.132}$$

$$\begin{aligned}\frac{d}{dt}\int_{\mathcal{U}} \rho_0 \phi_t(X) \wedge V \, |dX| = \int_{\partial\mathcal{U}} \phi_t(X) \wedge \mathsf{T}(N) + \mathsf{M}(N) \, |dS| + \\ \int_{\mathcal{U}} \rho_0 \phi_t(X) \wedge b + \rho_0 c \, |dX| \,,\end{aligned} \tag{5.133}$$

$$\dot{x} \wedge \sigma(\dot{\partial}) + \dot{\mathsf{m}}(\dot{\partial}) + \rho c = 0, \tag{5.134}$$

$$\dot{\phi_t}(X) \wedge \mathsf{T}(\dot{\partial}) + \dot{\mathsf{M}}(\dot{\partial}) + \rho_0 c = 0. \tag{5.135}$$

These expressions have consequences that require further investigation. We will consider the two configurations separately.

Spatial Configuration

We can express $\dot{x} \wedge \sigma(\dot{\partial})$ as,

$$\dot{x} \wedge \sigma(\dot{\partial}) = e_i \wedge \sigma(e^i) = \sigma^{ai} e_i \wedge e_a, \tag{5.136}$$

and we can express $\dot{\mathsf{m}}(\dot{\partial})$ as,

$$\begin{aligned} \dot{\mathsf{m}}(\dot{\partial}) &= \left(\partial_i(\mathsf{m}^{Ai}) + \gamma^A_{iB}\mathsf{m}^{Bi} + \gamma^i_{ik}\mathsf{m}^{Ak}\right) e_A \\ &= \left(\partial_i(\mathsf{m}^{Ii}) + \gamma^I_{iJ}\mathsf{m}^{Ji} + \gamma^i_{ik}\mathsf{m}^{Ik}\right) e_I + \mathsf{m}^{Ii}\gamma^{(1,2)}_{iI} e_1 \wedge e_2 \\ &= \mathsf{m}^{Ii}{}_{|i} e_I + \mathsf{m}^{Ii}\gamma^{(1,2)}_{iI} e_{(1,2)}, \end{aligned} \tag{5.137}$$

where we have used the fact that $\mathsf{m}^{(1,2)i} = 0$, and the final equality defines $\mathsf{m}^{Ii}{}_{|i}$. This allows us to write the local form of conservation of angular momentum as,

$$\sigma^{ai} e_i \wedge e_a + \mathsf{m}^{Ii}{}_{|i} e_I + \mathsf{m}^{Ii}\gamma^{(1,2)}_{iI} e_{(1,2)} + \rho c^I e_I = 0. \tag{5.138}$$

We can write the three bivector components of this expression separately,

$$\begin{aligned} e_1 \wedge e_3 \text{ component}: &\quad \sigma^{31} + \mathsf{m}^{(1,3)i}{}_{|i} + \rho c^{(1,3)} = 0, \\ e_2 \wedge e_3 \text{ component}: &\quad \sigma^{32} + \mathsf{m}^{(2,3)i}{}_{|i} + \rho c^{(2,3)} = 0, \\ e_1 \wedge e_2 \text{ component}: &\quad \sigma^{21} - \sigma^{12} + \mathsf{m}^{Ii}\gamma^{(1,2)}_{iI} = 0. \end{aligned} \tag{5.139}$$

These three component expressions are in many ways the key to shell theory. The first two tell us that if m, ρ, and c are known, then σ^{3i} are known. σ^{3i} gives the stress acting normal to the shell, and so we see that the stress normal to the shell is not independent of the other dynamic properties. The ultimate consequence of this is that no constitutive law is needed for these stress components. Instead, constitutive laws will be provided for σ^{ij}, the components of stress within the plane of the shell, and for m. The $e_1 \wedge e_2$ component gives us a symmetry relationship, but not one as simple as in three-dimensional elasticity. To express this we will make use of the previously derived results for γ^A_{iB} and $\mathbf{m}$. Using these we can

write the $e_1 \wedge e_2$ component of conservation of angular momentum as,

$$\sigma^{21} - \sigma^{12} + \mathbf{m}^{2i}\mathsf{b}^1{}_i - \mathbf{m}^{1i}\mathsf{b}^2{}_i = 0. \tag{5.140}$$

We now define the **modified Cauchy stress** $\tilde{\sigma}$ as,

$$\begin{aligned} \tilde{\sigma}(y) &= \sigma(y) - \mathsf{b}\bar{\mathbf{m}}(y), \\ \tilde{\sigma}^{ij} = \sigma^{ij} - \mathsf{b}^i{}_k\bar{\mathbf{m}}^{kj} &= \sigma^{ij} - \mathsf{b}^i{}_k\mathbf{m}^{jk}, \quad \tilde{\sigma}^{3i} = \sigma^{3i}. \end{aligned} \tag{5.141}$$

This allows us to write the $e_1 \wedge e_2$ component of conservation of angular momentum as,

$$\tilde{\sigma}^{21} - \tilde{\sigma}^{12} = 0, \tag{5.142}$$

i.e. conservation of angular momentum implies that the modified Cauchy stress $\tilde{\sigma}$ is symmetric within the plane of the shell.

Reference Configuration

We can express $\dot{\phi_t(X)} \wedge \mathsf{T}(\dot{\partial})$ as,

$$\dot{\phi_t(X)} \wedge \mathsf{T}(\dot{\partial}) = (E_i \cdot \partial\phi_t(X)) \wedge \mathsf{T}(E^i) = \mathsf{F}(E_i) \wedge \mathsf{T}(E^i) = \mathsf{F}(E_i) \wedge \mathbf{F}\mathsf{S}(E^i) = \mathsf{S}^{ai} e_i \wedge e_a, \tag{5.143}$$

and we can express $\dot{\mathsf{M}}(\dot{\partial})$ as,

$$\begin{aligned} \dot{\mathsf{M}}(\dot{\partial}) &= \left(\partial_i(\mathsf{M}^{Ai}) + \gamma^A_{iB}\mathsf{M}^{Bi} + \Gamma^i_{ik}\mathsf{M}^{Ak}\right) e_A \\ &= \left(\partial_i(\mathsf{M}^{Ii}) + \gamma^I_{iJ}\mathsf{M}^{Ji} + \Gamma^i_{ik}\mathsf{M}^{Ik}\right) e_I + \mathsf{M}^{Ii}\gamma^{(1,2)}_{iI} e_1 \wedge e_2 \\ &= \mathsf{M}^{Ii}{}_{|i} e_I + \mathsf{M}^{Ii}\gamma^{(1,2)}_{iI} e_{(1,2)}, \end{aligned} \tag{5.144}$$

where we have used the fact that $\mathsf{M}^{(1,2)i} = 0$, and the final equality defines $\mathsf{M}^{Ii}{}_{|i}$. This allows us to write the local form of conservation of angular momentum as,

$$\mathsf{S}^{ai} e_i \wedge e_a + \mathsf{M}^{Ii}{}_{|i} e_I + \mathsf{M}^{Ii}\gamma^{(1,2)}_{iI} e_{(1,2)} + \rho c^I e_I = 0. \tag{5.145}$$

We can write the three bivector components of this expression separately,

$$\begin{aligned} e_1 \wedge e_3 \text{ component}: &\quad \mathsf{S}^{31} + \mathsf{M}^{(1,3)i}{}_{|i} + \rho c^{(1,3)} = 0, \\ e_2 \wedge e_3 \text{ component}: &\quad \mathsf{S}^{32} + \mathsf{M}^{(2,3)i}{}_{|i} + \rho c^{(2,3)} = 0, \\ e_1 \wedge e_2 \text{ component}: &\quad \mathsf{S}^{21} - \mathsf{S}^{12} + \mathsf{M}^{Ii}\gamma^{(1,2)}_{iI} = 0. \end{aligned} \tag{5.146}$$

This can be interpreted in the same manner as the component expressions for conservation of angular momentum on the spatial configuration, except that now stresses normal to the shell are encoded in S^{3i} and the symmetry relationship is slightly altered. We can write the $e_1 \wedge e_2$ component as,

$$\mathsf{S}^{21} - \mathsf{S}^{12} + \mathbf{N}^{2i}\mathsf{b}^1{}_i - \mathbf{N}^{1i}\mathsf{b}^2{}_i = 0. \tag{5.147}$$

Hence if we define the **modified second Piola-Kirchhoff stress tensor** as,

$$\begin{gathered} \tilde{\mathsf{S}}(Y) = \mathsf{S}(Y) - \mathsf{F}^{-1}\mathsf{b}\mathsf{F}\bar{\mathbf{N}}(Y), \\ \tilde{\mathsf{S}}^{ij} = \mathsf{S}^{ij} - \mathsf{b}^i{}_k\bar{\mathbf{N}}^{kj} = \mathsf{S}^{ij} - \mathsf{b}^i{}_k\mathbf{N}^{jk}, \quad \tilde{\mathsf{S}}^{3i} = \mathsf{S}^{3i}, \end{gathered} \tag{5.148}$$

then the $e_1 \wedge e_2$ component of conservation of angular momentum implies that,

$$\tilde{\mathsf{S}}^{21} - \tilde{\mathsf{S}}^{12} = 0, \tag{5.149}$$

i.e. that the modified second Piola-Kirchhoff stress tensor $\tilde{\mathsf{S}}$ is symmetric within the plane of the shell.

5.5.4 Energy

u: internal energy per unit mass defined over the spatial configuration

U: internal energy per unit mass defined over the reference configuration

$\dot{q}$: heat addition per unit mass per unit time from external sources, defined on the spatial configuration

$\mathfrak{q}$: heat flux per unit length defined on the spatial configuration

$\dot{Q}$: heat addition per unit mass per unit time from external sources, defined on the reference configuration

$\mathfrak{Q}$: heat flux per unit length defined on the spatial configuration

ω: angular velocity defined on the spatial configuration

Ω: angular velocity defined on the reference configuration

These defined quantities are related by,

$$\begin{aligned} U(X,t) = u(\phi_t(X),t), \quad \dot{Q}(X,t) = \dot{q}(\phi_t(X),t), \\ \mathfrak{Q} = \det \mathsf{F}\mathsf{F}^{-1}(\mathfrak{q}), \quad \Omega(X,t) = \omega(\phi_t(X),t). \end{aligned} \tag{5.150}$$

Using these definitions we can write conservation of energy as,

$$\begin{aligned} \frac{d}{dt}\int_{\phi_t(\mathcal{U})} \rho\left(u+\frac{v^2}{2}\right)|dx| = \int_{\partial\phi_t(\mathcal{U})} v\cdot\sigma(n) - \omega\cdot\mathsf{m}(n) - \mathfrak{q}\cdot n \,|ds| \\ + \int_{\phi_t(\mathcal{U})} \rho v\cdot b - \rho\omega\cdot c + \rho\dot{q}\,|dx|\,, \end{aligned} \tag{5.151}$$

$$\begin{aligned} \frac{d}{dt}\int_{\mathcal{U}} \rho_0\left(U+\frac{V^2}{2}\right)|dX| = \int_{\partial\mathcal{U}} V\cdot\mathsf{T}(N) - \Omega\cdot\mathsf{M}(N) - \mathfrak{Q}\cdot N \,|dS| \\ + \int_{\mathcal{U}} \rho_0 V\cdot b - \rho_0\Omega\cdot c + \rho_0\dot{Q}\,|dX|\,. \end{aligned} \tag{5.152}$$

$$\rho\frac{Du}{Dt} = \mathrm{tr}(\tilde{\sigma}\mathsf{l}^+) + \mathrm{tr}(\mathbf{m}\mathsf{u}) + \rho\dot{q} - \partial\cdot\mathfrak{q}, \tag{5.153}$$

$$\rho_0\frac{\partial U}{\partial t} = \mathrm{tr}(\tilde{\mathsf{S}}\mathsf{L}^+) + \mathrm{tr}(\mathbf{N}\mathsf{U}) + \rho\dot{Q} - \partial\cdot\mathfrak{Q}. \tag{5.154}$$

The negative sign in front of the inner products between angular velocity and torques is explained in §A. The derivation of the two local expressions is given below.

Spatial Configuration

Making use of conservation of mass and momentum, conservation of energy can be expressed locally on the spatial configuration as,

$$\rho\frac{Du}{Dt} = \dot{v}\cdot\sigma(\dot{\partial}) - \dot{\omega}\cdot\mathsf{m}(\dot{\partial}) - \omega\cdot\dot{\mathsf{m}}(\dot{\partial}) - \rho\omega\cdot c + \rho\dot{q} - \partial\cdot\mathfrak{q}. \tag{5.155}$$

Taking the inner product of the conservation of angular momentum equation with ω we obtain,

$$\begin{aligned}
(\dot{\mathsf{m}}(\dot{\partial}) + \rho c)\cdot\omega &= -(e_i\wedge\sigma(e^i))\cdot\omega \\
&= (\sigma(e^i)\wedge e_i)\cdot\omega \\
&= \sigma(e^i)\cdot(e_i\cdot\omega) \\
&= \sigma(e^i)\cdot\Big(-(\omega_{(1,3)}\delta^1_i + \Omega_{(2,3)}\delta^2_i)e^3 + \omega_{(1,2)}\delta^2_i e^1 - \Omega_{(1,2)}\delta^1_i e^2)\Big) \\
&= -\sigma^{3i}(\omega_{(1,3)}\delta^1_i + \omega_{(2,3)}\delta^2_i) + \sigma^{1i}\omega_{(1,2)}\delta^2_i - \sigma^{2i}\omega_{(1,2)}\delta^1_i \\
&= -\sigma^{31}\omega_{(1,3)} - \sigma^{32}\omega_{(2,3)} - (\sigma^{21} - \sigma^{12})\omega_{(1,2)}.
\end{aligned} \tag{5.156}$$

Furthermore, we can write $\dot{\omega}\cdot\mathsf{m}(\dot{\partial}) = \omega_{I|i}\mathsf{m}^{Ii}$, where $\omega_{I|i}$ is given by,

$$\begin{aligned}
\omega_{I|i} &= \frac{\partial\omega_I}{\partial x^i} - \omega_A\gamma^A_{iI} \\
&= \frac{\partial\omega_I}{\partial x^i} - \omega_J\gamma^J_{iI} - \omega_{(1,2)}\gamma^{(1,2)}_{iI}
\end{aligned} \tag{5.157}$$

If we use the substitutions $\omega_{(1,3)} = -v_{3|1}$, $\omega_{(2,3)} = -v_{3|2}$, $\omega_{(1,2)} = \omega_3$, $\mathsf{m}^{(1,3)i} = \mathbf{m}^{1i}$, $\mathsf{m}^{(2,3)i} =$

$\mathbf{m}^{2i}$, we can write $\rho\omega\cdot c+\omega\cdot\dot{\mathsf{m}}(\dot{\partial})+\dot{\omega}\cdot\mathsf{m}(\dot{\partial})$ as,

$$\begin{aligned}\rho\omega\cdot c+\omega\cdot\dot{\mathsf{m}}(\dot{\partial})+\dot{\omega}\cdot\mathsf{m}(\dot{\partial}) &= -\sigma^{31}\omega_{(1,3)}-\sigma^{32}\omega_{(2,3)}-(\sigma^{21}-\sigma^{12})\omega_{(1,2)}\\ &\quad+\left(\frac{\partial\omega_I}{\partial x^i}-\omega_J\gamma^J_{iI}-\omega_{(1,2)}\gamma^{(1,2)}_{iI}\right)\mathsf{m}^{Ii}\\ &=\sigma^{31}v_{3|1}+\sigma^{32}v_{3|2}-(\sigma^{21}-\sigma^{12})\omega_3+\left(\frac{\partial\omega_I}{\partial x^i}-\omega_J\gamma^J_{iI}\right)\mathsf{m}^{Ii}\\ &\quad-\omega_3\left(\gamma^{(1,2)}_{i(1,3)}\mathsf{m}^{(1,3)i}+\gamma^{(1,2)}_{i(2,3)}\mathsf{m}^{(2,3)i}\right)\\ &=\sigma^{3i}v_{3|i}-\left(\frac{\partial v_{3|i}}{\partial x^j}-v_{3|k}\gamma^k_{ji}\right)\mathbf{m}^{ij}\\ &\quad-\omega_3\left(\sigma^{21}-\sigma^{12}-\mathsf{b}^2{}_i\mathbf{m}^{1i}+\mathsf{b}^1{}_i\mathbf{m}^{2i}\right)\\ &=\sigma^{3i}v_{3|i}-\left(\frac{\partial v_{3|i}}{\partial x^j}-v_{3|k}\gamma^k_{ji}\right)\mathbf{m}^{ij},\end{aligned}\tag{5.158}$$

where the final equality makes use of the $e_1\wedge e_2$ component of conservation of angular momentum. We can make further progress by writing,

$$\begin{aligned}\rho\omega\cdot c+\omega\cdot\dot{\mathsf{m}}(\dot{\partial})+\dot{\omega}\cdot\mathsf{m}(\dot{\partial}) &= \sigma^{3i}v_{3|i}-\left(\frac{\partial v_{3|i}}{\partial x^j}-v_{3|k}\gamma^k_{ji}+v_{k|i}\mathsf{b}^k{}_j\right)\mathbf{m}^{ij}\\ &\quad+v_{k|i}\mathsf{b}^k{}_j\mathbf{m}^{ij}\\ &=\sigma^{3i}v_{3|i}-\mathsf{l}_{3i|j}\mathbf{m}^{ij}+v_{k|i}\mathsf{b}^k{}_j\mathbf{m}^{ij}.\end{aligned}\tag{5.159}$$

We can also write $\dot{v}\cdot\sigma(\dot{\partial})$ as,

$$\dot{v}\cdot\sigma(\dot{\partial})=v_{a|i}\sigma^{ai}.\tag{5.160}$$

Now we are in a position to write conservation of energy as,

$$\begin{aligned}\rho\frac{Du}{Dt} &= v_{a|i}\sigma^{ai}-\sigma^{3i}v_{3|i}+\mathsf{l}_{3i|j}\mathbf{m}^{ij}-v_{k|i}\mathsf{b}^k{}_j\mathbf{m}^{ij}+\rho\dot{q}-\partial\cdot\mathsf{q}\\ &=\sigma^{ij}v_{i|j}+\mathsf{l}_{3i|j}\mathbf{m}^{ij}-v_{k|i}\mathsf{b}^k{}_j\mathbf{m}^{ij}+\rho\dot{q}-\partial\cdot\mathsf{q}\\ &=(\sigma^{ij}-\mathsf{b}^i{}_k\mathbf{m}^{jk})v_{i|j}+\mathsf{l}_{3i|j}\mathbf{m}^{ij}+\rho\dot{q}-\partial\cdot\mathsf{q}.\end{aligned}\tag{5.161}$$

We recognise the term $(\sigma^{ij}-\mathsf{b}^i{}_k\mathbf{m}^{jk})$ as the modified stress $\tilde{\sigma}^{ij}$, which we have shown is symmetric. We can also use u, which was defined when considering strain rates. Recalling

that $\tilde{\sigma}$, l^+, and u are symmetric, this allows us to write conservation of energy as,

$$\begin{aligned}\rho\frac{Du}{Dt} &= \tilde{\sigma}^{ij}\mathsf{l}^+_{ij} + \mathbf{m}^{ij}\mathsf{u}_{ij} + \rho\dot{q} - \partial\cdot\mathfrak{q} \\ &= \mathrm{tr}(\tilde{\sigma}\mathsf{l}^+) + \mathrm{tr}(\mathbf{m}\mathsf{u}) + \rho\dot{q} - \partial\cdot\mathfrak{q}.\end{aligned} \tag{5.162}$$

Reference Configuration

Making use of conservation of mass and momentum, conservation of energy can be expressed in local form on the reference configuration as,

$$\rho_0\frac{\partial U}{\partial t} = \dot{V}\cdot\mathsf{T}(\dot{\partial}) - \dot{\Omega}\cdot\mathsf{M}(\dot{\partial}) - \Omega\cdot\dot{\mathsf{M}}(\dot{\partial}) - \rho_0\Omega\cdot c + \rho\dot{Q} - \partial\cdot\mathfrak{Q}. \tag{5.163}$$

Making use of conservation of angular momentum we obtain,

$$\rho_0\frac{\partial U}{\partial t} = \dot{V}\cdot\mathsf{T}(\dot{\partial}) - \dot{\Omega}\cdot\mathsf{M}(\dot{\partial}) + \Omega\cdot(\dot{\phi_t(X)}\wedge\mathsf{T}(\dot{\partial})) + \rho\dot{Q} - \partial\cdot\mathfrak{Q}. \tag{5.164}$$

S is related to T by $\mathsf{T}(Y) = \mathbf{F}\mathsf{S}(Y)$, so we can write conservation of energy as,

$$\rho_0\frac{\partial U}{\partial t} = \dot{V}\cdot\mathbf{F}\mathsf{S}(\dot{\partial}) - \dot{\Omega}\cdot\mathsf{M}(\dot{\partial}) + \Omega\cdot(\mathsf{F}(E_i)\wedge\mathbf{F}\mathsf{S}(E^i)) + \rho\dot{Q} - \partial\cdot\mathfrak{Q}. \tag{5.165}$$

The first term on the right hand side in this expression can be expressed as,

$$(E_i\cdot\partial V)\cdot\mathbf{F}\mathsf{S}(E^i) = (E_i\cdot\partial V)\cdot\mathbf{F}(E_a)\mathsf{S}^{ai} = (\mathsf{F}(E_i)\cdot\partial v)\cdot\mathsf{F}(E_a)\mathsf{S}^{ai} = v_{a|i}\mathsf{S}^{ai}. \tag{5.166}$$

We can write $\Omega\cdot(\mathsf{F}(E_i)\wedge\mathbf{F}\mathsf{S}(E^i)) - \dot{\Omega}\cdot\mathsf{M}(\dot{\partial})$ as,

$$\begin{aligned}\Omega\cdot(\mathsf{F}(E_i)\wedge\mathbf{F}\mathsf{S}(E^i)) - \dot{\Omega}\cdot\mathsf{M}(\dot{\partial}) &= \omega_A e^A\cdot(e_i\wedge e_a)\mathsf{S}^{ai} - (e_i\cdot\partial\omega)\cdot e_I\mathsf{M}^{Ii} \\ &= \omega_i\mathsf{S}^{3i} + \omega_3(\mathsf{S}^{21} - \mathsf{S}^{12}) \\ &\quad - \left(\frac{\partial\omega_I}{\partial x^i} - \omega_J\gamma^J_{iI} - \omega_{(1,2)}\gamma^{(1,2)}_{iI}\right)\mathsf{M}^{Ii} \\ &= \omega_i\mathsf{S}^{3i} + \omega_3\left(\mathsf{S}^{21} - \mathsf{S}^{12} + \mathsf{M}^{(2,3)i}\mathsf{b}^1{}_i - \mathsf{M}^{(1,3)i}\mathsf{b}^2{}_i\right) \\ &\quad - \left(\frac{\partial\omega_I}{\partial x^i} - \omega_J\gamma^J_{iI}\right)\mathsf{M}^{Ii} \\ &= \omega_i\mathsf{S}^{3i} - \left(\frac{\partial\omega_I}{\partial x^i} - \omega_J\gamma^J_{iI}\right)\mathsf{M}^{Ii},\end{aligned} \tag{5.167}$$

where, for convenience, we have defined $\omega_1 = \omega_{(1,3)}$, $\omega_2 = \omega_{(2,3)}$, and $\omega_3 = \omega_{(1,2)}$. We recall that the first two components are given by,

$$\omega_{(1,3)} = v_{3|1}, \quad \omega_{(2,3)} = v_{3|2}. \tag{5.168}$$

Using these expressions for the components of ω we obtain,

$$\begin{aligned} \Omega \cdot (\mathsf{F}(E_i) \wedge \mathbf{F}\mathsf{S}(E^i)) - \dot{\Omega} \cdot \mathsf{M}(\dot{\partial}) &= -v_{3|i}\mathsf{s}^{3i} + \left(\frac{\partial v_{3|i}}{\partial x^j} - v_{3|k}\gamma^k_{ji} + v_{k|i}\mathsf{b}^k{}_j \right) \mathbf{M}^{ij} \\ &\quad - v_{k|i}\mathsf{b}^k{}_j \mathbf{M}^{ij} \\ &= -v_{3|i}\mathsf{S}^{3i} + \mathsf{l}_{3i|j}\mathbf{M}^{ij} - v_{k|i}\mathsf{b}^k{}_j \mathbf{M}^{ij}. \end{aligned} \tag{5.169}$$

Using this we can express conservation of energy as,

$$\begin{aligned} \rho_0 \frac{\partial U}{\partial t} &= \mathsf{S}^{ai} v_{a|i} - \mathsf{S}^{3i} v_{3|i} + \mathbf{M}^{ij}\mathsf{l}_{3i|j} - v_{k|i}\mathsf{b}^k{}_j \mathbf{M}^{ij} + \rho\dot{Q} - \partial \cdot \mathfrak{Q} \\ &= \mathsf{S}^{ij} v_{i|j} - \mathsf{b}^i{}_k \mathbf{M}^{jk} v_{i|j} + \mathbf{M}^{ij}\mathsf{l}_{3i|j} + \rho\dot{Q} - \partial \cdot \mathfrak{Q} \\ &= (\mathsf{S}^{ij} - \mathsf{b}^i{}_k \mathbf{N}^{jk}) v_{i|j} + \mathbf{N}^{ij}\mathsf{l}_{3i|j} + \rho\dot{Q} - \partial \cdot \mathfrak{Q}. \end{aligned} \tag{5.170}$$

We recognise the term in the brackets as the modified Piola-Kirchhoff stress tensor $\tilde{\mathsf{S}}$. Recalling that $\tilde{S}$, L^+, and U are symmetric we can write conservation of energy as,

$$\begin{aligned} \rho_0 \frac{\partial U}{\partial t} &= \tilde{\mathsf{S}}^{ij}\mathsf{L}^+_{ij} + \mathbf{N}^{ij}\mathsf{U}_{ij} + \rho\dot{Q} - \partial \cdot \mathfrak{Q} \\ &= \mathrm{tr}(\tilde{\mathsf{S}}\mathsf{L}^+) + \mathrm{tr}(\mathbf{N}\mathsf{U}) + \rho\dot{Q} - \partial \cdot \mathfrak{Q}. \end{aligned} \tag{5.171}$$

5.6 Constitutive Laws

The basic constitutive relationships are arrived at by combining the kinematic results relating to the rate of strain with conservation of energy, along with some constitutive assumptions. This can be done on the reference and spatial configurations, and we will deal with these separately. As in three-dimensional elasticity, we will consider isothermal elasticity.

5.6.1 Spatial Configuration

Considering conservation of energy, the symmetry of u within the term $\mathrm{tr}(\mathbf{m}\mathsf{u})$ means that only the symmetric part of $\mathbf{m}$ contributes to conservation of energy. The first **constitu-**

tive assumption is that $\mathbf{m}$ is symmetric. This is in line with [Naghdi, 1972]. Using the kinematic results for $\dot{\mathsf{e}}$ and $\dot{\mathsf{h}}$, we can now write conservation of energy as,

$$\rho\frac{Du}{Dt} = \mathrm{tr}(\tilde{\sigma}\dot{\mathsf{e}}) + \mathrm{tr}(\mathbf{m}\dot{\mathsf{h}}). \tag{5.172}$$

The second assumption is that the constitutive relationships are local, and that u is a function only of e and h. Using the chain rule of differentiation we obtain,

$$\frac{Du}{Dt} = \frac{\partial u}{\partial \mathsf{e}_{ij}}\frac{D\mathsf{e}_{ij}}{Dt} + \frac{\partial u}{\partial \mathsf{h}_{ij}}\frac{D\mathsf{h}_{ij}}{Dt}. \tag{5.173}$$

Combining this with the two constitutive relationships we obtain,

$$\tilde{\sigma}(y) = \rho\frac{\partial u}{\partial \mathsf{e}(y)}, \quad \mathbf{m}(y) = \rho\frac{\partial u}{\partial \mathsf{h}(y)}. \tag{5.174}$$

5.6.2 Reference Configuration

Considering conservation of energy, the symmetry of U within the term $\mathrm{tr}(\mathbf{N}\mathsf{U})$ means that only the symmetric part of $\mathbf{N}$ contributes to conservation of energy. The first **constitutive assumption** is that $\mathbf{N}$ is symmetric. This is in line with [Naghdi, 1972]. Using the kinematic results for $\dot{\mathsf{E}}$ and $\dot{\mathsf{H}}$, we can now write conservation of energy as,

$$\rho_0\frac{\partial U}{\partial t} = \mathrm{tr}(\tilde{\mathsf{S}}\dot{\mathsf{E}}) + \mathrm{tr}(\mathbf{N}\dot{\mathsf{H}}). \tag{5.175}$$

The second assumption is that the constitutive relationships are local, and that U is a function only of E and H. Using the chain rule of differentiation we obtain,

$$\frac{\partial U}{\partial t} = \frac{\partial U}{\partial \mathsf{E}_{ij}}\frac{\partial \mathsf{E}_{ij}}{\partial t} + \frac{\partial U}{\partial \mathsf{H}_{ij}}\frac{\partial \mathsf{H}_{ij}}{\partial t}. \tag{5.176}$$

Combining this with the two constitutive relationships we obtain,

$$\tilde{\mathsf{S}}(Y) = \rho\frac{\partial U}{\partial \mathsf{E}(Y)}, \quad \mathbf{N}(Y) = \rho\frac{\partial U}{\partial \mathsf{H}(y)}. \tag{5.177}$$

5.6.3 The Energy of Deformation

[Koiter, 1966] proposes the following form for $\rho_0 U$, which can be regarded as the extension of the Saint Venant-Kirchhoff material to shells,

$$\rho_0 U = \frac{Eh}{2(1-\nu^2)}\left((1-\nu)\,\mathrm{tr}(\mathsf{E}^2) + \nu\,\mathrm{tr}(\mathsf{E})^2\right) + \frac{Eh^3}{24(1-\nu^2)}\left((1-\nu)\,\mathrm{tr}(\mathsf{H}^2) + \nu\,\mathrm{tr}(\mathsf{H})^2\right), \tag{5.178}$$

where E is Young's modulus, ν is Poisson's ratio, and h is the thickness of the shell. From this we obtain the following relationships,

$$\begin{aligned} \mathsf{S}(Y) - \mathsf{F}^{-1}\mathsf{b}\mathsf{F}\mathbf{N}(Y) &= \frac{Eh}{1-\nu^2}\left((1-\nu)\mathsf{E}(Y) + \nu\,\mathrm{tr}(\mathsf{E})Y\right), \\ \mathbf{N}(Y) &= \frac{Eh^3}{12(1-\nu^2)}\left((1-\nu)\mathsf{H}(Y) + \nu\,\mathrm{tr}(\mathsf{H})Y\right). \end{aligned} \tag{5.179}$$

Note that this only provides the part of S that is tangential to $\mathcal{B}$. The non-tangential part (S^{3i}) is found using conservation of angular momentum.

5.7 Perturbations

As in three dimensional elasticity, we assume that initially the body $\mathcal{B}$ is deformed according to the displacement U_0, which satisfies the steady governing equations. We then perturb this deformed state such that $U = U_0 + \epsilon U'$. Neglecting all terms in the governing equations preceded by ϵ^2 or a greater power, we obtain the following approximations,

Deformation gradient

$$\begin{aligned} \mathsf{F}(Y) &= Y + Y\cdot\partial U_0 + \epsilon Y\cdot\partial U' = \mathsf{F}_0(Y) + \epsilon\mathsf{F}'(Y), \\ \det\mathsf{F} &= \det\mathsf{F}_0 + \epsilon\det\mathsf{F}_0\,\mathrm{tr}(\mathsf{F}_0^{-1}\mathsf{F}'), \\ \mathsf{F}^{-1}(Y) &= \mathsf{F}_0^{-1}(Y) - \epsilon\mathsf{F}_0^{-1}\mathsf{F}'\mathsf{F}_0^{-1}(Y), \\ \det\mathsf{F}^{-1} &= \det\mathsf{F}_0^{-1} + \epsilon\det\mathsf{F}_0^{-1}\,\mathrm{tr}(\mathsf{F}'\mathsf{F}_0^{-1}). \end{aligned} \tag{5.180}$$

Strain tensor

$$2\mathsf{E}(Y) = \bar{\mathsf{F}}_0\mathsf{F}_0(Y) - Y + \epsilon\left(\bar{\mathsf{F}}_0\mathsf{F}'(Y) + \bar{\mathsf{F}}'\mathsf{F}_0(Y)\right) = 2\mathsf{E}_0(Y) + 2\epsilon\mathsf{E}'(Y). \tag{5.181}$$

Convected frame

$$\begin{aligned} e_i &= \mathsf{F}_0(E_i) + \epsilon \mathsf{F}'(E_i), \\ e_3 &= \frac{\det \mathsf{F}_0^{-1}}{\mathfrak{V}} \mathsf{F}_0(E_1) \times \mathsf{F}_0(E_2) + \epsilon \frac{\det \mathsf{F}_0^{-1}}{\mathfrak{V}} \big(\mathsf{F}'(E_1) \times \mathsf{F}_0(E_2) \\ &\qquad + \mathsf{F}_0(E_1) \times \mathsf{F}'(E_2) - \operatorname{tr}(\mathsf{F}' \mathsf{F}_0^{-1}) \mathsf{F}_0(E_1) \times \mathsf{F}_0(E_2) \big) \\ &= e_{30} + \epsilon e_3'. \end{aligned} \tag{5.182}$$

Modified deformation gradient

$$\begin{aligned} \mathbf{F}(Y) &= \mathsf{F}_0(Y) + \epsilon \mathsf{F}'(Y) + (Y \cdot E_3) e_{30} + \epsilon (Y \cdot E_3) e_3' \\ &= \mathbf{F}_0(Y) + \epsilon \mathbf{F}'(Y). \end{aligned} \tag{5.183}$$

Convected second fundamental form $\bar{\mathsf{F}}\mathsf{b}\mathsf{F}$

$$\begin{aligned} \bar{\mathsf{F}}\mathsf{b}\mathsf{F}(Y) &= Y^i E^j e_{30} \cdot \partial_i \mathsf{F}_0(E_j) + \epsilon Y^i E^j \left(e_{30} \cdot \partial_i \mathsf{F}'(E_j) + e_3' \cdot \partial_i \mathsf{F}_0(E_j) \right) \\ &= (\bar{\mathsf{F}}\mathsf{b}\mathsf{F})_0(Y) + \epsilon (\bar{\mathsf{F}}\mathsf{b}\mathsf{F})'(Y). \end{aligned} \tag{5.184}$$

The tensor $\mathsf{F}^{-1}\mathsf{b}\mathsf{F}$

$$\begin{aligned} \mathsf{F}^{-1}\mathsf{b}\mathsf{F}(Y) &= Y^i E_j e_{30} \cdot \partial_i \bar{\mathsf{F}}_0^{-1}(E^j) + \epsilon Y^i E_j \left(-e_{30} \cdot \partial_i \bar{\mathsf{F}}_0^{-1} \bar{\mathsf{F}}' \bar{\mathsf{F}}_0^{-1}(E^j) + e_3' \cdot \partial_i \bar{\mathsf{F}}_0^{-1}(E^j) \right) \\ &= (\mathsf{F}^{-1}\mathsf{b}\mathsf{F})_0(y) + \epsilon (\mathsf{F}^{-1}\mathsf{b}\mathsf{F})'(y). \end{aligned} \tag{5.185}$$

Change of curvature tensor H

$$\mathsf{H}(Y) = (\bar{\mathsf{F}}\mathsf{b}\mathsf{F})_0(Y) - \mathsf{B}(y) + \epsilon (\bar{\mathsf{F}}\mathsf{b}\mathsf{F})'(Y) = \mathsf{H}_0(Y) + \epsilon \mathsf{H}'(Y). \tag{5.186}$$

Modified second reference couple-stress tensor $\mathbf{N}$

$$\begin{aligned} \mathbf{N}(y) &= \frac{Eh^3}{12(1-\nu^2)} \big((1-\nu) \mathsf{H}_0(y) + \nu \operatorname{tr}(\mathsf{H}_0) y \big) + \epsilon \frac{Eh^3}{12(1-\nu^2)} \big((1-\nu) \mathsf{H}'(y) + \nu \operatorname{tr}(\mathsf{H}') y \big) \\ &= \mathbf{N}_0(y) + \epsilon \mathbf{N}'(y). \end{aligned} \tag{5.187}$$

First reference couple-stress tensor M

$$\begin{aligned}\mathsf{M}(Y) &= \mathsf{F}\mathbf{N}(Y) \wedge e_3 \\ &= \mathsf{F}_0\mathbf{N}_0(Y) \wedge e_{30} + \epsilon\left(\mathsf{F}'\mathbf{N}_0(Y) \wedge e_{30} + \mathsf{F}_0\mathbf{N}'(Y) \wedge e_{30} + \mathsf{F}_0\mathbf{N}_0(Y) \wedge e_3'\right) \\ &= \mathsf{M}_0(y) + \epsilon\mathsf{M}'(y).\end{aligned} \tag{5.188}$$

Second Piola-Kirchhoff stress tensor S

$$\begin{aligned}\mathsf{S}(Y) \approx{}& \frac{Eh}{1-\nu^2}\left((1-\nu)\mathsf{E}_0(Y) + \nu\,\mathrm{tr}(\mathsf{E}_0)Y\right) + \epsilon\frac{Eh}{1-\nu^2}\left((1-\nu)\mathsf{E}'(Y) + \nu\,\mathrm{tr}(\mathsf{E}')Y\right) \\ &+ (\mathsf{F}^{-1}\mathsf{b}\mathsf{F})_0\mathbf{N}_0(Y) + \epsilon\left((\mathsf{F}^{-1}\mathsf{b}\mathsf{F})_0\mathbf{N}'(Y) + (\mathsf{F}^{-1}\mathsf{b}\mathsf{F})'\mathbf{N}_0(Y)\right) \\ ={}& \mathsf{S}_0(Y) + \epsilon\mathsf{S}'(Y).\end{aligned} \tag{5.189}$$

First Piola-Kirchhoff stress tensor T

$$\begin{aligned}\mathsf{T}(Y) &= \mathbf{F}_0\mathsf{S}_0(y) + \epsilon\left(\mathbf{F}_0\mathsf{S}'(y) + \mathbf{F}'\mathsf{S}_0(y)\right) \\ &= \mathsf{T}_0(y) + \epsilon\mathsf{T}'(y).\end{aligned} \tag{5.190}$$

Conservation of mass

$$\begin{gathered}\frac{\partial}{\partial t}(\rho\det\mathsf{F}) = \frac{\partial}{\partial t}\left(\rho\left(\det\mathsf{F}_0 + \epsilon\det\mathsf{F}_0\,\mathrm{tr}(\mathsf{F}_0^{-1}\mathsf{F}')\right)\right) = 0, \\ \text{we define } \rho_0 = \rho\det\mathsf{F}_0, \quad \rho' = \rho\det\mathsf{F}_0\,\mathrm{tr}(\mathsf{F}_0^{-1}\mathsf{F}').\end{gathered} \tag{5.191}$$

Conservation of momentum

$$\rho_0\frac{\partial^2 U'}{\partial t^2} = \dot{\mathsf{T}}'(\dot{\partial}) + \rho_0 b' + \rho' b_0. \tag{5.192}$$

Conservation of angular momentum

$$\mathsf{F}_0(E_i) \wedge \mathsf{T}'(E^i) + \mathsf{F}'(E_i) \wedge \mathsf{T}_0(E^i) + \dot{\mathsf{M}}'(\dot{\partial}) + \rho_0 c' + \rho' c_0 = 0. \tag{5.193}$$

5.7.1 Small Deformations

If we assume $U_0 = 0$ then we obtain the following simplifications,

$$\begin{aligned}
\mathsf{F}(Y) &= Y + \epsilon Y \cdot \partial U' = U + \epsilon \mathsf{F}'(Y), \\
\mathsf{F}^{-1}(Y) &= Y - \epsilon \mathsf{F}'(Y), \\
2\mathsf{E}(y) &= \epsilon \left(\mathsf{F}'(Y) + \bar{\mathsf{F}}'(Y) \right) = Y \cdot \partial U + \dot{\partial}(Y \cdot \dot{U}), \\
\det \mathsf{F} &= 1 + \epsilon \operatorname{tr}(\mathsf{F}') = 1 + \epsilon \partial \cdot U', \\
\det \mathsf{F}^{-1} &= 1 - \epsilon \operatorname{tr}(\mathsf{F}') = 1 - \epsilon \partial \cdot U', \\
e_i &= E_i + \epsilon \mathsf{f}'(E_i) = E_i + \epsilon E_i \cdot \partial U', \\
e^i &= E^i - \epsilon \bar{\mathsf{F}}'(E^i) = E^i - \epsilon \dot{\partial}(E^i \cdot \dot{U}'), \\
e_3 &= E_3 + \epsilon \left(\frac{1}{\mathfrak{V}} (E_1 \cdot \partial U') \times E_2 + \frac{1}{\mathfrak{V}} E_1 \times (E_2 \cdot \partial U') - (\partial \cdot u') E_3 \right).
\end{aligned} \tag{5.194}$$

Following the method of [Ciarlet, 2005], and using the coordinate independent notation of geometric algebra, the change of curvature tensor takes the form,

$$\mathsf{H}(Y) = \epsilon E^j \left((E_j \cdot \dot{\partial} \dot{\bar{\mathsf{F}}}'(Y)) \cdot E_3 \right). \tag{5.195}$$

From this it is clear how the linearised change of curvature tensor is closely related to the E_3 components of the second derivative of the displacement field U'.

Using these results and applying the formulas of the previous section we have, $\mathsf{S}_0(Y) = 0$, $\mathsf{T}_0(Y) = 0$, $\mathbf{N}_0(Y) = 0$, $\mathsf{M}_0(Y) = 0$, and,

$$\begin{aligned}
\mathbf{N}'(Y) &= \frac{E_y h^3}{12(1-\nu^2)} \left((1-\nu)\mathsf{H}'(Y) + \nu \operatorname{tr}(\mathsf{H}')Y \right). \\
\mathsf{S}(Y) &= \frac{E_y h}{1-\nu^2} \left((1-\nu)\mathsf{E}'(Y) + \nu \operatorname{tr}(\mathsf{E}')Y \right) \\
&\quad + \frac{E_y h^3}{12(1-\nu^2)} \left((1-\nu)\mathsf{B}\mathsf{H}'(Y) + \nu \operatorname{tr}(\mathsf{H}')\mathsf{B}(Y) \right), \\
\mathsf{M}'(Y) &= \mathbf{N}'(Y) \wedge E_3.
\end{aligned} \tag{5.196}$$

Conservation of momentum and angular momentum can be written as,

$$\rho_0 \frac{\partial^2 U'}{\partial t^2} = \dot{\mathsf{S}}'(\dot{\partial}) + \rho_0 b', \tag{5.197}$$

$$E_i \wedge \mathsf{S}'(E^i) + \dot{\mathsf{M}}'(\dot{\partial}) + \rho' c_0 = 0. \tag{5.198}$$

5.8 Summary

In this chapter, we have developed a complete and self consistent theory of elasticity in shells using geometric algebra. This has provided several advances in the field, and will be of vital importance as we develop understanding of self-excited oscillations of flexible tubes.

We have shown that the first fundamental form is actually just the identity function by considering the coordinate free definition. We have also clarified the difference between $\det \mathsf{g}$, which is independent of coordinates, and $\sqrt{\det(\mathsf{g}_{ij})}$, which is not. The geometric interpretation of the latter is clarified by its relationship to the volume form $\mathfrak{v}$, which is defined in terms of the pseudoscalar.

The second fundamental form also benefits from a coordinate free definition, and we have been able to clarify the link between this and the Christoffel coefficients.

Following this theme, the coordinate free definition of the strain tensor illustrates more clearly how the metric tensors (first fundamental forms) can only be used to describe strain if convected coordinates are used.

Similarly, the coordinate free definition of the change of curvature tensor shows the explicit dependence of H on the deformation gradient F, which is hidden when convected coordinates are used.

We have used rotors for the first time to help understand curvature and its changes. Firstly, this allows the range and domain of R to be easily extended to $\mathbb{E}^3$. It also allows a new representation of the change of curvature tensor which explicitly shows contributions due to strain combined with initial curvature and variation in the rotation. This will be of particular significance when we consider the oscillations of flexible tubes.

The coordinate free approach has been applied to the rate of deformation tensors, and we have used bivectors for the first time in shell theory to represent angular velocity. This allows a simple relationship between the rotation tensor $\mathsf{R}(Y) = RY\tilde{R}$ and the angular velocity ω to be derived.

The use of bivectors also extends to the representation of torques. The bivector definitions of m, M, and N have obvious physical meaning. As the conservation laws are derived we see that it is convenient to use the related vector quantities $\mathbf{m}$, $\mathbf{M}$, and $\mathbf{N}$. However, it is now clearer that while these are convenient vector quantities, they do not follow the usual conventions used to relate bivector torques to vector torques (see §A), which explains for the first time why [Naghdi, 1972] (among others) found it necessary to use apparently unphysical definitions of angular velocity and moment.

Our coordinate free approach significantly simplifies linearisation of the equations of motion about a deformed state, and this will be vital when we consider the vibration modes of tubes representing the airways, which, as has been discussed, are held in axial tension.

Chapter 6

Experimental Repeatability, Definitions, and the Failure of Linear Theory

We are interested in why self-excited oscillations in flexible tubes occur. Therefore, we require a repeatable way of observing the onset of oscillations. Protocol 1 (§3.6.1) allows us to do this. In this chapter we will explain how conditions at onset are found, investigate the repeatability of these observations, determine the effect of changing the up- and downstream conditions on the oscillations, and demonstrate the failure of naive linear theory to predict the frequency at which oscillations occur.

Before this though we will illustrate how our experiments are of direct relevance to wheezing. In §3.3 we showed that the geometry of the tubes used in previous experiments limited their utility to our project. The geometry of the tubes that we have investigated are illustrated in fig. 6.1, along with approximate values in the lung for comparison. In addition, we use air as the working fluid, and rubber as the tube material. Therefore, the density ratio is correct, and the material properties of the tube match those of the airways ($E = 1\,\mathrm{MPa}$, $\nu = 0.5$).

Data from the experiments detailed in this chapter is available at [Gregory and Agarwal, 2017a,b].

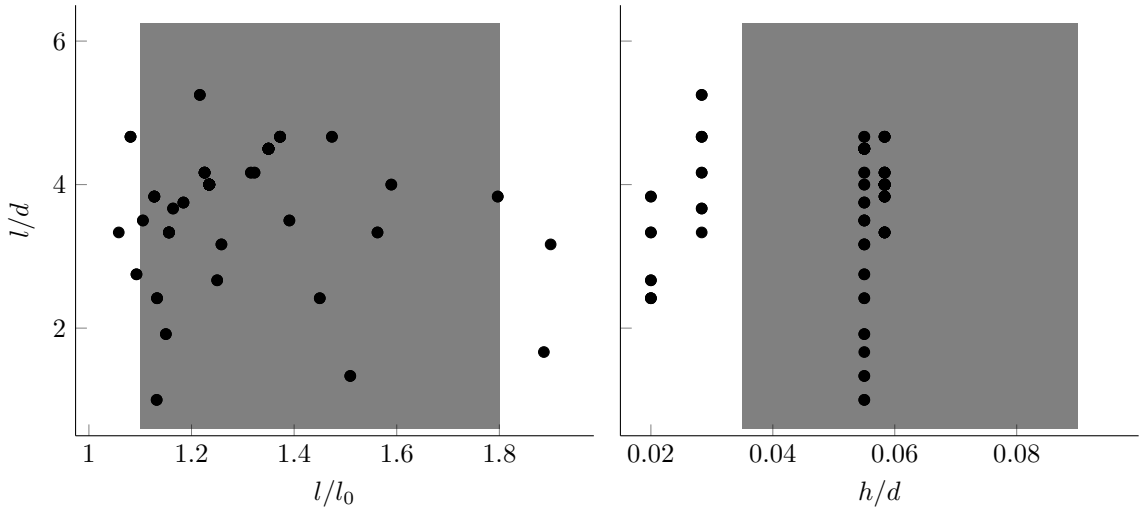


Figure 6.1: The geometric parameters of the flexible tubes used while investigating self-excited oscillations. The shaded regions represent the typical values of the geometric parameters found in the upper airways of the lung.

6.1 Determining Conditions at Onset

The results from a single experimental run, obtained using protocol 1, are shown in fig. 6.2. The run takes around 10 min, during which $p_d - p_e$ is first slowly ramped down, then held, then slowly ramped back up to zero. Over this period we have plotted the moving averages $\bar{p}_1 - p_e$, $\bar{p}_2 - p_e$, and Q, and $p_u - p_e$ and $p_d - p_e$. Spectrograms of p_1, p_2, and the acoustic pressure p_a are also shown, with their time axes aligned.

To begin with, the reduction of $p_d - p_e$ results in a greater flow Q through the rig, and results in pressure drops at all the locations through the rig. All these pressure drops increase in size as $p_d - p_e$ is lowered further. The drop in pressure within the rig means the there is a transmural pressure difference trying to squash the flexible tube, meaning that it narrows. The narrowing of the tube makes the pressure drop $\bar{p}_1 - \bar{p}_2$ larger as a proportion of the overall pressure drop in the rig. This has a tendency to reduce the flowrate, and eventually, this effect dominates, and Q and $\bar{p}_1 - p_e$ level off. The levelling off of Q and $\bar{p}_1 - p_e$ roughly corresponds to the tube almost completely collapsing. Shortly after this, oscillations are also observed, which can be seen in fig. 6.2 from the spectrograms. After the onset of oscillations, as $p_d - p_e$ is lowered, the tube goes through a sequence of different oscillation modes, but in this thesis we are going to focus on the onset of oscillations.

All three spectrograms in fig. 6.2 are very similar, the main difference being the amplitude

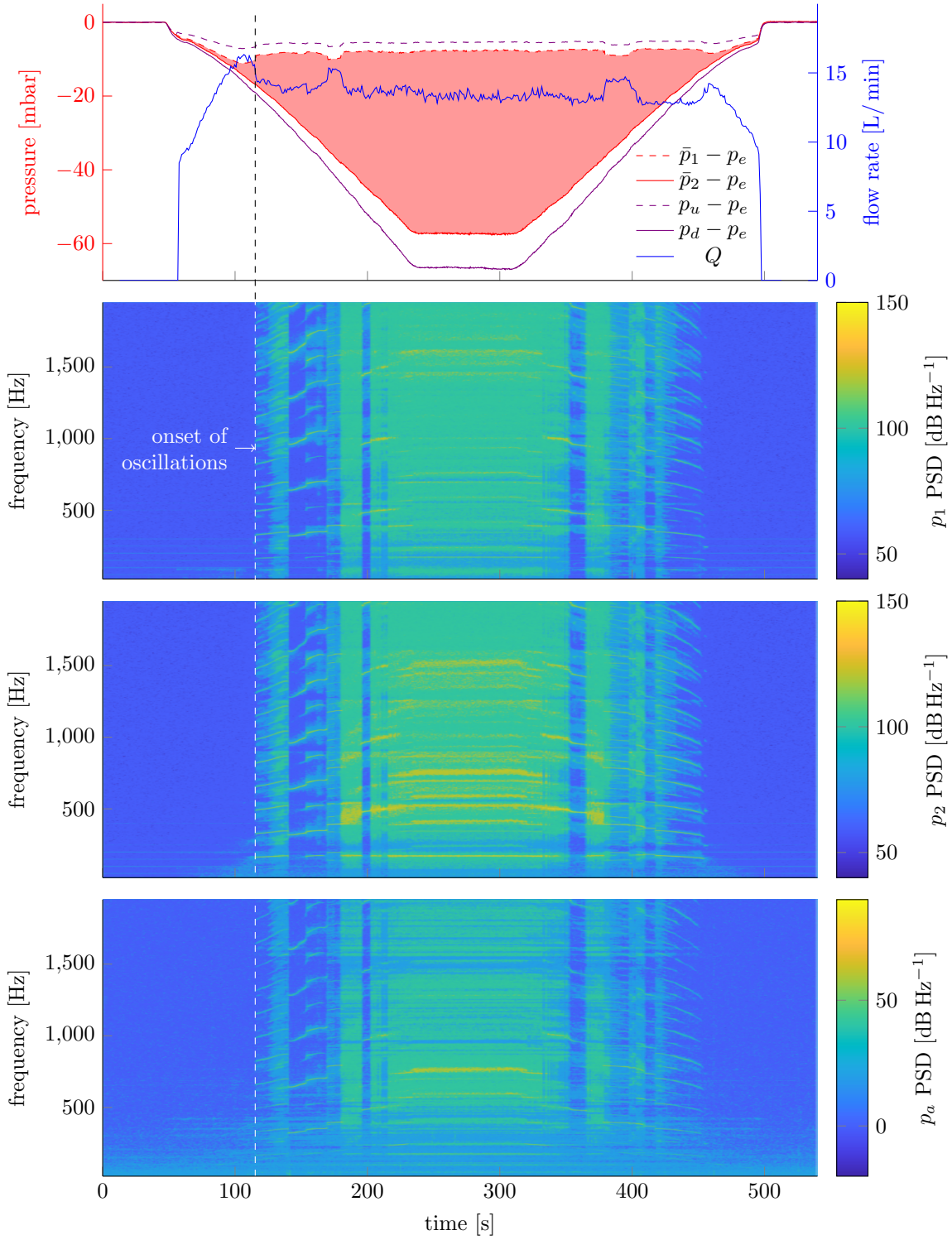


Figure 6.2: Results from a single experimental run, obtained using protocol 1.

of the oscillations. p_1 and p_2 are both measuring hydrodynamic pressure changes, and so show much larger variations than p_a. Of p_1 and p_2, the latter has the larger amplitude, which we believe is due to the convection of eddies and other flow structures past the downstream end of the tube as the tube oscillates, which do not directly affect p_1.

In fig. 6.2 the onset of self-excited oscillations is marked at $t = 115\,\mathrm{s}$. This can be found automatically by searching for the time at which the overall sound power level in the spectrogram exceeds the mean sound power level of the first 40 s by more than 4 standard deviations. In fig. 6.3 we show an expanded plot of the pressures, the flowrate, and the spectrogram of p_2 near to onset. The dominant frequency of the oscillations at onset can be seen, as can the values of $\bar{p}_1 - p_e$ and $\bar{p}_2 - p_e$. Q is the most difficult to define, and we take the roughly constant value of Q before the sudden drop at onset. Error bars indicate the uncertainty we have in these values. Hence, it is possible for us to measure the values of $\bar{p}_1 - p_e$, $\bar{p}_2 - p_e$, Q, and the frequency of oscillations at the onset of those oscillations, which we denote f. This has been done for all of the tubes indicated in fig. 6.1.

To understand how repeatable the measurements of the conditions at the onset of oscillations are, we consider a subset of the experiments in which a tube with $h = 0.35\,\mathrm{mm}$ and $d = 6\,\mathrm{mm}$ was considered in 4 configurations; $(l_0 = 20.4\,\mathrm{mm}, l = 23\,\mathrm{mm})$, $(l_0 = 20.4\,\mathrm{mm}, l = 25\,\mathrm{mm})$,$(l_0 = 20.4\,\mathrm{mm}, l = 28\,\mathrm{mm})$, $(l_0 = 17.3\,\mathrm{mm}, l = 20\,\mathrm{mm})$. For each of these configurations 6 runs were completed (24 runs in total). At onset we measure 4 variables: $\bar{p}_1 - p_e$, $\bar{p}_2 - p_e$, Q, and f, and these are shown for each of the 6 repeat runs, and for the 4 different tubes, in fig. 6.4. From this we can see that $\bar{p}_1 - p_e$ and $\bar{p}_2 - p_e$ are generally repeatable to within $\pm 2\,\mathrm{mbar}$, Q is repeatable to with $\pm 1.5\,\mathrm{L/\,min}$, and f is repeatable to within $\pm 20\,\mathrm{Hz}$.

6.2 The Effect of Boundary Conditions on Oscillations

It has been noted by that the up- and downstream flow conditions in the experimental rig can influence the oscillations observed in Starling resistors. We have investigated this by changing the lengths of the UCFT and DCFT ((5) and (5′) in fig. 3.16). Specifically, we have performed two sets of experiments, which are outlined in table 6.1. In each of these sets a single flexible tube was chosen, and the lengths of the UCFT and DCFT were varied.

By changing the rig while keeping the flexible tube the same, we are able to see the effect that the rig has on onset conditions. In fig. 6.5 we show the onset conditions that were

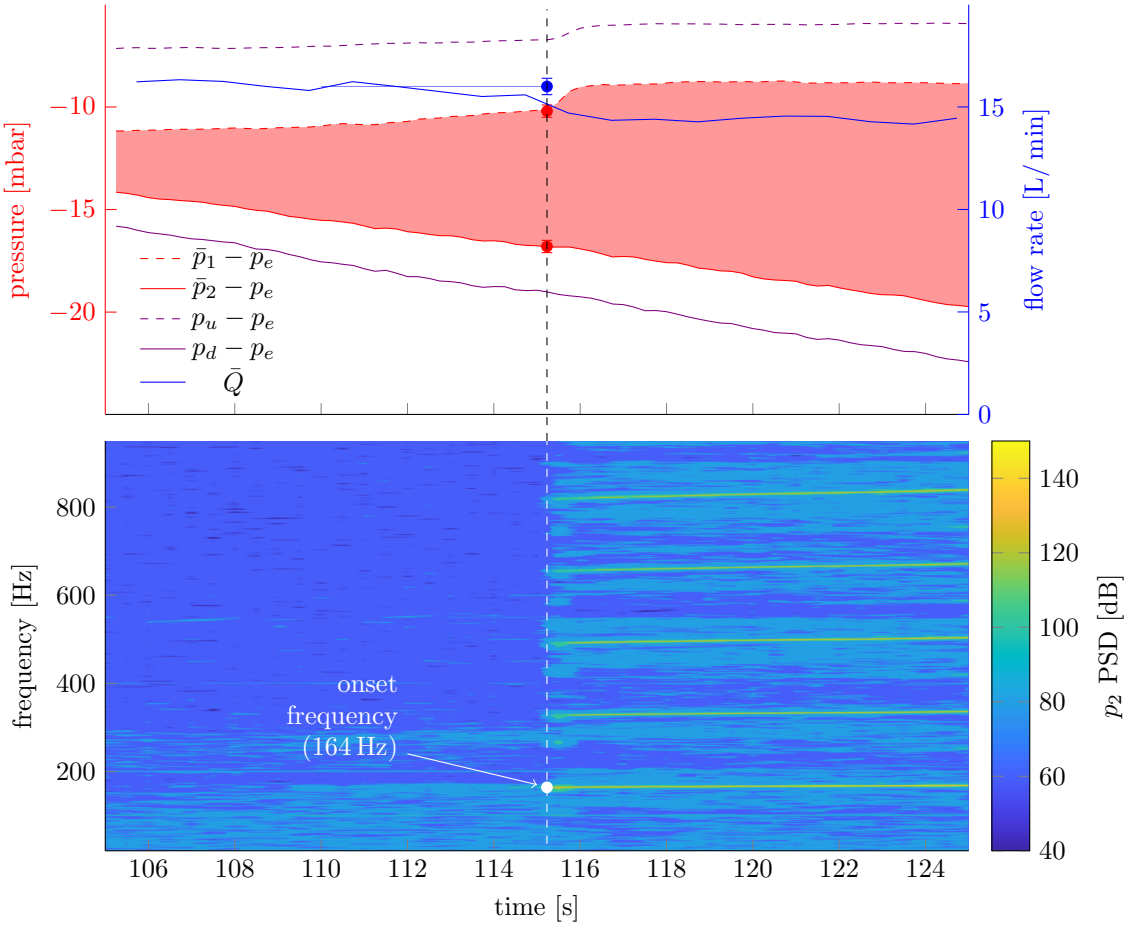


Figure 6.3: A zoomed in section of fig. 6.2, focussing on the onset of oscillations, measured using 4 different flexible tubes.

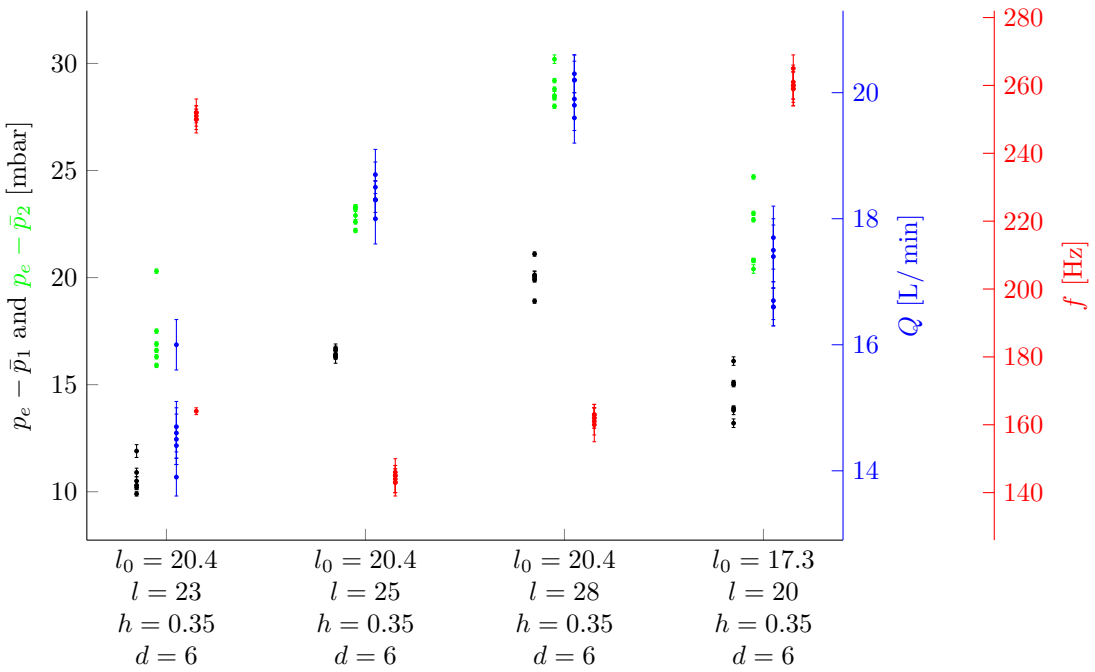


Figure 6.4: The repeatability of conditions at the onset of self-excited oscillations. All geometric parameters are in mm.

Table 6.1: Rig configurations for experiments investigating the effect up boundary conditions on oscillations (all geometric parameters are in mm). All other experiments in fig. 6.1 were perfomed using the UCFT and DCFT lengths marked with a $\star$.

$l_0 = 20,\ l = 27,\ h = 0.33,\ d = 6$		
UCFT length	DCFT length	
948	989	
948	440	$\star$
948	152	
$l_0 = 19.44,\ l = 24,\ h = 0.35,\ d = 6$		
UCFT length	DCFT length	
988	989	
440	989	
152	989	
988	440	
440	440	
152	440	
988	152	
440	152	
152	152	

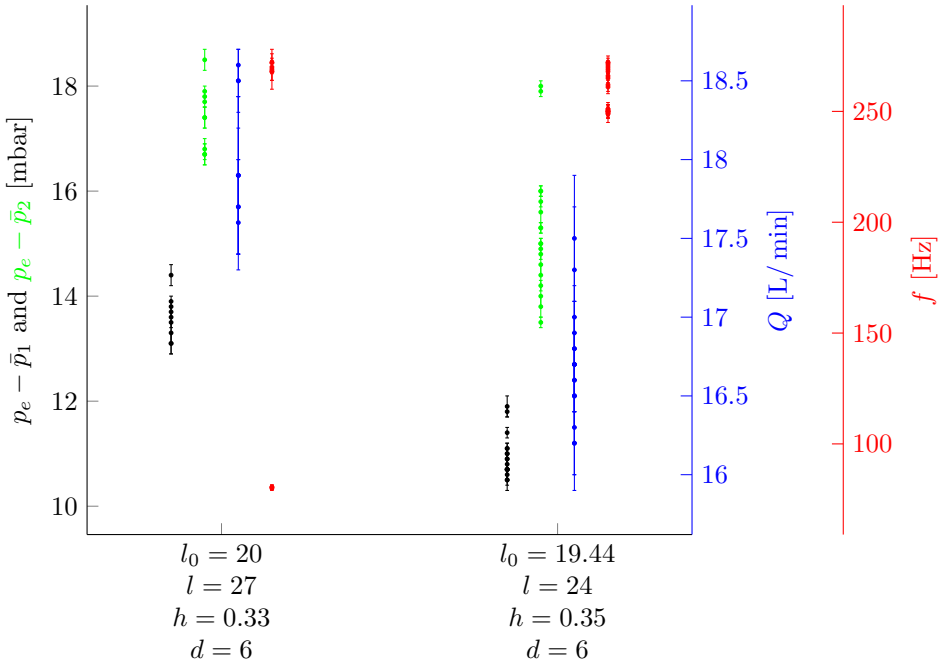


Figure 6.5: The effect of the up- and downstream experimental rig on the conditions observed at the onset of oscillations. All geometric parameters are in mm.

observed using the rig configurations given in table 6.1. From this we can see that variation in $\bar{p}_1 - p_e$, $\bar{p}_2 - p_e$, and Q is accounted for by the expected variations seen in the previous section. Most of the frequency results are accounted for in this way as well, with a single exception corresponding the flexible tube with $l_0 = 20\,\text{mm}, l = 27\,\text{mm}, h = 0.33\,\text{mm}, d = 6\,\text{mm}$ when used with a UCFT length of 948 mm and a DCFT length of 989 mm. In this instance the observed frequency at onset is significantly lower than in the other experiments (~ 80 compared to $\sim 260\,\text{Hz}$). We believe that in this case, the tube is oscillating in the first acoustic resonant mode of parts (5), (6), (7), (6′), and (5′) of the experimental rig (see fig. 3.16). The length of these parts of the rig together is 2114 mm. The first acoustic mode of a tube of this length occurs when the wavelength of the sound wave is twice the length of the tube. Since the speed of sound is $340\,\text{m}\,\text{s}^{-1}$ this corresponds to a frequency of,

$$\frac{340\,\text{m}\,\text{s}^{-1}}{2 \times 2.114\,\text{m}} = 80.4\,\text{Hz}. \tag{6.1}$$

This matches well with the observed onset frequency of $80\,\text{Hz} \pm 2\,\text{Hz}$.

We have observed one example of what is probably "lock in", where the frequency of oscillation of the flexible tube is set by the acoustic resonance of the surrounding environ-

ment. However, in all other cases, the surrounding rig is not observed to have any affect on the frequency of oscillation. It is worth noting that this is the only result (including all experiments completed for the thesis) for which lock in was observed. This suggests that most of the time the up- and downstream parts of the rig do not effect the onset frequency, but there are a few very finely balanced cases where lock in with an acoustic mode is possible. This is still a very different result from those seen in experiments with water as the working fluid, as we can see no effect due to the inertiance or resistance of the up- and downstream parts of the rig, as is observed by [Wang et al., 2009].

The effect of the up- and downstream rig has now been accounted for, but it is also necessary to consider the effect of the air surrounding the oscillating tube. We have already shown that unsteady pressure variations in this region are small compared to the transmural pressure (see §3.2.4), but we should also consider the inertia of the surrounding air. The velocity field generated by the oscillating tube can be estimated using basic acoustics. The tube can be considered compact at the frequencies under consideration ($ka \approx 6 \times 10^{-3}$), so the flow around the tube can be considered incompressible. If the amplitude of tube wall motions is a, then the flow field around the tube is given by $u_r = \imath\omega a(a/r)e^{\imath\omega t}$. Hence, we expect that the region of air significantly affected by the motion of the flexible tube to be a cylindrical annulus of outer radius $2a$ and inner radius a. The mass per unit length of the air in this annulus will be $10^{-4}\mathrm{kg\,m^{-1}}$ compared to $6 \times 10^{-3}\,\mathrm{kg\,m^{-1}}$ for the tube itself. Hence we expect that the inertia of the surrounding air will not play an important role. It is worth noting that the tube walls usually move in an approximation to a quadrupole rather than a monopole, meaning that this estimate of the mass of moving air surrounding the tube is an upper limit.

6.3 Linear Oscillation Modes of Axially Strained Cylinders

We know that the inertia of the tube wall is far greater than that of the fluid. The density of the tube wall is around 1000 times that of the fluid, and the mass of the tube is greater than that of the fluid in the tube by a factor of approximately 100 (depending on the exact tube thickness and radius). Therefore, a naive first attempt to estimate the frequencies of the oscillations can be made by finding the normal modes of oscillation of cylindrical flexible tubes held in axial tension, given l_0, l, h, a, E, and ν. In this section we will calculate these

normal modes, and demonstrate the failure of this approach.

One of the advantages of using geometric algebra in shell theory, demonstrated in §5.7, is the ease with which linearised equations of motion can be set up about an initially strained state. In this section we will derive the equations of motion for an axially strained cylindrical shell. Since we are using these results to demonstrate the failure of simple linearised theory to predict onset conditions, we need to be very sure that the solution we find is correct, and that failure is not due to some approximation in finding the solution. For this reason, we solve the linearised problem in two separate ways, analytically and using Chebyshev polynomials, and validate both of these methods against three dimensional linearised elasticity for the case in which $l = l_0$.

6.3.1 Equations of Motion

We take the reference configuration $\mathcal{B}$ to be a cylinder with length l_0 and radius $a = -1/C$ (C is the curvature, and is negative). On this cylinder we introduce the coordinate system $\{X^1, X^2\}$, where $-l_0/2 \leqslant X^1 \leqslant l_0/2$ is the axial coordinate and $0 \leqslant X^2 < 2\pi a$ is the azimuthal coordinate. The basis vectors associated with this coordinate system $\{E_i = \partial X/\partial X^i\}$ are orthonormal, hence, $\Gamma^i_{jk} = 0$. In addition,

$$\begin{aligned} \mathsf{B}_{12} = \mathsf{B}_{21} = \Gamma^3_{12} = \Gamma^3_{21} = -\Gamma^2_{13} = -\Gamma^1_{23} = 0, \\ \mathsf{B}_{11} = \Gamma^3_{11} = -\Gamma^1_{13} = 0, \quad \mathsf{B}_{22} = \Gamma^3_{22} = -\Gamma^2_{23} = C. \end{aligned} \tag{6.2}$$

We take the background deformation to be uni-axial strain such that $U_0(X) = U_0(X^1, X^2) = \varepsilon X^1 E_1$, where $\varepsilon = (l - l_0)/l_0$. Hence $\mathsf{F}_0(Y) = Y + \varepsilon(Y \cdot E_1)E_1$. We also define $\lambda = 1 + \varepsilon = l/l_0$. Using this and following the perturbation approach of §5.7 (and noting that ε is the initial axial strain, while ϵ is the size of the perturbation), we obtain the following results,

Determinant of F

$$\begin{aligned} \det \mathsf{F} &= 1 + \varepsilon + \epsilon(1 + \varepsilon)\left(\partial \cdot U' - \tfrac{\varepsilon}{\lambda}\partial_1 U'_1\right) \\ &= \lambda\left(1 + \epsilon\partial \cdot U'\right) - \epsilon\varepsilon\partial_1 U'_1, \\ \det \mathsf{F}^{-1} &= \tfrac{1}{\lambda} - \tfrac{\epsilon}{\lambda}\left(\partial \cdot U' - \tfrac{\varepsilon}{\lambda}\partial_1 U'_1\right) \\ &= \tfrac{1}{\lambda}\left(1 - \epsilon\partial \cdot U'\right) + \tfrac{\epsilon\varepsilon}{\lambda^2}\partial_1 U'_1. \end{aligned} \tag{6.3}$$

Strain tensor

$$\begin{aligned}(\mathsf{E}_0)_{11} &= \tfrac{1}{2}\varepsilon^2 + \varepsilon, \quad (\mathsf{E}_0)_{12} = (\mathsf{E}_0)_{21} = 0, \quad (\mathsf{E}_0)_{22} = 0,\\ (\mathsf{E}')_{11} &= (1+\varepsilon)\partial_1 U_1', \quad (\mathsf{E}')_{22} = \partial_2 U_2' - C U_3',\\ (\mathsf{E}')_{12} &= (\mathsf{E}')_{21} = \tfrac{1}{2}(\partial_1 U_2' + \partial_2 U_1') + \tfrac{\varepsilon}{2}\partial_2 U_1'.\end{aligned} \tag{6.4}$$

Convected frame

$$\begin{aligned}e_1 &= \lambda E_1 + \epsilon \partial_1 U', \quad e_2 = E_2 + \epsilon \partial_2 U',\\ e^1 &= \tfrac{1}{\lambda} E_1 - \tfrac{\epsilon}{\lambda}\left(\partial_1 U' - \tfrac{\varepsilon}{\lambda} E_1\right), \quad e^2 = E_2 - \epsilon \partial_2 U',\\ e_{30} = E_3, \quad e_3' &= -\left(\partial \cdot U' - \frac{\varepsilon}{\lambda}\partial_1 U_1'\right) E_3 + \tfrac{1}{\lambda}\partial_1 U' \times E_2 + E_1 \times \partial_2 U'.\end{aligned} \tag{6.5}$$

Convected second fundamental form $\bar{\mathsf{F}}\mathsf{b}\mathsf{F}$

$$\begin{aligned}(\bar{\mathsf{F}}\mathsf{b}\mathsf{F})_0(Y) &= \mathsf{B}(Y),\\ (\bar{\mathsf{F}}\mathsf{b}\mathsf{F})'(Y) &= Y^i E^j \Big(E_3 \cdot \partial_i \partial_j U' - \left(\partial \cdot U' - \tfrac{\varepsilon}{\lambda}\partial_1 U_1'\right) E_3 \cdot \partial_i \mathsf{F}_0(E_j)\\ &\qquad + \tfrac{1}{\lambda}(\partial_1 U' \times E_2) \cdot \partial_i \mathsf{F}_0(E_j) + (E_1 \times \partial_2 U') \cdot \partial_i \mathsf{F}_0(E_j)\Big).\end{aligned} \tag{6.6}$$

Taking the last two terms we can write,

$$\begin{aligned}(\partial_1 U' \times E_2) \cdot \partial_i \mathsf{F}_0(E_j) &= \lambda_j (\partial_1 U' \times E_2) \cdot \partial_i E_j\\ &= \lambda_j (\partial_1 U' \times E_2) \cdot (\Gamma^3_{ij} E_3)\\ &= \lambda_j \Gamma^3_{ij} (E_2 \times E_3) \cdot \partial_1 U'\\ &= \lambda_j \Gamma^3_{ij} E_1 \cdot \partial_1 U',\end{aligned} \tag{6.7}$$

and,

$$\begin{aligned}(E_1 \times \partial_2 U') \cdot \partial_i \mathsf{F}_0(E_j) &= \lambda_j (E_1 \times \partial_2 U') \cdot \partial_i E_j\\ &= \lambda_j (E_1 \times \partial_2 U') \cdot (\Gamma^3_{ij} E_3)\\ &= \lambda_j \Gamma^3_{ij} (E_3 \times E_1) \cdot \partial_2 U'\\ &= \lambda_j \Gamma^3_{ij} E_2 \cdot \partial_2 U',\end{aligned} \tag{6.8}$$

where we have employed the notation $\lambda_1 = \lambda, \lambda_2 = 1$, and no sum over j is implied.

Hence, $(\bar{\mathsf{F}}\mathsf{b}\mathsf{F})'$ can be written as,

$$\begin{aligned}(\bar{\mathsf{F}}\mathsf{b}\mathsf{F})'(Y) &= Y^i E^j \Big(E_3 \cdot \partial_i \partial_j U' - \lambda_j \left(\partial \cdot U' - \tfrac{\varepsilon}{\lambda} \partial_1 U_1' \right) \Gamma^3_{ij} \\ &\qquad + \tfrac{\lambda_j}{\lambda} \Gamma^3_{ij} E_1 \cdot \partial_1 U' + \lambda_j \Gamma^3_{ij} E_2 \cdot \partial_2 U' \Big) \\ &= Y^i E^j E_3 \cdot \partial_i \partial_j U' \\ &= E^j \left((E_j \cdot \dot{\partial} \dot{\mathsf{F}}'(Y)) \cdot E_3 \right).\end{aligned} \tag{6.9}$$

The tensor $\mathsf{F}^{-1}\mathsf{b}\mathsf{F}$ The fact that $\mathbf{N}_0$ is 0 means that we only need to express $(\mathsf{F}^{-1}\mathsf{b}\mathsf{F})_0$ in order to find the second Piola-Kirchhoff stress tensor S.

$$(\mathsf{F}^{-1}\mathsf{b}\mathsf{F})_0(Y) = Y^i E_j E_3 \cdot \partial_i \bar{\mathsf{F}}_0^{-1}(E^j) = Y^i E_j \tfrac{1}{\lambda_j} E_3 \cdot \partial_i E^j = Y^i E_j \tfrac{1}{\lambda_j} \mathsf{B}^j{}_i. \tag{6.10}$$

The only non-zero component of B is $\mathsf{B}^2{}_2 = C$. Combining this with $\lambda_1 = \lambda$, $\lambda_2 = 1$, we see that we can write,

$$(\mathsf{F}^{-1}\mathsf{b}\mathsf{F})_0(Y) = \mathsf{B}(Y). \tag{6.11}$$

Change of curvature tensor H

$$\begin{aligned}\mathsf{H}_0(Y) &= (\bar{\mathsf{F}}\mathsf{b}\mathsf{F})_0(Y) - \mathsf{B}(Y) = 0, \\ \mathsf{H}'(Y) &= (\bar{\mathsf{F}}\mathsf{b}\mathsf{F})'(Y).\end{aligned} \tag{6.12}$$

We can write this in component form as,

$$\begin{gathered}\mathsf{H}'_{11} = \partial_1 \partial_1 U_3', \quad \mathsf{H}'_{22} = \partial_2 \partial_2 U_3' + 2C \partial_2 U_2' - C^2 U_3', \\ \mathsf{H}'_{12} = \mathsf{H}'_{21} = \partial_1 \partial_2 U_3' + C \partial_1 U_2'.\end{gathered} \tag{6.13}$$

Modified second reference couple-stress tensor $\mathbf{N}$

$$\begin{aligned}\mathbf{N}_0(Y) &= \frac{Eh^3}{12(1-\nu^2)} \left((1-\nu)\mathsf{H}_0(Y) + \nu \operatorname{tr}(\mathsf{H}_0) Y \right) = 0, \\ \mathbf{N}'(Y) &= \frac{Eh^3}{12(1-\nu^2)} \left((1-\nu)\mathsf{H}'(Y) + \nu \operatorname{tr}(\mathsf{H}') Y \right).\end{aligned} \tag{6.14}$$

In component form we have,

$$\begin{aligned} \mathbf{N}'_{11} &= \frac{Eh^3}{12(1-\nu^2)}(\mathsf{H}'_{11}+\nu\mathsf{H}'_{22}), \quad \mathbf{N}'_{22} = \frac{Eh^3}{12(1-\nu^2)}(\mathsf{H}'_{22}+\nu\mathsf{H}'_{11}), \\ \mathbf{N}'_{12} &= \frac{Eh^3}{12(1+\nu)}\mathsf{H}'_{12}, \quad \mathbf{N}'_{21} = \frac{Eh^3}{12(1+\nu)}\mathsf{H}'_{21}. \end{aligned} \tag{6.15}$$

First reference couple-stress tensor M

$$\begin{aligned} \mathsf{M}'(Y) &= \mathsf{F}_0\mathbf{N}'(Y)\wedge E_3 \\ &= Y^j\mathbf{N}'_{ij}\mathsf{F}_0(E_i)\wedge E_3 \\ &= Y^j\lambda_i\mathbf{N}'_{ij}E_i\wedge E_3 \\ &= Y^j\mathbf{M}'_{ij}E_i\wedge E_3. \end{aligned} \tag{6.16}$$

From this we have,

$$\mathsf{M}'_{(1,3)i} = \mathbf{M}'_{1i} = \lambda\mathbf{N}'_{1i}, \quad \mathsf{M}'_{(2,3)i} = \mathbf{M}'_{2i} = \mathbf{N}'_{2i}. \tag{6.17}$$

Second Piola-Kirchhoff stress tensor S

$$\begin{aligned} \mathsf{S}_0(Y) &= \frac{Eh}{1-\nu^2}\left((1-\nu)\mathsf{E}_0(Y)+\nu\,\mathrm{tr}(\mathsf{E}_0)Y\right), \\ \mathsf{S}'(Y) &= \frac{Eh}{1-\nu^2}\left((1-\nu)\mathsf{E}'(Y)+\nu\,\mathrm{tr}(\mathsf{E}')Y\right)+\mathsf{B}\mathbf{N}'(Y) \\ &= \frac{Eh}{1-\nu^2}\left((1-\nu)\mathsf{E}'(Y)+\nu\,\mathrm{tr}(\mathsf{E}')Y\right) \\ &\quad+\frac{Eh^3}{12(1-\nu^2)}\left((1-\nu)\mathsf{B}\mathsf{H}'(Y)+\nu\,\mathrm{tr}(\mathsf{H}')\mathsf{B}(Y)\right). \end{aligned} \tag{6.18}$$

In component form we have,

$$\begin{aligned} (\mathsf{S}_0)_{11} &= \frac{Eh}{1-\nu^2}\left(\frac{1}{2}\varepsilon^2+\varepsilon\right), \quad (\mathsf{S}_0)_{12} = (\mathsf{S}_0)_{21} = 0, \\ (\mathsf{S}_0)_{22} &= \frac{Eh}{1-\nu^2}\nu\left(\frac{1}{2}\varepsilon^2+\varepsilon\right) \end{aligned} \tag{6.19}$$

$$\begin{aligned} \mathsf{S}'_{11} &= \frac{Eh}{1-\nu^2}(\mathsf{E}'_{11}+\nu\mathsf{E}'_{22})+C\mathbf{N}'_{22}, \quad \mathsf{S}'_{22} = \frac{Eh}{1-\nu^2}(\mathsf{E}'_{22}+\nu\mathsf{E}'_{11}), \\ \mathsf{S}'_{12} &= \frac{Eh}{1+\nu}\mathsf{E}'_{12}, \quad \mathsf{S}'_{21} = \frac{Eh}{1+\nu}\mathsf{E}'_{21}+C\mathbf{N}'_{21}. \end{aligned} \tag{6.20}$$

First Piola-Kirchhoff stress tensor T

$$\begin{aligned}\mathsf{T}'(Y) &= \mathsf{F}_0\mathsf{S}'(Y) + \mathsf{F}'\mathsf{S}_0(Y)\\ &= Y^j\mathsf{S}'_{ij}\mathsf{F}_0(E_i) + Y^j(\mathsf{S}_0)_{ij}\mathsf{F}'(E_i)\\ &= Y^j\lambda_i\mathsf{S}'_{ij}E_i + Y^j(\mathsf{S}_0)_{ij}\partial_i U'.\end{aligned} \tag{6.21}$$

Conservation of momentum

$$\begin{aligned}\rho_0\frac{\partial^2 U'_1}{\partial t^2} &= \partial_1\mathsf{T}'_{11} + \partial_2\mathsf{T}'_{12},\\ \rho_0\frac{\partial^2 U'_2}{\partial t^2} &= \partial_1\mathsf{T}'_{21} + \partial_2\mathsf{T}'_{22} - C\mathsf{T}'_{32},\\ \rho_0\frac{\partial^2 U'_3}{\partial t^2} &= \partial_1\mathsf{T}'_{31} + \partial_2\mathsf{T}'_{32} + C\mathsf{T}'_{22}.\end{aligned} \tag{6.22}$$

The components T'_{ij} have been expressed, but to find T'_{3i} we need to make use of conservation of angular momentum.

Conservation of angular momentum We can write $\dot{\mathsf{m}}'(\dot{\partial})$ as,

$$\begin{aligned}\dot{\mathsf{M}}'(\dot{\partial}) &= \left(\partial_i(\mathsf{M}'^{Ji}) + \mathsf{M}'^{Ki}\Gamma^J_{iK} + \mathsf{M}'^{Jj}\Gamma^i_{ij}\right)E_J + \mathsf{M}'^{Ki}\Gamma^{(1,2)}_{iK}E_{(1,2)}\\ &= (\partial_i\mathsf{M}'_{(1,3)i})E_1\wedge E_3 + (\partial_i\mathsf{M}'_{(2,3)i})E_2\wedge E_3\\ &\quad + \left(\mathsf{M}'_{(1,3)i}\Gamma^{(1,2)}_{i(1,3)} + \mathsf{M}'_{(2,3)i}\Gamma^{(1,2)}_{i(2,3)}\right)E_1\wedge E_2\\ &= (\partial_i\mathsf{M}'_{(1,3)i})E_1\wedge E_3 + (\partial_i\mathsf{M}'_{(2,3)i})E_2\wedge E_3\\ &\quad + \left(-\mathsf{M}'_{(1,3)i}\mathsf{B}^2{}_i + \mathsf{M}'_{(2,3)i}\mathsf{B}^1{}_i\right)E_1\wedge E_2\\ &= (\partial_i\mathbf{M}'_{1i})E_1\wedge E_3 + (\partial_i\mathbf{M}'_{2i})E_2\wedge E_3 - C\mathbf{M}'_{12}E_1\wedge E_2\\ &= \lambda(\partial_i\mathbf{N}'_{1i})E_1\wedge E_3 + (\partial_i\mathbf{N}'_{2i})E_2\wedge E_3 - \lambda C\mathbf{N}'_{12}E_1\wedge E_2.\end{aligned} \tag{6.23}$$

Conservation of angular momentum contains the terms $\mathsf{F}_0(E_i)\wedge\mathsf{T}'(E^i)+\mathsf{F}'(E_i)\wedge\mathsf{T}_0(E^i)$. The first of these can be written as $\lambda_i\mathsf{T}'_{ai}E_i\wedge E_a$. $\mathsf{T}_0(E^i)$ can be expanded as,

$$\begin{aligned}\mathsf{T}_0(E_1) &= \frac{Eh}{2(1-\nu^2)}\varepsilon(1+\varepsilon)(2+\varepsilon)E_1 = \beta_1 E_1,\\ \mathsf{T}_0(E_2) &= \frac{Eh}{2(1-\nu^2)}\nu\varepsilon(2+\varepsilon)E_2 = \beta_2 E_2,\end{aligned} \tag{6.24}$$

where the final equalities define β_i. This allows us to write $\mathsf{F}'(E_i) \wedge \mathsf{T}_0(E^i)$ as,

$$\mathsf{F}'(E_i) \wedge \mathsf{T}_0(E^i) = \beta_i \mathsf{F}'_{ai} E_a \wedge E_i, \tag{6.25}$$

where the components F'_{ai} are given by $\mathsf{F}'_{ai} = U'_{a|i}$. Assuming that there are no body moments present, we can now express conservation of angular momentum as,

$$\lambda_i \mathsf{T}'_{ai} E_i \wedge E_a - \beta_i \mathsf{F}'_{ai} E_i \wedge E_a + \lambda(\partial_i \mathbf{N}'_{1i}) E_1 \wedge E_3 + (\partial_i \mathbf{N}'_{2i}) E_2 \wedge E_3 - \lambda C \mathbf{N}'_{12} E_1 \wedge E_2 = 0. \tag{6.26}$$

The $E_1 \wedge E_3$ and $E_2 \wedge E_3$ components of this expression lead to,

$$\lambda \mathsf{T}'_{31} - \beta_1 \mathsf{F}'_{31} + \lambda(\partial_i \mathbf{N}'_{1i}) = 0, \quad \mathsf{T}'_{32} - \beta_2 \mathsf{F}'_{32} + (\partial_i \mathbf{N}'_{2i}) = 0, \tag{6.27}$$

Which allows us to express T_{3i} as,

$$\mathsf{T}'_{31} = \frac{\beta_1}{\lambda} \mathsf{F}'_{31} - \partial_1 \mathbf{N}'_{11} - \partial_2 \mathbf{N}'_{12}, \quad \mathsf{T}'_{32} = \beta_2 \mathsf{F}'_{32} - \partial_1 \mathbf{N}'_{21} - \partial_2 \mathbf{N}'_{22}. \tag{6.28}$$

Using all of the results given above, we can express conservation of momentum as,

$$\begin{aligned}
\frac{1-\nu^2}{Eh} \rho_0 \frac{\partial^2}{\partial t^2} \begin{bmatrix} U'_1 \\ U'_2 \\ U'_3 \end{bmatrix} &= \begin{bmatrix} \partial_1^2 + \frac{1-\nu}{2}\partial_2^2 & \frac{1+\nu}{2}\partial_1\partial_2 & -\nu C \partial_1 \\ \frac{1+\nu}{2}\partial_1\partial_2 & \frac{1-\nu}{2}\partial_1^2 + \partial_2^2 & -C\partial_2 \\ \nu C \partial_1 & C\partial_2 & -C^2 \end{bmatrix} \begin{bmatrix} U'_1 \\ U'_2 \\ U'_3 \end{bmatrix} \\
&+ C^2 h^2 \begin{bmatrix} 0 & 0 & 0 \\ 0 & \frac{1-\nu}{6}\partial_1^2 + \frac{1}{3}\partial_2^2 & -\frac{1}{6}C\partial_2 + \frac{1}{6C}\partial_2^3 + \frac{1}{6C}\partial_1^2\partial_2 \\ 0 & \frac{1}{6}C\partial_2 - \frac{1}{6C}\partial_2^3 - \frac{1}{6C}\partial_1^2\partial_2 & -C^2 + \frac{1}{6}(\nu\partial_1^2 + \partial_2^2) - \frac{1}{12C^2}(\partial_1^2 + \partial_2^2)^2 \end{bmatrix} \begin{bmatrix} U'_1 \\ U'_2 \\ U'_3 \end{bmatrix} \\
&+ \frac{\varepsilon(2+\varepsilon)}{2} \begin{bmatrix} 3\partial_1^2 + \partial_2^2 & \frac{1+\nu}{2+\varepsilon}\partial_1\partial_2 & -\frac{2\nu C}{2+\varepsilon}\partial_1 \\ \frac{1+\nu}{2+\varepsilon}\partial_1\partial_2 & \partial_1^2 + \nu\partial_2^2 - \nu C^2 & -2\nu C\partial_2 \\ \frac{2\nu C}{2+\varepsilon}\partial_1 & 2\nu C\partial_2 & \partial_1^2 + \nu\partial_2^2 - \nu C^2 \end{bmatrix} \begin{bmatrix} U'_1 \\ U'_2 \\ U'_3 \end{bmatrix}.
\end{aligned} \tag{6.29}$$

We non-dimensionalise our coordinates by making the substitutions $s = CX^1$, $\theta = CX^2$,

and $\tau = \omega t$ to obtain,

$$\Omega^2 \begin{bmatrix} \partial_\tau^2 & 0 & 0 \\ 0 & \partial_\tau^2 & 0 \\ 0 & 0 & -\partial_\tau^2 \end{bmatrix} \begin{bmatrix} U_1' \\ U_2' \\ U_3' \end{bmatrix} = \begin{bmatrix} \partial_s^2 + \frac{1-\nu}{2}\partial_\theta^2 & \frac{1+\nu}{2}\partial_s\partial_\theta & -\nu\partial_s \\ \frac{1+\nu}{2}\partial_s\partial_\theta & \frac{1-\nu}{2}\partial_s^2 + \partial_\theta^2 & -\partial_\theta \\ -\nu\partial_s & -\partial_\theta & 1 \end{bmatrix} \begin{bmatrix} U_1' \\ U_2' \\ U_3' \end{bmatrix}$$
$$+ \alpha \begin{bmatrix} 0 & 0 & 0 \\ 0 & 2(1-\nu)\partial_s^2 + 4\partial_\theta^2 & -2\partial_\theta + 2\partial_\theta^3 + 2\partial_s^2\partial_\theta \\ 0 & -2\partial_\theta + 2\partial_\theta^3 + 2\partial_s^2\partial_\theta & 12 - 2(\nu\partial_s^2 + \partial_\theta^2) + (\partial_s^2 + \partial_\theta^2)^2 \end{bmatrix} \begin{bmatrix} U_1' \\ U_2' \\ U_3' \end{bmatrix}$$
$$+ \frac{\varepsilon(2+\varepsilon)}{2} \begin{bmatrix} 3\partial_s^2 + \partial_\theta^2 & \frac{1+\nu}{2+\varepsilon}\partial_s\partial_\theta & -\frac{2\nu}{2+\varepsilon}\partial_s \\ \frac{1+\nu}{2+\varepsilon}\partial_s\partial_\theta & \partial_s^2 + \nu\partial_\theta^2 - \nu & -2\nu\partial_\theta \\ -\frac{2\nu}{2+\varepsilon}\partial_s & -2\nu\partial_\theta & \nu - \partial_s^2 - \nu\partial_\theta^2 \end{bmatrix} \begin{bmatrix} U_1' \\ U_2' \\ U_3' \end{bmatrix}. \quad (6.30)$$

Here we have defined the following dimensionless quantities,

$$\Omega^2 = \rho_0 a^2 \omega^2 \frac{1-\nu^2}{Eh} = \rho_s a^2 \omega^2 \frac{1-\nu^2}{E}, \quad \alpha = \frac{h^2}{12a^2}. \quad (6.31)$$

These equations of motion are subject to the following boundary conditions,

$$\begin{aligned} U' \text{ periodic at } \theta = 0, 2\pi, \\ U_a' = \partial_s U_3' = 0 \text{ at } s = \pm l_0/2a. \end{aligned} \quad (6.32)$$

6.3.2 Analytical Solution

Equation (6.30) and its boundary conditions are an eigenvalue problem, which we solve by adapting the method of Leissa, 1973. Note that for this section only, the symbols λ, M, B, and C are repurposed for convenience. We first assume that U' takes the form,

$$\begin{aligned} U_1' &= Ae^{\lambda s}\cos n\theta \cos\tau, \\ U_2' &= Be^{\lambda s}\sin n\theta \cos\tau, \\ U_3' &= Ce^{\lambda s}\cos n\theta \cos\tau. \end{aligned} \quad (6.33)$$

In this section, λ is an unknown wavenumber parameter, and *not* l/l_0. Substituting this into eq. (6.30) we obtain,

$$\Omega^2 \begin{bmatrix} -1 & 0 & 0 \\ 0 & -1 & 0 \\ 0 & 0 & 1 \end{bmatrix} \begin{bmatrix} A \\ B \\ C \end{bmatrix} = \begin{bmatrix} \lambda^2 - \frac{1-\nu}{2} n^2 & \frac{1+\nu}{2}\lambda n & \nu\lambda \\ -\frac{1+\nu}{2}\lambda n & \frac{1-\nu}{2}\lambda^2 - n^2 & -n \\ \nu\lambda & n & 1 \end{bmatrix} \begin{bmatrix} A \\ B \\ C \end{bmatrix}$$
$$+ \alpha \begin{bmatrix} 0 & 0 & 0 \\ 0 & 2(1-\nu)\lambda^2 - 4n^2 & 2n + 2n^3 - 2\lambda^2 n \\ 0 & -2n - 2n^3 + 2\lambda^2 n & 12 - 2(\nu\lambda^2 - n^2) + (\lambda^2 - n^2)^2 \end{bmatrix} \begin{bmatrix} A \\ B \\ C \end{bmatrix}$$
$$+ \frac{\varepsilon(2+\varepsilon)}{2} \begin{bmatrix} 3\lambda^2 - n^2 & \frac{1+\nu}{2+\varepsilon}\lambda n & -\frac{2\nu}{2+\varepsilon}\lambda \\ -\frac{1+\nu}{2+\varepsilon}\lambda n & \lambda^2 - \nu(1+n^2) & 2\nu n \\ -\frac{2\nu}{2+\varepsilon}\lambda & -2\nu n & \nu(1+n^2) - \lambda^2 \end{bmatrix} \begin{bmatrix} A \\ B \\ C \end{bmatrix}. \quad (6.34)$$

We can express eq. (6.34) as,

$$\begin{bmatrix} \mathsf{M}_{11} & \mathsf{M}_{12} & \mathsf{M}_{13} \\ \mathsf{M}_{21} & \mathsf{M}_{22} & \mathsf{M}_{23} \\ \mathsf{M}_{31} & \mathsf{M}_{32} & \mathsf{M}_{33} \end{bmatrix} \begin{bmatrix} A \\ B \\ C \end{bmatrix} = 0. \quad (6.35)$$

In order for this equation to hold for a non trivial $[A, B, C]^T$, we require $\det \mathsf{M} = 0$. This leads to an eighth order equation in λ,

$$\lambda^8 + g_6\lambda^6 + g_4\lambda^4 + g_2\lambda^2 + g_0 = 0, \quad (6.36)$$

where the coefficients $g_i, i = 0, 2, 4, 6$ are algebraic expressions in terms of $n, \nu, \alpha, \varepsilon, \Omega^2$. There will be 8 roots to this equation, but by noting that it is a quartic in λ^2, we can see that these 8 roots can be written in the form,

$$\lambda = \pm\lambda_1,\ \pm\lambda_2,\ \pm\lambda_3,\ \pm\lambda_4. \quad (6.37)$$

Each of these values $\lambda_i, i = 1, \ldots, 4$ is a function of $n, \nu, \alpha, \varepsilon, \Omega^2$. By taking λ to be any of these solutions we have ensured that M has a vanishing determinant for any value of Ω^2.

Given a particular value of λ, A, B, and C can be determined. We denote the values of A, B, and C corresponding to $\lambda = \lambda_i$ by A_i, B_i and C_i respectively, and we denote M assuming $\lambda = \lambda_i$ by M^i (i can take any of the values $1, 2, 3, 4$). If we make the substitution $\lambda_i \mapsto -\lambda_i$ then the matrix M^i becomes,

$$\begin{bmatrix} \mathsf{M}^i_{11} & \mathsf{M}^i_{12} & \mathsf{M}^i_{13} \\ \mathsf{M}^i_{21} & \mathsf{M}^i_{22} & \mathsf{M}^i_{23} \\ \mathsf{M}^i_{31} & \mathsf{M}^i_{32} & \mathsf{M}^i_{33} \end{bmatrix} \mapsto \begin{bmatrix} \mathsf{M}^i_{11} & -\mathsf{M}^i_{12} & -\mathsf{M}^i_{13} \\ -\mathsf{M}^i_{21} & \mathsf{M}^i_{22} & \mathsf{M}^i_{23} \\ -\mathsf{M}^i_{31} & \mathsf{M}^i_{32} & \mathsf{M}^i_{33} \end{bmatrix}. \tag{6.38}$$

Given that $\mathsf{M}^i[A_i, B_i, C_i]^T = 0$, we can also write,

$$\begin{bmatrix} \mathsf{M}^i_{11} & -\mathsf{M}^i_{12} & -\mathsf{M}^i_{13} \\ -\mathsf{M}^i_{21} & \mathsf{M}^i_{22} & \mathsf{M}^i_{23} \\ -\mathsf{M}^i_{31} & \mathsf{M}^i_{32} & \mathsf{M}^i_{33} \end{bmatrix} \begin{bmatrix} A_i \\ -B_i \\ -C_i \end{bmatrix} = 0. \tag{6.39}$$

Hence, if we know the values of A, B, C corresponding to λ_i, then we also know the values corresponding to $-\lambda_i$.

Our solution may be written as a sum of any linear combination of the 8 solutions corresponding to the different values that λ can take. We can write this in full as,

$$\begin{aligned} U_1' &= \left(\sum_{i=1}^{4} \eta_i^+ A_i e^{\lambda_i s} + \sum_{i=1}^{4} \eta_i^- A_i e^{-\lambda_i s} \right) \cos n\theta \cos \tau, \\ U_2' &= \left(\sum_{i=1}^{4} \eta_i^+ B_i e^{\lambda_i s} - \sum_{i=1}^{4} \eta_i^- B_i e^{-\lambda_i s} \right) \sin n\theta \cos \tau, \\ U_3' &= \left(\sum_{i=1}^{4} \eta_i^+ C_i e^{\lambda_i s} - \sum_{i=1}^{4} \eta_i^- C_i e^{-\lambda_i s} \right) \cos n\theta \cos \tau, \end{aligned} \tag{6.40}$$

where η_i^+ and η_i^- are arbitrary constants. By defining a new set of constants by $\eta_i^+ = \xi_i^+ + \xi_i^-$

and $\eta_i^- = \xi_i^+ - \xi_i^-$ we can rewrite this expression as,

$$\begin{aligned} U_1' &= \sum_{i=1}^{4} A_i \left[\xi_i^+(e^{\lambda_i s} + e^{-\lambda_i s}) + \xi_i^-(e^{\lambda_i s} - e^{-\lambda_i s})\right] \cos n\theta \cos \tau, \\ U_2' &= \sum_{i=1}^{4} B_i \left[\xi_i^+(e^{\lambda_i s} - e^{-\lambda_i s}) + \xi_i^-(e^{\lambda_i s} + e^{-\lambda_i s})\right] \sin n\theta \cos \tau, \\ U_3' &= \sum_{i=1}^{4} C_i \left[\xi_i^+(e^{\lambda_i s} - e^{-\lambda_i s}) + \xi_i^-(e^{\lambda_i s} + e^{-\lambda_i s})\right] \cos n\theta \cos \tau. \end{aligned} \tag{6.41}$$

We could have considered 8 terms separately, however this representation is convenient as it separates the parts of U_a' that are symmetric and antisymmetric in the axial coordinate s.

We are now in a position to consider boundary conditions. The ends of our tube are clamped. If we choose our coordinate system origin to be at the midway point on the tube, and we define $p = l_0/2a$, then the boundary conditions on U_a' may be written as,

$$U_1'|_{s=\pm p} = U_2'|_{s=\pm p} = U_3'|_{s=\pm p} = \left.\frac{\partial U_3'}{\partial s}\right|_{s=\pm p} = 0 \quad \forall \theta, \tau. \tag{6.42}$$

$\partial U_3'/\partial s$ can be written as,

$$\frac{\partial U_3'}{\partial s} = \sum_{i=1}^{4} C_i \lambda_i \left[\xi_i^+(e^{\lambda_i s} + e^{-\lambda_i s}) + \xi_i^-(e^{\lambda_i s} - e^{-\lambda_i s})\right] \cos n\theta \cos \omega t. \tag{6.43}$$

To show how our boundary conditions are applied let us take some general function $\beta(s)$, which we say must satisfy the boundary conditions $\beta(p) = \beta(-p) = 0$ where p is a known constant. We can decompose β into symmetric and antisymmetric functions $\beta(s) = \beta_+(s) + \beta_-(s)$ where $\beta_+(-s) = \beta_+(s)$ and $\beta_-(-s) = -\beta_-(s)$. Substituting this into the boundary condition we have,

$$\beta_+(p) + \beta_-(p) = \beta_+(p) - \beta_-(p) = 0. \tag{6.44}$$

This implies that $\beta_+(p) = 0$ and $\beta_-(p) = 0$ individually. Using this result we can write our

boundary conditions as,

$$\begin{bmatrix} A_1(e^{\lambda_1 p}+e^{-\lambda_1 p}) & A_2(e^{\lambda_2 p}+e^{-\lambda_2 p}) & A_3(e^{\lambda_3 p}+e^{-\lambda_3 p}) & A_4(e^{\lambda_4 p}+e^{-\lambda_4 p}) \\ B_1(e^{\lambda_1 p}-e^{-\lambda_1 p}) & B_2(e^{\lambda_2 p}-e^{-\lambda_2 p}) & B_3(e^{\lambda_3 p}-e^{-\lambda_3 p}) & B_4(e^{\lambda_4 p}-e^{-\lambda_4 p}) \\ C_1(e^{\lambda_1 p}-e^{-\lambda_1 p}) & C_2(e^{\lambda_2 p}-e^{-\lambda_2 p}) & C_3(e^{\lambda_3 p}-e^{-\lambda_3 p}) & C_4(e^{\lambda_4 p}-e^{-\lambda_4 p}) \\ C_1\lambda_1(e^{\lambda_1 p}+e^{-\lambda_1 p}) & C_2\lambda_2(e^{\lambda_2 p}+e^{-\lambda_2 p}) & C_3\lambda_3(e^{\lambda_3 p}+e^{-\lambda_3 p}) & C_4\lambda_4(e^{\lambda_4 p}+e^{-\lambda_4 p}) \end{bmatrix} \begin{bmatrix} \xi_1^+ \\ \xi_2^+ \\ \xi_3^+ \\ \xi_4^+ \end{bmatrix} = 0,$$

$$\begin{bmatrix} A_1(e^{\lambda_1 p}-e^{-\lambda_1 p}) & A_2(e^{\lambda_2 p}-e^{-\lambda_2 p}) & A_3(e^{\lambda_3 p}-e^{-\lambda_3 p}) & A_4(e^{\lambda_4 p}-e^{-\lambda_4 p}) \\ B_1(e^{\lambda_1 p}+e^{-\lambda_1 p}) & B_2(e^{\lambda_2 p}+e^{-\lambda_2 p}) & B_3(e^{\lambda_3 p}+e^{-\lambda_3 p}) & B_4(e^{\lambda_4 p}+e^{-\lambda_4 p}) \\ C_1(e^{\lambda_1 p}+e^{-\lambda_1 p}) & C_2(e^{\lambda_2 p}+e^{-\lambda_2 p}) & C_3(e^{\lambda_3 p}+e^{-\lambda_3 p}) & C_4(e^{\lambda_4 p}+e^{-\lambda_4 p}) \\ C_1\lambda_1(e^{\lambda_1 p}-e^{-\lambda_1 p}) & C_2\lambda_2(e^{\lambda_2 p}-e^{-\lambda_2 p}) & C_3\lambda_3(e^{\lambda_3 p}-e^{-\lambda_3 p}) & C_4\lambda_4(e^{\lambda_4 p}-e^{-\lambda_4 p}) \end{bmatrix} \begin{bmatrix} \xi_1^- \\ \xi_2^- \\ \xi_3^- \\ \xi_4^- \end{bmatrix} = 0. \tag{6.45}$$

Therefore, for a non-trivial solution, the determinant one of these two matrices must be zero. If we take n, ν, α, p to be given, then we are solving for Ω^2 such that one or both of these determinants vanishes. Once Ω^2 has been found, the coefficients $\xi_i, i = 1, \ldots, 4$ can be found. The algebraic expressions being solved here are very long, but a graphical approach to the problem can work. For convenience we denote the upper matrix in eq. (6.45) $\mathsf{B}^+ = \mathsf{B}^+(n, \nu, \alpha, \varepsilon, p, \Omega^2)$, and the lower matrix $\mathsf{B}^- = \mathsf{B}^-(n, \nu, \alpha, \varepsilon, p, \Omega^2)$.

6.3.3 Chebyshev Solution

We also develop a numerical solution using Chebyshev polynomials, following the method outlined by [Johnson, 1996]. Note that for this section only, the symbols u, b, c, and N are repurposed for convenience. We start similarly to the analytical solution by assuming that U_a' take the form,

$$\begin{aligned} U_1' &= \hat{u}_1(s)\cos n\theta \cos\tau, \\ U_2' &= \hat{u}_2(s)\sin n\theta \cos\tau, \\ U_3' &= \hat{u}_3(s)\cos n\theta \cos\tau. \end{aligned} \tag{6.46}$$

Under this assumption we can write conservation of momentum as,

$$\Omega^2 \begin{bmatrix} -1 & 0 & 0 \\ 0 & -1 & 0 \\ 0 & 0 & 1 \end{bmatrix} \begin{bmatrix} \hat{u}_1 \\ \hat{u}_2 \\ \hat{u}_3 \end{bmatrix} = \begin{bmatrix} \partial_s^2 - \frac{1-\nu}{2} n^2 & \frac{1+\nu}{2} n\partial_s & -\nu\partial_s \\ -\frac{1+\nu}{2} n\partial_s & \frac{1-\nu}{2}\partial_s^2 - n^2 & n \\ -\nu\partial_s & -n & 1 \end{bmatrix} \begin{bmatrix} \hat{u}_1 \\ \hat{u}_2 \\ \hat{u}_3 \end{bmatrix}$$
$$+ \alpha \begin{bmatrix} 0 & 0 & 0 \\ 0 & 2(1-\nu)\partial_s^2 - 4n^2 & 2n + 2n^3 - 2n\partial_s^2 \\ 0 & -2n - 2n^3 + 2n\partial_s^2 & 12 + 2n^2 - 2\nu\partial_s^2 + (\partial_s^2 - n^2)^2 \end{bmatrix} \begin{bmatrix} \hat{u}_1 \\ \hat{u}_2 \\ \hat{u}_3 \end{bmatrix}$$
$$+ \frac{\varepsilon(2+\varepsilon)}{2} \begin{bmatrix} 3\partial_s^2 - n^2 & \frac{1+\nu}{2+\varepsilon} n\partial_s & -\frac{2\nu}{2+\varepsilon}\partial_s \\ -\frac{1+\nu}{2+\varepsilon} n\partial_s & \partial_s^2 - \nu(1+n^2) & 2\nu n \\ -\frac{2\nu}{2+\varepsilon}\partial_s & -2\nu n & \nu(1+n^2) - \partial_s^2 \end{bmatrix} \begin{bmatrix} \hat{u}_1 \\ \hat{u}_2 \\ \hat{u}_3 \end{bmatrix}. \quad (6.47)$$

Defining $\mathsf{u} = [\hat{u}_1, \hat{u}_2, \hat{u}_3]^T$, and making the change of variables $z = s/(l_0/2a) = s/p$ we can write eq. (6.47) as,

$$\mathsf{A}_4 \frac{d^4}{dz^4}\mathsf{u} + \mathsf{A}_2 \frac{d^2}{dz^2}\mathsf{u} + \mathsf{A}_1 \frac{d}{dz}\mathsf{u} + \mathsf{A}_0\mathsf{u} = \Omega^2 \mathsf{A}\mathsf{u}. \quad (6.48)$$

The change of variables from s to z means that our differential equation is now defined over the domain $-1 \leqslant z \leqslant 1$, which is necessary to use the Chebyshev method. To proceed we express $\hat{u}_a(z)$ as sums of Chebyshev polynomials $T_n(z)$,

$$\hat{u}_1(z) = \sum_{n=0}^{N} a_n T_n(z), \quad \hat{u}_2(z) = \sum_{n=0}^{N} b_n T_n(z), \quad \hat{u}_3(z) = \sum_{n=0}^{N} c_n T_n(z). \quad (6.49)$$

Derivatives of these functions can be expressed as,

$$\frac{d^q \hat{u}}{dz^q} = \sum_{n=0}^{N-q} a_n^{(q)} T_n(z) \text{ where } a_n^{(q)} = (\mathsf{E}^q)_{nm} a_m. \quad (6.50)$$

E is an matrix that turns the operation of differentiation into matrix multiplication. E is square ($N+1$ by $N+1$), but the bottom row is all zeros. Consequently the last q rows of E^q are all zeros, which is why the sum in the above expression only goes to $N-q$. For convenience we define the vectors $\mathsf{a} = [a_0, \ldots, a_N]^T$, $\mathsf{b} = [b_0, \ldots, b_N]^T$, and $\mathsf{c} = [c_0, \ldots, c_N]^T$.

If we define I to be the $N+1$ by $N+1$ identity matrix, eq. (6.48) allows us to write,

$$\left(\begin{bmatrix} \mathsf{A}_{4,11}\mathsf{E}^4 & \mathsf{A}_{4,12}\mathsf{E}^4 & \mathsf{A}_{4,13}\mathsf{E}^4 \\ \mathsf{A}_{4,21}\mathsf{E}^4 & \mathsf{A}_{4,22}\mathsf{E}^4 & \mathsf{A}_{4,23}\mathsf{E}^4 \\ \mathsf{A}_{4,31}\mathsf{E}^4 & \mathsf{A}_{4,32}\mathsf{E}^4 & \mathsf{A}_{4,33}\mathsf{E}^4 \end{bmatrix} + \begin{bmatrix} \mathsf{A}_{2,11}\mathsf{E}^2 & \mathsf{A}_{2,12}\mathsf{E}^2 & \mathsf{A}_{2,13}\mathsf{E}^2 \\ \mathsf{A}_{2,21}\mathsf{E}^2 & \mathsf{A}_{2,22}\mathsf{E}^2 & \mathsf{A}_{2,23}\mathsf{E}^2 \\ \mathsf{A}_{2,31}\mathsf{E}^2 & \mathsf{A}_{2,32}\mathsf{E}^2 & \mathsf{A}_{2,33}\mathsf{E}^2 \end{bmatrix} + \begin{bmatrix} \mathsf{A}_{1,11}\mathsf{E} & \mathsf{A}_{1,12}\mathsf{E} & \mathsf{A}_{1,13}\mathsf{E} \\ \mathsf{A}_{1,21}\mathsf{E} & \mathsf{A}_{1,22}\mathsf{E} & \mathsf{A}_{1,23}\mathsf{E} \\ \mathsf{A}_{1,31}\mathsf{E} & \mathsf{A}_{1,32}\mathsf{E} & \mathsf{A}_{1,33}\mathsf{E} \end{bmatrix} + \begin{bmatrix} \mathsf{A}_{0,11}\mathsf{I} & \mathsf{A}_{0,12}\mathsf{I} & \mathsf{A}_{0,13}\mathsf{I} \\ \mathsf{A}_{0,21}\mathsf{I} & \mathsf{A}_{0,22}\mathsf{I} & \mathsf{A}_{0,23}\mathsf{I} \\ \mathsf{A}_{0,31}\mathsf{I} & \mathsf{A}_{0,32}\mathsf{I} & \mathsf{A}_{0,33}\mathsf{I} \end{bmatrix} \right) \begin{bmatrix} \mathsf{a} \\ \mathsf{b} \\ \mathsf{c} \end{bmatrix} = \Omega^2 \begin{bmatrix} -\mathsf{I} & & \\ & -\mathsf{I} & \\ & & \mathsf{I} \end{bmatrix} \begin{bmatrix} \mathsf{a} \\ \mathsf{b} \\ \mathsf{c} \end{bmatrix}. \tag{6.51}$$

This is a $3(N+1)$-dimensional eigenvalue problem, however, the fact that the bottom q rows of E^q are all zeros means that it is not well posed. To overcome this we must make use of the boundary conditions, which we can write as,

$$\hat{u}_1|_{z=\pm1} = \hat{u}_2|_{z=\pm1} = \hat{u}_3|_{z=\pm1} = \left.\frac{d\hat{u}_3}{dz}\right|_{z=\pm1} = 0. \tag{6.52}$$

To express these using the Chebyshev polynomials we make use of the results,

$$\begin{aligned} T_n(\pm1) &= (\pm1)^n, \\ \frac{d^q}{dx^q}T_n(\pm1) &= (\pm1)^{n+q}\prod_{k=0}^{q-1}\frac{n^2-k^2}{2k+1} \text{ for } q \geqslant 1. \end{aligned} \tag{6.53}$$

This allows us to write our boundary conditions as,

$$\sum_{n=0}^{N}(\pm1)^n a_n = 0, \quad \sum_{n=0}^{N}(\pm1)^n b_n = 0, \quad \sum_{n=0}^{N}(\pm1)^n c_n = 0, \quad \sum_{n=0}^{N}(\pm1)^{n+1} n^2 c_n = 0. \tag{6.54}$$

Using this, we can now solve the $3(N+1)$-dimensional eigenvalue problem, which will tell us Ω^2, a, b, and c, which in turn provides an approximate solution to the overall eigenvalue-eigenmode problem.

6.3.4 Finite Element Solution

We wish to be able to validate both the analytical and Chebyshev solutions against three dimensional linearised elasticity when $l = l_0$, i.e. $\varepsilon = 0$. To solve the three dimensional problem we will make use of the finite element method. This provides some validation of our solution techniques, and of the shell theory we have developed.

When small perturbations to an undeformed body are considered, conservation of momentum is given by,

$$\rho_s \frac{\partial^2 U'}{\partial t^2} = \dot{\sigma}(\dot{\nabla}), \tag{6.55}$$

We consider a cylindrical shell of length $l(= l_0)$, wall thickness h, and radius to midsurface a. We will express the equations of motion in terms of the standard cylindrical polar coordinates r, θ, z, with unit basis vectors e_r, e_θ, e_z. For compactness, we rewrite U' as u. u is decomposed as $u = u_r e_r + u_\theta e_\theta + u_z e_z$. The constitutive law allows us to express σ as,

$$\begin{aligned}
\sigma(e_r) &= \frac{E}{2(1+\nu)}\left[2(\partial_r u_r)e_r + \left(r\partial_r \tfrac{u_\theta}{r} + \tfrac{1}{r}\partial_\theta u_r\right)e_\theta + \left(\partial_r u_z + \partial_z u_r\right)e_z\right] \\
&\quad + \frac{E}{2(1+\nu)(1-2\nu)}\left(\tfrac{1}{r}\partial_r(ru_r) + \tfrac{1}{r}\partial_\theta u_\theta + \partial_z u_z\right)e_r, \\
\sigma(e_\theta) &= \frac{E}{2(1+\nu)}\left[\left(r\partial_r \tfrac{u_\theta}{r} + \tfrac{1}{r}\partial_\theta u_r\right)e_r + 2\left(\tfrac{1}{r}\partial_\theta u_\theta + \tfrac{u_r}{r}\right)e_\theta + \left(\tfrac{1}{r}\partial_\theta u_z + \partial_z u_\theta\right)e_z\right] \\
&\quad + \frac{E}{2(1+\nu)(1-2\nu)}\left(\tfrac{1}{r}\partial_r(ru_r) + \tfrac{1}{r}\partial_\theta u_\theta + \partial_z u_z\right)e_\theta, \\
\sigma(e_z) &= \frac{E}{2(1+\nu)}\left[\left(\partial_r u_z + \partial_z u_r\right)e_r + \left(\tfrac{1}{r}\partial_\theta u_z + \partial_z u_\theta\right)e_\theta + 2(\partial_z u_z)e_z\right] \\
&\quad + \frac{E}{2(1+\nu)(1-2\nu)}\left(\tfrac{1}{r}\partial_r(ru_r) + \tfrac{1}{r}\partial_\theta u_\theta + \partial_z u_z\right)e_z.
\end{aligned} \tag{6.56}$$

Taking the inner product of conservation of momentum with the test function v, assuming a time dependence of $\sin \omega t$, and integrating over $\mathcal{B}$, we obtain the weak form,

$$\int_{\mathcal{B}} -\rho_s \omega^2 v \cdot u \, |dx| = \int_{\mathcal{B}} v \cdot \dot{\sigma}(\dot{\nabla}) \, |dx| = \int_{\partial\mathcal{B}} v \cdot \sigma(n) \, |ds| - \int_{\mathcal{B}} \dot{v} \cdot \sigma(\dot{\nabla}) \, |dx| \,. \tag{6.57}$$

$\mathcal{B}$ occupies the region $-l/2 \leqslant z \leqslant l/2$, $a - h/2 \leqslant r \leqslant a + h/2$. The tube is held rigidly at either end, and we assume that there is no normal stress on the free surfaces. This means

that the weak form becomes,

$$\int_{\mathcal{B}} \rho_s \omega^2 v \cdot u \, |dx| = \int_{\mathcal{B}} \dot{v} \cdot \sigma(\dot{\nabla}) \, |dx| \,, \tag{6.58}$$

which can be written in component form as,

$$\begin{aligned} \int_B \rho_s \omega^2 (v_r u_r + v_\theta u_\theta + v_z u_z) |dx| &= \int_B (\partial_r v) \cdot \sigma(e_r) + \tfrac{1}{r} (\partial_\theta v) \cdot \sigma(e_\theta) + (\partial_z v) \cdot \sigma(e_z) \, |dx| \\ &= \int_B v_{r|r} \sigma_{rr} + v_{\theta|r} \sigma_{\theta r} + v_{z|r} \sigma_{zr} \\ &\quad + \tfrac{1}{r} \left(v_{r|\theta} \sigma_{r\theta} + v_{\theta|\theta} \sigma_{\theta\theta} + v_{z|\theta} \sigma_{z\theta} \right) \\ &\quad + v_{r|z} \sigma_{rz} + v_{\theta|z} \sigma_{\theta z} + v_{z|z} \sigma_{zz} \, |dx| \,, \end{aligned} \tag{6.59}$$

where the components $v_{a|b}$ are given by,

$$\begin{aligned} v_{r|r} = \partial_r v_r, \quad v_{\theta|r} = \partial_r v_\theta, \quad v_{z|r} = \partial_r v_z \\ v_{r|\theta} = \partial_\theta v_r - v_\theta, \quad v_{\theta|\theta} = \partial_\theta v_\theta + v_r, \quad v_{z|\theta} = \partial_\theta v_z, \\ v_{r|z} = \partial_z v_r, \quad v_{\theta|z} = \partial_z v_\theta, \quad v_{z|z} = \partial_z v_z, \end{aligned} \tag{6.60}$$

and the components σ_{ab} are given by,

$$\begin{aligned} \sigma_{rr} &= \tfrac{E}{2(1+\nu)} \left(2\partial_r u_r + \tfrac{1}{1-2\nu} \left(\tfrac{1}{r} \partial_r (r u_r) + \tfrac{1}{r} \partial_\theta u_\theta + \partial_z u_z \right) \right), \\ \sigma_{\theta\theta} &= \tfrac{E}{2(1+\nu)} \left(2 \left(\tfrac{1}{r} \partial_\theta u_\theta + \tfrac{u_r}{r} \right) + \tfrac{1}{1-2\nu} \left(\tfrac{1}{r} \partial_r (r u_r) + \tfrac{1}{r} \partial_\theta u_\theta + \partial_z u_z \right) \right), \\ \sigma_{zz} &= \tfrac{E}{2(1+\nu)} \left(2\partial_z u_z + \tfrac{1}{1-2\nu} \left(\tfrac{1}{r} \partial_r (r u_r) + \tfrac{1}{r} \partial_\theta u_\theta + \partial_z u_z \right) \right), \\ \sigma_{\theta r} &= \sigma_{r\theta} = \tfrac{E}{2(1+\nu)} \left(r \partial_r \tfrac{u_\theta}{r} + \tfrac{1}{r} \partial_\theta u_r \right), \\ \sigma_{zr} &= \sigma_{rz} = \tfrac{E}{2(1+\nu)} \left(\partial_r u_z + \partial_z u_r \right), \\ \sigma_{z\theta} &= \sigma_{\theta z} = \tfrac{E}{2(1+\nu)} \left(\tfrac{1}{r} \partial_\theta u_z + \partial_z u_\theta \right). \end{aligned} \tag{6.61}$$

We now assume that u and v take the form,

$$\begin{aligned} u_r(r,\theta,z) = \hat{u}_r(r,z) \cos n\theta, \quad v_r(r,\theta,z) = \hat{v}_r(r,z) \cos n\theta, \\ u_\theta(r,\theta,z) = \hat{u}_\theta(r,z) \sin n\theta, \quad v_\theta(r,\theta,z) = \hat{v}_\theta(r,z) \sin n\theta, \\ u_z(r,\theta,z) = \hat{u}_z(r,z) \cos n\theta, \quad v_z(r,\theta,z) = \hat{v}_z(r,z) \cos n\theta, \end{aligned} \tag{6.62}$$

For convenience we also introduce the notation $\mathfrak{c} = \cos n\theta$ and $\mathfrak{s} = \sin n\theta$. We also choose to non-dimensionalise all lengths using the scale a. Our domain now becomes $-l/2a \leqslant z \leqslant l/2a$, $1 - h/2a \leqslant r \leqslant 1 + h/2a$. The components $v_{a|b}$ may now be written as,

$$\begin{aligned}
v_{r|r} &= \tfrac{1}{a}(\partial_r \hat{v}_r)\,\mathfrak{c} = \tfrac{1}{a}\hat{v}_{r|r}\,\mathfrak{c}, \quad v_{\theta|r} = \tfrac{1}{a}(\partial_r \hat{v}_\theta)\,\mathfrak{s} = \tfrac{1}{a}\hat{v}_{\theta|r}\,\mathfrak{s}, \quad v_{z|r} = \tfrac{1}{a}(\partial_r v_z)\,\mathfrak{c} = \tfrac{1}{a}\hat{v}_{z|r}\,\mathfrak{c} \\
v_{r|\theta} &= -(n\hat{v}_r + \hat{v}_\theta)\,\mathfrak{s} = \hat{v}_{r|\theta}\,\mathfrak{s}, \quad v_{\theta|\theta} = (n\hat{v}_\theta + \hat{v}_r)\,\mathfrak{c} = \hat{v}_{\theta|\theta}\,\mathfrak{c}, \quad v_{z|\theta} = -n\hat{v}_z\,\mathfrak{s} = \hat{v}_{z|\theta}\,\mathfrak{s}, \\
v_{r|z} &= \tfrac{1}{a}(\partial_z \hat{v}_r)\,\mathfrak{c} = \tfrac{1}{a}\hat{v}_{r|z}\,\mathfrak{c}, \quad v_{\theta|z} = \tfrac{1}{a}(\partial_z \hat{v}_\theta)\,\mathfrak{s} = \tfrac{1}{a}\hat{v}_{\theta|z}\,\mathfrak{s}, \quad v_{z|z} = \tfrac{1}{a}(\partial_z \hat{v}_z)\,\mathfrak{c} = \tfrac{1}{a}\hat{v}_{z|z}\,\mathfrak{c},
\end{aligned} \tag{6.63}$$

and the components σ_{ab} can now be written as,

$$\begin{aligned}
\sigma_{rr} &= \tfrac{E}{a(1-\nu^2)}\tfrac{1-\nu}{2}\left(2\partial_r\hat{u}_r + \tfrac{1}{1-2\nu}\left(\tfrac{1}{r}\partial_r(r\hat{u}_r) + \tfrac{n}{r}\hat{u}_\theta + \partial_z\hat{u}_z\right)\right)\mathfrak{c} = \tfrac{E}{a(1-\nu^2)}\hat{\sigma}_{rr}\,\mathfrak{c}, \\
\sigma_{\theta\theta} &= \tfrac{E}{a(1-\nu^2)}\tfrac{1-\nu}{2}\left(2\left(\tfrac{n}{r}\hat{u}_\theta + \tfrac{\hat{u}_r}{r}\right) + \tfrac{1}{1-2\nu}\left(\tfrac{1}{r}\partial_r(r\hat{u}_r) + \tfrac{n}{r}\hat{u}_\theta + \partial_z\hat{u}_z\right)\right)\mathfrak{c} = \tfrac{E}{a(1-\nu^2)}\hat{\sigma}_{\theta\theta}\,\mathfrak{c}, \\
\sigma_{zz} &= \tfrac{E}{a(1-\nu^2)}\tfrac{1-\nu}{2}\left(2\partial_z\hat{u}_z + \tfrac{1}{1-2\nu}\left(\tfrac{1}{r}\partial_r(r\hat{u}_r) + \tfrac{n}{r}\hat{u}_\theta + \partial_z\hat{u}_z\right)\right)\mathfrak{c} = \tfrac{E}{a(1-\nu^2)}\hat{\sigma}_{zz}\,\mathfrak{c}, \\
\sigma_{\theta r} &= \sigma_{r\theta} = \tfrac{E}{a(1-\nu^2)}\tfrac{1-\nu}{2}\left(r\partial_r\tfrac{\hat{u}_\theta}{r} - \tfrac{n}{r}\hat{u}_r\right)\mathfrak{s} = \tfrac{E}{a(1-\nu^2)}\hat{\sigma}_{\theta r}\,\mathfrak{s} = \tfrac{E}{a(1-\nu^2)}\hat{\sigma}_{r\theta}\,\mathfrak{s}, \\
\sigma_{zr} &= \sigma_{rz} = \tfrac{E}{a(1-\nu^2)}\tfrac{1-\nu}{2}\left(\partial_r\hat{u}_z + \partial_z\hat{u}_r\right)\mathfrak{c} = \tfrac{E}{a(1-\nu^2)}\hat{\sigma}_{zr}\,\mathfrak{c} = \tfrac{E}{a(1-\nu^2)}\hat{\sigma}_{rz}\,\mathfrak{c}, \\
\sigma_{z\theta} &= \sigma_{\theta z} = \tfrac{E}{a(1-\nu^2)}\tfrac{1-\nu}{2}\left(-\tfrac{n}{r}\hat{u}_z + \partial_z\hat{u}_\theta\right)\mathfrak{s} = \tfrac{E}{a(1-\nu^2)}\hat{\sigma}_{z\theta}\,\mathfrak{s} = \tfrac{E}{a(1-\nu^2)}\hat{\sigma}_{\theta z}\,\mathfrak{s}\,.
\end{aligned} \tag{6.64}$$

The factor $E/(a(1-\nu^2))$ has been extracted to ensure that the nondimensionalisation is consistent with that used with shell theories. We can now perform the integration over θ in the weak form. Assuming $n > 0$ we obtain,

$$\begin{aligned}
\int \Omega^2(\hat{v}_r\hat{u}_r + \hat{v}_\theta\hat{u}_\theta + \hat{v}_z\hat{u}_z)\,r dr dz = \int r\Big(&\hat{v}_{r|r}\hat{\sigma}_{rr} + \hat{v}_{\theta|r}\hat{\sigma}_{\theta r} + \hat{v}_{z|r}\hat{\sigma}_{zr}\Big) \\
&+ \hat{v}_{r|\theta}\hat{\sigma}_{r\theta} + \hat{v}_{\theta|\theta}\hat{\sigma}_{\theta\theta} + \hat{v}_{z|\theta}\hat{\sigma}_{z\theta} \\
&+ r\Big(\hat{v}_{r|z}\hat{\sigma}_{rz} + \hat{v}_{\theta|z}\hat{\sigma}_{\theta z} + \hat{v}_{z|z}\hat{\sigma}_{zz}\Big)\;dr dz
\end{aligned} \tag{6.65}$$

where Ω^2 is given by,

$$\Omega^2 = \rho_s a^2 \omega^2 \frac{1-\nu^2}{E}. \tag{6.66}$$

ρ_s is the mass per unit volume of the shell, and so is related to ρ_0 (the mass per unit area) by $\rho_s = \rho_0/h$. Hence, we can see that the definition of Ω^2 is consistent between sections. This weak form can be implemented using Fenics [Logg et al., 2012] to solve the eigenproblem

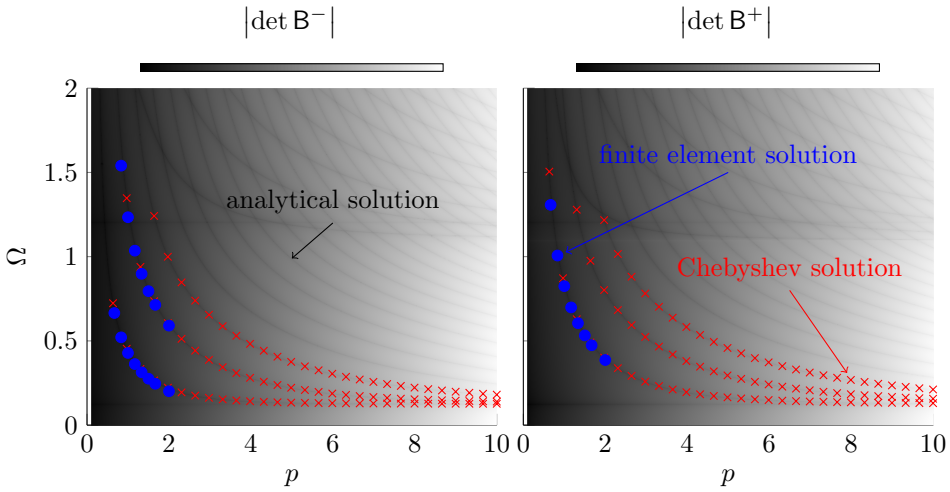


Figure 6.6: Eigenfrequencies of a cylindrical shell with clamped-clamped boundary conditions. Ω is plotted as a function of p, given $\varepsilon = 0$, $n = 2$, $\nu = 0.4$, $\alpha = 0.001$. Red crosses indicate results from the Chebyshev solution method. Filled blue circles indicate results from three dimensional linearised elasticity, found using the finite element method.

with finite elements.

6.3.5 Validation

To compare solutions to the eigenvalue/eigenmode problem we consider a tube with $\varepsilon = 0$, $n = 2$, $\nu = 0.4$, and $\alpha = 0.33^2/12 \times 3^2 = 0.001$. We investigate how the dimensionless frequency Ω depends on p. To find the analytical solution we plot $|\det \mathsf{B}^+|$ and $|\det \mathsf{B}^-|$ over a range of Ω and p values. Solutions will correspond to points in this plot where the determinant goes to zero. We plot solutions from the Chebyshev and finite element over this in fig. 6.6, which indicates very good agreement between the three methods. This indicates that our implementations of the solution methods have been successful, and also provides some validation of our shell theory. This is further supported by the comparison of the eigenmodes found using the three different methods shown in fig. 6.7.

6.3.6 Failure to Predict Onset Frequency

For each of the tube geometries shown in fig. 6.1, for which protocol 1 was followed, we can calculate the eigenfrequencies of the first few modes of oscillation of the corresponding axially strained cylinder. These are compared to the observed frequencies at onset in fig. 6.8, in which it is clear that there is no correlation between the two.

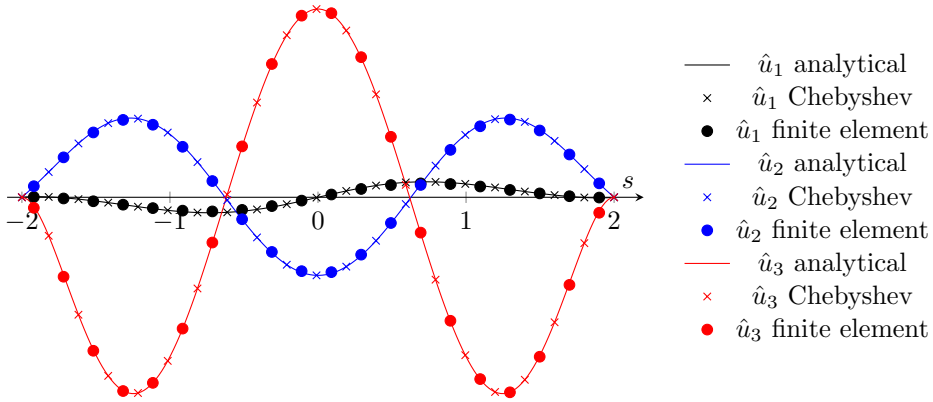


Figure 6.7: Eigenmode of a cylindrical shell with clamped-clamped boundary conditions, with parameters $\varepsilon = 0$, $n = 2$, $\nu = 0.4$, $\alpha = 0.001$, $p = 2$, and $\Omega = 0.597$.

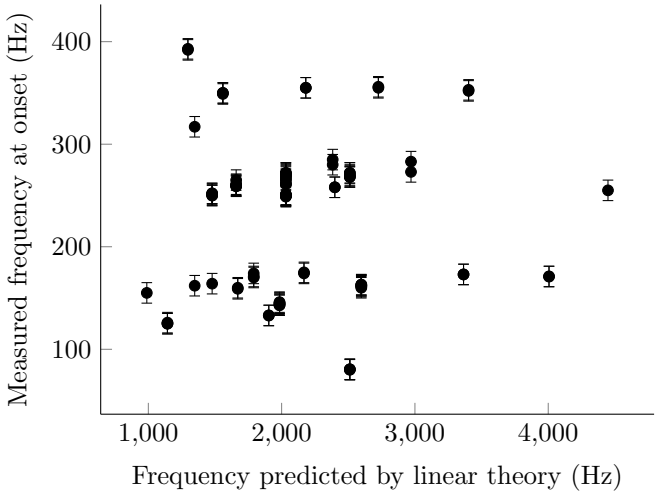


Figure 6.8: The first mode of oscillation of a cylinder, assuming an azimuthal mode number of 2, $E = 1\,\mathrm{MPa}$, $\nu = 0.5$, $\rho_s = 1000\,\mathrm{kg\,m^{-3}}$, calculated for each of the experiments in fig. 6.1 and compared with the observed onset frequency.

6.4 Group and Phase Velocity

We have seen that the linear theory fails to predict onset frequencies on its own, however, in later sections it will be useful to have an understanding of the speed at which elastic waves travel along the tube. To find this we consider eq. (6.30), which we duplicate here for convenience,

$$\Omega^2 \begin{bmatrix} \partial_\tau^2 & 0 & 0 \\ 0 & \partial_\tau^2 & 0 \\ 0 & 0 & -\partial_\tau^2 \end{bmatrix} \begin{bmatrix} U_1' \\ U_2' \\ U_3' \end{bmatrix} = \begin{bmatrix} \partial_s^2 + \frac{1-\nu}{2}\partial_\theta^2 & \frac{1+\nu}{2}\partial_s\partial_\theta & -\nu\partial_s \\ \frac{1+\nu}{2}\partial_s\partial_\theta & \frac{1-\nu}{2}\partial_s^2 + \partial_\theta^2 & -\partial_\theta \\ -\nu\partial_s & -\partial_\theta & 1 \end{bmatrix} \begin{bmatrix} U_1' \\ U_2' \\ U_3' \end{bmatrix}$$
$$+ \alpha \begin{bmatrix} 0 & 0 & 0 \\ 0 & 2(1-\nu)\partial_s^2 + 4\partial_\theta^2 & -2\partial_\theta + 2\partial_\theta^3 + 2\partial_s^2\partial_\theta \\ 0 & -2\partial_\theta + 2\partial_\theta^3 + 2\partial_s^2\partial_\theta & 12 - 2(\nu\partial_s^2 + \partial_\theta^2) + (\partial_s^2 + \partial_\theta^2)^2 \end{bmatrix} \begin{bmatrix} U_1' \\ U_2' \\ U_3' \end{bmatrix}$$
$$+ \frac{\varepsilon(2+\varepsilon)}{2} \begin{bmatrix} 3\partial_s^2 + \partial_\theta^2 & \frac{1+\nu}{2+\varepsilon}\partial_s\partial_\theta & -\frac{2\nu}{2+\varepsilon}\partial_s \\ \frac{1+\nu}{2+\varepsilon}\partial_s\partial_\theta & \partial_s^2 + \nu\partial_\theta^2 - \nu & -2\nu\partial_\theta \\ -\frac{2\nu}{2+\varepsilon}\partial_s & -2\nu\partial_\theta & \nu - \partial_s^2 - \nu\partial_\theta^2 \end{bmatrix} \begin{bmatrix} U_1' \\ U_2' \\ U_3' \end{bmatrix}, \quad (6.67a)$$

$$\text{where } \Omega^2 = \rho_0 a^2 \omega^2 \frac{1-\nu^2}{Eh} = \rho_s a^2 \omega^2 \frac{1-\nu^2}{E}, \quad \alpha = \frac{h^2}{12a^2}. \quad (6.67b)$$

To find the **group and phase velocities** of waves in this system we assume a solution of the form,

$$\begin{aligned} U_1' &= Ae^{\imath ks} \cos n\theta \cos \tau, \\ U_2' &= Be^{\imath ks} \sin n\theta \cos \tau, \\ U_3' &= Ce^{\imath ks} \cos n\theta \cos \tau, \end{aligned} \quad (6.68)$$

which, when substituted into eq. (6.30) gives,

$$\Omega^2 \begin{bmatrix} -1 & 0 & 0 \\ 0 & -1 & 0 \\ 0 & 0 & 1 \end{bmatrix} \begin{bmatrix} A \\ B \\ C \end{bmatrix} = \begin{bmatrix} -k^2 - \frac{1-\nu}{2} n^2 & \frac{1+\nu}{2} \imath k n & \nu \imath k \\ -\frac{1+\nu}{2} \imath k n & -\frac{1-\nu}{2} k^2 - n^2 & -n \\ \nu \imath k & n & 1 \end{bmatrix} \begin{bmatrix} A \\ B \\ C \end{bmatrix}$$
$$+ \alpha \begin{bmatrix} 0 & 0 & 0 \\ 0 & -2(1-\nu)k^2 - 4n^2 & -2n(1+n^2+k^2) \\ 0 & 2n(1+n^2+k^2) & 12 + 2(\nu k^2 + n^2) + (k^2+n^2)^2 \end{bmatrix} \begin{bmatrix} A \\ B \\ C \end{bmatrix}$$
$$+ \frac{\varepsilon(2+\varepsilon)}{2} \begin{bmatrix} -3k^2 - n^2 & \frac{1+\nu}{2+\varepsilon} \imath k n & -\frac{2\nu}{2+\varepsilon} \imath k \\ -\frac{1+\nu}{2+\varepsilon} \imath k n & -k^2 - \nu(1+n^2) & 2\nu n \\ -\frac{2\nu}{2+\varepsilon} \imath k & -2\nu n & \nu(1+n^2) + k^2 \end{bmatrix} \begin{bmatrix} A \\ B \\ C \end{bmatrix}, \quad (6.69)$$

which we write in the more compact form $\mathsf{M}[A\ B\ C]^T = 0$. The dispersion relation is then given by $\det \mathsf{M} = 0$. This is a 6th order polynomial in Ω of the form,

$$a\Omega^6 + b\Omega^4 + c\Omega^2 - 1 = 0, \quad (6.70)$$

which we can see is actually a 3rd order polynomial in Ω^2. Hence the 6 roots of this polynomial will take the form,

$$\Omega = \pm\Omega_1,\ \pm\Omega_2,\ \pm\Omega_3, \quad (6.71)$$

where Ω_i are functions of k, n, ν, α, and ε. Mathematica is used to find the (very long) algebraic expressions for Ω_i.

The longitudinal dependence of the solution has the form $e^{\imath k s} = e^{-\imath k X^1/a}$, hence, if λ is the longitudinal wavelength of the waves under consideration, then $k = 2\pi a/\lambda = k'a$, where k' is the dimensional wavenumber, while k is dimensionless. From the dispersion relationship we have found $\Omega = \Omega(k, n, \nu, \alpha)$. For the group and phase velocity we need $\omega = \omega(k', \ldots)$, from which we can calculate the group and phase velocities as $c_g = \partial\omega/\partial k'$ and $c_p = \omega/k'$

respectively. Given that $\omega = \Omega\sqrt{E/\rho_s(1-\nu^2)a^2}$ we have,

$$\begin{aligned} c_p &= \frac{\omega}{k'} = \frac{a}{k}\frac{\Omega}{a}\sqrt{\frac{E}{\rho_s(1-\nu^2)}} = \frac{\Omega}{k}\sqrt{\frac{E}{\rho_s(1-\nu^2)}}, \\ c_g &= \frac{\partial\omega}{\partial k'} = a\frac{\partial\omega}{\partial k} = \frac{\partial\Omega}{\partial k}\sqrt{\frac{E}{\rho_s(1-\nu^2)}}. \end{aligned} \tag{6.72}$$

Hence, given k, n, ν, α, ε, and $\sqrt{E/\rho_s(1-\nu^2)}$, we can calculate three group velocities and three phase velocities using Ω_1, Ω_2, and Ω_3. This will be of use in §8.

6.5 Summary

In this chapter we have shown how protocol 1 (see §3.6.1) can be used to find the conditions at the onset of self-excited oscillations in flexible tubes. We have demonstrated an acceptable repeatability in the measurement of the conditions at onset, given a particular tube, quantifying the observed variability.

The effect of the boundary conditions on the oscillations observed has been shown to be far more limited than when water has been used as the working fluid, with the geometry of the flexible tube being by far the most significant factor.

Applying the linearised theory derived in §5.7 to an axially strained cylinder, we have shown that this approach fails to predict the frequency at onset of oscillations. Understanding this failure is an important aim of the remaining chapters of this thesis. We will begin with a more detailed observation of the oscillations themselves, which have been recorded in detail using high speed cameras.

Chapter 7

3D Motion of the Tube: Stereoscopic Reconstruction and Scaling

In protocol 2 (see §3.6.2) we describe how multiple high speed cameras are used to record self-excited oscillations of flexible tubes. The use of *multiple* cameras, recording simultaneously, allows the three-dimensional shape of the flexible tube during oscillations to be reconstructed. In this chapter we will describe this process in detail, and present some useful results based on the reconstruction. The work and results presented in this chapter form the basis for our article [Gregory et al., 2017c].

Data from the experiments detailed in this chapter is available at [Gregory et al., 2017b].

7.1 Three dimensional Reconstruction

It is well understood that if we have certain information about two cameras, and we take an image of a point in three dimensional space from both of these cameras, then using the position of the point in both images, the three dimensional location can be found, or **triangulated** [Hartley and Zisserman, 2004]. The specific information we need about the two cameras is divided into intrinsic and extrinsic information.

The **intrinsic** information of a camera is the set of properties that would define an imaginary pinhole camera that you could replace the real camera with, and obtain identical

images, assuming that the pinhole camera is positioned in the same place as the real camera. The pinhole camera model is often appended with a model to account for radial and tangential distortion of the image by the lens. The **extrinsic** information of a camera is the position and orientation of the camera relative to some origin.

To find the intrinsic and extrinsic properties of two cameras, we can take multiple images of chequerboards from both. Generally we take images of 10 to 20 differently oriented chequerboards (giving 20 to 40 images) to get a good estimate of the properties. Finding these parameters is known as **calibrating** the camera. Obtaining the chequerboard images is included in protocol 2, and we performed calibration using the MATLAB® computer vision system toolbox [MATLAB, 2017].

With two calibrated cameras, we can triangulate a point in three dimensional space if the point is visible in both images. To reconstruct the motion of the surface of a flexible tube, we must do this for multiple points on the tube surface, and at multiple times. A difficulty in doing this is that, in every image taken, there are multiple points visible. In order for reconstruction of the tube to be successful, we must be able to identify precisely which point is which in each camera's image, and in images taken at different times. This association of points between the images of the two cameras, and between images taken at different times, is the subject of the following section.

7.1.1 Image Processing

The high speed cameras record at 12 500 fps, and are triggered together, so that every $\Delta t = 80\,\mu s$ two images of the flexible tube are taken. A schematic of the two cameras and the flexible tube is shown in fig. 7.1, in which the cameras are represented with their pinhole models. Dots are drawn on the flexible tube (shown in white in fig. 7.1), which indicate a set of **material points** that we would like to track over time in three dimensions.

To find the three-dimensional tracks of the material points, we must first find the locations of the dots within each image. We refer to these coordinate pairs, measured in pixels, as **points**. The dots on the tube surface are drawn in white, are spaced by approximately 1 mm, and have a diameter of approximately 0.7 mm. We take the material points to be the centres of the dots, and we find them by first taking a two-dimensional convolution of the

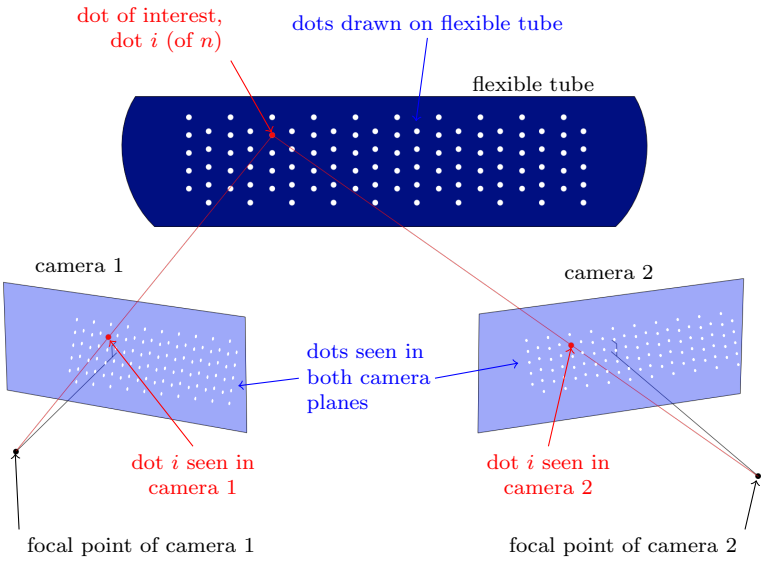


Figure 7.1: Schematic of the high speed camera setup.

image with a "mexican hat" function of the form,

$$\frac{1}{\pi\sigma^4}\left(1-\frac{u^2+v^2}{2\sigma^2}\right)e^{-\frac{u^2+v^2}{2\sigma^2}}, \tag{7.1}$$

where σ is the expected radius of the dot in the image, and u, v are pixel coordinates. The convolution effectively smooths the image, removing any artefacts from drawing the dots, leaving peaks in the centroid of each dot. These peaks are then used as the locations of each point.

Hence at each time instance, we have two collections of points, representing the material points as seen from each camera. If there are n points on the tube, and m frames in our video, then in total we will have found the locations of $2nm$ points. To make use of this data, we need to identify each unique material point in each camera and over time.

To associate points across time for a single camera's set of images, the points at t and $t+\Delta t$ are compared, and if two points are within a certain distance of each other, then it is assumed that these represent the same point. This works because the frame rate (12 500 fps) is much larger than the frequency of the observed vibrations (approximately 500 Hz), so motions between frames are small.

A pair of corresponding points in the two camera images are illustrated in Figure 7.1, but finding these pairings at each instant in time is more complex. First we consider the

line drawn from the focal point of camera 2 to dot i in the image, which we will call a **ray**. Anything on this ray in three-dimensional space will appear at the same highlighted location in camera 2. However, from camera 1, the ray will appear as a line. Therefore, if a point's location is known in one camera image, then it must lie on a specific line in the other image. This line is known as an **epipolar line** [Hartley and Zisserman, 2004]. Hence, for a pair of points, one in each camera image, to correspond to the same material point, they must each lie on the epipolar line of the other. However, because of the specific arrangement of the cameras and dots, this does not usually provide a unique set of pairs. The relative positioning of the cameras means that the epipolar lines are all approximately horizontal, and the dots drawn on the tube are arranged in horizontal rows, so multiple dots can be very close to a given epipolar line. To overcome this, we specify 10 corresponding point pairs between the two images (20 points in total), and these 10 pairs are then used to find the best fitting projective transformation from camera 1 to camera 2. Applying this transformation to the image from camera 1 places each point close to the corresponding point in the image from camera 2, allowing all the remaining point pairs to be found. This result is then checked for consistency with the epipolar line condition.

In addition to tracing material points over time as the self-excited oscillations occur, we must also find the locations of the material points on the tube when it is unstrained. This is necessary for the calculation of the kinematic variables described in §5.3, which we will use to investigate the dynamics of the self-excited oscillation more closely. To achieve this a single image is taken from each camera when the tube is held in its unstrained state. Pairing of points must then also be completed between the two images of the tube in its unstrained state and images from the high speed video of self-excited oscillations. This pairing is done using the methods described in the previous paragraph.

Once point pairs are known over time, the camera calibration can be used to find three-dimensional traces over time of the material points. The spatial resolution of this trace is limited by the size of the pixels in the high speed video. This results in point traces with distinct jumps in position. These jumps are by no more than 0.1 mm in three-dimensional space, compared to variations in position on the order of 2 mm over the course of the self-excited oscillations. An example of such a trace is shown in fig. 7.2. For this reason we

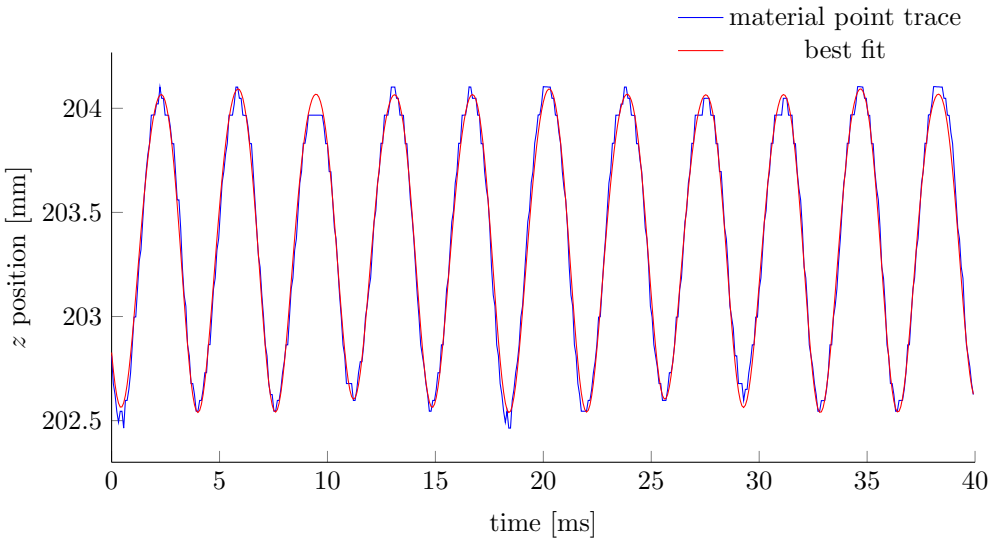


Figure 7.2: The z component of a three dimensional material point trace, along with a fit based on eq. (7.2).

smooth the three-dimensional point traces by fitting functions of the form,

$$\sum_{i=1}^{8} A_i \sin(\omega_i t), \tag{7.2}$$

to the three position components, where A_i and ω_i are chosen to fit the empirical data. These fits work well because the videos are of quasi-steady behaviour at the onset of oscillation, and the observed motions are close to sinusoidal. 8 terms have been found to be sufficient to match the experimental data. This smoothing is necessary in order for derivatives of the point traces to give meaningful results.

7.1.2 Kinematic Reconstruction

So far we have shown how we can obtain multiple three dimensional traces of material points on the surface of a flexible tube, and the three dimensional positions of these material points when the tube is not strained. We now need to take these three dimensional traces and use them to calculate the kinematic variables (the strain tensor E and the change of curvature tensor H) of the deformed surface.

For each material point we have three fits of the type illustrated in fig. 7.2, representing the three components of the material points motion in three dimensional space. If there are N material points then we have $3N$ functions, $x_i(t), y_i(t), z_i(t),\ i = 1, \ldots, N$, and $3N$ locations

$x_{0i}, y_{0i}, z_{0i},\ i = 1, \ldots, N$ representing the material points over time and at their undeformed locations respectively. We differentiate $x_i(t), y_i(t), z_i(t)$ to get the material velocity and acceleration at the N positions, $\dot{x}_i(t), \dot{y}_i(t), \dot{z}_i(t),\ i = 1, \ldots, N$ and $\ddot{x}_i(t), \ddot{y}_i(t), \ddot{z}_i(t),\ i = 1, \ldots, N$.

First of all we assign coordinate values to each of the N material points, representing the value of the convected coordinates $\{x^i\}, i = 1, 2$ at these locations. At a given time $t = \tau$ we fit polynomial functions $x_p(x^1, x^2), y_p(x^1, x^2), z_p(x^1, x^2)$ to the N points $x_i(\tau), y_i(\tau), z_i(\tau),\ i = 1, \ldots, N$, so that we now have the three-dimensional position of a set of points on the shell as a function of the chosen convected coordinates. We also fit polynomial functions $\dot{x}_p(x^1, x^2), \dot{y}_p(x^1, x^2), \dot{z}_p(x^1, x^2)$ and $\ddot{x}_p(x^1, x^2), \ddot{y}_p(x^1, x^2), \ddot{z}_p(x^1, x^2)$ to the sets of velocities and accelerations $\dot{x}_i(\tau), \dot{y}_i(\tau), \dot{z}_i(\tau),\ i = 1, \ldots, N$ and $\ddot{x}_i(\tau), \ddot{y}_i(\tau), \ddot{z}_i(\tau),\ i = 1, \ldots, N$. The positions of the material points in their unstrained state $x_{0i}, y_{0i}, z_{0i},\ i = 1, \ldots, N$ are used to find the polynomial functions $x_{0p}(x^1, x^2), y_{0p}(x^1, x^2), z_{0p}(x^1, x^2)$, which represent the unstrained surface of the tube. All of these polynomial functions can be differentiated with respect to the convected coordinates $\{x^i\}, i = 1, 2$ to find any kinematic quantities of interest from §5.3.

In fig. 7.3 we show an example result from this process. The raw images from the high speed cameras are shown, with the material points identified. These points are shown after being triangulated in three dimensions along with the surface fitted to them. This surface is plotted twice more, but coloured according to the value of the two **principal strains** (the eigenvalues of E). Over these surfaces we have also shown the directions associated with the principal strains (eigenvectors of E). An eigenvalue of 1 corresponds to no strain, a value less than 1 corresponds to compression, and a value greater than 1 corresponds to tension. The eigenvectors give the direction in which the strain is occurring. We can see that the first principal strain is approximately aligned with the longitudinal direction, and is tensile. This is due to the dominant pre-strain of the elastic tube. By contrast, the second principal strain, which is primarily in the azimuthal direction, is a mixture of compression and tension, and is generally closer to 1.

In fig. 7.4 we show the **principal curvatures** of the deformed surface, i.e. the eigenvectors and values of b. For a cylinder, which the tube is in its undeformed state, the principal curvatures would be 0 in the longitudinal direction and $1/a = 0.33\,\mathrm{mm}^{-1}$ in the azimuthal direction. We see that in the deformed tube the curvatures are still closely aligned to the

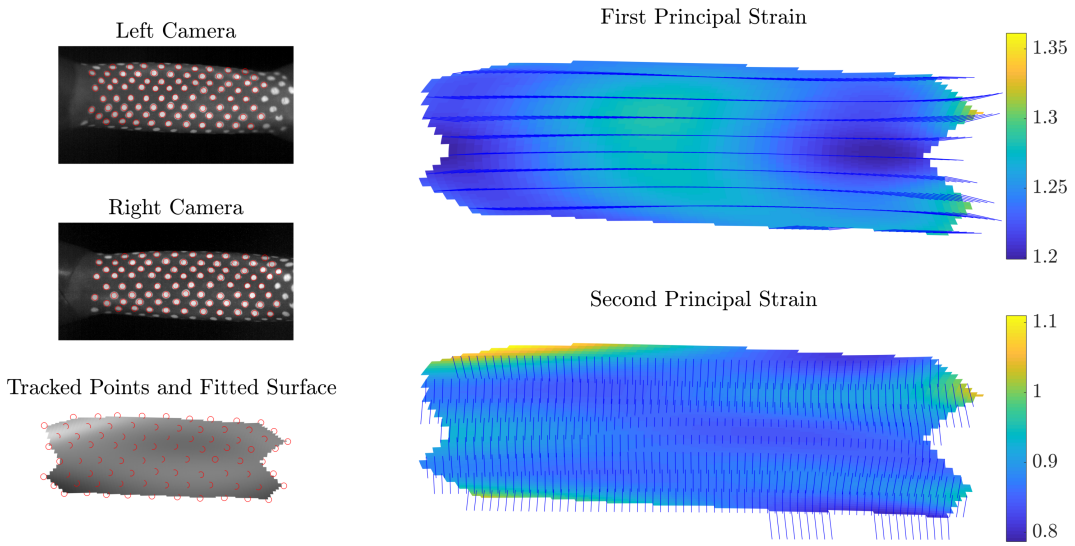


Figure 7.3: A typical image of the principal strains of the flexible tubes, shown along with the principal strain directions (illustrated with unit vectors). On the left the original high speed camera images are shown with the tracked surface points, and a view of the three-dimensional triangulation with the surface fitted to them.

longitudinal and azimuthal directions, and can see that the squashing of the tube results in a slightly negative longitudinal curvature and a slight reduction in the azimuthal curvature towards the centre of the tube.

7.2 Kinematic Calculations

To gain a better physical understanding of the deformation of flexible tubes during self-excited oscillations, we will consider the energy of deformation, since this is what is differentiated to obtain the constitutive equations, and ultimately defines the form taken by the dynamical equations.

From §5.6.3, the energy of deformation is given by,

$$\rho_0 U = \frac{Eh}{2(1-\nu^2)}\left((1-\nu)\,\mathrm{tr}(\mathsf{E}^2)+\nu\,\mathrm{tr}(\mathsf{E})^2\right)+\frac{Eh^3}{24(1-\nu^2)}\left((1-\nu)\,\mathrm{tr}(\mathsf{H}^2)+\nu\,\mathrm{tr}(\mathsf{H})^2\right). \quad (7.3)$$

U is the internal energy per unit mass of the shell, defined on the reference configuration, ρ_0 is the time independent area density of the shell on the reference configuration, E is Young's modulus, ν is Poisson's ratio, h is the shell thickness (which in Koiter's theory is assumed constant), E is the two-dimensional Green-Lagrange strain tensor defined on the reference

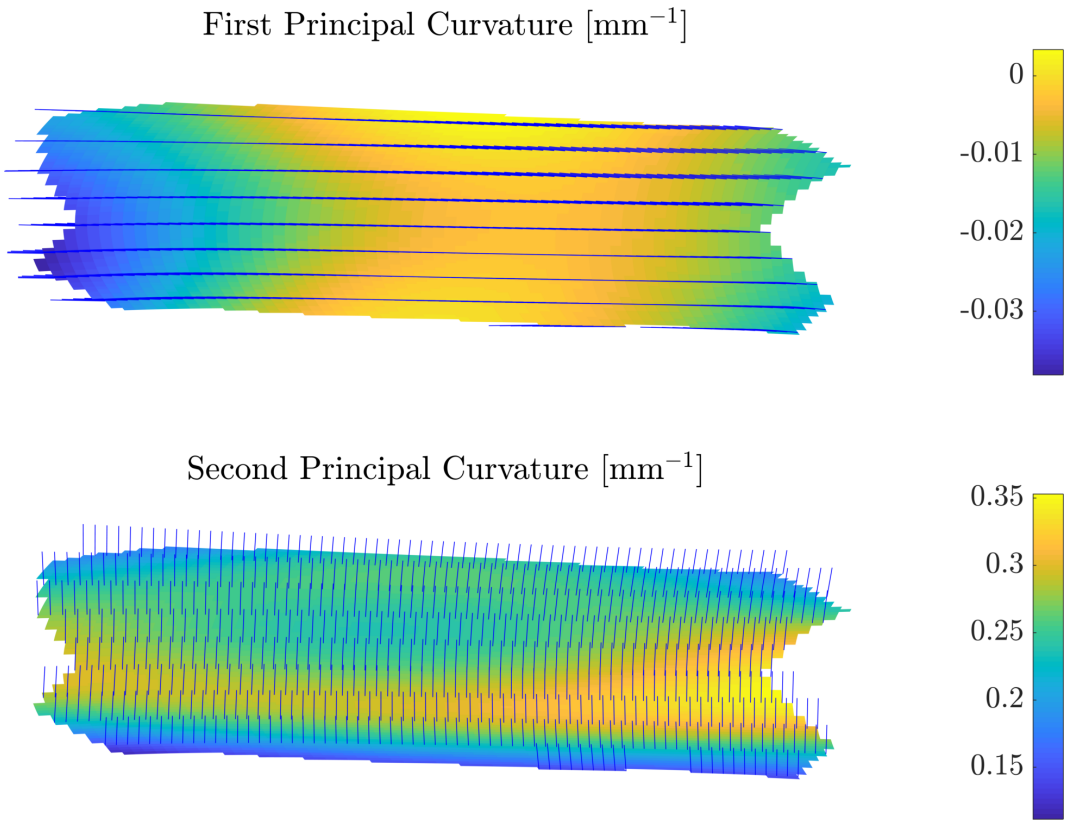


Figure 7.4: A typical image of the principal curvatures of the flexible tube, shown along with the principal curvature directions (illustrated with unit vectors).

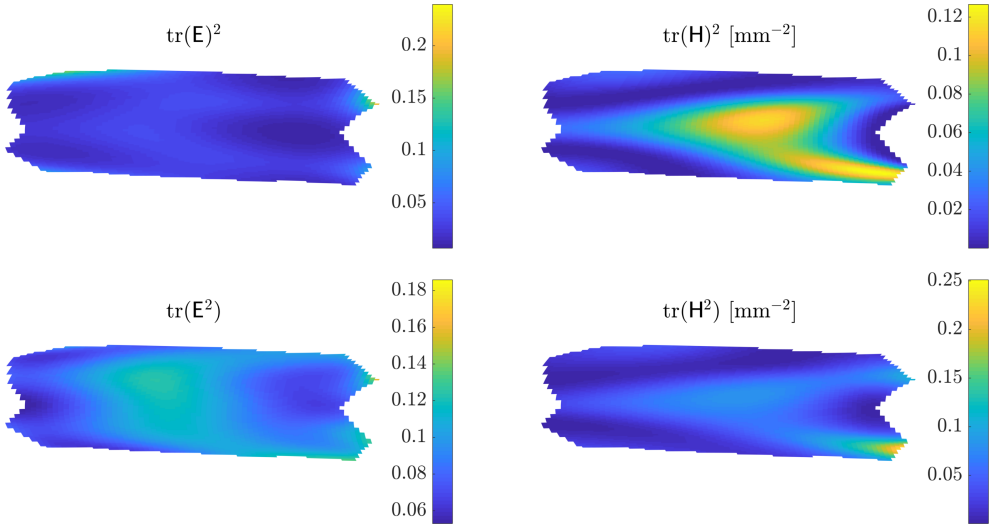


Figure 7.5: Values of the kinematic variables $\mathrm{tr}(\mathsf{E}^2)$, $\mathrm{tr}(\mathsf{E})^2$, $\mathrm{tr}(\mathsf{H}^2)$, and $\mathrm{tr}(\mathsf{H})^2$.

configuration, H is the change of curvature tensor, and tr is the trace operator.

The energy of deformation is split into two terms. The first represents energy associated with stretching, and the second energy associated with bending. Both of these quantities are independent of the chosen coordinate system. We wish to compare their relative importance. To do this we first calculate the kinematic quantities $\mathrm{tr}(\mathsf{E}^2)$, $\mathrm{tr}(\mathsf{E})^2$, $\mathrm{tr}(\mathsf{H}^2)$, and $\mathrm{tr}(\mathsf{H})^2$ in fig. 7.5. Using these values we can find the stretching and bending energies, and these are shown in fig. 7.6, from which it is clear that the bending energy is around 2 orders of magnitude smaller than the stretching energy. We find this result to be typical of the oscillations we observe. This is an important simplification, as if we neglect the bending energy, the order of the equations governing the shell reduce from 4 to 2.

7.3 Scaling Analysis

We now wish to understand why bending energy is dominated by stretching energy, and under what circumstances this will be continue to be true. To do this we develop a scaling analysis, which will rely heavily on the new way of expressing the **change of curvature tensor** H developed in §5.3.5. As a reminder, $\mathsf{H}(Y)$ can be expressed as,

$$\begin{aligned}\mathsf{H}(Y) &= (\mathsf{U}-\mathsf{G})\mathsf{B}(Y) - \bar{\mathsf{F}}\left((RE_3\tilde{R})\cdot(Y\cdot\partial B)\right)\\ &= (\mathsf{U}-\mathsf{G})\mathsf{B}(Y) - \bar{\mathsf{F}}\left(e_3\cdot(Y\cdot\partial B)\right).\end{aligned} \tag{7.4}$$

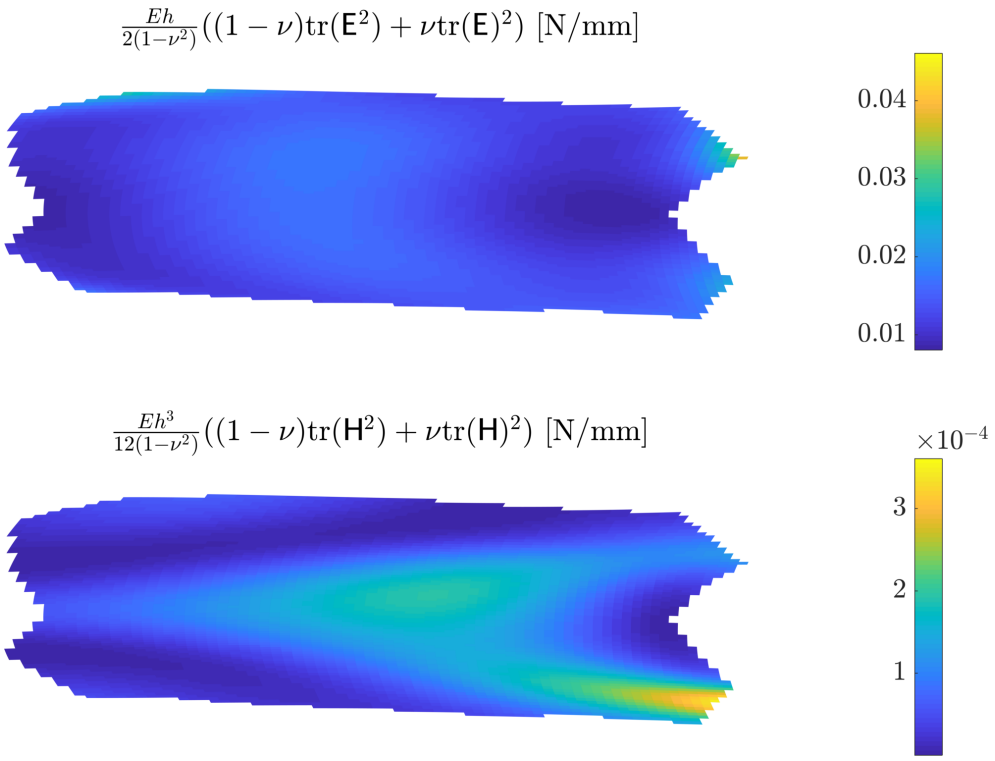


Figure 7.6: The stretching energy (top image) and bending energy (bottom image) associated with the deformation of the flexible tube.

The first term in this expression expresses how, if the reference configuration $\mathcal{B}$ is curved, then stretching will result in a change of curvature. The second term expresses how variation in the rotor $R = \exp(-B/2)$, which characterises local rotations between the reference and spatial configurations, over the shell also gives rise to a change of curvature.

To progress, we need to estimate the kinematic quantities $\mathrm{tr}(\mathsf{E}^2)$, $\mathrm{tr}(\mathsf{E})^2$, $\mathrm{tr}(\mathsf{H}^2)$, and $\mathrm{tr}(\mathsf{H})^2$. If α_i are the eigenvalues of the linear function A, then $\mathrm{tr}(\mathsf{A})^2 = \alpha_1^2 + 2\alpha_1\alpha_2 + \alpha_2^2$ and $\mathrm{tr}(\mathsf{A}^2) = \alpha_1^2 + \alpha_2^2$. We know that the eigenvalues of the **strain tensor** E are $\frac{1}{2}(\lambda_i^2 - 1)$ (λ_i are the **principal strains**) and that $\lambda_1 \sim \lambda$, $\lambda_2 \sim 1$, where λ is the initial axial strain of the tube. This allows us to get an order of magnitude estimate for $\mathrm{tr}(\mathsf{E}^2)$ and $\mathrm{tr}(\mathsf{E})^2$ of $(\lambda^2 - 1)^2/4$. If we take $\lambda = 1.3$ then we have $\mathrm{tr}(\mathsf{E}^2) \sim \mathrm{tr}(\mathsf{E})^2 \sim 0.1$, which is in agreement with fig. 7.5.

To understand bending in the tube we consider the representation of H derived in §5.3.5, and given in eq. (7.4). We can write the action of $\mathsf{U}(Y)$ as $\mathsf{U}(Y) = \lambda_1(Y \cdot \hat{W}_1)\hat{W}_1 + \lambda_2(Y \cdot \hat{W}_2)\hat{W}_2$, where $\hat{W}_i$ are the unit eigenvectors of U. Using the approximation $\lambda_1 \approx \lambda$ and $\lambda_2 \approx 1$ this becomes $\mathsf{U}(Y) \approx \lambda(Y \cdot \hat{W}_1)\hat{W}_1 + (Y \cdot \hat{W}_2)\hat{W}_2$. We can write $\mathsf{B}(Y)$ as $\mathsf{B}(Y) = C(Y \cdot \hat{E}_2)\hat{E}_2$,

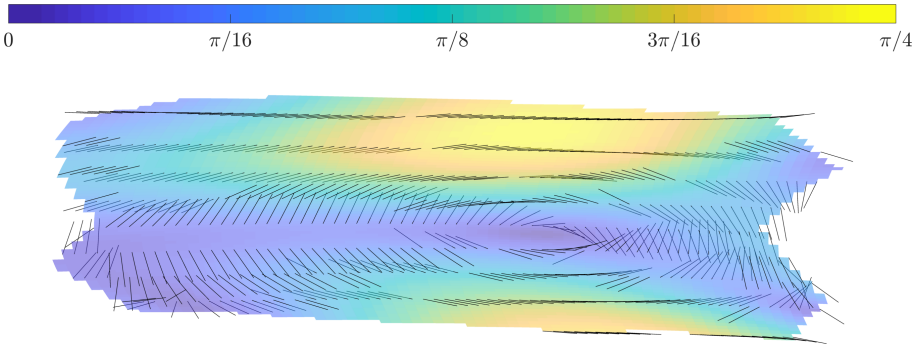


Figure 7.7: A visualisation of the rotation R. The axis of rotation is shown along with the absolute value of the angle of rotation (in radians).

where $\hat{E}_i$ are the unit eigenvectors of B, and C is the principal curvature of the undeformed tube in the azimuthal direction. Combining these we have,

$$\begin{aligned} \mathsf{UB}(Y) - \mathsf{B}(Y) &= \mathsf{U}(CY \cdot \hat{E}_2\hat{E}_2) - CY \cdot \hat{E}_2\hat{E}_2 \\ &\approx CY \cdot \hat{E}_2(\lambda\hat{E}_2 \cdot \hat{W}_1\hat{W}_1 + \hat{E}_2 \cdot \hat{W}_2\hat{W}_2) - CY \cdot \hat{E}_2\hat{E}_2. \end{aligned} \tag{7.5}$$

We know from Figure 7.3 that $\hat{W}_1$ and $\hat{W}_2$ are approximately aligned with the longitudinal and circumferential directions, so we can write $\hat{E}_2 \cdot \hat{W}_1 \approx 0$ and $\hat{E}_2 \cdot \hat{W}_2 \approx 1$. Using this we obtain,

$$\mathsf{UB}(Y) - \mathsf{B}(Y) \approx CY \cdot \hat{E}_2\hat{W}_2 - CY \cdot \hat{E}_2\hat{E}_2 \approx 0. \tag{7.6}$$

This is saying that because the directions of principal strain and principal curvature are approximately perpendicular, the influence of strain on change of curvature is removed.

We are now in a position to consider the rotor R, since it is changes in this multivector over the surface of the shell that are responsible for the change of curvature. R represents the rotation, and is characterised by the bivector B, whose magnitude gives the rotation angle in radians, and whose plane gives the plane of rotation. In fig. 7.7 we visualise the angle and axis of rotation encoded in the rotation tensor R, corresponding to a typical deformation. The axes of rotation shown in fig. 7.7 are primarily tangential to the surface, so the bivector B will be dominated by the components $e_1 \wedge e_3$ and $e_2 \wedge e_3$, with little rotation in the $e_1 \wedge e_2$ plane, i.e. about the normal vector e_3. Hence, we can write B as,

$$B = \theta_1 e^1 \wedge e_3 + \theta_2 e^2 \wedge e_3 = \theta_i e^i \wedge e_3. \tag{7.7}$$

We have used the reciprocal frame $\{e^i\}$ instead of of $\{e_i\}$ because it will allow us to use the property $\bar{\mathsf{F}}(e^i) = E^i$*.

Substituting B into the second part of the change of curvature tensor given in eq. (7.4), using the fact that e_3 is normal to e^1 and e^2, and $\gamma^3_{i3} = 0$, we obtain,

$$\begin{aligned}\bar{\mathsf{F}}\left(e_3 \cdot (Y \cdot \partial B)\right) &= Y^i \bar{\mathsf{F}}\left(-\partial_i(\theta_j)e^j + \theta_j \gamma^j_{ik} e^k\right) \\ &= -Y^i \partial_i(\theta_j) E^j + Y^i \theta_j \gamma^j_{ik} E^k.\end{aligned} \tag{7.8}$$

Therefore, given that the first part of H in eq. (7.4) is zero, $E_i \cdot \mathsf{H}(E_j) = \mathsf{H}_{ij}$ is given by,

$$\mathsf{H}_{ij} = \partial_j \theta_i - \theta_k \gamma^k_{ji}. \tag{7.9}$$

We know that H is symmetric, so from this we see that our earlier assumption on the form of B must be joined by the condition $\partial_i \theta_j = \partial_j \theta_i$ to produce consistent results.

The frame $\{E_i\}$ can be chosen by us to be orthonormal. More specifically, we can align E_1 with the longitudinal direction and E_2 with the azimuthal direction on the unstrained cylindrical tube. From fig. 7.3 we can see that under a typical deformation these basis vectors remain close to the axial and azimuthal directions. In fig. 7.8 we give a schematic illustration of how E_i maps to e_i. In fig. 7.8 we have also labelled the values of θ_i where they are obvious. The regions where $|\theta_2| \approx \pi/4$ can be seen empirically in fig. 7.7. There are two unknown values of θ_1 shown as question marks. We can estimate the largest value of these rotations by assuming a straight line from the clamped tube end and the centre of the tube when the tube collapses completely at the centre. In this case $\theta_1 \sim \arctan(a/(l/2))\lambda$ where a is the tube radius and l is the tube length in its deformed state. The multiplication by λ is necessary because θ_1 is the $e^1 \wedge e_3$ component, and e^1 is shortened by a factor of λ compared to the unit vector E^1. Up to angles of 30°, $\tan\theta$ is within 10 % of θ, so we will take $\theta_1 \sim \lambda a/(l/2) = a/(l_0/2)$ at the point in question, where l_0 is the unstrained length of the tube. This, and the values of θ_i shown in fig. 7.8, allows us to make the following

*The coordinate system is convected, so $e_i = \mathsf{F}(E_i)$, and as always $e^i \cdot e_j = E^i \cdot E_j = \delta^i_j$. Hence $\delta^i_j = e^i \cdot \mathsf{F}(E_j) = \bar{\mathsf{F}}(e^i) \cdot E_j$, from which it is clear that $\bar{\mathsf{F}}(e^i) = E^i$.

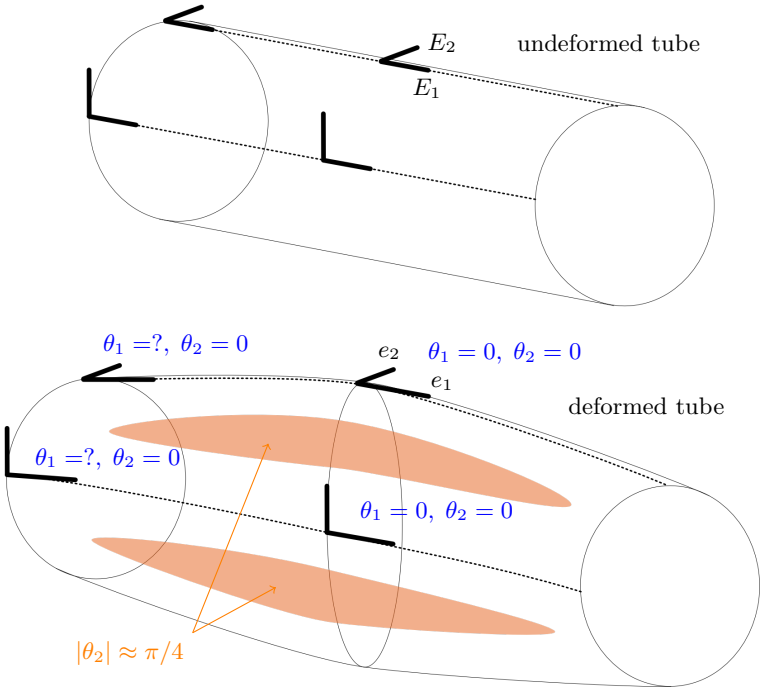


Figure 7.8: A schematic of the deformation of the flexible tube.

estimates,

$$\begin{aligned} \partial_1\theta_1 &\sim \frac{a}{l_0/2}\frac{1}{l_0/2} = \frac{4a}{l_0^2}, \\ \partial_1\theta_2 = \partial_2\theta_1 &\sim \frac{\pi/4}{l_0/2} = \frac{\pi}{2l_0}, \\ \partial_2\theta_2 &\sim \frac{\pi/4}{2\pi a/8} = \frac{1}{a}. \end{aligned} \tag{7.10}$$

Because of replacement of arctan with the identity function, our estimate for $\partial_1\theta_1$ will be an overestimate when the tube is very short.

We can also estimate the values of the coefficients γ^i_{jk} using Figure 7.8,

$$\begin{aligned} \partial_1 e_1 &\sim \frac{a}{(l_0/2)^2} e_3, \\ \partial_2 e_1 = \partial_1 e_2 &\sim 0, \\ \partial_2 e_2 &\sim \frac{1}{a} e_3. \end{aligned} \tag{7.11}$$

From this we see that the changes in the basis vectors are primarily in the e_3 direction, meaning that they do not contribute to H_{ij}.

If we take l_0 to be much larger than a, then the dominant term in H_{ij} will be $1/a$, but

even if l_0 and a are a similar order of magnitude, all of the H_{ij} terms will be of the order $1/a$. Hence, we expect $\mathrm{tr}(\mathsf{H}^2)$ and $\mathrm{tr}(\mathsf{H})^2$ will scale as $(1/a)^2 = (1/3\,\mathrm{mm})^2 = 0.1\,\mathrm{mm}^{-2}$.

Given these scalings for $\mathrm{tr}(\mathsf{E}^2)$, $\mathrm{tr}(\mathsf{E})^2$, $\mathrm{tr}(\mathsf{H}^2)$, and $\mathrm{tr}(\mathsf{H})^2$, and the values $E = 1\,\mathrm{MPa}$, $\nu = 0.5$, and $h = 0.3\,\mathrm{mm}$, we can obtain scalings for the bending and stretching energy given in eq. (7.3),

$$\begin{aligned} \text{stretching energy} &\sim 0.02\,\mathrm{N\,mm^{-1}}, \\ \text{bending energy} &\sim 1.5 \times 10^{-4}\,\mathrm{N\,mm^{-1}}. \end{aligned} \tag{7.12}$$

These agree very well with the measured stretching and bending energy in fig. 7.6, and indicate that given the kind of deformation we have observed in our Starling resistors at onset, i.e. where the strain energy is dominated by the effects of pre-strain, the axis aligned with the largest strain remains close to perpendicular to the axis aligned with the largest curvature, rotations are mostly about axes tangential to the shell, and changes in the rotation scale with the change of rotation about the longitudinal axis in the azimuthal direction, stretching energy will dominate bending energy. Moreover, this result remains valid even when the tube length gets close to the tube diameter. This is significant for our considerations of the lung, since the length to diameter ratio of tubes in the lung typically varies from 1 to 6 [Horsfield and Cumming, 1968].

7.4 Summary

We have developed a method using two simultaneously recording high speed cameras to reconstruct the motion of an oscillating flexible tube in three dimensions. This has allowed us to directly calculate kinematic quantities associated with the oscillation, and specifically have been able to show that the energy associated with stretching is 2 orders of magnitude greater than the energy associated with bending. We have been able to explain this result using a scaling analysis based on the novel way of representing the change of curvature developed in §5.3.5. The result relies on the fact that the strain energy is dominated by the effects of pre-strain, the axis aligned with the largest strain remains close to perpendicular to the axis aligned with the largest curvature, rotations are mostly about axes tangential to the shell, and changes in the rotation scale with the change of rotation about the longitudinal axis in the azimuthal direction. Further to this, our scaling analysis remains valid even when the tube length gets close to the tube diameter. Hence we have provided a scaling

analysis, confirmed by experiment, that allows us to say that bending energy is dominated by stretching energy during self-excited oscillations in the airways of the lung. This should allow the use of membrane theory to model the tube during oscillations, which reduces the order of the equations of motion from 4 to 2, and will also be of relevance to our results regarding onset conditions in §8.

Chapter 8

Mechanism for the Onset of Wheezing

In §7 we made a detailed investigation of the self-excited oscillations that occur in flexible tubes, specifically the first oscillations to occur after onset. In this chapter our aim is to explain why onset happens.

We will use the high speed video from protocol 2, and the experimental runs from protocol 1 (see §3.6.1). One experimental run from protocol 1 is illustrated in fig. 6.2, in which the lead up to the onset of oscillations can be seen before $t = 115\,\mathrm{s}$. The shape of the plots of $\bar{p}_1 - p_e$, $\bar{p}_2 - p_e$, and Q in fig. 6.2 in the lead up to onset are typical of all the experimental runs. To start with both $\bar{p}_1 - p_e$ and $\bar{p}_2 - p_e$ drop and Q increases as $p_d - p_e$ is lowered. $\bar{p}_2 - p_e$ falls fairly steadily, but there comes a critical point at which $\bar{p}_1 - p_e$ levels off and starts to rise, and Q levels off and starts to fall. Around this time oscillations start. Explaining this process in detail is the focus of this chapter.

Protocol 1 has been designed so that, in the lead up to onset, the system moves through a series of quasi-steady states. Each of these states is a balance between equilibrium of the fluid and equilibrium of the tube. We will investagate the equilibrium of these two systems separately, before bringing together the results to understand the equilibrium of the entire experimental rig, and more importantly, its stability.

Before considering equilibrium in detail, we will first discuss observations from high speed video obtained using protocol 2. It is worth noting that when collecting high speed video it is necessary for the experimenter to ensure that the oscillation that is recorded is the same

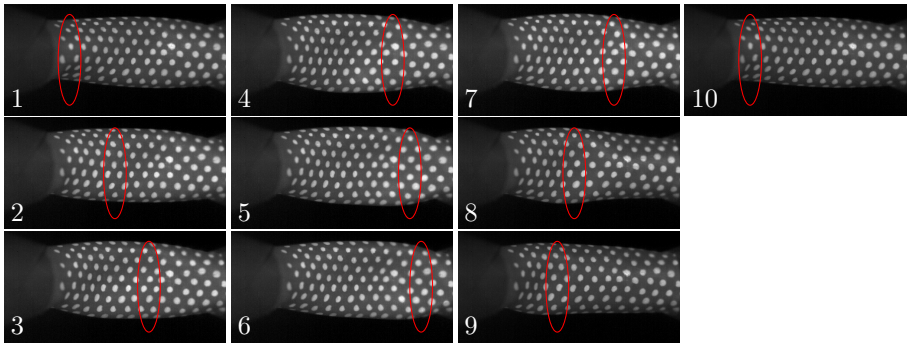


Figure 8.1: High speed video of self-excited oscillations just after onset. A longitudinal wave is observed, and its position in the sequence of images is indicated by the red ellipse. The elapsed time between each image is 4 ms.

as the oscillation observed using protocol 1. For all the videos discussed in this chapter this condition has been met.

8.1 High Speed Video of Onset

Figure 8.1 shows a set of stills from a video where oscillations have just started. The first important observation to make is that the oscillations are occurring about a strongly deformed state of the tube, which was already alluded to in the introduction. The second observation is that there is a visible wave that travels the length of the tube, and that in the time taken for the wave to travel down the tube and back again, the tube also opens and closes once. The position of the longitudinal wave has been indicated in fig. 8.1 over the course of one cycle.

These are observations that we have seen consistently in high speed videos of oscillations just after onset, as defined in the previous section. The presence of longitudinal waves synchronised with the opening and closing of the tube is strongly indicative that it is the coupling of two modes of oscillation that gives rise to instability. However, we know from §6.3 that these modes cannot be purely elastic, and must involve the fluid. All of the videos are available at [Gregory et al., 2017b], and some can also be seen on our group website acoustics.eng.cam.ac.uk. The longitudinal wave is clearest in live playback.

We now need to use measurements from protocol 1 to corroborate our observations from high speed video, and develop our understanding of the physics that produces them.

8.2 Equilibrium of the Tube

To understand the equilibrium of the flexible tube in the lead up to onset, we need information about its deformation. In §7 we described a process by which we could get detailed information about the deformation of the tube during oscillation (see protocol 2), but the high speed cameras used for this process can only record for approximately 1.5 s, which is not long enough to capture the process of oscillation onset. In addition, the three dimensional data presented in §7 only gives information about one side of the tube. We know that the oscillations observed are close to symmetric (i.e. have an azimuthal wave number of 2), so for the purpose of estimating the scale of the stretching and bending energy this is not a problem. However, to understand onset we will require more detailed information about the whole cross-sectional shape of the tube.

One observation that is of use here is that, as the tube partially collapses in the lead up to onset, it does so approximately symmetrically in the up- and downstream direction, i.e. the narrowest point of the tube lies midway between the up- and downstream attachment points. This is the same as the way in which flexible tubes collapse when no flow is present. Therefore, to understand equilibrium of the tube, we will consider equilibrium in the absence of flow, and assume that this applies before oscillations start.

The equilibrium of a collapsible tube in the absence of fluid flow is usually characterised by a **tube law**. This is a description of how the cross-sectional area of the tube at its narrowest point, i.e. halfway between the tube supports, varies as the difference between the internal and external pressure (the transmural pressure) is varied. We label the cross-sectional area of the tube at its narrowest point (at the contraction) A_c, and the pressure at this location p_c. Since there is no flow, p_c will be equal to p_1 and p_2 in this section, but later on it will be important to distinguish them. The tube law is the function $p_e - p_c = f_t(A_c)$, which is implicitly also dependent on the geometric parameters and material properties of the tube.

Considerable work has been done developing tube laws [Bertram, 1987; Kozlovsky et al., 2014; Whittaker et al., 2010a], however, we have been unable to find a tube law that is applicable to tubes that are relatively short ($l_0/a \lesssim 5$) and that are held in axial strain ($l/l_0 > 1$). Hence, we have found it necessary to empirically measure the tube law for ourselves.

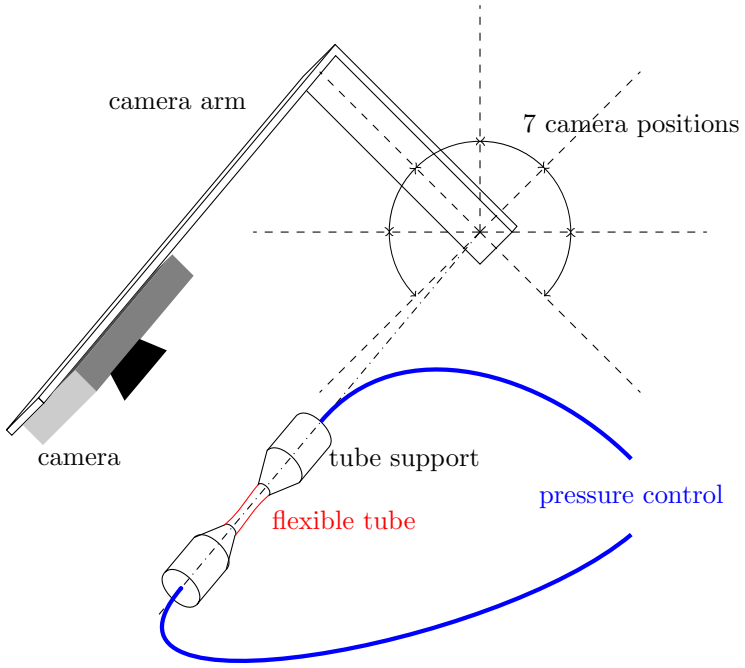


Figure 8.2: The rig used to measure the tube law.

8.2.1 Multiple Camera Setup

To measure how the cross-sectional area of the tube A_c changes as $p_e - p_c$ is varied, we use the experimental rig illustrated in fig. 8.2. The flexible tube is held between two supports, and the distance between these supports can be controlled to within 0.1 mm. The supports are designed so that the tube is not strained radially, i.e. the diameter of the supports matches that of the tube (as with the supports detailed in fig. 3.18), and so that their rotational axes of symmetry are in line, i.e. the tube is held straight.

The pressure inside the tube is controlled with a syringe, and is measured using a Digitron 2028P manometer. With a single flexible tube attached to the rig, the pressure inside is chosen, and 7 images are taken from the $m = 7$ positions illustrated in fig. 8.2. These camera positions are chosen so that each point on the tube can be seen in at least 2 and more usually 3 or 4 images. To find A_c, a ring of material points are marked on the tube halfway between the supports. Using the 7 images, the three dimensional positions of these material points can be found, and the cross-section of the tube at its narrowest point can be reconstructed, allowing A_c to be measured.

As in §7.1, to enable three dimensional reconstruction, the imaging system must be

calibrated. However, this is more complex than in §7.1 since there are more than two positions from which images are taken. We use a method outlined by [Lasenby and Stevenson, 2001]. The method has required some modification, which has been done with the collaboration of Joan Lasenby.

Since a single camera is used to take all of the images, only one set of **intrinsic** information is needed. The **extrinsic** information consists of the rotations and translations from the first camera position to the other six. The camera used is an Olympus SP-560 UZ, with an f-number of 7.1, a shutter speed of 1/100s, a 50 mm zoom, an ISO of 50, manually focused at 10 cm.

A chequerboard was set up in 48 orientations, and images were taken from all 7 camera positions, though not every chequerboard could be seen from every camera position. By ignoring which position the camera was in when each image was taken, every chequerboard image was used to find the intrinsic parameters of the camera. The chequerboard defines 54 points, so the 48 chequerboard orientations define $n = 48 \times 54 = 2592$ distinct **world points**. To find the extrinsic properties of the camera we must set up two arrays. The first is called the **occlusion field**, an n by m array of zeros and ones. If element i, j is a one, then world point i is visible from camera j, and is not if it is zero. The second is an n by m by 2 array, which we call the **data array**, in which element i, j contains the pixel coordinates (u, v) of world point i seen in the image from camera j. This is only meaningful if the corresponding element in the occlusion field is one.

If the pixel coordinates (u, v) of a point and the intrinsic properties of the camera are known then we can find the camera coordinates (x, y) of the point (see fig. 8.3 and [Lasenby and Stevenson, 2001]), the distinction being that camera coordinates have units of mm instead of pixels. Hence the data array can be converted to contain the camera coordinates in place of the pixel coordinates. With this in place, calibration can proceed.

To start, a set of rotations and translations between the camera positions are assumed. With this, any of the world points can be triangulated using the method illustrated in fig. 8.3. The rays from the focal point of each camera through the point on the image plane of the camera are projected out. The world point is found by finding the point in three dimensions that minimises the sum of the distances to each of the rays. We will denote this distance d_i for world point $i = 1, \ldots, n$. External calibration is performed by finding the rotations and

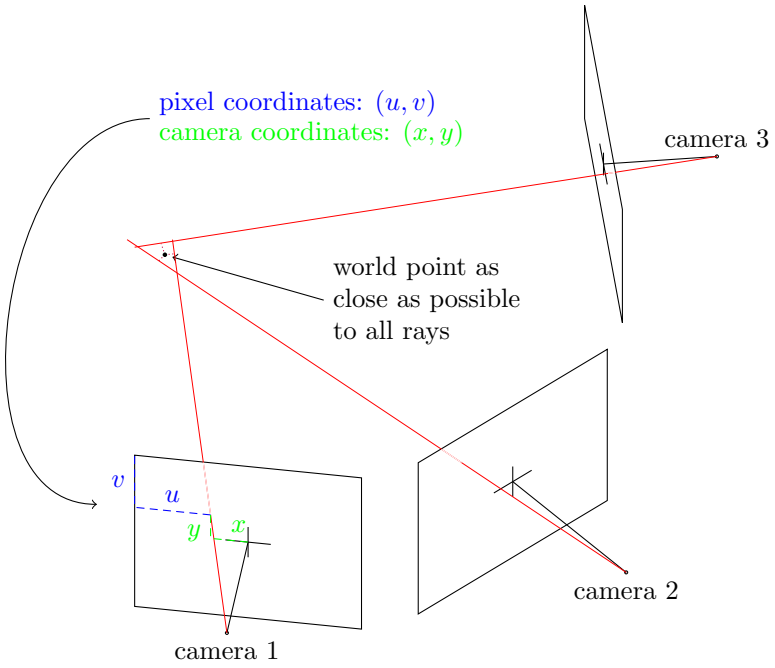


Figure 8.3: Projection from an image to a point in three dimensions.

translations between the cameras that minimises,

$$\sum_{i=1}^{n} d_i. \tag{8.1}$$

An in house code was provided by Joan Lasenby to do this, which needed to be adapted from the original form based on [Lasenby and Stevenson, 2001] to account for the sparsity of the occlusion field in our application.

8.2.2 Reconstructing the Tube Cross-Section

A set of images of a flexible tube are shown in fig. 8.4. The flexible tube shown in these images has a total of 15 material points marked on it, and using these locations, the material points can be triangulated. However, there is some uncertainty in the location of the material points as seen in each of the 7 images. More specifically, each point is only found to within an accuracy of approximately 5 pixels. We account for this by triangulating the position of each material point many times, but each time, the pixel coordinates have a random number added to them, which is drawn from a normal distribution with a standard deviation of 5. In this way we end up with a scatter of material points for each of the marked points on the

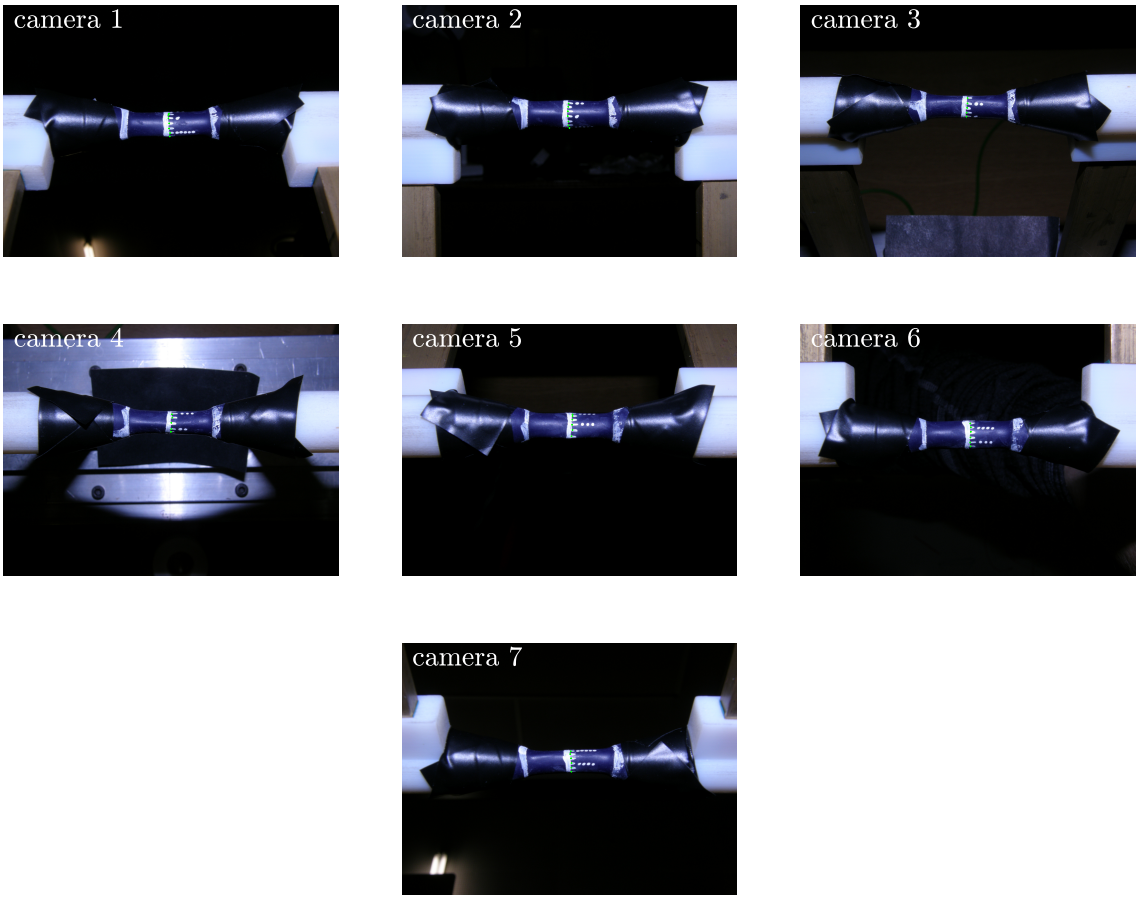


Figure 8.4: Raw images used to find a tubes cross-sectional area. World points are identified in each image by green crosses

flexible tube, and this represents the uncertainty in the measured position of each material point. For the set of images shown in fig. 8.4, the estimated triangulated positions are shown in fig. 8.5, in which we have used 100 random samples to create the point clouds in the figure.

We need to extract the tube's cross-sectional shape from the points shown in fig. 8.5. This shape must be a closed curve that passes through each of the point clouds. In addition, we know that the flexible tube will resist being curved too much. To find a curve that satisfies these constraints we use a modified form of **curve-shortening flow**. Classical curve-shortening flow is a way of deforming curves in flat two-dimensional Euclidean space ($\mathbb{E}^2$). Given a curve $x(s) \in \mathbb{E}^2$, where s is a scalar parameter, we write down an evolution equation for all points on the curve,

$$\frac{\partial x}{\partial t} = \kappa n. \tag{8.2}$$

where κ is the curvature of the curve, and n is the unit normal vector. The unit tangent is

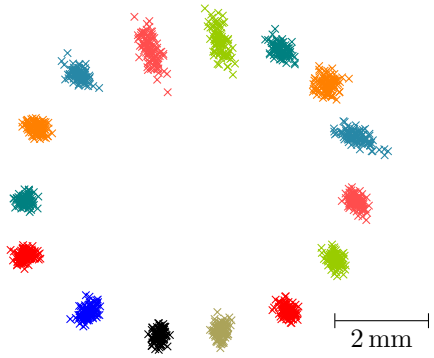


Figure 8.5: Triangulation of the material points shown in fig. 8.4, with added random noise to account for uncertainty.

given by $\tau = \partial x/\partial s/\left|\partial x/\partial s\right|$, and using this κ is given by $\kappa = \left|\partial \tau/\partial s\right|$. The normal vector n is always chosen such that is points towards the local centre of curvature of the point on the curve $x(s)$ under consideration. Any closed, non-self-intersecting curve, for which the necessary derivatives exist, will eventually become a circle when evolved in this way. This circle will then simply shrink in size [White, 2002, theorems 2 and 3]. In this way, complex and highly curved shapes are deformed into something as smooth as possible, which is a property we would like to exploit.

We need to modify this process so that our closed curve also has a tendency to move towards the point clouds derived from the triangulation process. To achieve this we add a second term to the evolution equation of the curve that pulls the curve towards nearby points. We denote the triangulated material points $y_i, i = 1, \ldots, N$, and the precise form that our evolution equation takes is,

$$\begin{aligned} \frac{\partial x}{\partial t} &= \left(\kappa + \sum_{i=1}^{N} (d_i/|d_i|) \cdot n \; f(|d_i|) \right) n, \\ d_i &= y_i - x, \quad f(z) = \frac{z}{\sigma} \exp\left(-\frac{z^2}{\sigma^2} \right), \end{aligned} \tag{8.3}$$

where σ is a scalar parameter that determines the size of the region of influence of a point y_i. The endpoint of a curve allowed to evolve in this way, starting from a circle enclosing all of the material points, is shown in fig. 8.6. This curve represents the *outer* wall of the tube, and we can construct the inner wall given the tube wall thickness, and this is also shown in fig. 8.6.

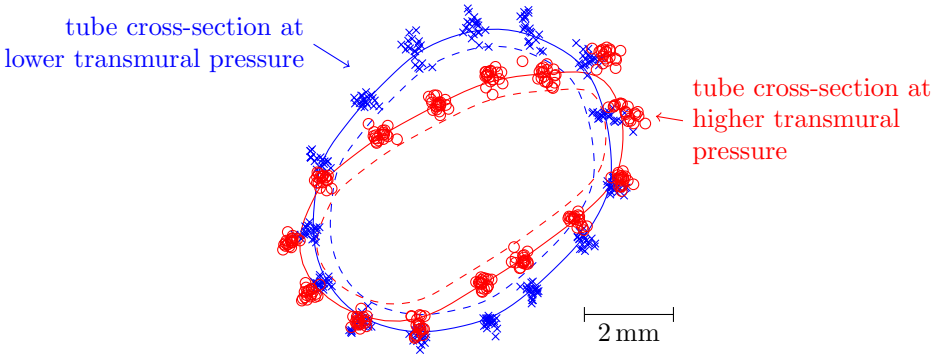


Figure 8.6: Fitting curves to tube cross-sections.

Table 8.1: Geometric parameters of tubes used to measure the tube law.

Tube Number	l/l_0	h/a	l_0/a
1	1.01	0.12	6.03
2	1.11	0.12	6.03
3	1.21	0.12	6.03
4	1.28	0.12	6.03
5	1.09	0.06	6.59
6	1.17	0.06	6.59
7	1.26	0.06	6.59
8	1.10	0.12	4.81
9	1.23	0.12	4.81
10	1.35	0.12	4.81
11	1.48	0.12	4.81

8.2.3 The Tube Law

Using the methods in §§8.2.1 and 8.2.2 we can measure A_c as a function of $p_e - p_c$. We are interested in how this function (the tube law) changes as the geometric parameters l_0/l, h/a, and l_0/a are varied. The tube law was measured for 11 different tubes, whose geometric parameters are given in table 8.1. Data from these experiments is available at [Gregory et al., 2017a].

We regard A_c as a function of the transmural pressure $(p_e - p_c)$, the geometry (l, l_0, a, h), and the material properties (E, ν),

$$A_c = f\left(p_e - p_c, l, l_0, a, h, E, \nu\right). \tag{8.4}$$

Our first assumption is that A_c does not depend on E and ν independently, but on $E/(1-\nu^2)$. This assumption is based on the form taken by the energy of deformation for thin shells,

in which E and ν only appear in this form (see §5.6.3). We can then non-dimensionalise [Barenblatt, 2003] the above relationship for A_c,

$$\frac{A_c}{\pi a^2} = f\left(\frac{p_e - p_c}{E/(1-\nu^2)}, \frac{l}{l_0}, \frac{h}{a}, \frac{l_0}{a}\right). \tag{8.5}$$

For each tube we obtain a set of A_c values with a corresponding set of $p_e - p_c$ values. Each pair of sets represent a single plot of A_c against $p_c - p_e$, and for each of these plots, there is an associated value of l/l_0, h/a, and l_0/a. We wish to find the values of α, β, γ, and δ such that when we plot,

$$\frac{A_c}{\pi a^2}\left(\frac{l}{l_0}\right)^{\alpha}, \tag{8.6}$$

against,

$$\frac{p_e - p_c}{E/(1-\nu^2)}\left(\frac{l}{l_0}\right)^{\beta}\left(\frac{h}{a}\right)^{\gamma}\left(\frac{l_0}{a}\right)^{\delta}, \tag{8.7}$$

the tube laws collapse onto a single curve. We have chosen to look for this functional form based on the observation that the tube law always has the same basic shape; it is either stretched or compressed along the pressure and area axes depending on the values of l/l_0, h/a, and l_0/a. Specifically, increasing l/l_0 results in compression along the area axis and stretching along the pressure axis, increasing h/a results in stretching along the pressure axis, and increasing l_0/a results in compression along the pressure axis. These observations mean that we expect to have $\alpha > 0$, $\beta < 0$, $\gamma < 0$, and $\delta > 0$.

The values of α, β, γ, and δ are those that minimise the difference between the curves we obtain when we plot eq. (8.7) against eq. (8.6). To do this we need to define what we mean by difference. We consider two tube laws, i and j, and assume that we have an estimate of the values α, β, γ, and δ. Then we plot eq. (8.7) against eq. (8.6) and normalise the axes so that the mean value in both directions is 1, and obtain a plot such as the one shown in fig. 8.7. Next we find the shortest distance from each point in tube law i to tube law j. When considering more than two tube laws, we find the shortest distances for all possible pairs, and then find the overall average of these shortest distances. To find the values of α, β, γ, and δ we run a non-linear optimisation to minimise this average shortest distance using the `fminunc` function in MATLAB®. The results of this optimisation were $\alpha = 1, \beta = -2, \gamma = -1, \delta = 1$, which results in the plot shown in fig. 8.8. Note that the integer values are not special, they are simply the values that fell out of the optimisation to

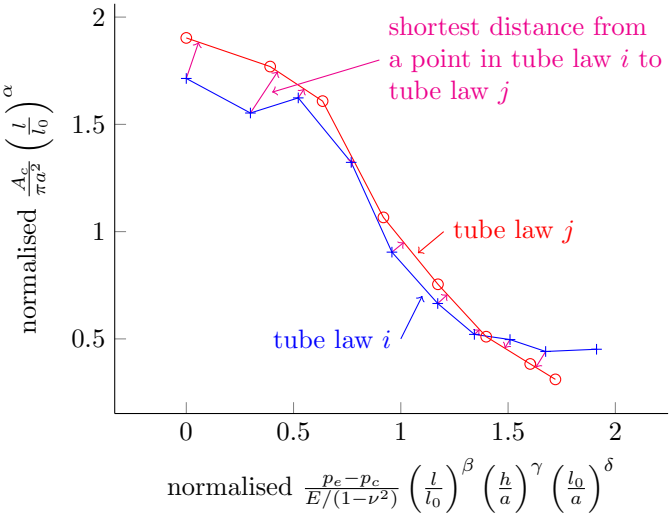


Figure 8.7: Measuring the difference between two tube laws.

an accuracy of 1 decimal place, which is all that can be expected when viewing the spread seen in fig. 8.8. This is the first generalised tube law valid for relatively short tubes held in axial tension.

8.3 Equilibrium of the Fluid

In this section we will consider the shape of the flexible tube to be fixed in some way, and then ask how the fluid flowing through the system responds and reaches equilibrium. Specifically, we are interested in finding how the pressure inside the tube p_c depends on the cross-sectional area A_c, and any other relevant geometric parameters of the tube.

In the experiments described in protocol 1 the far upstream pressure p_e and far downstream pressure p_d are controlled, and the flow then reaches equilibrium. Hence we are looking for how $p_e - p_c$ depends on A_c and $p_e - p_d$. We call this the **fluid law**, and will denote it $p_e - p_c = f_f(A_c, p_e - p_d)$.

To obtain the fluid law, first we will find how the overall pressure drop across the experimental rig $(p_e - p_d)$ depends on the flowrate Q and A_c. This can then be used to find Q given a value of A_c and $p_e - p_d$. Using Q we can then find $p_e - p_c$, and hence the fluid law.

We break down the overall pressure drop $p_e - p_d$ into four parts,

$$p_e - p_d = (p_e - p_1) + (p_1 - p_c) + (p_c - p_2) + (p_2 - p_d). \tag{8.8}$$

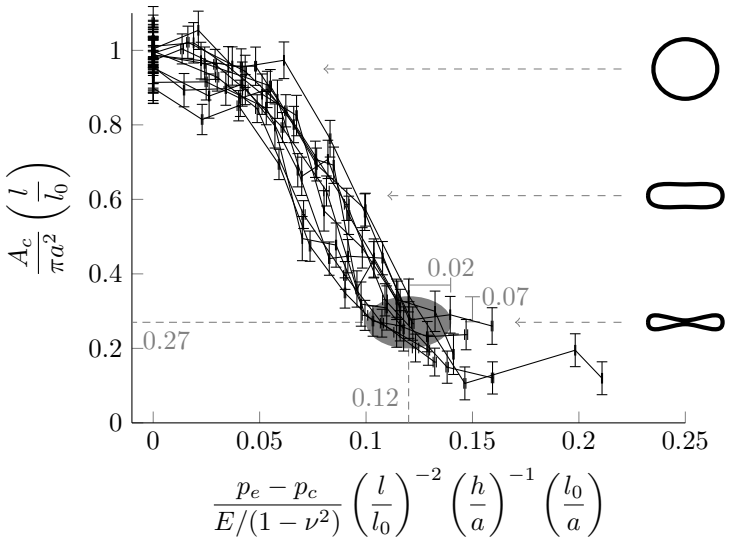


Figure 8.8: The tube law.

Either side of the flexible tube are a set of components (settling chambers, tubes, flow meters, contractions, expansions) for which the relationship between the flowrate through them and the pressure drop across them is predictable if the flow is steady or quasi-steady [Miller, 1990]. Upstream of the flexible tube we characterise the overall relationship between $p_e - p_1$ and Q by the function $p_e - p_1 = f_u(Q)$. This includes pressure drops due to the flow meter (2), upstream settling chamber (3), clean flow inlet (4), upstream clean flow tube (5), and contraction (6) (the numbers refer to fig. 3.16). Similarly, downstream of the flexible tube, the overall relationship between $p_2 - p_d$ and Q is characterised by $p_2 - p_d = f_d(Q)$, which includes pressure drops due to the expansion ($6'$), downstream clean flow tube ($5'$), and the sudden expansion into the downstream settling chamber ($3'$). These functions could be found by considering data in [Miller, 1990], but it is simpler for us to find them empirically directly from our experimental data recorded before the tube starts to oscillate. This is shown in fig. 8.9.

To completely characterise the rig we need to know how $p_1 - p_c$ and $p_c - p_2$ depend on Q, A_c, and other geometric parameters of the flexible tube. We denote these relationships $p_1 - p_c = f_1(Q, A_c)$ and $p_c - p_2 = f_2(Q, A_c)$, and we can write them as,

$$p_1 - p_c = f_1(Q, A_c) = \frac{1}{2}\rho Q^2 \left((1 + K_c)A_c^{-2} - A_1^{-2}\right), \tag{8.9a}$$

$$p_c - p_2 = f_2(Q, A_c) = \rho \frac{Q^2}{A_2}\left(A_2^{-1} - (K_d - 1)A_c^{-1}\right). \tag{8.9b}$$

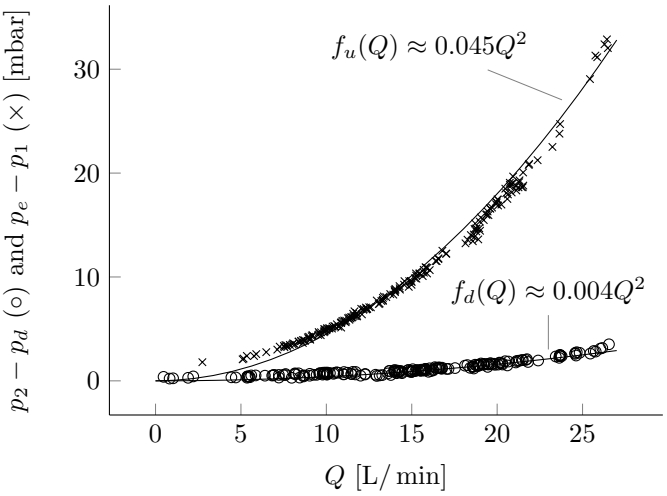


Figure 8.9: Pressure-flow relationships for the experimental rig in fig. 3.16

These equations are Bernoulli with loss coefficients K_c and K_d, which in general are a function of A_c and the flexible tube geometry. $K_c = 0$ or $K_d = 0$ imply that the Bernoulli equation holds, and in reality both of the coefficients will be greater than zero. [Miller, 1990] gives a wide range of information on loss coefficients. For the contraction from A_1 to A_c, K_c will be between 0.01 and 0.1 [Miller, 1990, §14.4], and its effects on the overall results of this report are not significant. Hence we will assume $K_c = 0.05$. If we model the expansion, from the narrowest point of the tube (A_c) to the point where p_2 is measured, as a sudden expansion in space (the flow separates as a jet past the narrowest point and reattaches by A_2), then it can be shown by an application of conservation of mass and momentum that $K_d = 1 - 2(A_c/A_2) + (A_c/A_2)^2$. K_d as a function of A_c/A_2 for a sudden expansion is shown in fig. 8.10. Bernoulli and sudden expansion are the two extremes. Bernoulli implies no loss and sudden expansion implies maximum loss due to mixing. The flow conditions in the segment between A_c and A_2 are somewhere in between these extremes. Empirical information for the loss coefficient K_d is available from [Miller, 1990, §11.2] for area ratios $A_c/A_2 > 0.25$, but the data does not cover the range of area coefficients needed in the present study ($0.1 < A_c/A_2 < 1$). Therefore, we must supplement the data by our own observations. We can find an approximate point on the curve of K_d against A_c/A_2 by noting that when oscillations start, the tube is almost fully collapsed, and so $A_c/A_2 \approx 0.2$. We know $p_1 - p_c = f_1(Q, A_c)$, and we have measured p_1 and p_2 at onset in multiple experiments, so we can find a single value of K_d corresponding to $A_c/A_2 \approx 0.2$. This is shown in fig. 8.10.

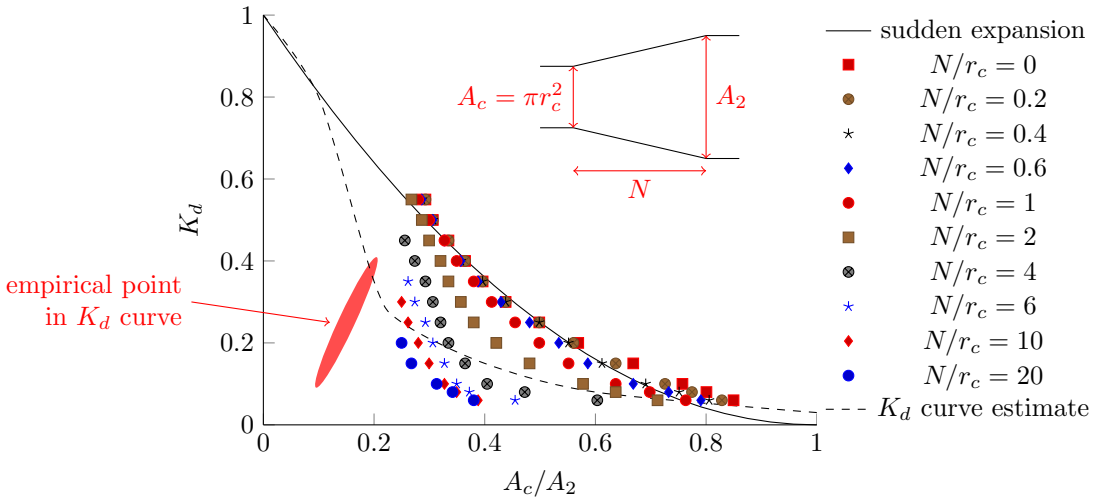


Figure 8.10: Dependence of the diffuser loss coefficient K_d on the area ratio A_c/A_2 and length ratio N/r_c. Data adapted from [Miller, 1990, §11.2].

The dashed curve combines this empirical point with the data from [Miller, 1990]. As A_c/A_2 approaches 1, K_d approaches 0 for a sudden expansion. The measured values of K_d nearly do this, but stay slightly above zero due to the presence of friction at the walls. When N/r_c is small, the diffuser is almost a sudden expansion, and we see that for $N/r_c \lesssim 0.4$, the measured values of K_d match quite well with the theoretical values for a sudden expansion. As N/r_c increases, K_d decreases, due to the more gradual expansion of the diffuser resulting in less separation and mixing loss. However, this trend does not continue indefinitely as A_c/A_2 is decreased, since at some point the flow will separate, and there will be a sudden increase in K_d. At very small values of A_c/A_2, we expect K_d to be that of a sudden expansion for this reason.

Given a curve for K_d, we have specified the function $p_c - p_2 = f_2(Q, A_c)$, and so eq. (8.8) can now be expressed as,

$$p_e - p_d = f_u(Q) + f_1(Q, A_c) + f_2(Q, A_c) + f_d(Q). \tag{8.10}$$

Given a value for $p_e - p_d$ and A_c, we can solve this equation to find $Q = Q(p_e - p_d, A_c)$. Then using this value of Q we can find $p_e - p_c = f_u(Q) + f_1(Q, A_c)$, and the desired fluid law, $p_e - p_c = f_f(A_c, p_e - p_d)$. Example fluid laws are plotted in fig. 8.11, obtained using the values of K_d shown in fig. 8.10. When A_c/A_2 is close to one, the flow through the flexible tube nearly satisfies the Bernoulli equation, and the flowrate is close to constant, meaning

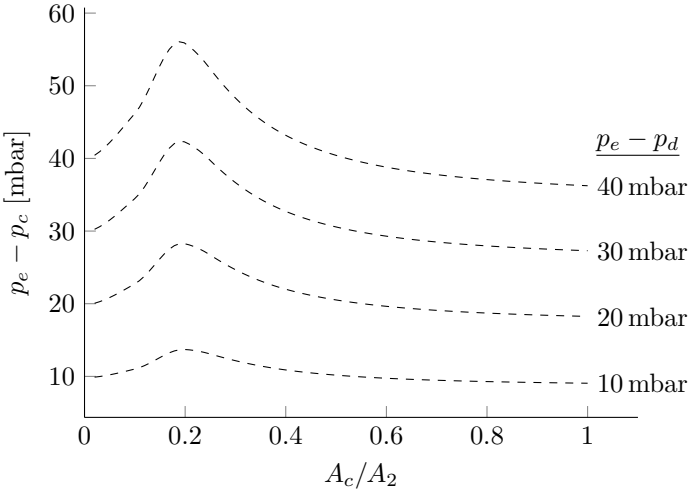


Figure 8.11: The fluid law.

that $p_e - p_c$ increases as A_c is lowered. However, when flow in the flexible tube separates the losses become much more significant, and the contractions provides more of an obstruction to flow, meaning that the flowrate starts to drop. This causes $p_e - p_c$ to fall as A_c approaches zero.

Our estimate of how K_d varies with A_c/A_2 is not quantitatively accurate, however, its general shape (a flatter region at higher A_c/A_2, with a sudden increase associated with flow separation) is fairly robust. Therefore, the fluid laws shown in fig. 8.11 are also of a representative shape, while lacking quantitative accuracy.

8.4 Stability

Equilibrium occurs when the fluid and tube laws are equal, i.e. $A_c = A_{c_0}$ such that $f_t(A_{c_0}) = f_f(A_{c_0}, p_e - p_d)$. Some example fluid and tube laws are plotted in fig. 8.12, and we can see that as $p_e - p_d$ is increased, the equilibrium point corresponds to a smaller A_c, and so the tube collapses. Because we lack quantitative information about K_d, we cannot use this to fully predict the tube behaviour, however, we can use it to understand why oscillations start, and we will be able to use the tube and fluid laws to show more rigorously the state of the tube at the onset of self-excited oscillations.

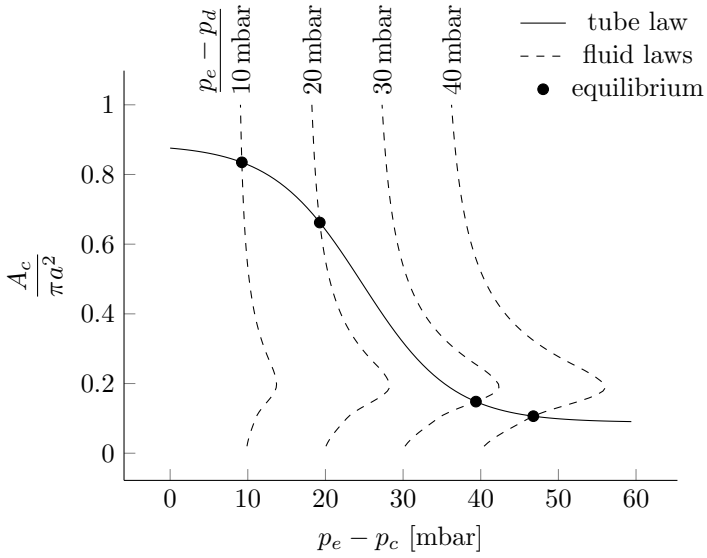


Figure 8.12: Equilibrium between the fluid and tube laws. The tube law is based on fig. 8.8.

8.4.1 Static Linear Stability

To understand the stability of an equilibrium solution, we start with $A_c = A_{c_0}$, given $p_e - p_d$, and then consider a small perturbation to the equilibrium by lowering A_c. In general this will change the value of $p_e - p_c$ to match the fluid law. If the new value of $p_e - p_c$ that is achieved is larger than the value required for equilibrium of the tube, then the tube will collapse further, leading to instability, but if it is smaller, then the tube will return to the original equilibrium. Hence, the system is statically unstable if,

$$\left.\frac{\partial f_f}{\partial A_c}\right|_{A_c=A_{c_0}} < \left.\frac{\partial f_t}{\partial A_c}\right|_{A_c=A_{c_0}} . \tag{8.11}$$

Given the shape that the tube and fluid laws take, there are two possibilities for the system's behaviour as $p_e - p_d$ is increased from zero, which are shown in fig. 8.13. In the first case (left), the equilibrium solution simply moves down the tube law as $p_e - p_d$ is increased, and all of these solutions are stable according to eq. (8.11). In the second case an unstable solution is present for some values of $p_e - p_d$ but never in isolation. Hence, this analysis fails to predict any self-excited oscillations.

It is worth noting that the static linear stability analysis provided here does pose a possible mechanism for the sudden closing or opening of the tube, which could be responsible for crackling sounds. The left column in fig. 8.13 shows that as $p_e - p_d$ is gradually increased,

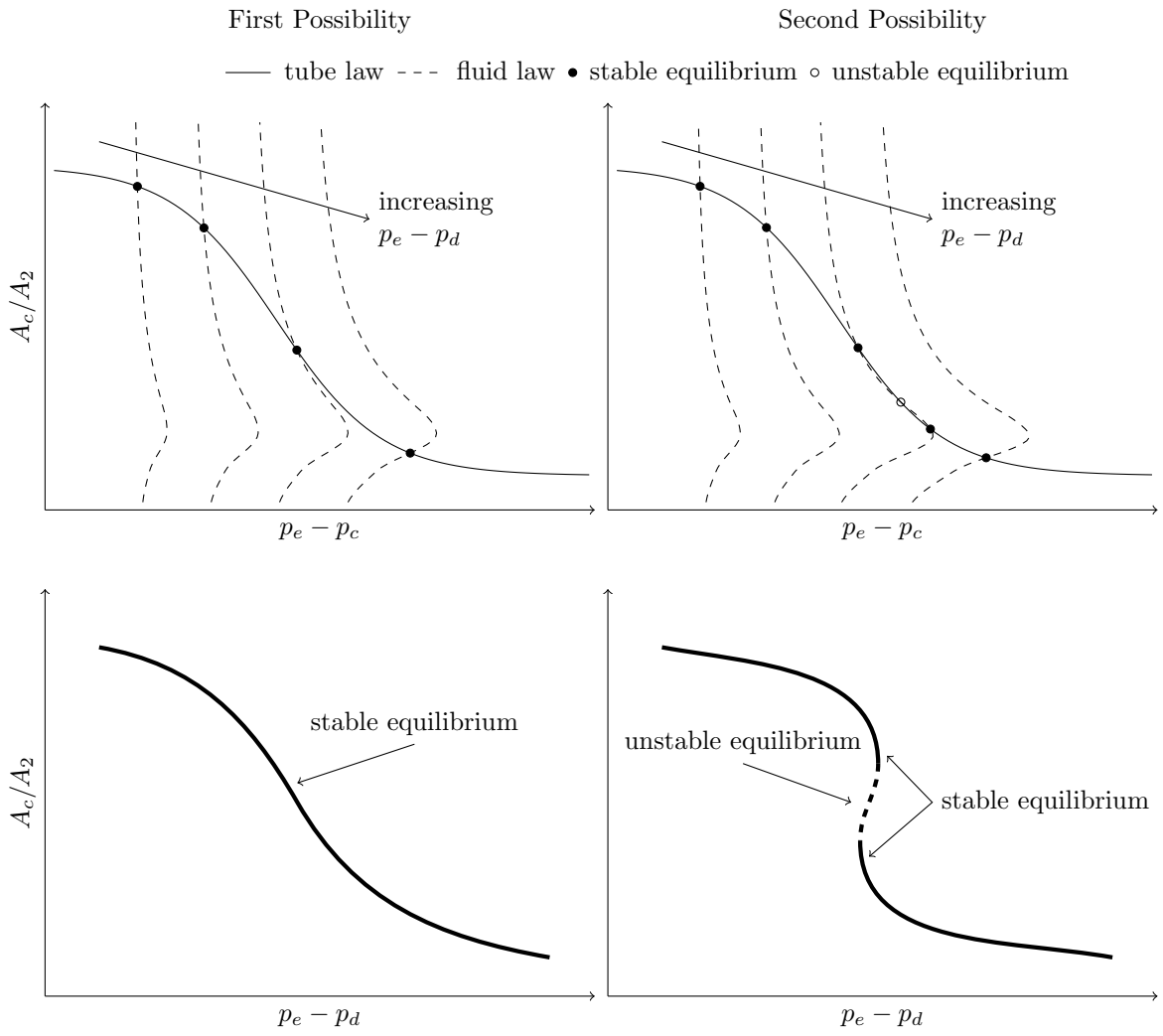


Figure 8.13: Linear stability of equilibrium solutions. Above we show the equilibrium solutions based on the intersections of the fluid and tube laws, and below we sketch the dependence of these equilibrium solutions on $p_e - p_d$. Note that two saddle node bifurcations can be seen in the bottom right plot [Strogatz, 1994].

the cross-sectional area of the tube will reduce smoothly, but the right column illustrates a situation in which there will come a point when the tube will suddenly snap closed when a saddle node bifurcation is reached. This is a good subject for future work.

8.4.2 Tube Shape at Onset

The static analysis fails to predict an instability, and this will be addressed further later, but using our understanding of equilibrium we can gain much more detailed information about the shape of the tube when oscillations are observed to start.

On the tube law shown in fig. 8.8 we have shaded the region corresponding to total collapse of the tube, i.e. when opposite walls of the tube touch. Hence we can say that, at total collapse $A_c = A_c^*$ and $p_e - p_c = (p_e - p_c)^*$, which satisfy,

$$\frac{A_c^*}{\pi a^2}\frac{l}{l_0} = 0.27 \pm 0.07, \tag{8.12a}$$

$$\frac{(p_e - p_c)^*}{E/(1-\nu^2)}\left(\frac{l}{l_0}\right)^{-2}\left(\frac{h}{a}\right)^{-1}\left(\frac{l_0}{a}\right) = 0.12 \pm 0.02. \tag{8.12b}$$

We would like to compare $p_e - p_c$ inside the tube when oscillations start to $(p_e - p_c)^*$, our hypothesis being that $p_e - p_c$ should be close to or slightly below $(p_e - p_c)^*$ at onset, since this is where the divergence instability is most likely. We do not measure $p_e - p_c$ directly, but we do measure $p_e - p_1$ and Q. Hence we can estimate $p_e - p_c$ by assuming $A_c = A_c^*$, and then using,

$$p_e - p_c = p_e - p_1 + f_1(Q, A_c^*), \tag{8.13}$$

from eq. (8.9a). In fig. 8.14 we plot $p_e - p_c$ found using eq. (8.13) against $(p_e - p_c)^*$ found using eq. (8.12b), for all the experimental runs indicated in fig. 6.1, indicating that the tube is almost completely collapsed when self excited oscillations start.

Previous research based on Starling resistors has tried to predict the onset of oscillations by considering the linear stability of flow through a cylindrical or nearly cylindrical tube [Hamadiche and Gad-el Hak, 2002; Kumaran, 1995a,b, 1998; Whittaker et al., 2010b]. This is not applicable to wheezing because oscillations are occurring about a highly deformed state. This is a new development in our understanding of self-excited oscillations of this type, and in addition, it is now possible to predict the transmural pressures that need to be reached in the airways of the lung, for example based on Horsfield's model [Horsfield and

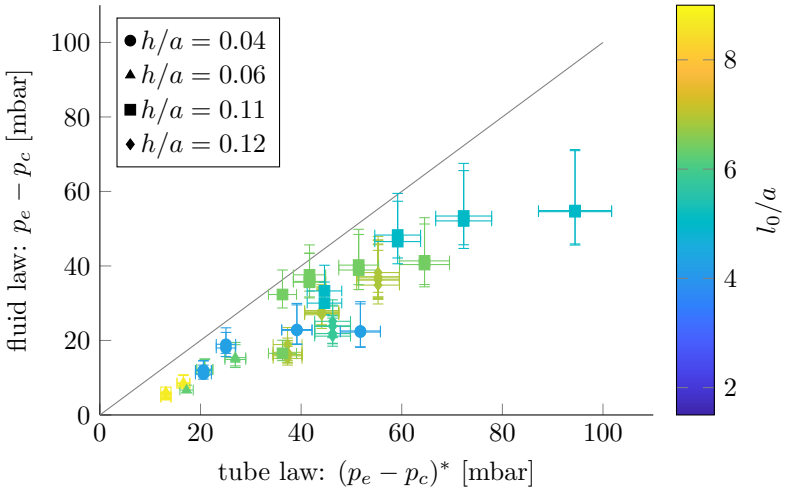


Figure 8.14: Agreement between collapse pressure predicted by tube law and measured at the onset of self-excited oscillations.

Cumming, 1968, in order for oscillations to occur. This can be used to make predictions regarding the effect of airway constriction and changes in material properties on wheezing, which will enable us to improve the specificity of diagnoses based on these sounds. For example, wheezing is also often associated with obstruction (Bohadana et al., 2014), and we can understand this in two ways. Obstruction will tend to increase pressure loss, and so in tubes downstream of the obstruction, p_1 will be lowered, increasing the likelihood of onset. In addition, if obstruction does not involve a stiffening of the airways, it has effectively reduced the transmural pressure necessary for collapse by narrowing the tube, which would again increase the likelihood of onset.

The result that oscillations start just before total collapse also supports the main result of §7: stretching energy dominates bending energy in the tube during oscillations just after onset. The tube law is split into three main regions; an initial flat region when the tube cross-section is close to circular ($p_e - p_c$ below 12 mbar in fig. 8.12), a fairly shallow decrease in area with increasing $p_e - p_c$ ($p_e - p_c$ between 12 mbar and 35 mbar in fig. 8.12), and a second flat region after the tube walls have come into contact ($p_e - p_c$ above 35 mbar in fig. 8.12). In the two flat regions, bending is playing a significant role in the deformation of the tube. In the first flat region it is bending that is critical to deciding when the tube buckles, which is what decides when the tube law will slope downward. In the second flat region, the opposite walls of the tube are touching, and so there is significant curvature of the tube, which again indicates that the bending energy will be significant. In the middle

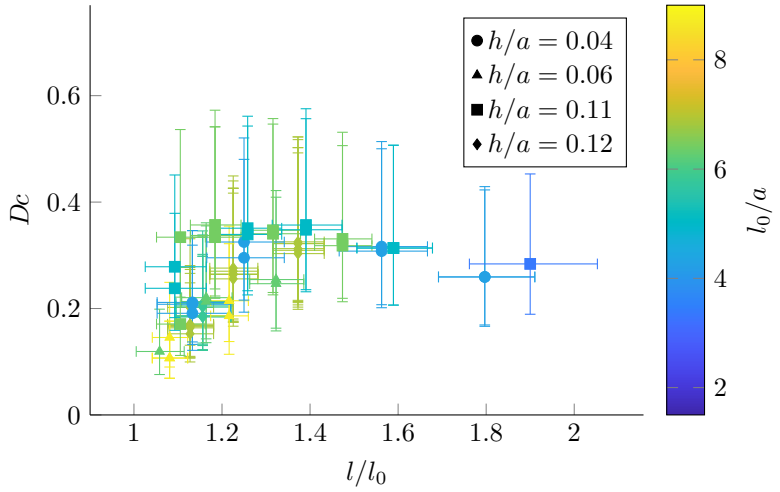


Figure 8.15: The dynamic to collapse pressure ratio observed at the onset of oscillations.

region of the tube low, it is stretching that is most important, as the curvature of the tube is not yet large, and in order for the opposite walls of the tube to touch, the distance from the centre of the tube to the supports at either end must increase. Hence, the result of §7 indicates that oscillations should occur in the middle region of the tube law, which agrees with our hypothesis that oscillations start close to or just before total collapse.

8.4.3 Refined Dimensional Analysis

In §3.1 a dimensionless variable was identified to compare pressures in the fluid and tube. This was Dc, the dynamic to collapse pressure ratio, which compares the dynamic pressure of the fluid to the transmural pressure difference required for the tube to collapse. Figure 3.12 shows that in previous experiments, Dc is of the order 10^{-5} (which is also the case in our own experiments), but this seems to suggest that the fluid does not play a significant role in the opening and closing of the tube. This cannot be the case, since without fluid flow there are no self-excited oscillations. Fundamentally, this is because Dc does not take into account the fact that the tube oscillates about a strongly deformed state.

Dc must be adjusted in two ways to understand how it is that fluid flow influences collapse. Firstly, the relevant collapse pressure is not the pressure at which the tube initially collapses, but the pressure at which the tube *totally* collapses. In previous work these pressures are very similar because the tubes considered were not held in tension, but in our experiments they are somewhat different. Secondly, the dynamic pressure used in Dc is that

at the point where p_1 is measured, but the dynamic pressure at the narrowest point of the tube will be significantly higher than this. This is the primary reason why Dc seems to be too low. If we use the collapse pressure (see eq. (8.12b)), and estimate the dynamic pressure of the fluid at the narrowest point of the tube, then we obtain a Dc of around 0.3, as shown in fig. 8.15. The collapse of our results shown in fig. 8.15 also gives us a good way of estimating the flowrate needed for the instability to happen.

8.4.4 Dynamic Instability

The instability considered in §8.4.1 is a **divergence instability**, for which we do not need to know specific details of the dynamical behaviour of the system. This does not predict self-excited oscillations, so clearly some aspect of the dynamical behaviour is important in the onset of oscillations.

To fully analyse this problem would require us to linearise the shell equations in §5 about the collapsed state of the tube, coupled to the Navier-Stokes equations linearised about the complex flow through the fully collapsed tube. There is no analytical way of doing this, and the resulting treatment would be highly complex. However, there are simpler methods that we can employ to get a good physical understanding of what is happening when self-excited oscillations start.

We know that the tube is at or close to total collapse at onset. The cross-sectional area of the flexible tube at onset indicates that the flow within the flexible tube has separated downstream of the narrowest section. When the tube law is close to total collapse, the "hump" in the fluid law has been passed, and this hump corresponds to the point at which flow within the tube separates.

The separation of flow within the tube suggests that eddies and other flow structures could play a significant role in exciting the oscillations. An initial test of this is the value of the Strouhal number during oscillations. We modify the Strouhal number used in §3.1, and define it based on the tube length l, and the average velocity in the uncollapsed part of the tube,

$$St = \frac{fl}{v}, \text{ where } v = \frac{Q}{\pi a^2}. \tag{8.14}$$

Defined in this way, the Strouhal number compares the time taken for an eddy to convect the tube length with the length of time for a single oscillation, and in fig. 8.16 we plot the

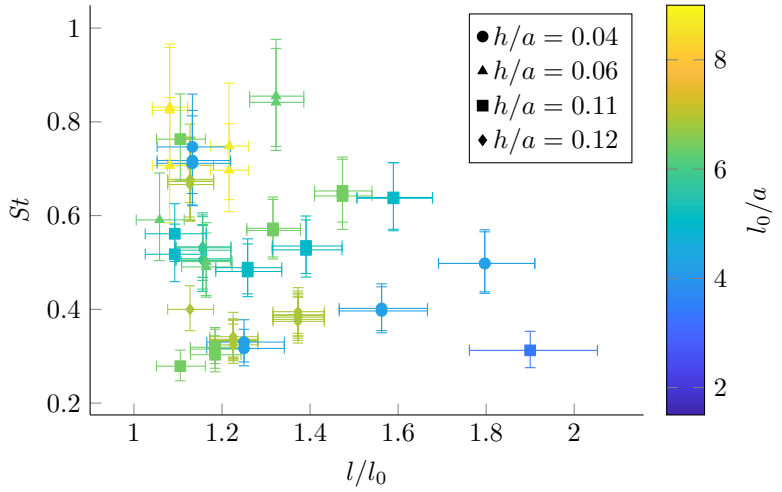


Figure 8.16: The value of the Strouhal number at the onset of self excited oscillations.

value of this variable at the onset of oscillations. The Strouhal number is between 0.2 and 1, which indicates that the convection of eddies through the tube can play a significant role.

We hypothesise that eddies shed from the narrowest section of the tube convect downstream, and in doing so excite a longitudinal wave in the tube, which reflects from the downstream end, and travels upstream as an elastic wave. If the frequency with which this wave bounces up and down the tube is the same as the natural frequency of an opening and closing mode of the tube, then this would extract energy from the flow and allow it to drive the oscillation of the tube, which is necessary for self excited oscillations. The value of the Strouhal number provides some evidence that this mechanism is correct, but further evidence is provided by direct observation of the high speed video of self-excited oscillations, which was discussed in §8.1. The videos show longitudinal waves travelling along the tubes as they open and close during oscillations.

We denote the speed of the downstream longitudinal wave v, and the speed of the upstream longitudinal wave c_g. Given the length of the tube, the frequency associated with the longitudinal wave is $1/(l/v + l/c_g)$. Hence, we expect $f(l/v + l/c_g)$ to be one. In fig. 8.17 we plot this quantity as observed in high speed video of the self excited oscillations just after onset, and we see that its value is as expected, apart from one run in which $f(l/v + l/c_g) = 0.5$. In this case, the longitudinal wave is bouncing up and down the tube twice every time the tube opens and closes.

§6.3 indicates that the longitudinal wave is not only controlled by elasticity. Therefore

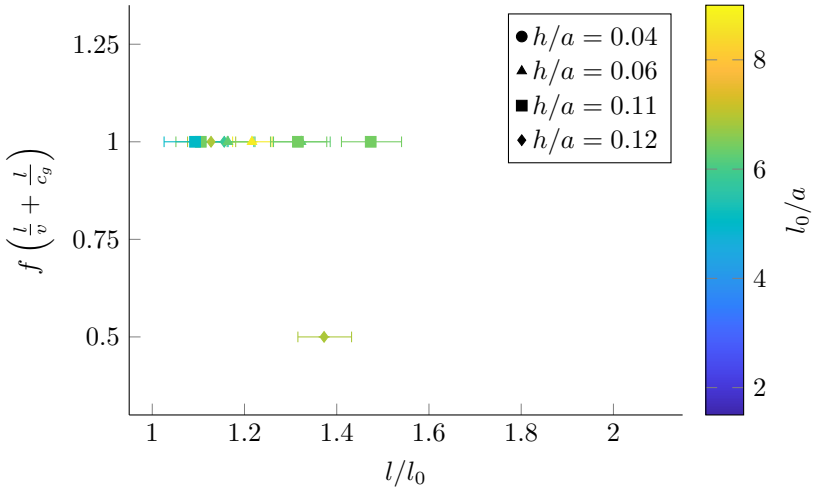


Figure 8.17: The frequency of oscillations at onset in high speed video.

we suggest that the downstream travelling wave is the result of a flow eddy being convected, while the upstream travelling wave is controlled by the wave speed of an elastic wave flowing through the tube.

The speed of the downstream travelling wave can be roughly estimated based on the flowrate as $v = Q/(\pi a^2)$. The upstream wave speed can be estimated using the **group velocity** of an axisymmetric elastic wave travelling axially. This corresponds to c_g from §6.4, with $n = 0$. ν, α, ε, and $\sqrt{E/\rho_s(1-\nu^2)}$ defined by the tube. The only unknown in determining c_g is the dimensionless wavenumber k. From the high speed video we can see that the wavelength of the longitudinal waves is between a and l, which means k is between 2π and $2\pi a/l$. In fig. 8.18 we plot $f(l/v + l/c_g)$ against the axial strain l/l_0, also indicating the other geometric parameters of the tube. We see that the Strouhal number covers the correct range, though the data is spread out due to the inaccuracy of c_g and v. Note that the prediction of frequency based purely on the elastic modes of the tube is wrong by an order of magnitude. This observation, combined with the high-speed video provides strong evidence that the frequency of oscillations at onset is set by the longitudinal waves.

For the proposed flutter mechanism at onset, the longitudinal vibration frequency must match the transverse vibration frequency (i.e. the frequency of oscillation of A_c). To understand how this is possible we note that onset occurs in a region of the tube law where the gradients of the fluid and tube law vary significantly. The difference between these gradients is effectively a stiffness for transverse oscillations, and so in this region the resonant frequency

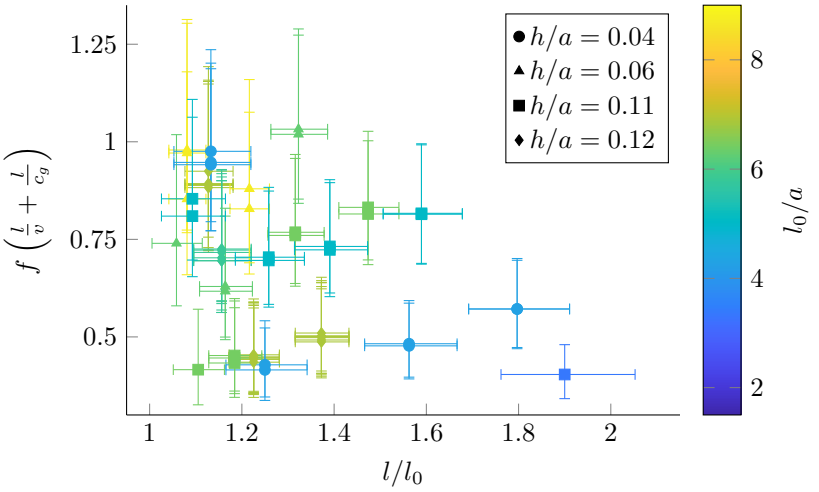


Figure 8.18: The frequency of oscillations at onset.

of transverse oscillations will vary significantly. Therefore, oscillations will start when the resonant frequency of transverse oscillations matches that of the longitudinal waves. The other place on the tube law that this could happen is when $p_e - p_d$ is small such that the tube just starts to close, but here the flow inside the tube will not have separated, and so there is no way for the flow to drive the longitudinal wave, and hence the oscillations cannot be self excited.

8.5 Applying the Mechanism to the Lung

According to the understanding developed in this chapter, in order for self-excited oscillations to happen, the transmural pressure across the tube wall must be large enough to bring the tube to near total collapse (fig. 8.14). In addition, flow through the tube must result in a dynamic pressure comparable to the collapse pressure of the tube, more specifically, the dynamic to collapse pressure ratio should match with fig. 8.15. If the flow through the tube satisfies these conditions then self-excited oscillations should appear, and their frequency can be estimated using the modified Strouhal number $f(l/v + l/c_g)$.

To apply this to the lung we need a model of airflow through the lung. We already have a model for the geometry of the airways themselves from Horsfield and Cumming, 1968; Horsfield et al., 1982. In §3.2.3 we used this to get crude estimates for the Reynolds number throughout the lung, but we now need a more detailed model for flowrates and pressures in different parts of the lung. To obtain this we will take the branching network of the lung from

the trachea down to (say) the 10th generation, then apply a pressure boundary condition at the top of the trachea and the end of each 10th generation tube. For example, it would be reasonable to assume that the pressure difference between the end of the trachea and the 10th generation is 500 Pa [Lai-Fook and Rodarte, 1991]. Given this pressure boundary condition we now assume that the pressure loss in each tube that makes up the airways satisfies the **Darcy-Weisbach equation**,

$$\frac{\Delta p}{l} = f_D \frac{\rho}{2} \frac{v^2}{d}, \tag{8.15}$$

where f_D is the **Darcy friction factor**, whose value is a function of the Reynolds number and the relative roughness of the tube wall. When flow through a tube is laminar ($Re < 2000$) f_D is given by $f_D = 64/\,Re$. When flow is turbulent, we use the expression recommended by [Jarić et al., 2011]. Given this pressure-flow relationship for all of the airway tubes and the pressure boundary condition already discussed, we can find the flowrates and pressure drops throughout the branching network of tubes under consideration.

In fig. 8.19 we show a visual representation of the airways (according to the Horsefield model), coloured according to the average fluid velocity through each tube, given that the overall pressure drop from the outermost airways to the end of the trachea is 500 Pa. We can see the general trend, with some local exceptions, of velocity getting lower as we mover further into the lung. In this example we have used the first 12 generations of the bronchial tree, which make the computation reasonably quick. In fig. 8.20 we have plotted the calculated fluid velocity at 4 different locations in the bronchial tree as a function of the number of bronchial generations included in the calculation. We can see that truncating the bronchial tree results in an overestimate of fluid velocity, but that the result is starting to converge as we increase the number of included generations above 12. It is not practical for us to include more than 13 generations in our computations, but it seems that this will still give us a reasonable estimate of the flow conditions in the upper airways.

We will now compare the transmural pressure calculated in the airways to the pressure required to collapse the tube. In fig. 8.21 we have again shown the Horsefield lung model, but now coloured by the ratio of the maximum transmural pressure p_{tm} (calculated from the flow model) to the collapse pressure $(p_e - p_c)^*$ (calculated using eq. (8.12b)). We can see that the transmural pressure is well below that needed for tube collapse. It is also clear

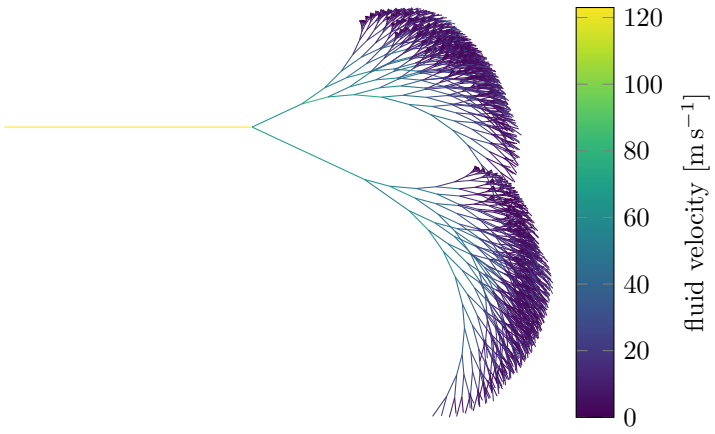


Figure 8.19: A visualisation of the first 12 generations of the Horsefield lung model, where airways are coloured according to the average fluid velocity through them given an overall pressure drop of 500 Pa.

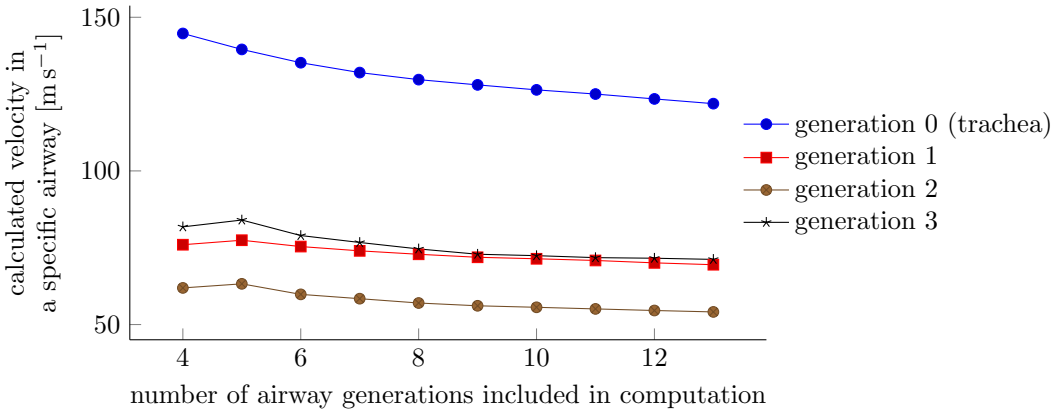


Figure 8.20: The convergence of the calculated fluid velocity at 4 locations in the bronchial tree as the number of bronchial generations included in the calculation is increased.

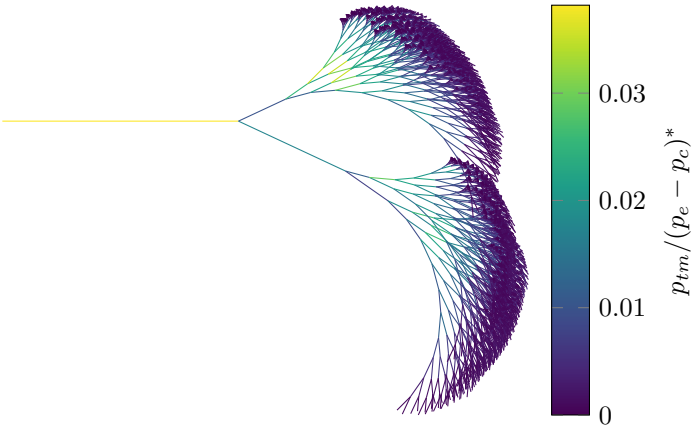


Figure 8.21: The ratio of the transmural pressure across and airway to the pressure required to collapse the airway. 13 generations of the bronchial tree were used for this calculation.

that the tubes closest to collapse are the trachea and the airways in generations 3–5 of the bronchial tree, which is where most wheezing is believed to occur. The fact that none of the airways are shown to be near collapse indicates that during normal breathing wheezing is unlikely, which is indeed what is observed in reality.

To investigate further we can plot the dynamic to collapse pressure ratio throughout the bronchial tree, as in fig. 8.22. We can see that in most of the tree Dc is too small for self excited oscillations (according to fig. 8.15), but it has approximately the right value in the trachea and (once again) in generations 3–5 of the bronchial tree. This indicates that the main barrier to self-excited oscillations is getting the transmural pressure large enough for the collapse pressure to be reached. This could be done by an obstruction resulting in a large pressure drop, which would lower the pressure in downstream tubes, increasing the transmural pressure. Of course, obstruction is the clinical condition most associated with wheezing.

There are a great many approximations in the flow model presented here, but it demonstrates how our understanding of onset can be applied to the lung, and even with these approximations we can gain some insight into common observations that are made of wheezing. There is also the possibility of using the modified Strouhal number to help to localise wheezes to particular generations of the airways using the observed frequencies.

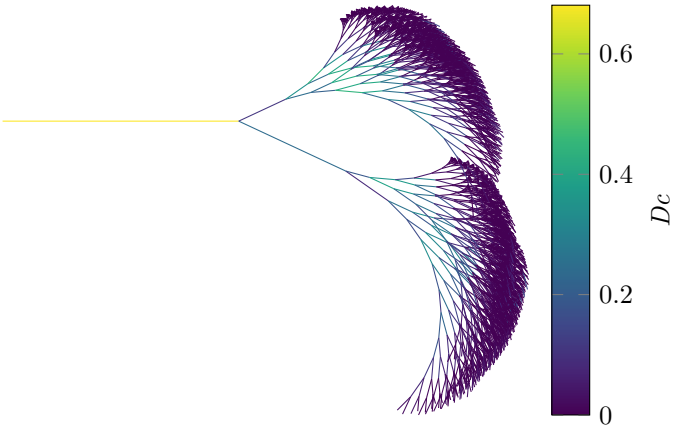


Figure 8.22: The ratio of the dynamic pressure of the fluid within the airway to the pressure required to collapse the airway. 13 generations of the bronchial tree were used for this calculation.

8.6 Summary

We have completed a detailed examination of the equilibrium of the flexible tube and the fluid flowing through our experimental rig. As part of this, we have found the first generalised tube law valid for short tubes held in axial tension, with a novel use of multiple camera stereoscopy.

Using our understanding of the equilibrium of these systems, we have been able to put forward and validate a flutter based model for the onset of self-excited oscillations, ruling out simpler explanations such as oscillations about the cylindrical state of the tube and divergence instability. Results from protocol 1 and protocol 2 support our model, with oscillations happening about a highly deformed state, but in such a way that stretching energy is dominated by bending energy.

The high degree of deformation during oscillations has helped to explain some apparently confusing results from our initial dimensional analysis in §3.1.

As well as gaining physical understanding of the mechanism behind the self-excited oscillations, we have developed a predictive tool for the onset of oscillations in any flexible tube with air flowing through it, which can be applied directly to the airways of the lung.

Chapter 9

Conclusions

We have completed the first experiments into self-excited oscillations of flexible tubes with fluid flowing through them that are of direct relevance to wheezing. To do this we have completed a dimensional analysis which has shown that the main dimensionless parameters that have not been matched by others are the density ratio, length to diameter ratio, and the axial strain of the tube, and we have been able to rectify this.

We have applied the field of geometric algebra to shell theory for the first time, clarifying the roles of angular momentum and velocity by representing them with bivectors. The main new result of this treatment is a new way of understanding changes of curvature through the use of rotors, which allows a more physical understanding of the change of curvature tensor than previous treatments using differential geometry.

The experimental rig was investigated in detail, demonstrating the repeatability of the frequency observed at the onset of oscillations, and showing that this frequency is not significantly influenced by changes to the rig up and downstream of the flexible tube. We have also linearised our shell equations about an axially strained cylinder to show that the normal modes of such a cylinder do not predict the onset frequency that we observe.

Three dimensional tracking of the surface of the tube has been used to show that during self-excited oscillations bending energy is dominated by strain energy. The new representation of the change of curvature tensor enables a new scaling analysis that shows that this will be the case for the airways in the lung.

To understand the mechanism behind the onset of oscillations we have developed a new tube law, valid for short tubes held in axial tension, through a novel use of multiple camera

stereoscopy, and described the equilibrium of the fluid flowing through the experimental rig. The combination of these equilibrium models allows the development of a flutter-based model for onset, which is supported by results from both experimental protocols. We have ruled out a divergence instability and shown that oscillations occur about a strongly deformed state. This has helped to explain some apparent problems with our initial dimensional analysis, and has also allowed us to create a predictive tool of direct relevance to wheezing in the lungs.

References

Addison, P. S. (2002). *The Illustrated Wavelet Transform Handbook: Applications in Science, Engineering, Medicine and Finance*. IOP Publishing, Bristol and Philadelphia.

Agalovyan, L. A. (2002). The solution asymptotics of classical and nonclassical, static and dynamic boundary-value problems for thin bodies. *Int. Appl. Mech.*, 38(7):765–782.

Al Jarad, N., Strickland, B., Bothamley, G., Lock, S., Logansinclair, R., and Rudd, R. (1993). Diagnosis of Asbestosis by a Time Expanded Wave-Form Analysis, Auscultation and High-Resolution Computed-Tomography - a Comparative-Study. *Thorax*, 48(4):347–353.

Alijani, F. and Amabili, M. (2014). Non-linear vibrations of shells: A literature review from 2003 to 2013. *Int. J. Non. Linear. Mech.*, 58:233–257.

Allingame, S., Williams, T., Jenkins, S., and Tucker, B. (1995). Accuracy and reliability of physiotherapists in the interpretation of tape-recorded lung sounds. *Aust J Physiother*, 41(3):179–184.

Alsmadi, S. and Kahya, Y. P. (2008). Design of a DSP-based instrument for real-time classification of pulmonary sounds. *Comput. Biol. Med.*, 38(1):53–61.

Altay, G. A. and Dokmeci, M. C. (2001). Coupled thermoelastic shell equations with second sound for high-frequency vibrations of temperature-dependent materials. *Int. J. Solids Struct.*, 38(16):2737–2768.

Altenbach, J., Altenbach, H., and Eremeyev, V. A. (2010). On generalized Cosserat-type theories of plates and shells: A short review and bibliography. *Arch. Appl. Mech.*, 80(1):73–92.

Andrès, E., Hajjam, A., and Brandt, C. (2012). Advances and innovations in the field of auscultation, with a special focus on the development of new intelligent communicating stethoscope systems. *Health Technol. (Berl).*, 2(1):5–16.

Antman, S. (2005). *Nonlinear problems of elasticity*. Springer-Verlag, Berlin, 2nd edition.

Armitstead, J. P., Bertram, C. D., and Jensen, O. E. (1996). A study of the bifurcation behaviour of a model of flow through a collapsible tube. *Bull. Math. Biol.*, 58(4):611–641.

Arnold, R. N. and Warburton, G. B. (1949). Flexural Vibrations of the Walls of Thin Cylindrical Shells Having Freely Supported Ends. *Proc. R. Soc. A Math. Phys. Eng. Sci.*, 197(1049):238–256.

Arthur, J. W. (2011). *Understanding geometric algebra for electromagnetic theory*. John Wiley and Sons, Checester.

Avramov, K. V. and Mikhlin, Y. V. (2013). Review of Applications of Nonlinear Normal Modes for Vibrating Mechanical Systems. *Appl. Mech. Rev.*, 65(2):020801.

Bahoura, M. (2006). Separation of Crackles From Vesicular Sounds Using Wavelet Packet Transform. *2006 IEEE Int. Conf. Acoust. Speed Signal Process. Proc.*, 2:II–1076–II–1079.

Barenblatt, G. I. (2003). *Scaling*. Cambridge University Press.

Baughman, R. P. and Loudon, R. G. (1984). Quantitation of wheezing in acute asthma. *Chest*, 86(5):718–722.

Baughman, R. P. and Loudon, R. G. (1985). Lung sound analysis for continuous evaluation of airflow obstruction in asthma. *Chest*, 88(3):364–368.

Beck, R., Elias, N., Shoval, S., Tov, N., Talmon, G., Godfrey, S., and Bentur, L. (2007). Computerized acoustic assessment of treatment efficacy of nebulized epinephrine and albuterol in RSV bronchiolitis. *BMC Pediatr.*, 7(1):22.

Bentur, L., Beck, R., Shinawi, M., Naveh, T., and Gavriely, N. (2003). Wheeze monitoring in children for assessment of nocturnal asthma and response to therapy. *Eur. Respir. J.*, 21(4):621–626.

Bertram, C. D. (1986). Unstable equilibrium behaviour in collapsible tubes. *J. Biomech.*, 19(1):61–69.

Bertram, C. D. (1987). The effects of wall thickness, axial strain and end proximity on the pressure-area relation of collapsible tubes. *J. Biomech.*, 20(9):863–876.

Bertram, C. D. (2003). Experimental Studies of Collapsible Tubes. In Carpenter, P. W. and Pedley, T. J., editors, *Flow past Highly Compliant Boundaries Collapsible Tubes*, pages 51–65. Kluwer Academic Publishers.

Bertram, C. D. and Butcher, K. S. A. (1992). A collapsible-tube oscillator is not readily enslaved to an external resonator. *J. Fluids Struct.*, 6(2):163–180.

Bertram, C. D. and Castles, R. J. (1999). Flow Limitation in Uniform Thick-Walled Collapsible Tubes. *J. Fluids Struct.*, 13(3):399–418.

Bertram, C. D. and Elliott, N. S. J. (2003). Flow-rate limitation in a uniform thin-walled collapsible tube, with comparison to a uniform thick-walled tube and a tube of tapering thickness. *J. Fluids Struct.*, 17(4):541–559.

Bertram, C. D. and Nugent, A. H. (2005). The Flow Field Downstream of an Oscillating Collapsed Tube. *J. Biomech. Eng.*, 127(1):39–45.

Bertram, C. D. and Pedley, T. J. (1982). A mathematical model of unsteady collapsible tube behaviour. *J. Biomech.*, 15(1):39–50.

Bertram, C. D. and Raymond, C. J. (1991). Measurements of Wave Speed and Compliance in a Collapsible Tube during Self-Excited Oscillations - a Test of the Choking Hypothesis. *Med. Biol. Eng. Comput.*, 29(5):493–500.

Bertram, C. D., Raymond, C. J., and Pedley, T. J. (1990). Mapping of instabilities for flow through collapsed tubes of differing length. *J. Fluids Struct.*, 4(2):125–153.

Bertram, C. D., Raymond, C. J., and Pedley, T. J. (1991). Application of nonlinear dynamics concepts to the analysis of self-excited oscillations of a collapsible tube conveying a fluid. *J. Fluids Struct.*, 5(4):391–426.

Bertram, C. D. and Sheppeard, M. D. (2000). Interactions of pulsatile upstream forcing with flow-induced oscillations of a collapsed tube: Mode-locking. *Med. Eng. Phys.*, 22(1):29–37.

Bertram, C. D., Truong, N. K., and Hall, S. D. (2008). PIV measurements of the flow field just downstream of an oscillating collapsible tube. *J. Biomech. Eng.*, 130(6):061011.

Bertram, C. D. and Tscherry, J. (2006). The onset of flow-rate limitation and flow-induced oscillations in collapsible tubes. *J. Fluids Struct.*, 22(8):1029–1045.

Bohadana, A., Izbicki, G., and Kraman, S. S. (2014). Fundamentals of Lung Auscultation. *N. Engl. J. Med.*, 370(8):744–751.

Broekhuizen, B. D. L., Sachs, A. P. E., and et al Verheij, T. J. (2012). Accuracy of symptoms, signs, and C-reactive protein for early chronic obstructive pulmonary disease. *Br J Gen Pr.*, 62(602):e632–e638.

Brower, R. W. and Noordergraaf, A. (1973). Pressure-flow characteristics of collapsible tubes: A reconciliation of seemingly contradictory results. *Ann. Biomed. Eng.*, 1(3):333–355.

Burke, M. A., Lucey, A. D., Howell, R. M., and Elliott, N. S. J. (2014). Stability of a flexible insert in one wall of an inviscid channel flow. *J. Fluids Struct.*, 48(C):435–450.

Cai, Z. X. and Luo, X. (2002). Self-excited oscillations in a fluid-beam collapsible channel. In *Am. Soc. Mech. Eng. Int. Mech. Eng. Congr. Expo.*, page 39025.

Cancelli, C. and Pedley, T. J. (1985). A separated-flow model for collapsible- tube oscillations. *J. Fluid Mech.*, 157:375–404.

Carrera, E. (2002). Theories and finite elements for multilayered, anisotropic, composite plates and shells. *Arch. Comput. Methods Eng.*, 9(2):87–140.

Cen, S. and Shang, Y. (2015). Developments of Mindlin-Reissner plate elements. *Math. Probl. Eng.*, 2015:456740.

Chappell, J. M., Iqbal, A., and Abbott, D. (2010). A simplified approach to electromagnetism using geometric algebra. Technical report.

Charbonneau, G., Racineux, J. L., Sudraud, M., and Tuchais, E. (1983). An accurate recording system and its use in breath sounds spectral analysis. *J Appl Physiol*, 55(4):1120–1127.

Charleston-Villalobos, S., Dominguez-Robert, L. F., González-Camarena, R., and Aljama-Corrales, A. T. (2006). Heart sounds interference cancellation in lung sounds. *Annu. Int. Conf. IEEE Eng. Med. Biol. - Proc.*, 1:1694–1697.

Chen, E. J., Novakofski, J., Kenneth Jenkins, W., and O'Brien, W. D. (1996). Young's modulus measurements of soft tissues with application to elasticity imaging. *IEEE Trans. Ultrason. Ferroelectr. Freq. Control*, 43(1):191–194.

Ciarlet, P. G. (2000). *Mathematical Elasticity, Volume III: Theory of Shells*. Elselvier.

Ciarlet, P. G. (2005). *An introduction to differential geometry with applications to elasticity*. Springer Netherlands.

Cohen, A. and Landsberg, D. (1984). Analysis and Automatic Classification of Breath Sounds. *IEEE Trans. Biomed. Eng.*, BME-31(9):585–590.

Cohen, R. T., Madadi, A., Blinder, M. A., Debaun, M. R., Strunk, R. C., and Field, J. J. (2011). Recurrent, severe wheezing is associated with morbidity and mortality in adults with sickle cell disease. *Am. J. Hematol.*, 86(9):756–761.

Coleman, J. J., Ferner, R. E., Klein, M., and Koff, R. S. (2014). Response to Fundamentals of Lung Auscultation N Engl J Med 2014,370,744-751. *N. Engl. J. Med.*, 370(21):2052–2053.

Complete Anatomy (2017). *version 3.2.0 (5321)*. 3D4Medical Ltd., Dublin, Ireland.

Conrad, W. A. (1969). Pressure-flow relationships in collapsible tubes. *IEEE Trans Biomed Eng*, 16(4):284–295.

Cosserat, E. and Cosserat, F. (1909). *Theorie des corps deformables*. Herman et Fils, Paris.

Cottin, V. and Cordier, J. F. (2012). Velcro crackles: The key for early diagnosis of idiopathic pulmonary fibrosis? *Eur. Respir. J.*, 40(3):519–521.

Cousins, C. and Sharp, C. (2004). Medical international procedures-reducing the radiation risks. *Clin. Radiol.*, 59(6):468–473.

Davies, C. and Carpenter, P. W. (1997). Instabilities in a plane channel flow between compliant walls. *J. Fluid Mech.*, 352(1997):205–243.

Dawson, S. V. and Elliott, E. A. (1977). Wave-speed limitation on expiratory flow - a unifying concept. *J. Appl. Physiol. Respir. Environ. Exerc. Physiol.*, 43(3):498–515.

de Jong, P. A., Long, F. R., Wong, J. C., Merkus, P. J., Tiddens, H. A., Hogg, J. C., and Coxson, H. O. (2006). Computed tomographic estimation of lung dimensions throughout the growth period. *Eur. Respir. J.*, 27(2):261–267.

Dodge, R. R. and Burrows, B. (1980). The prevalence and incidence of asthma and asthma-like symptoms in a general population sample. *Am. Rev. Respir. Dis.*, 122(4):567–575.

Doran, C. and Lasenby, A. N. (2003). *Geometric Algebra for Physicists*. Cambridge University Press, Cambridge.

Dorantes-Méndez, G., Charleston-Villalobos, S., González-Camarena, R., Chi-Lem, G., and Aljama-Corrales, T. (2008a). Imaging of simulated crackle sounds distribution on the chest. *Conf. Proc. IEEE Eng. Med. Biol. Soc.*, 2008(c):4801–4804.

Dorantes-Méndez, G., Charleston-Villalobos, S., González-Camarena, R., Chi-Lem, G., Carrillo, J. G., and Aljama-Corrales, T. (2008b). Crackles detection using a time-variant autoregressive model. *Proc. Annu. Int. Conf. IEEE EMBS*, pages 1894–1897.

Dorst, L., Doran, C. J. L., and Lasenby, J. (2002). *Applications of Geometic Algebra in Computer Science and Engineering*. Springer.

Dorst, L. and Lasenby, J. (2011). *Guide to Geometric Algebra in Practice*. Springer.

Du, Q., Zou, G., Zhang, B., and Wan, Z. (2015). Simplified theoretical solution of circular toroidal shell with ribs under uniform external pressure. *Thin-Walled Struct.*, 96:49–55.

Eck, N. J. V. and Waltman, L. (2014). Visualizing bibliometric networks. In Ding, Y., Rousseau, R., and Wolfram, D., editors, *Meas. Sch. impact Methods Pract.*, pages 285–320. Springer International Publishing.

Edlund, B. L. O. (2007). Buckling of metallic shells: Buckling and postbuckling behaviour of isotropic shells, especially cylinders. *Struct. Control Heal. Monit.*, 14(4):693–713.

Elliott, E. A. and Dawson, S. V. (1977). Test of wave-speed theory of flow limitation in elastic tubes. *J. Appl. Physiol.*, 43(3):516–522.

Ellis, P. D. M., Harries, M. L. L., Ffowcs Williams, J. E., and Shneeerson, J. M. (1992). The relief of snoring by nasal surgery. *Clin. Otolaryngol. Allied Sci.*, 17(6):525–527.

Falk, T. H. and Chan, W.-Y. Y. (2008). Modulation filtering for heart and lung sound separation from breath sound recordings. In *Proc. Annu. Int. Conf. IEEE EMBS*, pages 1859–1862. IEEE.

Farshidianfar, A. and Oliazadeh, P. (2012). Free Vibration Analysis of Circular Cylindrical Shells: Comparison of Different Shell Theories. *Int. J. Mech. Appl.*, 2(5):74–80.

Fenton, T. R., Pasterkamp, H., Tal, A., and Chernick, V. (1985). Automated Spectral Characterization of Wheezing in Asthmatic Children. *IEEE Trans. Biomed. Eng.*, BME-32(1):50–55.

Ferns, T. and West, S. (2008). The art of auscultation: evaluating a patient's respiratory pathology. *Br. J. Nurs.*, 17(12):772–777.

Finkelstein, E. (2008). The Ultimate Acoustic Stethoscope Review. http://www.forusdocs.com/reviews/Acoustic_Stethoscope_Review_page4.htm.

Fischl, M. A., Pitchenik, A., and Gardner, L. B. (1981). An Index Predicting Relapse and Need for Hospitalization in Patients with Acute Bronchial Asthma. *N. Engl. J. Med.*, 305(14):783–789.

Fiz, J. A., Jané, R., Homs, A., Izquierdo, J., García, M. A., and Morera, J. (2002). Detection of wheezing during maximal forced exhalation in patients with obstructed airways. *Chest*, 122(1):186–191.

Flietstra, B., Markuzon, N., Vyshedskiy, A., and Murphy, R. L. (2011). Automated analysis of crackles in patients with interstitial pulmonary fibrosis. *Pulm. Med.*, 2011(2):590506.

Forgacs, P. (1967). Crackles and Wheezes. *Lancet*, 290(7508):203–205.

Forgacs, P. (1978a). *Lung Sounds*. Baillière Tindall.

Forgacs, P. (1978b). The functional basis of pulmonary sounds. *Chest*, 73(3):399–405.

Francis, N. A., Melbye, H., Kelly, M. J., Cals, J. W., Hopstaken, R. M., Coenen, S., and Butler, C. C. (2013). Variation in family physicians' recording of auscultation abnormalities in patients with acute cough is not explained by case mix. A study from 12 European networks. *Eur J Gen Pr.*, 19(2):77–84.

Fung, Y. C. (1969). *A First Course in Continuum Mechanics*. Prentice-Hall.

Fung, Y. C. and Cowin, S. C. (1993). *Biomechanics: Mechanical Properties of Living Tissues*. Springer, 2nd edition.

Gavriely, N., Kelly, K. B., Grotberg, J. B., and Loring, S. H. (1987). Forced expiratory wheezes are a manifestation of airway flow limitation. *J. Appl. Physiol.*, 62(6):2398–2403.

Gavriely, N., Palti, Y., Alroy, G., and Grotberg, J. B. (1984). Measurement and theory of wheezing breath sounds. *J. Appl. Physiol.*, 57(2):481–492.

Gavriely, N., Shee, T. R., Cugell, D. W., and Grotberg, J. B. (1989). Flutter in flow-limited collapsible tubes: a mechanism for generation of wheezes. *J. Appl. Physiol.*, 66(5):2251–2261.

Gavrilenko, G. D. and Croll, J. G. A. (2004). Reduced-stiffness method in the theory of shells. *Int. Appl. Mech.*, 40(7):715–743.

Ghaderi, F., Mohseni, H. R., and Sanei, S. (2011). Localizing heart sounds in respiratory signals using singular spectrum analysis. *IEEE Trans. Biomed. Eng.*, 58(12):3360–3367.

Gnitecki, J., Moussavi, Z. M. K., and Pasterkamp, H. (2008). Diagnostic potential in state space parameters of lung sounds. *Med. Biol. Eng. Comput.*, 46(1):93–99.

Godfrey, S., Edwards, R. H. T., Campbell, E. J. M., Armitage, P., and Oppenheimer, E. A. (1969). Repeatability of physical signs in airways obstruction. *Thorax*, 24(4):4–9.

Gregory, A. L. and Agarwal, A. (2017a). Oscillation of Flexible Tubes - Onset and Subsequent Behaviour - The Effect of the Rig [Dataset]. DOI:https://doi.org/10.17863/CAM.15226.

Gregory, A. L. and Agarwal, A. (2017b). Oscillation of Flexible Tubes - Onset and Subsequent Behaviour [Dataset]. DOI:https://doi.org/10.17863/CAM.15218.

Gregory, A. L., Agarwal, A., and Lasenby, J. (2017a). Collapse of Flexible Tubes - The Tube Law [Dataset]. DOI:https://doi.org/10.17863/CAM.15699.

Gregory, A. L., Agarwal, A., and Lasenby, J. (2017b). Oscillation of Flexible Tubes - High Speed Video of Onset [Dataset]. DOI:https://doi.org/10.17863/CAM.10363.

Gregory, A. L., Agarwal, A., and Lasenby, J. (2017c). Using geometric algebra to represent curvature in shell theory with applications to Starling resistors. *R. Soc. Open Sci.*, 4(11):171212.

Gregory, A. L., Agarwal, A., Lasenby, J., and Sinayoko, S. (2015). Geometric Algebra and an Acoustic Space Time for Propagation in Non-Uniform Flow. In *Proc. 22nd Int. Congr. Sound Vib.*, Florence.

Gregory, A. L., Lasenby, J., and Agarwal, A. (2017d). The Elastic Theory of Shells using Geometric Algebra. *R. Soc. Open Sci.*, 4(3):170065.

Gregory, A. L., Sinayoko, S., Agarwal, A., and Lasenby, J. (2014). An acoustic spacetime and the Lorentz transformation in aeroacoustics. *Int. J. Aeroacoustics*, 14(7):977–103.

Grigorenko, Y. M. and Gulyaev, V. I. (1991). Nonlinear problems of shell theory and solution methods (review). *Prikl. Mekhanika*, 27(10):3–23.

Grotberg, J. B. and Davis, S. H. (1980). Fluid-dynamic flapping of a collapsible channel: Sound generation and flow limitation. *J. Biomech.*, 13(3):219–230.

Grotberg, J. B. and Gavriely, N. (1989). Flutter in collapsible tubes: a theoretical model of wheezes. *J. Appl. Physiol.*, 66(5):2262–2273.

Grotberg, J. B. and Jensen, O. E. (2004). Biofluid Mechanics in Flexible Tubes. *Annu. Rev. Fluid Mech.*, 36(1):121–147.

Grotberg, J. B. and Reiss, E. L. (1982). A subsonic flutter anomaly. *J. Sound Vib.*, 80(3):444–446.

Grotberg, J. B. and Reiss, E. L. (1984). Subsonic flapping flutter. *J. Sound Vib.*, 92(3):349–361.

Güler, I., Polat, H., and Ergün, U. (2005). Combining neural network and genetic algorithm for prediction of lung sounds. *J. Med. Syst.*, 29(3):217–231.

Guntupalli, K. K., Alapat, P. M., Bandi, V. D., and Kushnir, I. (2008). Validation of automatic wheeze detection in patients with obstructed airways and in healthy subjects. *J. Asthma*, 45(10):903–907.

Gurung, A., Scrafford, C. G., Tielsch, J. M., Levine, O. S., and Checkley, W. (2011). Computerized lung sound analysis as diagnostic aid for the detection of abnormal lung sounds: A systematic review and meta-analysis. *Respir. Med.*, 105(9):1396–1403.

Gutiérrez, F. and Leon, L. (2000). Elemental Mercury Embolism to the Lung. *N. Engl. J. Med.*, 342(24):1791.

Guz, A. N., Chernyshenko, I. S., Chekhov, V. N., Chekhov, V. N., and Shnerenko, K. I. (1979). Investigations in the theory of thin shells with openings (review). *Sov. Appl. Mech.*, 15(11):1015–1043.

Hadjileontiadis, L. J. (2005a). Wavelet-based enhancement of lung and bowel sounds using fractal dimension thresholding - Part II: Application results. *IEEE Trans. Biomed. Eng.*, 52(6):1050–1064.

Hadjileontiadis, L. J. (2005b). Wavelet-Based Enhancement of Lung and Bowel Sounds Using Fractal Dimension Thresholding Part I: Methodology. *IEEE Trans. Biomed. Eng.*, 52(6):1143–1148.

Hamadiche, M. and Gad-el Hak, M. (2002). Temporal Stability of Flow Through Viscoelastic Tubes. *J. Fluids Struct.*, 16(3):331–359.

Hartley, R. and Zisserman, A. (2004). *Multiple view geometry in computer vision*. Cambridge University Press, 2nd edition.

Heil, M. and Hazel, A. L. (2011). Fluid-Structure Interaction in Internal Physiological Flows. *Annu. Rev. Fluid Mech.*, 43(1):141–162.

Heil, M. and Jensen, O. E. (2003). Flows in deformable tubes and channels. In Carpenter, P. W. and Pedley, T. J., editors, *Flow past Highly Compliant Boundaries Collapsible Tubes*, pages 15–49. Kluwer Academic Publishers.

Heil, M. and Waters, S. L. (2006). Transverse flows in rapidly oscillating elastic cylindrical shells. *J. Fluid Mech.*, 547:185–214.

Heil, M. and Waters, S. L. (2008). How rapidly oscillating collapsible tubes extract energy from a viscous mean flow. *J. Fluid Mech.*, 601:199–227.

Hestenes, D. (2011). The Shape of Differential Geometry in Geometric Calculus. In Dorst, L. and Lasenby, J., editors, *Guid. to Geom. Algebr. Pract.*, pages 393–410. Springer.

Hestenes, D. and Sobczyk, G. (1984). *Clifford Algebra to Geometric Calculus*. A Unified Language for Mathematics and Physics. D. Reidel Publishing Company.

Homs-Corbera, A., Fiz, J. A., Morera, J., and Jané, R. (2004). Time-Frequency Detection and Analysis of Wheezes during Forced Exhalation. *IEEE Trans. Biomed. Eng.*, 51(1):182–186.

Hoppin, F. G., Hughes, J. M. B., and Mead, J. (1977). Axial forces in the bronchial tree. *J. Appl. Physiol.*, 42(5):773–781.

Horsfield, K. and Cumming, G. (1968). Morphology of the bronchial tree in man. *Respir. Physiol.*, 26(2):173–182.

Horsfield, K., Kemp, W., and Phillips, S. (1982). An asymmetrical model of the airways of the dog lung. *J. Appl. Physiol.*, 52(1):21–26.

Huang, L. (1998). Reversal of the Bernoulli Effect and Channel Flutter. *J. Fluids Struct.*, 12(2):131–151.

Huang, L. (2001). Viscous flutter of a finite elastic membrane in Poiseuille flow. *J. Fluids Struct.*, 15(7):1061–1088.

Huang, L. and Ffowcs Williams, J. E. (1999). Neuromechanical interaction in human snoring and upper airway obstruction. *J. Appl. Physiol.*, 86(6):1759–1763.

Huang, L., James Quinn, S., Ellis, P. D. M., and Ffowcs Williams, J. E. (1995). Biomechanics of snoring. *Endeavour*, 19(3):96–100.

Jarić, M., Kolendić, P., Budimir, N., and Genić, V. (2011). A Review of Explicit Approximations of Colebrook's Equation. *FME Trans.*, 39:67–71.

Jensen, O. E. (2013). Instabilities of flows through deformable tubes and channels. In Denier, J. and Finn, M., editors, *Mech. Down Under*, pages 101–116. Springer, Dordrecht.

Johnson, D. (1996). Chebyshev Polynomials in the Spectral Tau Method and Applications to Eigenvalue Problems. Technical Report NASA CR-198451, National Aeronautics and Space Administration, Washington D.C.

Jung, C. H., Ryu, J. S., Baek, S. W., Oh, J. H., Woo, N. S., Kim, H. K., and Kim, J. H. (2013). Radiation exposure of the hand and chest during C-arm fluoroscopy-guided procedures. *Korean J. Pain*, 26(1):51–56.

Kahya, Y. P. and Yilmaz, C. A. (2000). Modeling of Respiratory Crackles. In *Annu. EMBS Int. Conf.*, pages 632–634.

Kamm, R. D. and Pedley, T. J. (1989). Flow in collapsible tubes: a brief review. *Trans. ASME. J. Biomech. Eng.*, 111(3):177–179.

Kandaswamy, A., Kumar, C. S., Ramanathan, R. P., Jayaraman, S., and Malmurugan, N. (2004). Neural classification of lung sounds using wavelet coefficients. *Comput. Biol. Med.*, 34(6):523–537.

Kawamura, T., Matsumoto, T., Tanaka, N., Kido, S., Jiang, Z., and Matsunaga, N. (2003). Crackle analysis for chest auscultation and comparison with high-resolution CT findings. *Radiat. Med.*, 21(6):258–266.

Kaya, E. M. and Elhilali, M. (2013). Abnormality detection in noisy biosignals. *Proc. Annu. Int. Conf. IEEE Eng. Med. Biol. Soc. EMBS*, 2013:3949–3952.

Kizilova, N., Hamadiche, M., and Gad-El-Hak, M. (2012). Mathematical models of biofluid flows in compliant ducts. *Arch. Mech.*, 64(1):65–94.

Koiter, W. (1966). On the nonlinear theory of thin elastic shells. *K. Ned. Akad. van Wet.*, 69B:1–54.

Kozlovsky, P., Zaretsky, U., Jaffa, A. J., and Elad, D. (2014). General tube law for collapsible thin and thick-wall tubes. *J. Biomech.*, 47(10):2378–2384.

Kraman, S. S. (1983). Speed of low-frequency sound through lungs of normal men. *J. Appl. Physiol.*, 55(6):1862–1867.

Kraman, S. S. (1986). Lung sounds for the clinician. *Arch. Intern. Med.*, 146(7):1411–1412.

Kucinschi, B. R., Scherer, R. C., DeWitt, K. J., and Ng, T. T. M. (2006). Flow Visualization and Acoustic Consequences of the Air Moving Through a Static Model of the Human Larynx. *J. Biomech. Eng.*, 128(3):380.

Kumaran, V. (1995a). Stability of fluid flow through a flexible tube at high Reynolds number. *J. Fluid Mech.*, 302:117–139.

Kumaran, V. (1995b). Stability of the viscous flow of a fluid through a flexible tube. *J. Fluid Mech.*, 294:259–281.

Kumaran, V. (1998). Stability of the flow of a fluid through a flexible tube at intermediate Reynolds number. *J. Fluid Mech.*, 357:123–140.

Kundu, P. K., Cohen, I. M., and Dowling, D. R. (2012). *Fluid Mechanics*. Elsevier, 5th edition.

Laënnec, R. T. H. (1819a). *On mediate auscultation, or a treatise on the diagnosis of diseases of the lungs and heart*. Thomas and George Underwood, London, 3rd edition.

Laënnec, R. T. H. (1819b). *Traité de L'Aucultation Médiate*. Brosson Chaudé, Paris.

Lai-Fook, S. J. and Rodarte, J. R. (1991). Pleural pressure distribution and its relationship to lung volume and interstitial pressure. *J. Appl. Physiol.*, 70(3):967–978.

Lancet (2006). A plea to abandon asthma as a disease concept. *Lancet*, 368(9537):705.

Lasenby, A. N., Doran, C. J. L., and Gull, S. (1998). Gravity, gauge theories and geometric algebra. *Philos. Trans. R. Soc. A Math. Phys. Eng. Sci.*, 356(1737):487–582.

Lasenby, J. and Stevenson, A. (2001). Using Geometric Algebra for Optical Motion Capture. In Corrochano, E. B. and Sobczyk, G., editors, *Geom. Algebr. with Appl. Sci. Eng.*, pages 147–169. Birkhäuser, Boston, MA.

Leissa, A. W. (1973). Vibration of shells. Technical Report NASA SP-288, National Aeronautics and Space Administration, Washington D.C.

Lenclud, C., Cuttitta, G., Gansbeke, D. V., Visconti, A., Muylem, A. V., Bellia, V., Yernault, J.-C., Muylem, A. V., and Yemault, J.-C. (1996). Evaluation of nocturnal bronchoconstriction by all night tracheal sound monitoring. *Thorax*, 5151(7):694–698.

Leuppi, J. D., Dieterle, T., Koch, G., Martina, B., Tamm, M., Perruchoud, A. P., Wildeisen, I., and Leimenstoll, B. M. (2005). Diagnostic value of lung auscultation in an emergency room setting. *Swiss Med. Wkly.*, 135(35-36):520–524.

Li, T., Tang, H., Qiu, T., and Park, Y. (2013). Heart sound cancellation from lung sound record using cyclostationarity. *Med. Eng. Phys.*, 35(12):1831–1836.

Li, Z., Batista Abreu, J. C., Leng, J., and Schafer, B. W. (2014). Review: Constrained finite strip method developments and applications in cold-formed steel design. *Thin-Walled Struct.*, 81(SI):2–18.

Lin, B.-S., Lin, B.-S., Wu, H. D., Chong, F.-C., and Chen, S.-J. (2006). Wheeze Recognition Based on 2D Bilateral Filtering of Spectrogram. *Biomed. Eng. Appl. Basis Commun.*, 18:128–137.

Liu, H., Luo, X., and Cai, Z. X. (2009a). Stability and Pressure Boundary Conditions in the Collapsible Channel Flows. In *ASME 2009 Press. Vessel. Pip. Div. Conf.*, page 77767. ASME.

Liu, H., Luo, X., and Cai, Z. X. (2011). Stability and energy budget of pressure-driven collapsible channel flows. *J. Fluid Mech.*, 705:348–370.

Liu, H., Luo, X., Cai, Z. X., and Pedley, T. J. (2009b). Sensitivity of unsteady collapsible channel flows to modelling assumptions. *Commun. Numer. Methods Eng.*, 25(5):483–504.

Logg, A., Mardal, K. A., and Wells, G. N. (2012). *Fenics: Automated Solution of Differential Equations by the Finite Element Method*. Lecture Notes in Computational Science and Engineering. Springer, Berlin, Heidelberg.

Lomboy, G. R., Suthasupradit, S., Kim, K. D., and Onate, E. (2009). Nonlinear formulations of a four-node quasi-conforming shell element. *Arch. Comput. Methods Eng.*, 16(2):189–250.

Lu, B. Y., Wu, H. D., Shih, S. R., Chong, F.-C., Hsueh, M. L., and Chen, Y. L. (2011). Combination of frequency and amplitude-modulated model for the synthesis of normal and wheezing sounds. *Australas. Phys. Eng. Sci. Med.*, 34(4):449–457.

Luo, X., Cai, Z. X., Li, W. G., and Pedley, T. J. (2008). The cascade structure of linear instability in collapsible channel flows. *J. Fluid Mech.*, 600:45–76.

Luo, X., Calderhead, B., Liu, H., and Li, W. (2007). On the initial configurations of collapsible channel flow. *Comput. Struct.*, 85(11-14):977–987.

Luo, X. and Pedley, T. J. (1996). A numerical simulation of unsteady flow in a two-dimensional collapsible channel. *J. Fluid Mech.*, 314:191–226.

Luo, X. and Pedley, T. J. (1998). The effects of wall inertia on flow in a two-dimensional collapsible channel. *J. Fluid Mech.*, 363(1998):253–280.

Mackerle, J. (2000). Finite element linear and nonlinear, static and dynamic analysis of structural elements - an addendum: A bibliography (1996-1999). *Eng. Comput. Int J Comput. Eng.*, 17(3):274–360.

Malhotra, B. D. and Chaubey, A. (2003). Biosensors for clinical diagnostics industry. *Sensors Actuators, B Chem.*, 91(1-3):117–127.

Malmberg, L. P., Sovijarvi, A. R. A., Paajanen, E., Piirila, P., Haahtela, T., and Katila, T. (1994). Changes in frequency spectra of breath sounds during histamine challenge test in adult asthmatics and healthy control subjects. *Chest*, 105(1):122–131.

Marini, J. J., Pierson, D. J., Hudson, L. D., and Lakshminarayan, S. (1979). The significance of wheezing in chronic airflow obstruction. *Am. Rev. Respir. Dis.*, 120(5):1069–1072.

Markel, H. (2006). The stethoscope and the art of listening. *N. Engl. J. Med.*, 354(6):551–553.

Marques, A., Bruton, A., and Barney, A. (2009). The reliability of lung crackle characteristics in cystic fibrosis and bronchiectasis patients in a clinical setting. *Physiol. Meas.*, 30(9):903–912.

Marsden, J. E., Hughes, T. J. R., and Carlson, D. E. (1994). *Mathematical Foundations of Elasticity*. Dover Publications Inc., New York.

MATLAB (2017). *version 9.2.0 (R2017a)*. The Mathworks Inc., Natick, Massachusetts.

Mayorga, P., Druzgalski, C., González, O. H., and Lopez, H. S. (2012). Modified classification of normal lung sounds applying Quantile vectors. *Proc. Annu. Int. Conf. IEEE Eng. Med. Biol. Soc. EMBS*, 2012:4262–4265.

Mayorga, P., Druzgalski, C., Morelos, R. L., González, O. H., and Vidales, J. (2010). Acoustics based assessment of respiratory diseases using GMM classification. *Proc. Annu. Int. Conf. IEEE EMBS*, pages 6312–6316.

Mazic, I., Sovilj, S., and Magjarevic, R. (2003). Analysis of Respiratory Sound in Asthmatics Infant. *Meas. Sci. Rev.*, 3(2):9–12.

McFadden, E. R., Kiser, R., and DeGroot, W. J. (1973). Acute bronchial asthma. Relations between clinical and physiologic manifestations. *N. Engl. J. Med.*, 288(5):221–225.

McRobie, A. (2017). The geometry of structural equilibrium. *R. Soc. Open Sci.*, 4:160759.

McRobie, A. and Lasenby, J. (1999). Simo - Vu Quoc rods using Clifford algebra. *Int. J. Numer. Methods Eng.*, 45(4):377–398.

Medina-Sánchez, M., Martínez-Domingo, C., Ramon, E., and Merkoçi, A. (2014). An inkjet-printed field-effect transistor for label-free biosensing. *Adv. Funct. Mater.*, 24(40):6291–6302.

Meslier, N., Charbonneau, G., and Racineux, J. L. (1995). Wheezes. *Eur. Respir. J.*, 8(11):1942–1948.

Miller, D. S. (1990). *Internal Flow Systems*. BHRA, 2nd edition.

Morgan, G. W. and Ferrante, W. (1955). Wave propagation in elastic tubes filled with streaming liquid. *J. Acoust. Soc. Am.*, 27(4):715–725.

Morgan, G. W. and Kiely, J. P. (1954). Wave Propagation in a Viscous Liquid Contained in a Flexible Tube. *J. Acoust. Soc. Am.*, 26(3):323–328.

Mukhopadhyay, T., Chakraborty, S., Dey, S., Adhikari, S., and Chowdhury, R. (2017). A Critical Assessment of Kriging Model Variants for High-Fidelity Uncertainty Quantification in Dynamics of composite Shells. *Arch. Comput. Methods Eng.*, 24(3):495–518.

Murphy, R. L., Holford, S. K., and Knowler, W. C. (1977). Visual lung-sound characterization by time-expanded wave-form analysis. *N. Engl. J. Med.*, 296(17):968–971.

Murphy, R. L., Vyshedskiy, A., Power-Charnitsky, V.-A., Bana, D. S., Marinelli, P. M., Wong-Tse, A., and Paciej, R. (2004). Automated Lung Sound Analysis in Patients With Pneumonia. *Respir. Care*, 49(12):1490–1497.

Murphy Jr., R. L., Gaensler, E. A., Holford, S. K., Del Bono, E. A., and Epler, G. (1984). Crackles in the early detection of asbestosis. *Am Rev Respir Dis*, 129(3):375–379.

Nagasaka, Y. (2012). Lung sounds in bronchial asthma. *Allergol. Int.*, 61(3):353–363.

Naghdi, P. M. (1972). The theory of shells and plates. In Flugge, S. and Truesdell, C., editors, *Handb. der Phys. (Encyclopedia Physics), Band VIa/2, Festkorpermechanik II (Mechanics Solids II)*, pages 425–640. Springer-Verlag.

Nakahara, M. (2003). *Geometry, Topology and Physics*, volume 822. IOP Publishing, London, 2nd edition.

Nath, A. R. and Capel, L. H. (1974). Inspiratory Crackles - Early and Late. *Thorax*, 29(2):223–227.

National Council on Radiation Protection and Measurements (1987). NCRP Report No. 93, Ionizing Radiation Exposure of the Population of the United States. *Health Phys.*, 97(1):1–5.

Negus, V. E. (1952). Humidification of the air passages. *Thorax*, 7(2):148–151.

Nunn, a. J. and Gregg, I. (1989). New regression equations for predicting peak expiratory flow in adults. *BMJ*, 298(6680):1068–1070.

Oruç, V., Özdinç, M., and Lu, Ç. . (2011). An Experimental Analysis of Airflow in Various Collapsible Tubes at the Onset of Self-Excited Oscillations. *Strojarstvo*, 53(3):153–163.

Pantos, I., Patatoukas, G., Katritsis, D. G., and Efstathopoulos, E. (2009). Patient radiation doses in interventional cardiology procedures. *Curr. Cardiol. Rev.*, 5(1):1–11.

Pasterkamp, H., Carson, C., Daten, D., and Oh, Y. (1989). Digital Respirosonography. *Chest*, 96(6):1405–1412.

Pasterkamp, H., Kraman, S. S., and Wodicka, G. R. (1997). Respiratory sounds: Advances beyond the stethoscope. *Am. J. Respir. Crit. Care Med.*, 156(3 I):974–987.

Pedley, T. J. and Luo, X. (1998). Modelling Flow and Oscillations in Collapsible Tubes. *Theor. Comput. Fluid Dyn.*, 10(1-4):277–294.

Picano, E. and Vano, E. (2011). The Radiation Issue in Cardiology: the time for action is now. *Cardiovasc. Ultrasound*, 9(1):35.

Piirila, P. (1992). Changes in crackle characteristics during the clinical course of pneumonia. *Chest*, 102(1):176–183.

Piirila, P. and Sovijarvi, A. R. A. (1995). Crackles: Recording, analysis and clinical significance. *Eur. Respir. J.*, 8(12):2139–2148.

Piskunov, V. G. and Rasskazov, a. O. (2002). Evolution of the theory of laminated plates and shells. *Methods*, 38(2):135–166.

Qiu, Y., Whittaker, A. R., Lucas, M. L., and Anderson, K. (2005). Automatic wheeze detection based on auditory modelling. *Proc. Inst. Mech. Eng. Part H J. Eng. Med.*, 219(3):219–227.

Reddy, J. N. and Arciniega, R. A. (2004). Shear Deformation Plate and Shell Theories: From Stavsky to Present. *Mech. Adv. Mater. Struct.*, 11(April 2015):535–582.

Reichert, S., Gass, R., Brandt, C., and Andrès, E. (2008). Analysis of respiratory sounds: state of the art. *Clin. Med. Circ. Respirat. Pulm. Med.*, 2:45–58.

Reyes, B. A., Charleston-Villalobos, S., González-Camarena, R., and Aljama-Corrales, T. (2008). Analysis of discontinuous adventitious lung sounds by Hilbert-Huang spectrum. In *Proc. Annu. Int. Conf. IEEE EMBS*, pages 3620–3623. IEEE.

Rice, D. A. (1983). Sound speed in pulmonary parenchyma. *J. Appl. Physiol.*, 54(1):304–308.

Riella, R. J., Nohama, P., and Maia, J. M. (2009). Method for automatic detection of wheezing in lung sounds. *Brazilian J. Med. Biol. Res.*, 42(7):674–684.

Riks, E. and Rankin, C. (1997). Computer simulation of the buckling behavior of thin shells under quasi static loads. *Arch. Comput. methods Eng.*, 4(4):325–351.

Robertson, A. J. and Coope, R. (1957). Rales, rhonchi, and Laennec. *Lancet*, 270(6992):417–423.

Röntgen, W. C. (1896). On a new kind of rays. *Nature*, 53(1369):274–277.

Rueter, D., Hauber, H. P., Droeman, D., Zabel, P., and Uhlig, S. (2010). Low-frequency ultrasound permeates the human thorax and lung: A novel approach to non-invasive monitoring. *Ultraschall der Medizin*, 31(1):53–62.

Sarvazyan, A. P., Urban, M. W., and Greenleaf, J. F. (2013). Acoustic Waves in Medical Imaging and Diagnostics. *Ultrasound Med. Biol.*, 39(7):1133–1146.

Schreur, H. J. W., Vanderschoot, J., Zwinderman, A. H., Dijkman, J. H., and Sterk, P. J. (1994). Abnormal lung sounds in patients with asthma during episodes with normal lung function. *Chest*, 106(1):91–99.

Schwartz, A. R. and Smith, P. L. (2013). CrossTalk proposal: The human upper airway does behave like a Starling resistor during sleep. *J. Physiol.*, 591(9):2229–2232.

Shabtai-Musih, Y., Grotberg, J. B., and Gavriely, N. (1992). Spectral content of forced expiratory wheezes during air, He, and SF6 breathing in normal humans. *J. Appl. Physiol.*, 72(2):629–635.

Shamass, R., Alfano, G., and Guarracino, F. (2015). An investigation into the plastic buckling paradox for circular cylindrical shells under non-proportional loading. *Thin-Walled Struct.*, 95:347–362.

Shamsi, H. and Ozbek, I. Y. (2012). Heart sound localization in chest sound using temporal fuzzy c-means classification. In *Proc. Annu. Int. Conf. IEEE EMBS*, pages 5286–5289. IEEE.

Shapiro, A. H. (1977). Steady Flow in Collapsible Tubes. *J. Biomech. Eng.*, 99(3):126–147.

She, J. and Bertram, C. D. (1996). Numerical simulation of collapsible-tube flows with sinusoidal forced oscillations. *Bull. Math. Bio.*, 58(6):1023–1046.

Shevchenko, V. P. (2007). Fundamental-solution methods in stress-concentration problems for thin elastic shells. *Int. Appl. Mech.*, 43(7):707–725.

Shim, C. S. and Williams, M. H. (1983). Relationship of wheezing to the severity of obstruction in asthma. *Arch. Intern. Med.*, 143(5):890–892.

Simitses, G. J. (1996). Buckling of moderately thick cylindrical shells: a review. *Compos. Part B Eng.*, 27(6):581–587.

Simo, J. C. and Vu-Quoc, L. (1988). On the dynamics in space of rods undergoing large motions - A geometrically exact approach. *Comput. Methods Appl. Mech. Eng.*, 66(2):125–161.

Soedel, W. (1981). *Vibrations of Shells and Plates*. Marcel Dekker, Inc., 3rd edition.

Sovijarvi, A. R. A., Vanderschoot, J., and Earis, J. E. (2000). Standardization of computerized respiratory sound analysis. *Eur. Respir. Rev.*, 10(77):585–649.

Spence, D. P., Bentley, S., Evans, D. H., and Morgan, M. D. (1992). Effect of methacholine induced bronchoconstriction on the spectral characteristics of breath sounds in asthma. *Thorax*, 47(9):680–683.

Standring, S. (2015). *Gray's Anatomy - The Anatomical Basis of Clinical Practice*. Elsevier, 41st edition.

Starcher, B. C. (1986). Elastin and the lung. *Thorax*, 41(8):577–85.

Stark, J. E., Shneerson, J. M., Higenbottam, T., and Flower, C. D. R. (1986). *Manual of Chest Medicine*. Churchill Livingstone.

Staszko, K., Lincho, C., and Engelke, V. (2006). Pulmonary auscultation terminology employed in Brazilian medical journals between January of 1980 and December of 2003. *J. bras. pneumol*, 32(5):400–404.

Stewart, P. S., Waters, S. L., and Jensen, O. E. (2010). Local instabilities of flow in a flexible channel: Asymmetric flutter driven by a weak critical layer. *Phys. Fluids*, 22(3):2–18.

Strogatz, S. H. (1994). *Nonlinear dynamics and chaos*. Perseus Books.

Tahani, M., Andakhshideh, A., and Maleki, S. (2016). Interlaminar stresses in thick cylindrical shell with arbitrary laminations and boundary conditions under transverse loads. *Compos. Part B Eng.*, 98:151–165.

Taplidou, S. a., Hadjileontiadis, L. J., Kitsas, I. K., Panoulas, K. I., Penzel, T., Gross, V., and Panas, S. M. (2004). On applying continuous wavelet transform in wheeze analysis. In *Proc. Annu. Int. Conf. IEEE EMBS*, volume 5, pages 3832–3835. IEEE.

Titze, I. R., Schmidt, S. S., and Titze, M. R. (1995). Phonation threshold pressure in a physical model of the vocal fold mucosa. *J. Acoust. Soc. Am.*, 97(5 Pt 1):3080–3084.

Tompsett, D. H. (1952). A new method for the preparation of bronchopulmonary casts. *Thorax*, 7(1):78–88.

Tornabene, F., Fantuzzi, N., Ubertini, F., and Viola, E. (2015). Strong formulation finite element method based on differential quadrature: A survey. *Appl. Mech. Rev.*, 67(2):020801.

Traister, R. S., Fajt, M. L., Landsittel, D., and Petrov, A. A. (2014). A novel scoring system to distinguish vocal cord dysfunction from asthma. *J. Allergy Clin. Immunol. Pract.*, 2(1):65–69.

Truong, N. K. and Bertram, C. D. (2009). The flow-field downstream of a collapsible tube during oscillation onset. *Commun. Numer. Methods Eng.*, 25(5):405–428.

Tsilingiris, P. T. (2008). Thermophysical and transport properties of humid air at temperature range between 0 and 100 C. *Energy Convers. Manag.*, 49(5):1098–1110.

Verghese, A., Charlton, B., Cotter, B., and Kugler, J. (2010). A history of physical examination texts and the conception of bedside diagnosis. *Trans. Am. Clin. Climatol. Assoc.*, 122:290–311.

von Mises, R. (1914). Der kritische Aussendruck zylindrischer Rohre. *Zeitschr. Ver. Deut. Ingr.*, 58:750–755.

von Mises, R. (1931). The critical external pressure of cylindrical tubes. Technical Report 309, U.S. Experimental Model Basin, Washington D.C.

von Mises, R. (1933). The Critical External Pressure of Cylindrical Tubes Under Uniform Radial and Axial Load. Technical Report 366, U.S. Experimental Model Basin, Washington D.C.

Vyshedskiy, A., Bezares, F., Paciej, R., Ebril, M., Shane, J., and Murphy, R. L. (2005). Transmission of crackles in patients with interstitial pulmonary fibrosis, congestive heart failure, and pneumonia. *Chest*, 128(3):1468–1474.

Vyshedskiy, A., Ishikawa, S., Lh, R., and Jr, M. (2011). Crackle Pitch and Rate Do Not Vary Significantly During a Single Automated-Auscultation Session in Patients With Pneumonia, Congestive Heart Failure, or Interstitial Pulmonary Fibrosis. *Respir Care*, 56(6):806–817.

Vyshedskiy, A. and Murphy, R. L. (2012). Crackle pitch rises progressively during inspiration in pneumonia, CHF, and IPF patients. *Pulm. Med.*, 2012:240160.

Walters, M. C., Heil, M., and Whittaker, R. J. (2017). The effect of wall inertia on high-frequency instabilities of flow through an elastic-walled tube. *Q. J. Mech. Appl. Math.*, 71(1):1–35.

Wang, J. W., Chew, Y. T., and Low, H. T. (2009). Effects of downstream system on self-excited oscillations in collapsible tubes. *Commun. Numer. Methods Eng.*, 25(5):429–445.

Wang, J. Y., Mesquida, P., and Lee, T. H. (2011a). Young's modulus measurement on pig trachea and bronchial airways. In *Proc. Annu. Int. Conf. IEEE EMBS*, pages 2089–2092, Boston, MA.

Wang, J. Y., Mesquida, P., Pallai, P., Corrigan, C. J., and Lee, T. H. (2011b). Dynamic elastic properties of human bronchial airway tissues. *arXiv*.

Weingarten, V. I. (1964). Free vibration of thin cylindrical shells. *AIAA J.*, 2(4):717–722.

Weitz, H. H. and Mangione, S. (2008). In defense of the stethoscope. *Respir. Care*, 53(3):355–369.

Wellman, A., Genta, P. R., Owens, R. L., Edwards, B. A., Sands, S. A., Loring, S. H., White, D. P., Jackson, A. C., Pedersen, O. F., and Butler, J. P. (2014). Test of the Starling resistor model in the human upper airway during sleep. *J. Appl. Physiol.*, 117(12):1478–1485.

West, J. B. (2016). *West's Respiratory Physiology: The Essentials*. Wolters Kluwer, 10th edition.

White, B. (2002). Evolution of curves and surfaces by mean curvature. In *Proc. Int. Congr. Math. Vol. I*, pages 525–538. Higher Ed. Press.

Whittaker, R. J., Heil, M., Jensen, O. E., and Waters, S. L. (2010a). A rational derivation of a tube law from shell theory. *Q. J. Mech. Appl. Math.*, 63(4):465–496.

Whittaker, R. J., Heil, M., Jensen, O. E., and Waters, S. L. (2010b). Predicting the onset of high-frequency self-excited oscillations in elastic-walled tubes. *Proc. R. Soc. A Math. Phys. Eng. Sci.*, 466(June):3635–3657.

Whittaker, R. J., Waters, S. L., Jensen, O. E., Boyle, J., and Heil, M. (2010c). The energetics of flow through a rapidly oscillating tube. Part 1. General theory. *J. Fluid Mech.*, 648:83–121.

Wilkins, R. L. and Dexter, J. R. (1990). Comparing RCPs to physicians for the description of lung sounds: are we accurate and can we communicate? *Respir. Care*, 35(10):969–976.

Williams, B., Boyle, M., and O'Meara, P. (2009). Can undergraduate paramedic students accurately identify lung sounds? *Emerg. Med. J.*, 26(8):580–582.

Xu, F., Billingham, J., and Jensen, O. E. (2013). Divergence-driven oscillations in a flexible-channel flow with fixed upstream flux. *J. Fluid Mech.*, 723:706–733.

Xu, F., Billingham, J., and Jensen, O. E. (2014). Reasonance-driven oscillations in a flexible channel flow with fixed upstream flux and a long downstream rigid segment. *J. Fluid Mech.*, 746:368–404.

Yang, H. T. Y., Saigal, S., Masud, A., and Kapania, R. K. (2000). A survey of recent shell finite elements. *Int. J. Numer. Methods Eng.*, 127(January 1999):101–127.

Yeginer, M. and Kahya, Y. P. (2009). Feature extraction for pulmonary crackle representation via wavelet networks. *Comput. Biol. Med.*, 39(8):713–721.

Yernault, J.-C. and Lenclud, C. (1989). Wheezing and Asthma. In *Prog. asthma COPD*, pages 61–69. Elselvier Science Publishers.

Zarutskii, V. A. (2001). the Theory and Methods of the Stress Strain Analysis of Ribbed Shells. *Int. Appl. Mech.*, 36(10):1259–1283.

Zhang, X., Ajaykumar, R., Sudharsan, N. M., and Kumar, K. (2005). Investigation of two-dimensional channel flow with a partially compliant wall using finite volume-finite difference approach. *Int. J. Numer. Methods Fluids*, 49(6):635–655.

Zhu, Y., Wang, Y., Luo, Z., Han, Q., and Wang, D. (2017). Similitude design for the vibration problems of plates and shells: A review. *Front. Mech. Eng.*, 12(2):253–264.

Appendix A

Work Done by Bivector Torque

Let ω and ω_v be the bivector and vector representations of the angular velocity of a body, related by $\omega = I_3\omega_v$. If q_v is the vector representation of the torque acting on the body then the rate at which work is done on the body is given by $\omega_v \cdot q_v$. Making use of [Doran and Lasenby, 2003, §4.1.3], we can write this as,

$$\begin{aligned}
\omega_v \cdot q_v &= -I_3^2\omega_v \cdot q_v \\
&= -\tfrac{1}{2}I_3^2(\omega_v q_v + q_v\omega_v) \\
&= -\tfrac{1}{2}I_3(I_3\omega_v q_v + I_3 q_v\omega_v) \\
&= -\tfrac{1}{2}I_3(\omega_v I_3 q_v + q_v I_3\omega_v) \\
&= -\tfrac{1}{2}\left((I_3\omega_v)(I_3 q_v) + (I_3 q_v)(I_3\omega_v)\right) \\
&= -(I_3\omega_v)\cdot(I_3 q_v) \\
&= -\omega\cdot(I_3 q_v)
\end{aligned} \tag{A.1}$$

The bivector representation of torque q is related to q_v by $q = I_3 q_v$ (see [Doran and Lasenby, 2003, §3.1.1]), and so the rate of work done by the torque q is given by $-\omega \cdot q$.

Index

adjoint, 74, 77
alveolar duct, 17
alveoli, 17
angular velocity, 115
auscultation, 4

bivector, 70, 119
bivector indices, 93
body forces, 81, 119
body moments, 119
boundary forces, 119
boundary moments, 119
bronchi, 17
bronchioles, 17

camera calibration, 172
camera parameters
    extrinsic, 172, 191
    intrinsic, 171, 191
Cauchy-Green tensor, 75
Cauchy deformation tensor, 76, 106
change of curvature tensor, 110, 179
Christoffel coefficients, 73, 99
cilia, 20
cilliated columnar cells, 20
Clara cell, 20
clinical correlations, 7, 13
collagen, 21
commutator product, 71
constitutive assumption, 89, 133
convected coordinates, 93
convected coordinate system, 74
convected second fundamental form, 109
couple-stress, 83
couple-stress tensor
    first reference, 122
    modified first reference, 123
    modified second reference, 123
    modified spatial, 123
    second reference, 122
    spatial, 121
cross product, 71
CT scanning, 5
curvature, 98, 176
    Gaussian, 99
    mean, 99
curve-shortening flow, 193

Darcy friction factor, 211
DarcyWeisbach equation, 211
deformation gradient, 74, 76
    modified, 107, 122
    polar decomposition, 75
density, 81, 119
directed element, 81

boundary, 84
displacement vector, 109
reference, 76
spatial, 77
divergence instability, 207

elastin, 21
epipolar line, 174
exterior product, 70

fibroblast, 21
fibrocartilage layer, 20
Finger tensor, 76, 106
first fundamental form, 97
fluid law, 197
frame, 71, 72, 95

group velocity, 167, 209

histology, 18

inner product, 70
isothermal, 88

k-nearest neighbour, 8

Laënnec, René, 4
lamina propria, 20
larynx, 17
lipoprotein, 20
local constitutive assumption, 88
lung sound
adventitious, 8, 12
continuous, 12
crackle, 8, 12
intermittent, 12
metric, 22
pleural rub, 12
rhonchus, 8, 12
vesicular, 8, 12
wheeze, 8, 12
lung tissue, 17

macrophage, 21
material derivative, 80, 114
material point, 71
metric, 72, 97, 105
motion, 71, 73
mucosa, 20
mucous gland, 20
multivector, 70

nasal cavity, 17
neural network, 8
normal basis vector, 95

occlusion field, 191
oral cavity, 17
outer product, 70

parenchyma, 17
perichondrium, 20
pharynx, 17
phase velocity, 167
phonopneumogram, 21
Piola tensor, 76, 106
principal strains, 75, 105, 176, 180
projective operator, 96
pseudoscalar, 70, 73, 95

rate of deformation tensor, 78, 114

second order, 117
ray, 174
reference configuration, 71, 93
rejection operator, 96
respiratory tract, 17
reverse, 70, 110
rotation rate tensor, 78, 114
rotor, 110

Saint Venant-Kirchhoff elastic material, 89
second fundamental form, 99
septal wall, 21
serous gland, 20
simple cuboidal epithelium, 20
smooth muscle, 20
spatial configuration, 71, 93
spectrogram, 22
stability, 187, 202
Starling resistor, 24, 37
experimental, 26
theoretical, 29
stethoscope, 4
strain tensor
Biot, 75
Eulerian-Almansi, 76, 107
Green-Lagrangian, 75, 77, 105, 180
logarithmic, 75
spatial, 76, 77, 107
stress, 81
stress principle of Euler and Cauchy, 82, 120
stress tensor
Cauchy, 84, 120
first Piola-Kirchhoff, 85, 122
modified Cauchy, 126
modified second Piola-Kirchhoff, 127
second Piola-Kirchhoff, 85, 122
submucosa, 20
surface forces, 81, 119
surface traction, 82
symmetric rate of deformation tensor, 78, 114

terminal bronchiole, 20
trachea, 17
transmural pressure, 39, 204
triangulation, 171
tube law, 189

ultrasound, 5

vector derivative, 72
intrinsic, 96
velocity
reference, 78, 114
spatial, 78, 114
volume form, 97

wavelet transform, 22
world point, 191